



HAL
open science

Caractérisation d'écoulements plasma sub- et supersoniques par spectroscopie d'émission : application au rayonnement de rentrée terrestre

Damien Le Quang Huy

► **To cite this version:**

Damien Le Quang Huy. Caractérisation d'écoulements plasma sub- et supersoniques par spectroscopie d'émission : application au rayonnement de rentrée terrestre. Other [cond-mat.other]. Université Blaise Pascal - Clermont-Ferrand II, 2014. English. NNT : 2014CLF22462 . tel-01153502

HAL Id: tel-01153502

<https://theses.hal.science/tel-01153502>

Submitted on 19 May 2015

HAL is a multi-disciplinary open access archive for the deposit and dissemination of scientific research documents, whether they are published or not. The documents may come from teaching and research institutions in France or abroad, or from public or private research centers.

L'archive ouverte pluridisciplinaire **HAL**, est destinée au dépôt et à la diffusion de documents scientifiques de niveau recherche, publiés ou non, émanant des établissements d'enseignement et de recherche français ou étrangers, des laboratoires publics ou privés.

N° d'ordre: 2462

Université Blaise Pascal
UF.F.R Sciences et Technologies

von Karman Institute for Fluid Dynamics
Aeronautics and Aerospace Department

ECOLE DOCTORALE DES SCIENCES
FONDAMENTALES N° 790

THESE
présentée pour obtenir le grade de
DOCTEUR D'UNIVERSITE

Spécialité: Physique des Plasmas
Le Quang Huy Damien

**Spectroscopic measurements of sub- and supersonic
plasma flows for the investigation of atmospheric re-entry
shock layer radiation**

Soutenue publiquement le 6 juin 2014, devant la comission d'examen.

Dr. L. Marraffa (ESA/ESTEC, Netherlands), Président
Prof. A. Chikhaoui (IUSTI, Université de Provence, France), Examineur
Prof. D. Hong (GREMI, Université d'Orléans, France), Examineur
Prof. P. André (LAEPT, Université Blaise Pascale, France)
Prof. O. Chazot (von Karman Institute for Fluid Dynamics, Belgium)
Dr. Y. Babou (von Karman Institute for Fluid Dynamics, Belgium)
Assoc. Prof. P. Boubert (CORIA, Université de Rouen, France)
Research Engineer A . K. Mohamed (ONERA, France)
Prof. Emer. M. Dudeck (Université Paris VI ,France)

VON KARMAN INSTITUTE FOR FLUID DYNAMICS
AERONAUTICS AND AEROSPACE DEPARTMENT

UNIVERSITÉ BLAISE PASCAL
LABORATOIRE ARC ÉLECTRIQUE ET PLASMAS THERMIQUES

**Spectroscopic Measurements of Sub- and Supersonic Plasma Flows for
the Investigation of Atmospheric Re-entry Shock Layer Radiation.**

Contact information:

D. Le Quang Huy
von Karman Institute for Fluid Dynamics
72 Chaussée de Waterloo
1640 Rhode-St-Genèse
BELGIUM

Mots clés: Plasma hors équilibre, source plasma, spectroscopie d'émission, écoulement supersonique.

Keywords: Non-equilibrium plasma, plasma wind tunnel, emission spectroscopy, supersonic flow.

Abstract

During planetary atmospheric entries, thermochemical non-equilibrium processes in the shock layer limit the reliability of aerothermal environment prediction. To improve prediction accuracy, non-equilibrium kinetic models are being developed. These models are experimentally assessed through the comparison with well characterized non-equilibrium experiments. For this purpose, the present work is dedicated to the thermodynamic characterization of non-equilibrium in high enthalpy reactive flows. Conversely to common studies that employ short duration facilities to investigate shock layer kinetics, we will assess the possibility of producing significant departure from equilibrium using radio-frequency and microwave stationary plasma flows, including supersonic plasma flows where vibrational non-equilibrium is strongly expected. Suitable spectroscopic diagnostics have been applied allowing future comparisons to be made between the microscopic description of the experiments and theoretical non-equilibrium models.

Résumé

Lors des rentrées atmosphériques, les processus thermo-chimiques hors équilibre dans la couche de choc limitent la fiabilité des prédictions aérothermiques. Afin d'améliorer l'exactitude de ces prévisions, des modèles cinétiques sont actuellement développés. Ces modèles sont expérimentalement évalués à l'aide d'expériences dans lesquelles un départ à l'équilibre thermodynamique est caractérisé. Pour cette raison, le présent travail est consacré à la caractérisation du déséquilibre thermodynamique au sein d'écoulements réactifs à haute enthalpie. La plupart des études expérimentales dédiées à la validation de modèles cinétiques à haute température emploient des installations communément appelées *tubes à choc*. De façon sigulière, nous évaluons ici la possibilité de générer un départ significatif à l'équilibre thermodynamique dans des écoulements plasma stationnaires, incluant des jets supersoniques dans lesquels le déséquilibre vibrationnel est fortement attendu. Des diagnostics spectroscopiques appropriés ont été appliqués, permettant de futures comparaisons avec des descriptions microscopiques issue de modèles théoriques.

Acknowledgements

I would like to thank prof. Pascal André for promoting this work and prof. Olivier Chazot for his constant support and encouragement.

A special thank goes to Dr. Yacine Babou for his tireless support and guidance.

I am grateful to the jury of this thesis for taking the time to read and discuss this dissertation.

I acknowledge prof. Arnaud Bultel and prof. Pascal Boubert for their precious collaboration and constructive suggestions.

I would like to express my deep acknowledgments to my colleagues, in particular to the *VKI Plasmatron team* for the good atmosphere and fruitful discussions.

Thanks to Dr. Bruno Lopez for endless passionate discussions.

Thanks to Dr. Damien Vacher for his experimental support.

Finally, I would like to express my gratitude to Prof. Michel Dudeck and Dr. Mario Lino da Silva for introducing me to the amazing world of atmospheric entries.

This personal work would not have been performed without the collaboration undertaken within the frame of several projects sponsored by the European Space Agency and the European Commission.

Contents

Acknowledgements	vii
1. Introduction	1
1.1. Thermochemical state of radiating shock layer	1
1.1.1. Collisional and radiative processes during re-entry.	4
1.1.2. Local thermodynamic equilibrium assumption.	5
1.2. Atmospheric entry shock layer radiation experiments	6
1.2.1. Past and future missions for in-situ radiation measurement.	6
1.2.2. Ground test facilities for re-entry plasmas duplication.	7
1.3. Objectives and overview of the dissertation	9
2. Plasma source ground test facilities	13
2.1. Construction of a microwave plasma torch driven by surface waves	13
2.1.1. Microwaves generation and transport.	14
2.1.2. Discharge region.	16
2.1.3. Comprehensive characterization of the microwave plasma source.	17
2.2. Inductively coupled plasma torch: Plasmatron facility	32
2.3. Nozzle flow and operating map	34
3. Plasma radiation and experimental rebuilding of emission spectra	39
3.1. Plasma radiation	39
3.1.1. Atomic line transition.	39
3.1.2. Electronic transition of diatomic molecules.	41
3.2. Experimental spectra elaboration	45
3.2.1. Image acquisition.	45
3.2.2. Image processing.	46
3.2.3. Local emission rebuilding.	48
3.2.4. Radiative transfer calculation.	53
4. Optical emission spectroscopy diagnostics	55
4.1. Plasma characterization using atomic contribution	55
4.1.1. Atomic line equilibrium radiation.	55
4.1.2. Atomic excited states distribution.	57
4.1.3. Stark broadening of hydrogen lines.	58
4.2. Plasma characterization using molecular contribution	64
4.2.1. Boltzmann population distribution of internal energy modes.	66
4.2.2. Electronic non-equilibrium.	72
4.2.3. Vibrational non-equilibrium.	75
5. Thermodynamic characterization of subsonic plasma flows	79
5.1. ICP air Plasmatron experiment	79
5.1.1. Boltzmann equilibrium of rotational and vibrational energy modes.	79
5.1.2. Non-LTE molecular emission.	81
5.1.3. Atomic LTE radiation.	89
5.1.4. Unbalanced recombining / ionizing processes.	96
5.2. Microwave sustained nitrogen discharge in the ignition region	99

5.2.1. Assessment of radiative transfer along the line of sight.	99
5.2.2. Effect of microwave power on rotational and vibrational energy modes. . .	100
5.2.3. Effect of operating pressure on rotational and vibrational energy modes. .	101
5.2.4. Electronic excited states of N_2 and N_2^+ molecular system.	105
6. Preliminary description of supersonic plasma flows	109
6.1. Topology	109
6.2. Experimental studies overview	111
6.3. Aerothermochemical processes	113
6.3.1. Weakly ionized plasma expansion	113
6.3.2. Weakly ionized stationary shock front	115
7. Thermodynamic characterization of supersonic plasma flows	119
7.1. ICP air Plasmatron experiment	119
7.1.1. Preliminary observations.	119
7.1.2. Quasi 1D isentropic approximation.	122
7.1.3. Two dimensional thermodynamic characterization.	128
7.2. Microwave sustained nitrogen post discharge	137
7.2.1. Reservoir thermal equilibrium state.	137
7.2.2. Post discharge frozen non-equilibrium state.	141
8. Conclusion	151
8.1. Contribution of the thesis	151
A. Waveguide based microwave device: cavity technical drawings	153
Bibliography	157
List of Tables	167
List of Figures	169

Chapter 1.

Introduction

Aerodynamic transport phenomena and radiative transport processes contribute to the elevated heat transfer rate onto the surface of atmospheric entry vehicles. Convective and radiative heat transfer components, constraining mission design and capabilities, are subject to the entry trajectory and speed, to the vehicle configuration and to the atmospheric composition. For typical re-entry mission, the radiative component on the stagnation point is about 30 % of the total heat flux at the peak radiative heating. Although its contribution can be significant, the radiative heating still remains a critical parameter to evaluate since population of excited states and transition probabilities must be known accurately in order to get reliable predictions.

Analytical expressions [1] or modern numerical codes can be used to evaluate roughly the stagnation point radiative heating based on the assumption that thermochemical equilibrium exists. However, equilibrium predictions fail to predict accurately the radiative heating. In other words and using rhetorical tautology, non-equilibrium shock layer kinetics can not be predicted through equilibrium models. Thermochemical non-equilibrium processes in the shock layer, including a strong level of ionization and high reaction rates are phenomena that limit the reliability of aerothermal environment prediction. Non-equilibrium kinetic models have to be developed in order to replicate the physical processes occurring in the shock layer where the excited gas is subject to complex collisional and radiative processes. Example of calculation involving advanced non-equilibrium kinetic models is presented in figure 1.1, referring to a well known EAST shock tube ground testing experiment. It represents the radiation normalized by the shock diameter D , as a function of the distance from the shock front. The equilibrium model strongly overestimates the radiative overshoot and prediction is greatly improved by the non-equilibrium kinetic model.

Non-equilibrium radiation and thermochemical models ([3], [4], [5], [6]) accounting for non-Boltzmann internal energy distributions and radiative transport in optically thick media are now-days largely developed to refine the predictions on the thermodynamic state in the shock layer. A correct estimation of the surface heat flux requires the validation of these chemical kinetics prediction capabilities. These models, based on collisional-radiative databases, might be experimentally assessed by comparing with well characterized non-equilibrium experiments. For this purpose, the present work is dedicated to the characterization of the thermodynamic non-equilibrium in high enthalpy reactive flows.

1.1. Thermochemical state of radiating shock layer

Planetary entries are characterized by collisional and radiative interaction processes in the high enthalpy shock layer in front of hypersonic flight vehicles traveling at interplanetary speeds. Starting from a high translational energy input in the shock formed in front of entry vehicles, the rotational, vibrational and electronic modes of the molecules are then excited by inter-particle collisions in the shock layer. Energy magnitudes associated with elemental collisional excitation or reaction processes are listed in table 1.1. If the collisions are energetic enough, and accounting for the lower dissociation potential of molecules in elevated vibrational states, dissociation and ionization phenomena may occur and be responsible for the presence of ionized species in the shock layer.

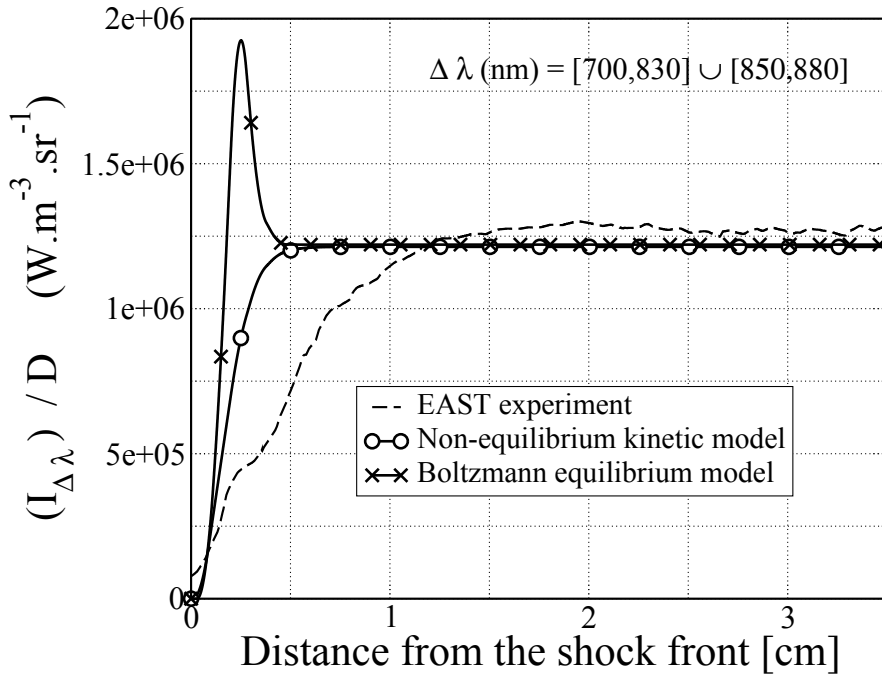


Figure 1.1.: Prediction of non-equilibrium EAST experiment radiation: (courtesy of M. Panesi & al. [2]).

Excitation/Reaction	Energies (eV)
Rotational excitation	10^{-3}
Vibrational excitation	10^{-1}
Electronic excitation	10^0
Dissociation	5×10^0
Ionization	10^1

Table 1.1.: Excitation/Reaction energies

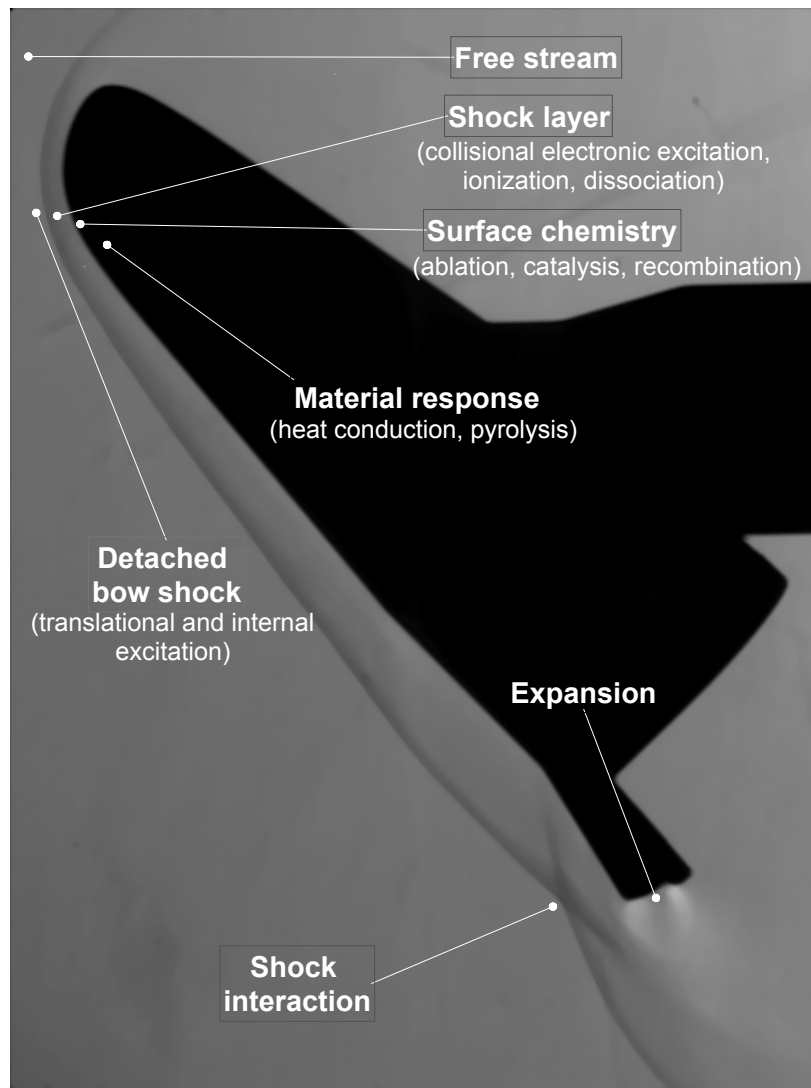


Figure 1.2.: Schematic of the physico-chemical processes and flow field surrounding IXV vehicle during the re-entry phase (Schlieren visualization courtesy of S. Paris [7]).

In the shock layer, the spontaneous de-excitation of the electronic excited states yields the emission of electromagnetic radiation lying between the ultraviolet (UV) and the infrared (IR) spectral region. This radiative flux is highly influenced by the non-equilibrium population distribution of the excited states. A microscopic description of shock layer processes is therefore mandatory to accurately describe the radiative component of the heat flux onto the wall of the vehicle. However, transient high enthalpy effects, strongly coupled to hypersonic aerodynamics, are still not characterized well for complex aeroheating processes such as those illustrated in figure 1.2. Over typical shock layer thickness of a few centimeters, chemical kinetics and radiative processes control the energy distribution of the internal energy modes in the shock layer. The time required for the gas to reach the thermodynamic equilibrium across the shock layer depends strongly on the collision frequency. Depending on the relaxation time scale, various

thermodynamic states are expected to occur along the stagnation streamline. The characteristic hydrodynamic time scale in the shock layer can be estimated to be about 10^{-6} s, for an entry velocity of 10 km.s^{-1} and a 10 cm shock layer thickness.

1.1.1. Collisional and radiative processes during re-entry.

Collisional processes

To characterize the thermodynamic state encountered in the shock layer, it is convenient to estimate the characteristic time scale of the chemical $\tau_{ch.}$ or thermal $\tau_{th.}$ relaxation processes occurring through collisions. Depending on the type of collision, we can distinguish between various energy exchange processes and their associated characteristic relaxation time scale. Each of these processes is responsible for the establishment of different stages of equilibrium. Elastic collisions are mainly responsible for heavy particle heating and relaxation towards translational equilibrium. Nonreactive inelastic collisions are involved in internal energy relaxation and chemical equilibrium is reached through reactive inelastic collisions. A range from faster to slower relaxation processes is commonly defined and complies with the following order:

$$\tau_{trans.} < \tau_{rot.} < \tau_{vib.} < \tau_{chem.} < \tau_{rec./ion.} < \tau_{el.} \quad [8]$$

where each relaxation time τ respectively stands for the translational motion of the particles, the molecular rotations, the molecular vibrations, the dissociation and the chemical reactions, the ionization/recombination, and the electronic relaxation.

In weakly ionized atomic or molecular plasmas, the slowest relaxation time (translational relaxation time) for establishing a Maxwell velocity distribution can be characterized by the time between particle collisions. Following the hard sphere model and using a simple description of the collision, the relaxation time $\tau_{trans.}$ can be expressed as a function of the collisional cross section σ_a as:

$$\tau_{trans.} = \frac{1}{\nu_c} = \frac{1}{n\sigma_a\bar{v}} \quad (1.1)$$

with n the density of the particles of mass m with a thermal speed \bar{v} and ν_c being the collision frequency. In a simple approach of kinetic gas theory, elastic scattering cross section may be approximated by:

$$\sigma_a [m^2] \sim \pi a_0^2 \sim 10^{-20} \text{ using Bohr radius } a_0. \quad (1.2)$$

Considering that thermal speed of particles is defined for atmospheric gas at 10 000 K, the translational relaxation time can be evaluated to about 10^{-7} s. In comparison, vibrational and chemical less efficient kinetic processes are characterized by typical relaxation time scale ranging from 10^{-5} s to 10^{-3} s which is adequate to observe departure from thermal or chemical equilibrium in the vehicle entry shock layer. When the radiation losses in the shock layer are significant, the equilibrium state also strongly depends on the radiative processes.

Radiative processes

Plasma radiation is an important mechanism of energy loss which has an effect on flow and thermal fields in the shock layer. Bound-free transition as photo-dissociation, photo-ionization and radiative recombination represented formally by:



and free-free transitions should be considered in the energy balance of entry plasmas. However, the spectroscopic diagnostics we use will be only dedicated to bound-bound transitions analysis. During an atmospheric entry, radiative energy originates mostly from electronic transition of atoms and molecules. The radiative lifetime $\tau_{rad.}$ for bound-bound transitions is given by the

$N_2(B^3\Pi_g)$	$\tau_{rad.}^{v'}$	$N_2(C^3\Pi_u)$	$\tau_{rad.}^{v'}$	$N_2^+(B^2\Sigma_u^+)$	$\tau_{rad.}^{v'}$
$v'=0$	$13.5 \cdot 10^{-6}$	$v'=0$	$36.7 \cdot 10^{-9}$	$v'=0$	$58.7 \cdot 10^{-9}$
$v'=1$	$11.0 \cdot 10^{-6}$	$v'=1$	$36.6 \cdot 10^{-9}$	$v'=1$	$58.0 \cdot 10^{-9}$
$v'=2$	$9.4 \cdot 10^{-6}$	$v'=2$	$36.9 \cdot 10^{-9}$	$v'=2$	$57.6 \cdot 10^{-9}$
$N_2^+(C^2\Sigma_u^+)$	$\tau_{rad.}^{v'}$	N	$\tau_{rad.}$	O	$\tau_{rad.}$
$v'=0$	$69.5 \cdot 10^{-9}$	694.517 nm	$5.46 \cdot 10^{-7}$	725.445 nm	$2.68 \cdot 10^{-7}$
$v'=1$	$66.9 \cdot 10^{-9}$	742.364 nm	$1.77 \cdot 10^{-7}$	777.194 nm	$2.71 \cdot 10^{-8}$
$v'=2$	$65.0 \cdot 10^{-9}$	818.802 nm	$8.00 \cdot 10^{-8}$	844.625 nm	$3.10 \cdot 10^{-8}$

Table 1.2.: Radiative lifetime [s] of molecular ($\tau_{rad.}^{v'}$) [9] and atomic ($\tau_{rad.}$) [10] bound-bound transitions.

reciprocal value over the sum of all possible transition probability A_{ul_k} from the upper electronic level u to all lower electronic levels l_k as defined in equation 1.4.

$$\tau_{rad.} = \left(\sum_k A_{ul_k} \right)^{-1} \quad (1.4)$$

Table 1.2 illustrates typical radiative time scale for transitions occurring during a re-entry. Radiative time scale is found to be close to the hydrodynamic time scale of a typical re-entry. The radiation can be trapped owing to the opacity of the shock layer. The radiative transport should then be considered to assess the population distribution of excited states. The resolution of the radiative transfer will be detailed in chapter 3, section 3.2.4.

1.1.2. Local thermodynamic equilibrium assumption.

In entry plasmas, non-equilibrium arises from the proximity between energy relaxation and aerodynamic time scale. Based on this assumption, several equilibrium criteria have been proposed. In shock layers, with sufficiently limited optical depth, Local Thermodynamic Equilibrium (LTE) is expected to hold if collisional rate processes dominate radiative processes. In this case, excited energy level population density is determined through the balance between collision induced transitions and collisional excitation. Griem [11] has established a criterion for the determination of a plasma's proximity to LTE. It states that the collisional population rate should be an order of magnitude above the radiative rate. Using average radiative lifetime and collisional cross-section of hydrogenic ions, the estimation of the minimum electron density required for the presence of LTE between energy levels in hydrogenic ions is given by equation 1.5.

$$N_e \geq 9 \times 10^{17} \left(\frac{\Delta^0 E}{E_H} \right)^3 \left(\frac{k_B T_e}{E_H} \right)^{1/2}, [\text{cm}^{-3}] \quad (1.5)$$

where $\Delta^0 E$ is the energy of the first excited state with respect to the ground state, E_H is the ionization energy of the hydrogenic ion and T_e is the electron temperature. Wilson [12] proposed another condition expressed in relation 1.6 that uses the ionization energy.

$$N_e \geq 5.6 \times 10^{17} \left(\frac{\Delta E(\infty)}{E_H} \right)^3 \left(\frac{k_B T_e}{E_H} \right)^{1/2}, [\text{cm}^{-3}] \quad (1.6)$$

where $\Delta E(\infty)$ is the energy level difference between the ground state and the first ionization state.

For the case of a homogeneous plasma shock front traveling at entry speed, Griem [11] has established an additional LTE criterion to account for transient chemical kinetic and radiative processes. It states that equilibration time must be sufficiently short for the establishment of a quasi-stationary near LTE state in the shock heated plasma. Non-equilibrium arises from the difference between local gas dynamical and collisional radiative time scales. The relaxation time is then determined locally by the slowest kinetic process in the shock layer. When the collision frequency is sufficiently high and the radiative processes contribution small, the excited species population variation rate is purely collisional. The characteristic time scale required to reach the Local Thermodynamic Equilibrium (LTE) can be estimated by the dimensionless Damköhler number Da , which is the ratio of the fluid motion time scale τ_{flow} to the internal energy relaxation or chemical reaction time scale $\tau_{ch./th.}$.

$$Da = \frac{\tau_{flow}}{\tau_{chemical/thermal}} \quad (1.7)$$

When $Da \rightarrow \infty$, short internal/chemical energy relaxation time scale allows the thermal/chemical state to adjust instantaneously to the changes in the flow. Conversely, when $Da \rightarrow 0$, the flow is frozen. Non-equilibrium flow conditions are obtained when the Damköhler number is close to unity.

1.2. Atmospheric entry shock layer radiation experiments

1.2.1. Past and future missions for in-situ radiation measurement.

In addition to their real time guidance payload, entry probes are instrumented for post-flight reconstruction. Some vehicles are equipped with additional sets of sensors exposed to the flow around the vehicle to directly measure the surrounding radiation. Few but valuable experiments have been conducted in-flight to measure radiation during the atmospheric entry phase. Shock layer radiation research includes a large proportion of flight data measurements in which the total heating is estimated using thermocouples embedded in the heat shield. Here, we recall only radiometry experiments measuring specifically the radiative heat flux component.

Optical instruments that measure radiation are frequently included in the payload of atmospheric entry probes and landing platforms. Unfortunately, only a few radiation payloads were dedicated to study radiative heating during the entry phase. Instead, the measurements focused on planetary science objectives. For example, the Descent Imager / Spectral Radiometer (DISR) aboard the Huygens Probe of the Cassini mission was dedicated to study the atmosphere of Titan during the descent [13]. The Beagle 2 Mars lander optical instruments were used for the chemical characterization of the Mars surface [14]. The ultraviolet spectrometer aboard the Rosetta space probe was designed to study the composition of comet's atmosphere and surface [15]. Infrared radiometers installed on Venera probes were used to perform thermal radiometry on Venus [16]. In-flight experiments that employ radiometry to assess the radiative heating from bow shocks during the entry phase are rare.

The highly successful FIRE project radiation flight experiments were conducted in the 1960s to determine bow shock emission ahead of the Apollo capsule blunt body [17], [18]. These radiometry and spectroradiometry measurements were carried out to characterize the radiative heating environment for Apollo lunar return missions. The heat shield of the re-entry capsule was instrumented with a spectrometer positioned on the stagnation point where it provides the spectral distribution of the incident radiation. In addition, a radiometer was capable of measuring the total radiation integrated over a large spectral range. Records were performed at various trajectory points that cover equilibrium and non-equilibrium thermodynamic flow regimes. Since then, radiation entry flight instrumentation has been solely dedicated to spectrally integrated measurements without fine spectral resolution. In 1967 for the Apollo 4 mission, stagnation

and offset radiometers were installed on the ablative heat shield of the prototype vehicle of the Apollo Command Module [19], [20]. One year later, the thermal performance of the spacecraft was demonstrated during the Apollo 6 mission in which similar radiation measurements were performed. In 1971, a multiple channel narrow band entry flux radiometer was installed on the PAET (Planetary Atmosphere Experiment Test vehicle) probe, providing spectrally resolved radiation in several discrete frequency spectrum regions [21], [22].

Complementary to entry probe measurements, rocket-borne experiments have been used to measure bow shock radiation at conditions similar to those encountered by entry probes. Although radiative heating does not contribute significantly to ballistic missile heating because of the relatively low flight velocities, rocket tests are still useful. Several high-speed re-entry tests were executed with Trailblazer II rocket flights at relatively low velocities at approximately 3.5 km/s. In particular, ultraviolet diagnostic experiments were carried out in 1990 to record bow shock ultraviolet radiance issued mainly from the nitric oxide γ -band system in the [190-400] nm wavelength range [23], [24], [25]. The Dual-mode Experiment on Bow-shock Interactions (DEBI) project was designed to study the thermal excitation of species in the flow field around missiles traveling at hypersonic velocities [26].

Apart from instrumenting entry vehicles, airborne and ground observation campaigns provide also precious information about aeroheating environment. In 2006, broadband flux and continuum spectral emission was recorded to study entry radiation and ablation products of the Stardust re-entry capsule [27]. In 2009, the controlled destructive re-entry of the Automated Transfer Vehicle (ATV-1) Jules Verne was observed and characterized. Spectroscopic and photometric data were collected from high altitude aircraft and complemented with UV/visible imaging and spectroscopy observations from the International Space Station (ISS) [28]. In 2010, the observation of Hayabusa SRC provided spectrally resolved emission spectra from near visible to near infrared frequencies [29].

Several future projects are designed to investigate the radiative heating during re-entry. The purpose of Orion Crew Exploration Vehicle (CEV), which was originally to provide crew transport to the ISS has been restated to perform orbital flight testing. This includes validation of the re-entry aerodynamic and aerothermal environment and Thermal Protection System (TPS) performance. For this purpose, a radiometer is integrated in the vehicle to measure the radiative component of the re-entry heating at two locations on the heat shield [30]. The RESPECT spectroscopic payload was developed to record spectrally resolved radiation on the vehicle surface in the future EXPERT (European eXPERimental Re-entry Testbed) mission [31]. The PHOEBUS hyper-velocity re-entry demonstrator was instrumented to measure radiative heat flux at the frontbody and afterbody of the capsule [32]. An atmospheric re-entry cubesat is being designed at the von Karman Institute to measure thermal radiation and assess TPS performance during the re-entry phase [33].

Despite these in-flight measurements, ground and airborne observations, the experimental chemical kinetics databases are far from complete, preventing accurate modeling of thermochemical and kinetic processes occurring during atmospheric entry. Furthermore, it exists several issues for obtaining accurate in-situ measurements. A key issue is that optical access may not compromise the integrity of the thermal protection. Also, the calibration of in-flight experiments is a challenging task and complex post flight analyzes are required to quantify the experimental error. During the Fire II mission, 23 % uncertainty was reported on the spectrally resolved intensity data. Also, the lack of information on back shell radiation and the absence of experimental data for non-Earth atmospheric conditions limit the validation of computational models.

1.2.2. Ground test facilities for re-entry plasmas duplication.

The improvement of optical measurement techniques and the completion of experimental databases useful for non-equilibrium calculations can be achieved through the use of wind tunnel controlled environment. On that account, ground test facilities have been developed to overcome the large

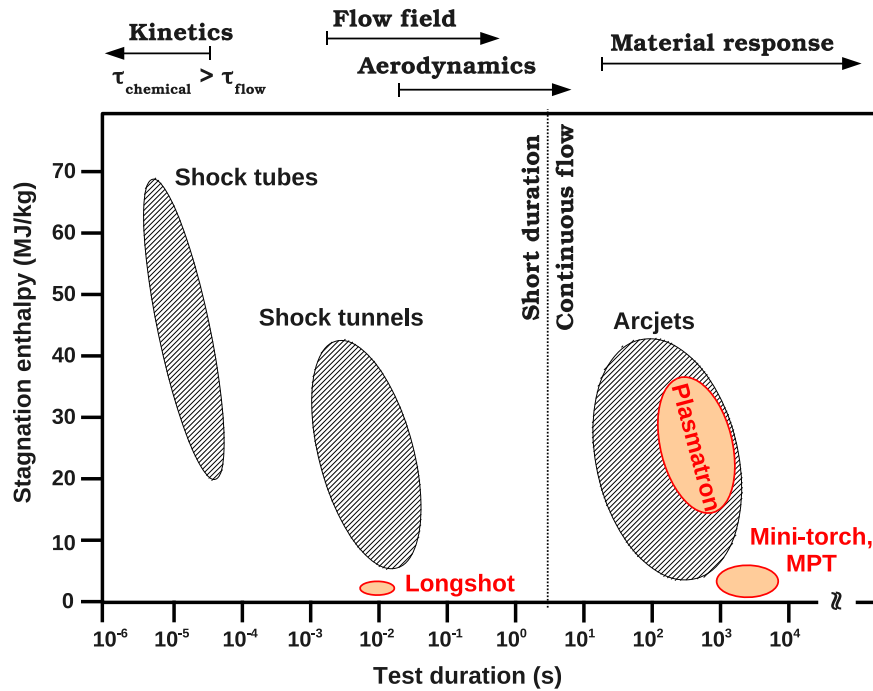


Figure 1.3.: Description and flow characterization of hypersonic facilities. Figure adapted from J.R. Maus & al. [36].

cost of missions and the difficulty of performing broad and accurate in-flight measurements. Different test facilities are used to improve the understanding of hypersonic aerothermal phenomena (aerothermal effects, catalycity, oxidation, TPS response...) related to atmospheric entries (figure 1.3). In test facilities, a number of flow parameters between the experimental model and flight vehicle can be matched. However, it is impossible to match all parameters at once, giving a complete similitude. For non-reactive gas, Reynolds and Mach number permit to duplicate respectively the aerodynamic phenomena due to viscous and compressible effects. Bushnell exposed some real gas effects that prevent from perfect duplication between wind tunnel testing and real flight of the Space Shuttle [34]. Real gas effect in high enthalpy flow can be duplicated in ground facilities using the binary scaling assumption which assumes that chemical kinetic processes scale with the density and characteristic length product. For thermal response material characterization, it is common to use the Local Heat Transfer Simulation (LHTS) [35] to reproduce high enthalpy flow on the stagnation point. Thermochemical equilibrium states can be replicated through the use of the dimensionless Damköhler number previously mentioned. On that account, aerospace facilities designed to partially replicate in-flight non-equilibrium plasma kinetic processes tend to be short duration facilities like shock tubes. In the last decade, the development of high-speed and high-resolution measurement techniques have galvanized high enthalpy shock tube experimental activities dedicated to planetary entry. Shock tubes allow to reproduce high enthalpy ($h_{tot} \approx 20-70$ MJ/kg), high speed (about 8-12 km/s for shock heated air) flows similar to those encountered during hypersonic entries. Shock tubes are largely used for shock radiation, ionization, and gas kinetics research associated with hypersonic entries. High enthalpy shock tube experiments aim to investigate the kinetic processes taking place after a pressure discontinuity wave traveling through a gaseous mixture representative of a planetary atmosphere. Non-equilibrium phenomena are very likely to occur in shock tube compressed flows. By matching various similitude parameters, the duplication of in-flight physical processes

can be conducted on sub-scaled models placed in the section of shock tube facilities. Although the similarity in the radiative losses is sometimes not maintained, kinetic processes can be investigated through direct comparison between ground test facility experiments and computational results. A large amount of experimental data obtained in shock tube experiments has been used for the validation of a non-equilibrium kinetic models. The Electric Arc Heated Shock Tube (EAST) [37], X2 hyper-velocity shock tunnel facility [38], High Enthalpy Shock Tunnel (HIEST)[39], High Velocity Shock Tube (HVST) [40], LENS Expansion Tunnel Facility [41] and soon the European Shock-Tube for High Enthalpy Research (ESTER) [42] are the major shock tube facilities in operation.

Complementary test facilities are required to overcome the limitation of short test duration of the order of microseconds. An alternative approach, related to plasma wind tunnels, can be employed to investigate high enthalpy non-equilibrium collisional-radiative processes. Large scale plasma wind tunnels (like 1.2 MW VKI Plasmatron [43]) are primarily dedicated to characterize the thermal response of TPS material. Conversely, small scale equilibrium plasma sources (like VKI 3 kW Microwave surfaguide [44]; LAEPT 3kW ICP [45]) are LTE sources useful for the development of spectroscopic databases. Subsonic plasma flows produced in direct current (DC) or radio-frequency (RF) discharges rarely achieve Local Thermodynamic Equilibrium (LTE) since elevated temperature of electrons, radiative losses, velocity and temperature gradients can result in departure from chemical and thermal equilibrium. Taking advantage of the non-equilibrium state inherent to each facility, non-equilibrium kinetic processes can be investigated through direct comparison with numerical simulation. In chapter 5, the non-equilibrium state of a subsonic plasma jets is investigated. However, in conventional subsonic plasma jets, the population of excited species reveals a Boltzmann distribution of internal energy modes. To obtain plasma flows with stronger departure from a Boltzmann equilibrium distribution of internal modes, we set new experimental arrangements generating supersonic plasma flows. Short flow residence times of continuous supersonic plasma jets are expected to reach stationary non-equilibrium state suitable to investigate non-equilibrium excitation mechanisms of internal modes. Also, taking advantage of their complex phenomenology, supersonic jets are adequate to validate compressible flow solvers and transport properties.

1.3. Objectives and overview of the dissertation

This research project addresses the experimental investigation of high enthalpy non-equilibrium re-entry flows such as those obtained behind strong shock waves during atmospheric entry. Conversely to common studies that employ short duration facilities to investigate shock layer non-equilibrium state, we will assess the possibility of producing relevant high enthalpy non-equilibrium (including vibrational non-equilibrium in particular) plasma flows using radio-frequency and microwave stationary plasma flows. Large scale RF Inductively Coupled Plasmatron (ICP) facility and small scale microwave discharge have been used to generate stationary plasma jets using either air or nitrogen gases in order to enlarge test cases devoted to the re-entry condition. Non-equilibrium plasma sources created through an electric field have already been extensively described and commonly used for technological applications. However, the state of vibrational non-equilibrium, instructive for atmospheric re-entry, is poorly documented. The aim of this thesis is to provide a thermodynamic characterization of high enthalpy non-equilibrium reactive flows, including supersonic plasma jets where vibrational non-equilibrium is strongly expected. For this purpose, suitable spectroscopic diagnostics have been applied allowing comparisons to be made between microscopic scale and theoretical non-equilibrium kinetic description. The manuscript is divided into seven parts:

In **Chapter I** a short introduction to shock layer thermochemical state has been given. Past shock layer radiation experiments conducted in-flight have been described and conventional

hypersonic ground test facilities generally used to partially replicate non-equilibrium kinetic processes have been presented. Alternatively to short duration experiments on ground, our motivation to investigate plasma kinetics through stationary supersonic plasma jet has been introduced.

Chapter II describes VKI plasma source facilities that include the RF Inductively Coupled Plasmatron (ICP) and the new Waveguide based Microwave Discharge (WMD) that we have installed. A theoretical description of the microwave system is given and a comprehensive characterization of the discharge, including plasma jet unsteadiness, coupling efficiency and radiative signature is performed at atmospheric pressure for various gases (Air, N₂, Ar). The Plasmatron facility, originally used for the characterization of Thermal Protection Material (TPM), is briefly introduced. Plasmatron emission unsteadiness during supersonic jet operation is presented. Finally, we recalled theoretical insight on supersonic nozzles which have been previously designed at VKI.

Chapter III gives theoretical insight on atomic and molecular plasma radiation. Radiative databases of interest are described. In particular, we focus on the spectroscopic database elaborated at *EM2C* research laboratory at Ecole Centrale Paris that we use to generate synthetic molecular spectra. The elaboration of atomic and molecular synthetic spectra are presented, including a detailed formulation of the partition functions and the presentation of the spectral broadening mechanisms taken into account. Also, we mention the improvement we bring to the spectroscopic measurement system. We describe the image processing procedure implemented to rebuild calibrated local emission spectra. An example of the rebuilding procedure is presented through the use of a synthetic signal. Finally, we present the approaches considered to solve the radiative transfer equation (RTE).

Chapter IV describes the spectroscopic diagnostics employed for the thermodynamic characterization of the discharges. It includes methods based on the absolute atomic line intensity and on the population distribution of atomic excited states. Also, characterization based on the hydrogen spectral line shape is considered for the determination of electron density. Finally, diagnostics based on molecular spectra fitting are formulated for various thermodynamic assumptions.

Chapter V is dedicated to the analysis of subsonic plasma jet experiments.

Firstly, the thermodynamic state of subsonic air plasma generated in VKI Plasmatron facility is investigated at pressure similar to Stardust re-entry radiative peak heating (273 mbar). Boltzmann energy distribution of internal energy modes is investigated using atomic and molecular transitions. A departure from complete LTE is observed.

Secondly, we characterize a nitrogen plasma in the ignition region of a Waveguide based Microwave Discharge (WMD) for pressures ranging from 10 mbar to 1 bar. Two-temperature approach is adopted to estimate the thermal non-equilibrium. The effect of operating pressure and input microwave power on rotational and vibrational excitation is discussed.

Chapter VI is a preliminary introduction to supersonic plasma flows. A theoretical description of cold supersonic jet is first given. Present applications and research fields based on supersonic plasma jet are then detailed, including technological progresses, and common characterization techniques. Aerothermochemical features of weakly ionized supersonic jet are given, focusing in particular on the expansion and compression regions.

Chapter VII is devoted to the analysis of supersonic plasma jet experiments.

Firstly, we assess the influence of the reactive processes on the structure of under-expanded air plasma flows generated in VKI Plasmatron facility. A direct comparison between the flow topology and isentropic models is executed. We perform a two dimensional macroscopic description of under-expanded air plasma flows using equilibrium spectroscopic diagnostics. We found that the atomic excited states distribution scheme deviates from a strict Boltzmann distribution.

Secondly, we study the non-equilibrium state of a supersonic nitrogen post discharge expanding from a hot reservoir at thermal equilibrium. The post-discharge is found to be chemically frozen and associated with a strong non-equilibrium distribution of the vibrational energy states.

This overall research was related to numerous contractual projects cited hereafter.

- *Aerothermo-Chemistry Models for Re-Entry Applications (ESA)*.
- *Validation of Aerothermodynamics Experimental and Computational Tools for the support of Future Mars Missions (ESA)*.
- *7th Frame Program project FP7: Planetary Integrated Models (EC)*.

Chapter 2.

Plasma source ground test facilities

Large scale Inductively Coupled Plasma (ICP) facility and small scale microwave discharge are used to generate stationary plasma jets.

We have installed at VKI a new plasma discharge facility, namely the Waveguide based Microwave Discharge (WMD). Similar system has been extensively used at atmospheric pressure in *EM2C* research laboratory, for the validation of spectroscopic and radiative databases [46], [47], [48]. In the present investigation, we install and adapt this system for low pressure environment and supersonic jet operation. We perform comprehensive characterization of subsonic microwave discharge for a large envelope of operating conditions and injection gases (Air, N₂, Ar). Operation with molecular gases contributes to the formation of a plasma column which size is slightly affected by the input power (~ 1 kW) and mass flow rate (~ 1 g.s⁻¹). The flow topology is however highly affected by the injection of argon atomic species which contributes to the generation of filamentary streamer discharge. In the molecular regime, coherent oscillations of the intensity of the discharge are observed along the plasma column. We set a *LabVIEW* environment in order to perform real time monitoring of the microwave coupling efficiency. We obtain steady operation through efficient coupling between the microwave power and the plasma load. We found that plasma emission unsteadiness and microwave power feeding are strongly correlated. We benefit from an existing high speed tomographic imaging setup to obtain the three dimensional reconstruction of the instantaneous emission of the jet. We found that the non-symmetric heating of the plasma load promote the presence of non-homogeneous region in the discharge. We also investigate typical radiative signatures for air and nitrogen mixtures whereas CO₂ discharges are not studied because a comprehensive analysis of CO₂ and CO₂- N₂ plasma produced by a similar WMD has already been conducted by Babou & al. [46]. A gas temperature of about 5000 K, weakly dependent on the input power, is determined. The Plasmatron facility is briefly discussed as it has already been extensively described [49]. This facility is originally used for the characterization of Thermal Protection Material (surface catalicity, ablation rates...) at subsonic velocities. As we use the facility in under-expanded supersonic regime, a study on the emission unsteadiness during such operation is presented.

2.1. Construction of a microwave plasma torch driven by surface waves

We install a new compact and flexible microwave plasma source (figure 2.1) using a waveguide-based configuration. A magnetron head (MH3.OW-S1 Richardson Electronics) operating at 2.45 GHz with SM1150T power supply produces microwave power in the kilowatt range transmitted through a rectangular waveguide (WR-340 adapted for $\lambda = 12.24$ cm wavelength) to the gas flowing in a discharge tube of 30 mm inner diameter. The discharge tube is a cylindrical dielectric quartz tube crossing the waveguide, transparent for electromagnetic waves and UV emission. This configuration is referred in literature as surfaguide [50]. Various gas injection strategies have been applied. Finally, a swirl injection is used allowing a steady flow operation.

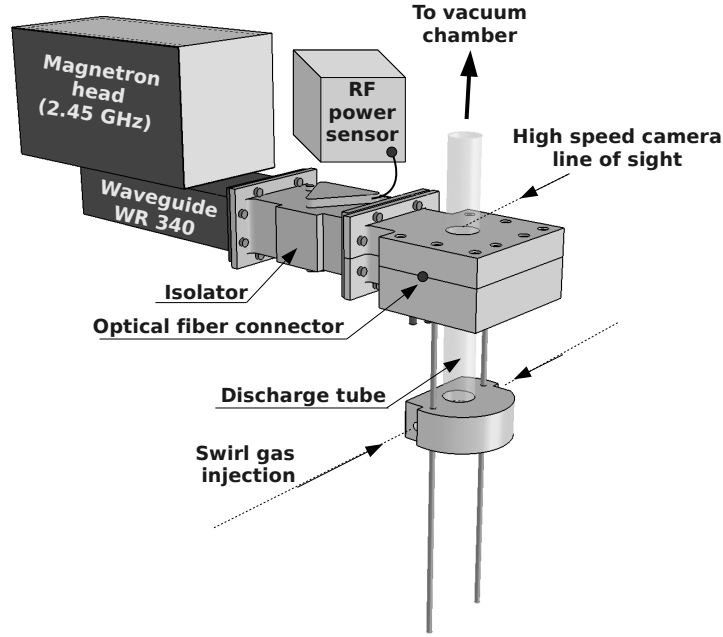


Figure 2.1.: Representation of VKI microwave plasma source.

2.1.1. Microwaves generation and transport.

The magnetron head generates microwave through the interaction of electron with an electromagnetic wave in cavity tuned to 2.45 GHz. In the present configuration, the microwave power from the magnetron is extracted towards a WR-340 ($86.36 \times 43.18 \text{ mm}^2$) rectangular waveguide. WR-340 waveguide is suitable for operating in the frequency range of 2.2 to 3.3 GHz. The

Mode	cutoff frequency (GHz)
TE ₁₀	1.735
TE ₀₁	3.470
TE ₂₀	3.470
TE ₁₁	4.173
TM ₁₁	4.173

Table 2.1.: Cutoff frequencies of the first modes in a WR-340 waveguide

cutoff frequencies of the first modes in a WR-340 waveguide are recalled in table 2.1 following the equation given in 2.1.

$$f_{c,mn} = \frac{1}{2\pi\sqrt{\mu\epsilon}} \sqrt{\left(\frac{m\pi}{a}\right)^2 + \left(\frac{n\pi}{b}\right)^2} \quad (2.1)$$

A single mode operation is obtained with the excitation of the transverse electric TE₁₀ mode. The electric field in the TE₁₀ mode is parallel to the narrow walls of the waveguide. Along the wide wall of the waveguide, the electric field is distributed as a sine function with a maximum close to the center of the discharge tube as illustrated in figure 2.2. Parameters of mode TE₁₀

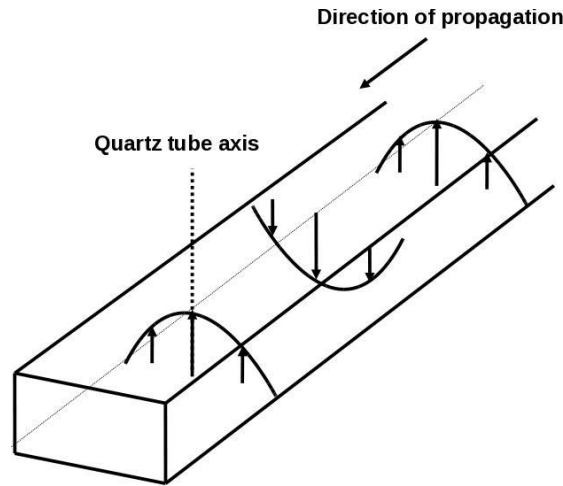


Figure 2.2.: Electric field distribution for TE_{10} mode.

Cutoff frequency	$f_{c,10}$ (GHz)	1.735
Cutoff wavelength	$\lambda_{c,10}$ (cm)	17.27
Free space wavelength	λ (cm)	12.25
Guide wavelength	λ_g (cm)	17.362
Modal impedance	Z_{10} (Ohm)	534.5

Table 2.2.: TE_{10} mode parameters

in a WR-340 rectangular waveguide for use at 2.45 GHz are recalled in table 2.2. Single mode operation is favorable to a good control on the coupling into field applicator. The generated discharge acts as a resistive load to absorb microwave power. The maximum power transferred into the discharge occurs when the admittance of microwave power generation and plasma load are equal to the transmission line characteristic admittance. Equivalent circuits of microwave systems can be found in references [51] and [50] for various surface wave launchers. Matching and tuning impedance systems are required to achieve the best coupling.

The efficiency of the power transferred from the microwave generator to the plasma depends mainly on the coupling efficiency at the interface between the waveguide and the quartz tube. The characteristic impedance presented by the plasma column to the wave is adapted to improve the energy transfer process. Generally, impedance tuning is performed using both movable waveguide plunger allowing to change the location of the maximum of the standing wave at the end of the waveguide and additional screws inside the waveguide positioned before the discharge region. In the present configuration, we use only tuning screws allowing to adapt the impedance circuit by slightly affecting the geometry of the waveguide section. Since an impedance mismatch has phase and amplitude components, both position and depth of the matching screws must be adjusted. For this purpose, three screws are positioned radially centered in the waveguide and manually adjusted for the depth of the insertion. Screws inside the waveguide provide a reactance across the waveguide which can be varied from capacitive to inductive by varying the depth of insertion. The distance between consecutive screws is fixed at $\lambda_g/8$. The termination of the waveguide is dimensioned so that the traveling wave is reflected back at the ending part of the waveguide leading to the formation of standing wave allowing more efficient coupling. The ending part of the waveguide is fixed at a distance of $\lambda_g/4$ from the tube axis.

The launching efficiency is defined as the fraction of the total power leaving the launcher that is converted into surface wave power flux. We assume that the amount of radiated power into space

is negligible compared with that transferred to the discharge. The reflected power is damped by an isolator (National electronics 2722 162 11171) allowing the microwave power to pass through in the forward but not the reverse direction preventing from any damages on the magnetron head in case of large reverse power occurring in case of unmatched impedance. This device tolerates 3 kW maximum input power ensuring an attenuation of the reverse power greater than 23 dB as the forward power is only attenuated of less than 0.3 dB. Also, the isolator allows to work into a matched load independent of discharge variations. In this way, the forwarded microwave power and the plasma load are electrically separated. The isolator is provided with monitoring probes (SMA) giving an RF voltage proportional to the measured power. Investigation of the efficiency of the plasma source operating with air is conducted and will be detailed in section 2.1.3. Although dielectric properties of the plasma vary with the chemical composition, coupling efficiency is found to be fairly similar with nitrogen gas.

2.1.2. Discharge region.

The heating of electrons by time-varying electric field is a common power deposition process taking place in RF and microwave induced plasma discharges. The collisions of electrons with other particles break the phase coherence between the motion of electrons with the oscillating electric field. The average electron velocity oscillates coherently but lags the electric field by less than 90° leading to a net ohmic transfer of power in the discharge. Microwave energy is absorbed in the plasma by free electrons and transmitted towards heavy particles by elastic collisions (increasing translational temperature of heavy particles) and inelastic collisions (enabling excitation and chemical reactions).

In general, plasma discharge is created, starting from an initial breakdown which evolves towards steady state discharge inside the quartz tube. Before ignition, the E-field has a maximum at the quartz tube axial position. Nevertheless, the electric field created is not sufficient to initiate the breakdown in air (E-field ~ 1.5 kV/cm). The ignition is then executed by using a metallic rode inserted manually into the quartz tube within the waveguide section. Among several tested materials (copper wire, metallic screw...), tungsten rode is found to provide efficient ignition. Tungsten rode provides a source of electrons for ionizing the plasmagene gas thanks to its relatively low work function ($\phi = 4.52$ eV). In accordance with Gauss theorem, the electric field is inversely proportional to the rode radius. We use a 0.5 mm diameter rode that provides efficient ignition. The ignition phase is illustrated in figure 2.3. Microwave power forwarded through the waveguide is converted into surface wave power when crossing the quartz tube. A conversion mode is operated at the waveguide and quartz tube interface. The discharge is sustained in the quartz tube by dissipation of electromagnetic energy through surface waves which propagate along the boundary between the plasma column and the quartz tube. Such plasma sheath surface wave sustained plasma column have been extensively studied ([52], [53], [54]).

The dispersion of electromagnetic wave of angular frequency ω in plasma is written as:

$$k = \frac{1}{c_0} \sqrt{\omega^2 - \omega_{pe}^2} \quad (2.2)$$

where ω_{pe}^2 stands for the electron plasma angular frequency. From 2.2, we notice that it exists two regimes for the propagation of the wave. A low collision regime $\omega^2 > \omega_{pe}^2$, where the wave propagates without decay similarly to the propagation in free space. In highly collisional situation ($\omega^2 < \omega_{pe}^2$), the wave is evanescent being damped over a typical length-scale δ and the wave propagates along the surface. The plasma may be described as a dielectric medium of complex permittivity ϵ_p [55]:

$$\epsilon_p = 1 - \left(\frac{\omega_{pe}^2}{\omega(\omega + j\nu_c^{e-n})} \right) \quad (2.3)$$

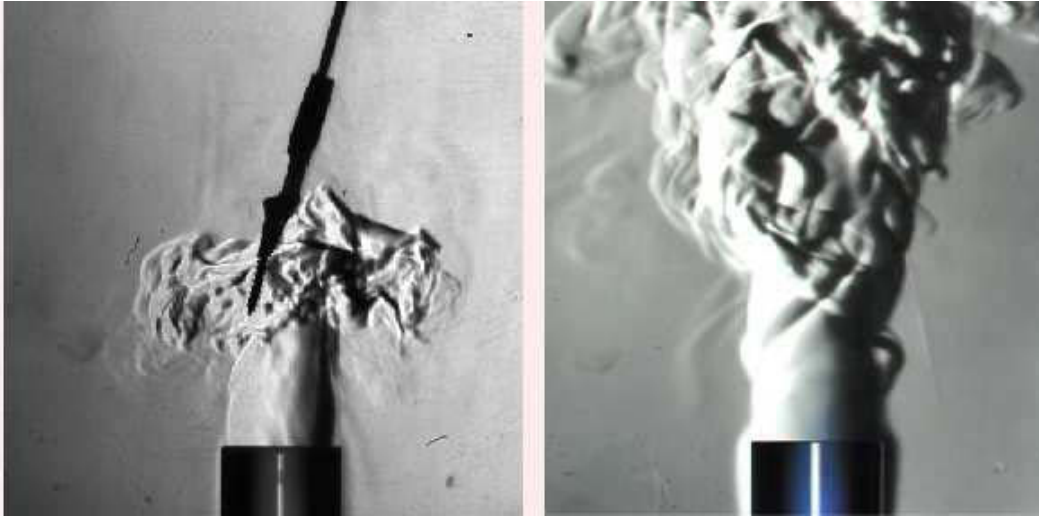


Figure 2.3.: Schlieren pictures taken above the quartz tube during the ignition phase (left) and the established flow (right).

where ν_c^{e-n} is the electron neutral collision frequency for momentum transfer and $j = \sqrt{-1}$. The surface wave can only propagate along the discharge column if the electron density exceeds a critical value n_c . We estimate the critical electron density to be of the order of 10^{17} m^{-3} in our conditions. It corresponds to the density for which electron plasma resonance occurs at the angular field frequency $\omega_{RF}/2\pi = 2.45 \text{ GHz}$. At 2.45 GHz microwave frequency and moderate pressure ($> 500 \text{ mbar}$ up to 1 bar), the penetration of electromagnetic waves into a plasma can be described as classical skin effect where the energy dissipation is due to collisions. In such collisional plasmas where electron-neutral collisions frequency ν_c^{e-n} is greater than microwave frequency f_{RF} , the number of collisions per microwave cycle is high (more than 10 collisions per microwave cycle at 6000 K, taking typical cross section for electron-neutral collisions of $5.0 \times 10^{-16} \text{ cm}^2$ taken from [56]). The mean free path is low (about $10 \mu\text{m}$), which implies that few ions reach the surface of the quartz tube within a microwave cycle. It minimizes the charge effect and ionic bombing of the surface.

Experimentally, it has been found that the propagation mode is related to the product of frequency and tube radius [57]. At the microwave frequency of 2.45GHz, only the so-called azimuthal symmetric mode ($m = 0$) is launched when the radius is smaller than 1 cm [58]. In our case, an inner diameter tube of 30 mm allows to sustain the discharge through the excitation of other modes where a combination of both transverse magnetic (TM) and transverse electric (TE) waves exists.

2.1.3. Comprehensive characterization of the microwave plasma source.

MPT operation settings and plasma flow conditions.

Photographs of plasma discharge obtained for various flow rates are given in figures 2.4 and 2.5. Considerable changes in the plasma flow topology is observed. Similar trends are observed for air and N_2 discharges. At low mass flow rate, classical axisymmetric topology is evidenced, while helicoidal shape is observed at higher rates. Internal recirculation zone at the end of high flow rate plasma jets is resulting from a vortex breakdown. As described by Brown & al. [59], in such situation, adverse pressure gradient and viscous diffusion yield to the establishment of divergent vortex core at the exit of the tube. The plasma column is constrained to a smaller

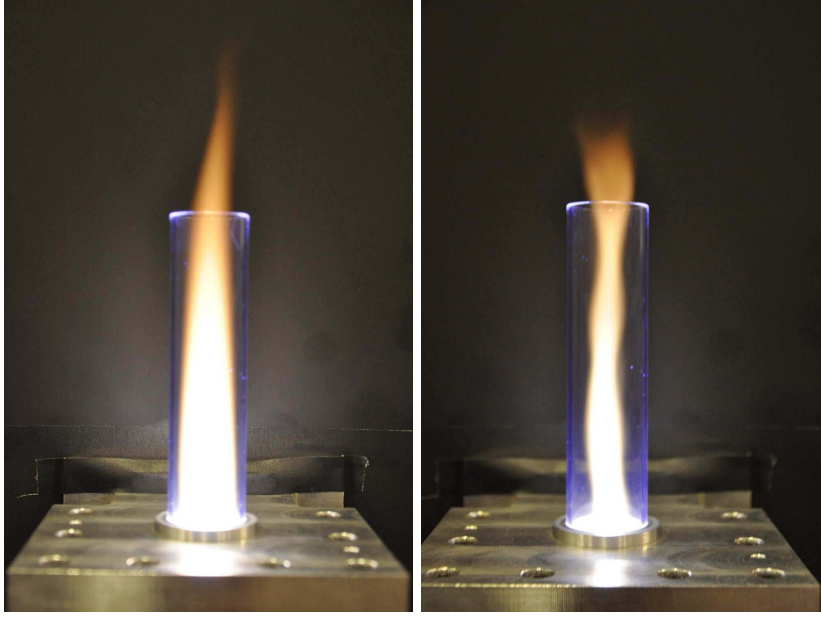


Figure 2.4.: 0.8 kW air plasma flow at 0.1 g.s^{-1} (left) and 1.5 g.s^{-1} (right).

diameter while increasing the injected swirling flow rate. Indeed, the increase of the swirl flow velocity leads to higher convection cooling on the edge of the quartz tube. Additionally to swirl injection, we test axial and axial/swirl gas injection. We found that axial injection leads to highly unsteady flows. The plasma volume is greatly affected by an increase of the power. Increasing the microwave power results in the expansion of the plasma in both radial and axial directions associated with an increase of the light intensity recorded through the line of sight. Conversely to operation with molecular gases, Argon discharge is characterized by filamentary structures which appear mainly concentrated at the interface between the plasma and the quartz tube as observed by Hong & al. [60]. As illustrated in figure 2.6, by increasing the power, we observe an increase in filament length and branching.

Plasma jet unsteadiness and coupling efficiency.

Plasma intensity unsteadiness is investigated by means of high speed imaging measurements using Phantom v7.0 8 bits CCD camera at the acquisition rate of 1 kHz. The examination of the unsteady feature of the flow intensity provides useful information about thermal inhomogeneity taking place in the plasma flow. Simple processing are applied to high speed frame records to uncover regions where intensity is higher or lower than the mean contribution. The evolution and transport of inhomogeneous pockets is investigated by removing the steady contribution to the recorded intensity as follows:

$$I^f(k) = I(k) - \frac{\sum_{k=1}^N I(k)}{N} \quad (2.4)$$

where N is the number of frame accounted to achieve the statistical convergence criterion on the mean intensity, k refers to the frame index and $I^f(k)$ represents the instantaneous intensity of the k frame. $I^f(k)$ frames are given for air plasma jet at different flow rates and various power in figures 2.7 and 2.8. Amplitude of thermal inhomogeneities increases as the flow rate is increased. Their maximum is found just above the waveguide and they tend to be damped along the jet axis. Also, alternate thermal pockets tend to stretch along the axial direction as the flow rate is increased. Increasing the power leads also to the generation of longer inhomoge-

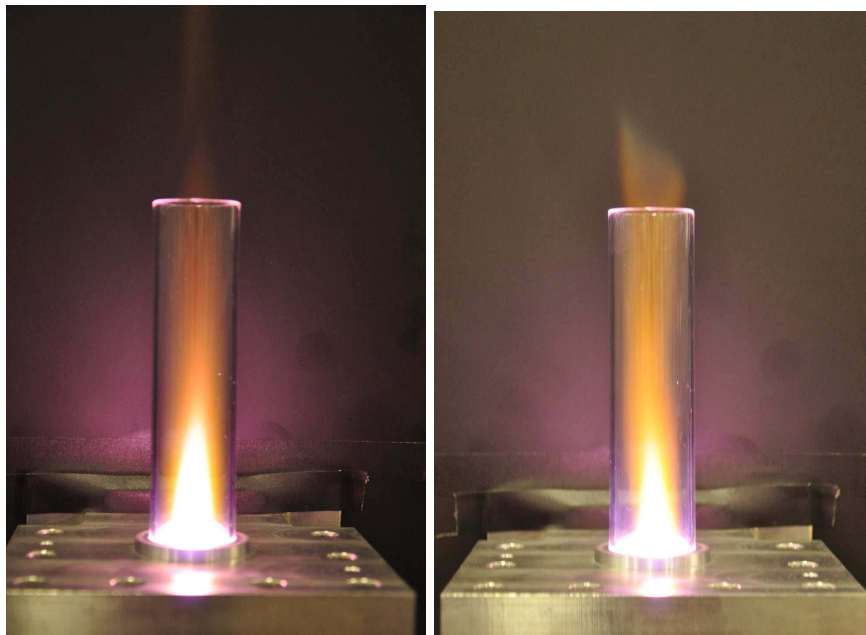


Figure 2.5.: 0.8 kW N₂ plasma flow at 0.1 g.s⁻¹ (left) and 1.5 g.s⁻¹ (right).

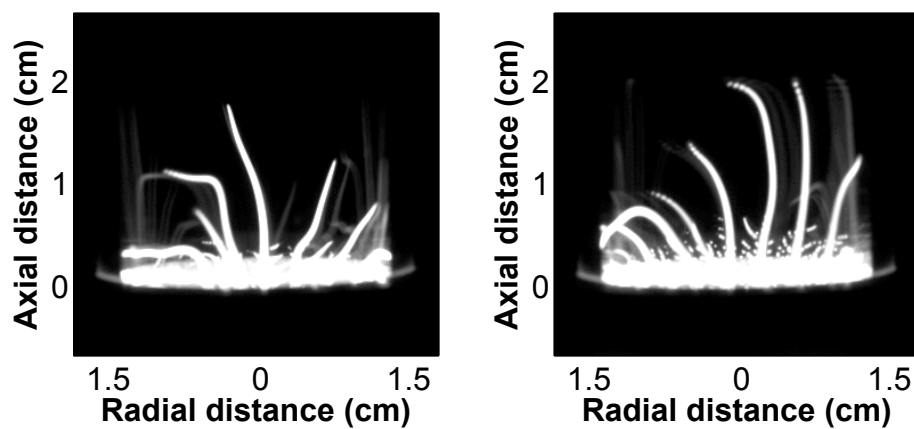


Figure 2.6.: Argon streamer regime at 0.6 kW (left) and 1.0 kW (right) microwave power.

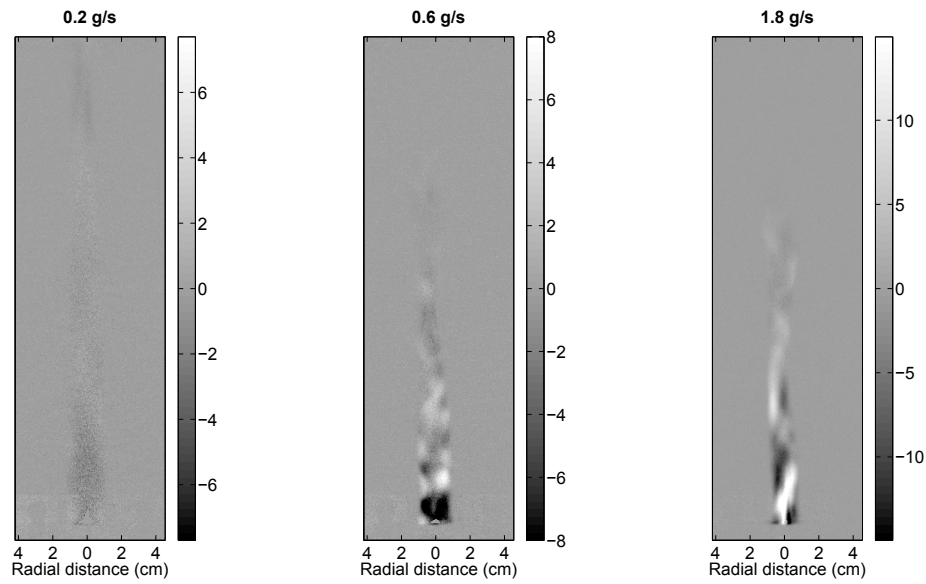


Figure 2.7.: Intensity fluctuation for 0.8 kW air plasma jet.

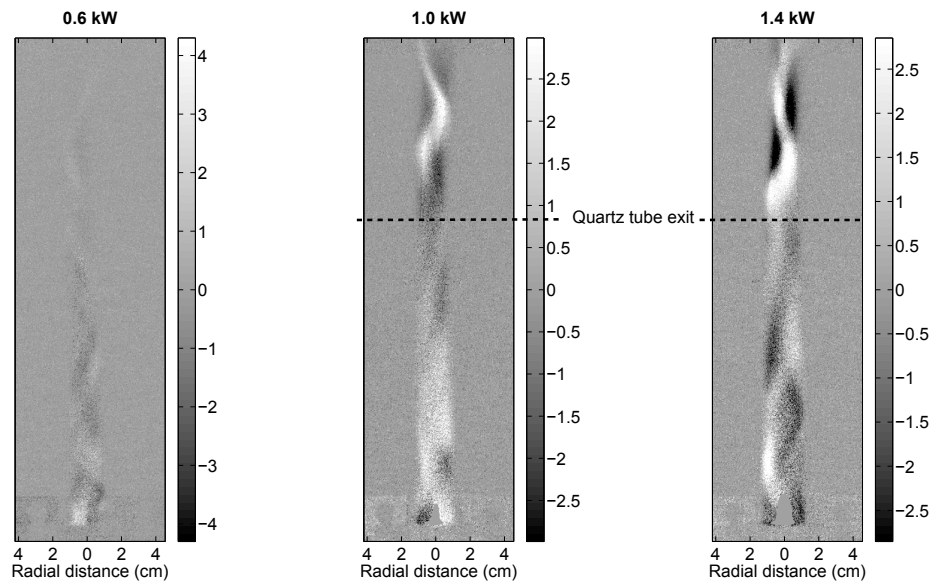


Figure 2.8.: Intensity fluctuation for 0.3 g.s⁻¹ air plasma jet.

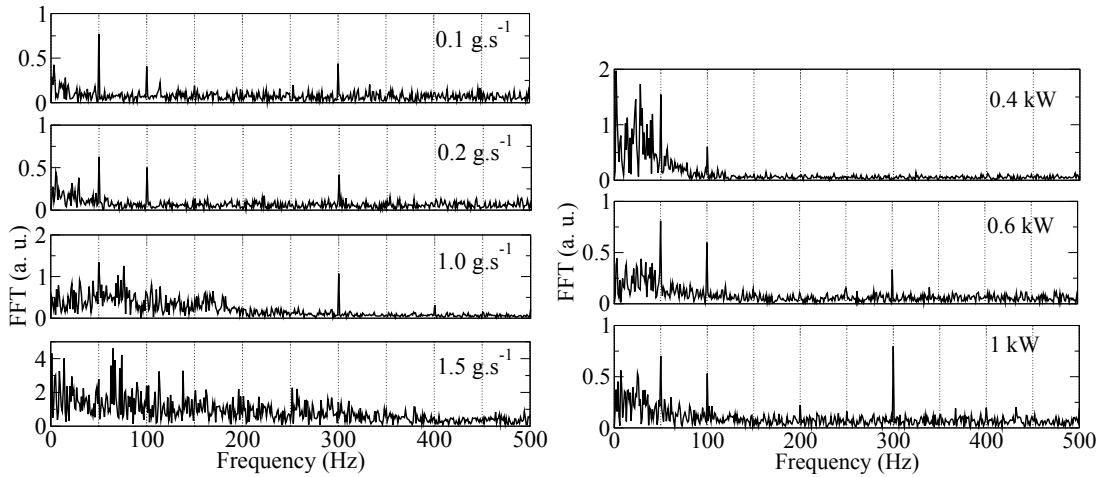


Figure 2.9.: Component frequencies of the emission fluctuation for 0.8 kW (left) and 0.3 g.s^{-1} (right) air plasma jet (1 cm above the waveguide).

neous pockets. At high power, confined plasma situation differs from the turbulent flow exiting the tube. Indeed, in Figure 2.8, 15 cm above the waveguide, the amplitude of the oscillations are accentuated due to the turbulent flow exiting the tube. Fourier transform of the optical intensity fluctuation is executed to evidence the heating modulation at well defined frequencies. Figure 2.9 shows the component frequencies of an intensity point located at 1 cm above the waveguide at the jet center line. At low mass flow rate, intensity oscillation signature is mainly composed of well defined peaks above 50 Hz (50, 100 and 300 Hz). These coherent peaks result from the modulated Joule heating of the power feeding circuit. Increasing the flow rate leads to the damping of these peaks vanishing into a noisy background rising towards low frequency range and related to the dynamic of the jet. It is found that operating at power slightly above the minimum threshold value required to sustain the discharge is leading to a highly unstable plasma flow. The unsteadiness of the flow resulting from thermal inhomogeneities generated by the power modulation is damped by increasing the power. Figure 2.9 evidences the effect of the input power on the plasma intensity dynamics. As the power is increased, the spectral dynamics of the oscillations is mostly driven by peaks above 100 Hz whereas moderate frequencies contribution tends to fade. Oscillations are damped along the axis of the jet. Above 6 cm axial distance, only the noisy contribution is observed as shown in figure 2.10.

To document the spatial behavior of the plasma jet local emission, a tomography setup based on a single CCD camera is used [61]. Assuming optically thin plasma column, three-dimensional instantaneous and mean emission distribution are rebuilt and are displayed in figures (2.11, 2.12, 2.13, 2.14 courtesy of Y. Babou [61]). The non-symmetric heating is evidenced through the observation of a swirling hot pocket.

In order to assess the robustness of the tomography technique, records are taken at the exit of the quartz tube where the effects of jet's shear layer entrainment are important and give rise to irregular structures. The lower flow rate case is consistent with the situation where plasma plume is flowing into a cold quiescent gas. It is characterized by a turbulent mixing at the jet boundary layer and a laminar core region. For the higher flow rate case, cyclonic flow arise from a vortex pressure breakdown. Tomography reveals the non-axisymmetric structure of the jet. For both cases, the mean emission distribution values exhibit concentric layer with monotonic profile decreasing from the center to the outer region.

Efficient coupling from the RF wave towards the plasma load ensures stable jet dynamics weakly affected by impedance adaptation. Forwarded and reflected microwave power were monitored

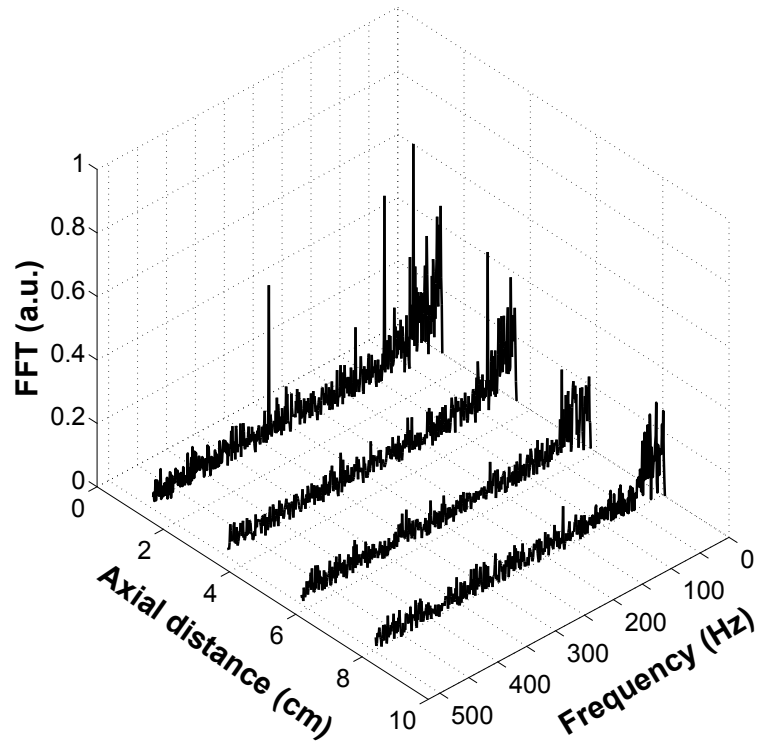


Figure 2.10.: Component frequencies of the emission fluctuation (air, $0.3 \text{ g}\cdot\text{s}^{-1}$, 0.8 kW).

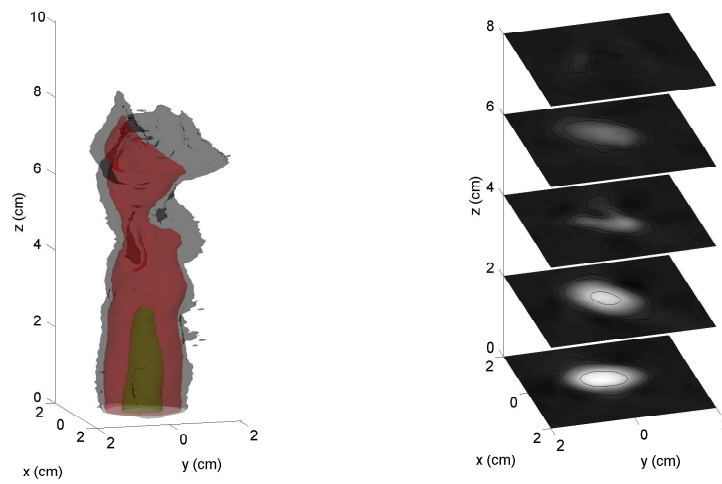


Figure 2.11.: Instantaneous emission distribution - low mass flow rate case ($0.9 \text{ g}\cdot\text{s}^{-1}$, 0.8 kW).

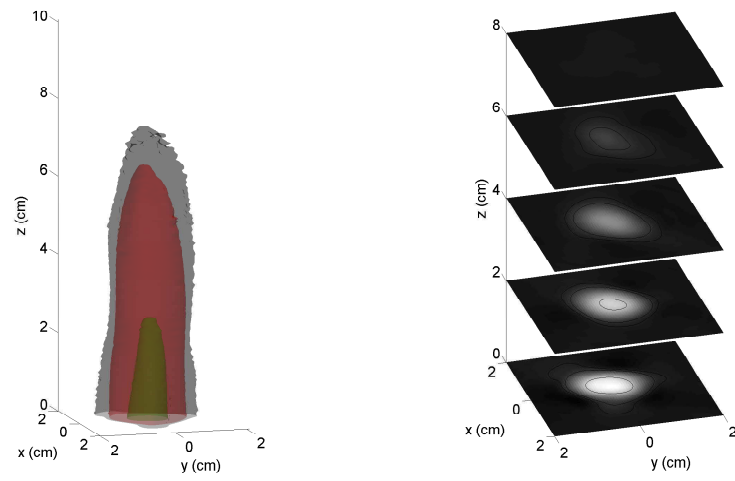


Figure 2.12.: Mean emission distribution - low mass flow rate case ($0.9 \text{ g}\cdot\text{s}^{-1}$, 0.8 kW).

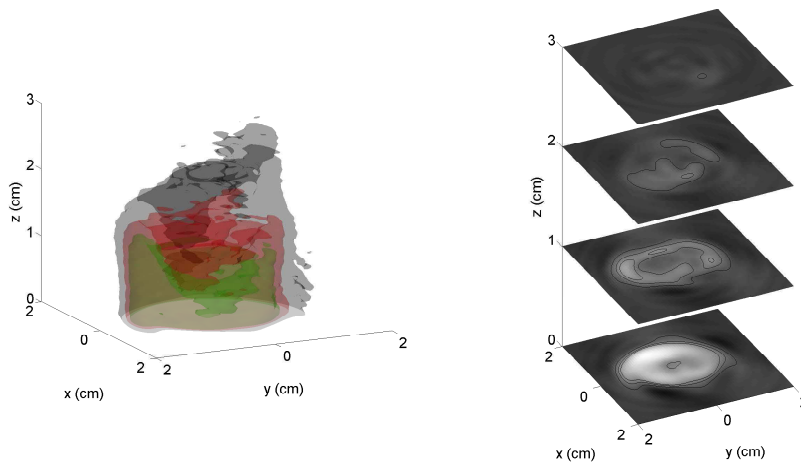


Figure 2.13.: Instantaneous emission distribution - high mass flow rate case ($1.3 \text{ g}\cdot\text{s}^{-1}$, 0.8 kW).

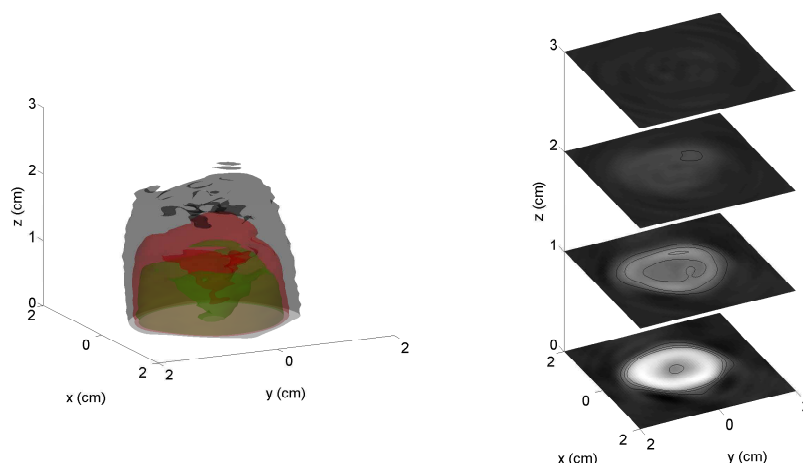


Figure 2.14.: Mean emission distribution - high mass flow rate case ($1.3 \text{ g}\cdot\text{s}^{-1}$, 0.8 kW).

at different flow rates and power for an air plasma. Alter RD8400 power sensor is used to measure the microwave signal at 2.45 GHz previously attenuated at 60 dB by the circulator device. It allows to measure the maximum waveguide power with a full scale 0-10 Vdc output voltage. Measurements were performed on the forwarded and reflected signals. Temporal and frequential forwarded and reflected power signal are plotted in Figure 2.15 and 2.16. The effect of the flow rate variation on the impedance matching is considerable. Forwarded power is always associated with coherent dynamics at 50 , 100 and 300 Hz similarly to light intensity oscillation in laminar flow condition. Conversely, reflected power is sensitive to the flow behavior. Like the light intensity exhibiting noisy dynamics in the low frequency range at high mass flow rate, the reflected power oscillation dynamics evolves also towards low frequency components. Power coupling and flow dynamics are strongly correlated.

Three screws, manually adjusted, are positioned inside the waveguide and the effect of the depth of the insertion on the power coupling is studied. For different configurations, the efficiency of the plasma source is illustrated in figure 2.17, where the reflected RF power is plotted versus the forwarded RF power. Efficient coupling must be adapted for each operating condition. In our experiments, an optimized screw configuration is selected for each operating condition so that we obtain high efficiency coupling combined with steady flow dynamics in the confined region. For this purpose, a *LabVIEW* environment is set allowing real time monitoring of the coupling efficiency.

Radiative signatures

Preliminary spectroscopic analysis consisted in the examination of radiative transitions of air and N_2 plasmas. Records were performed along the line of sight by means of a low resolution Optical Emission Spectroscopy (OES) measurements. For simplicity we assume that optical line-of-sight radiance is mostly composed of the local emission in the central core of the plasma column. Relative intensity calibration is performed within the UV and Visible spectral range combining the response of a halogen and a deuterium source (DH-2000 Mikropack). Relative response curve is displayed in figure 2.18. Typical radiative signatures are displayed in figure 2.19 and 2.20. Air radiative signature is mainly constituted of molecular emission from O_2 Schumann-Runge in the spectral domain below $\sim 600 \text{ nm}$ and of NO systems ($\beta, \gamma, \delta, \epsilon$) peaking

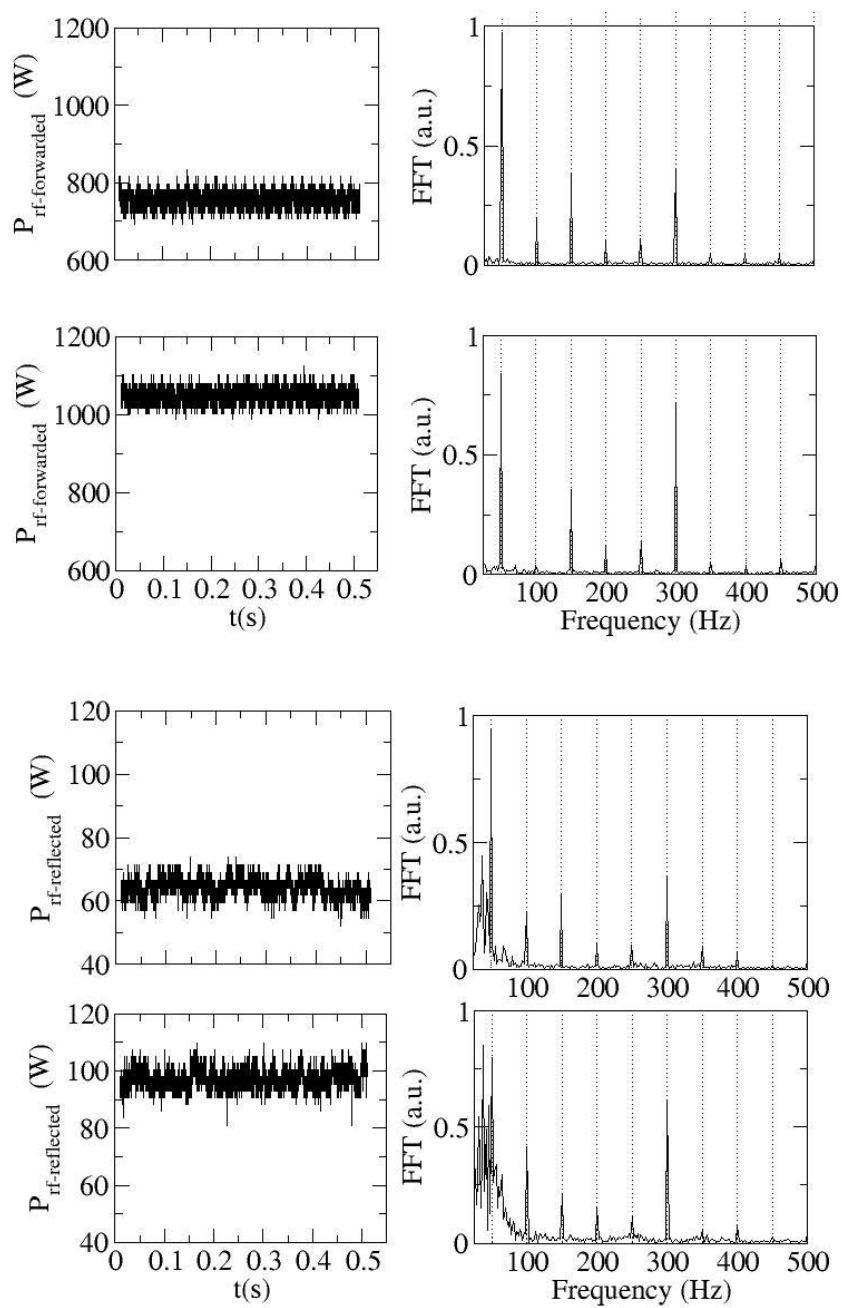


Figure 2.15.: Forwarded (top) and reflected (bottom) RF microwave power at $0.1 \text{ g}\cdot\text{s}^{-1}$ with associated Fourier fluctuation analysis.

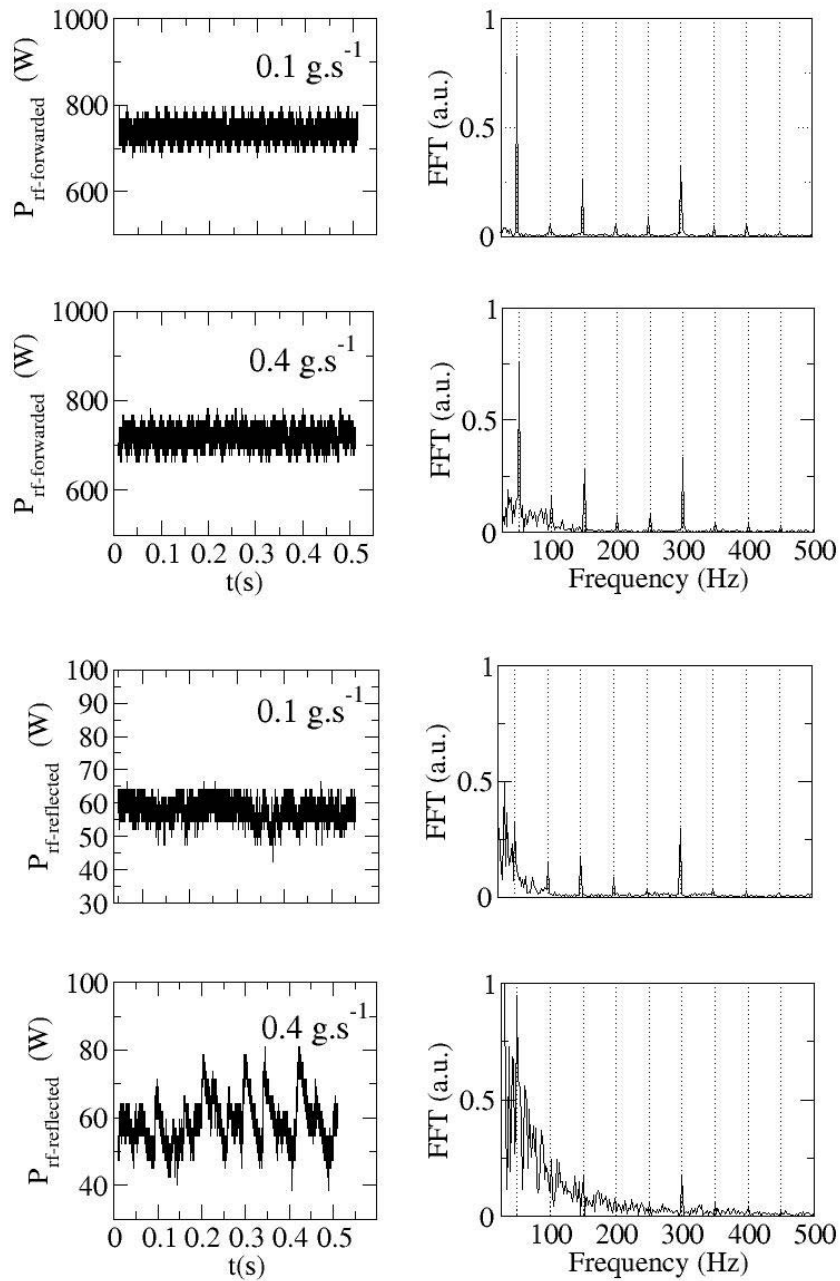


Figure 2.16.: Forwarded (top) and reflected (bottom) RF microwave power at different mass flow rates with associated Fourier fluctuation analysis.

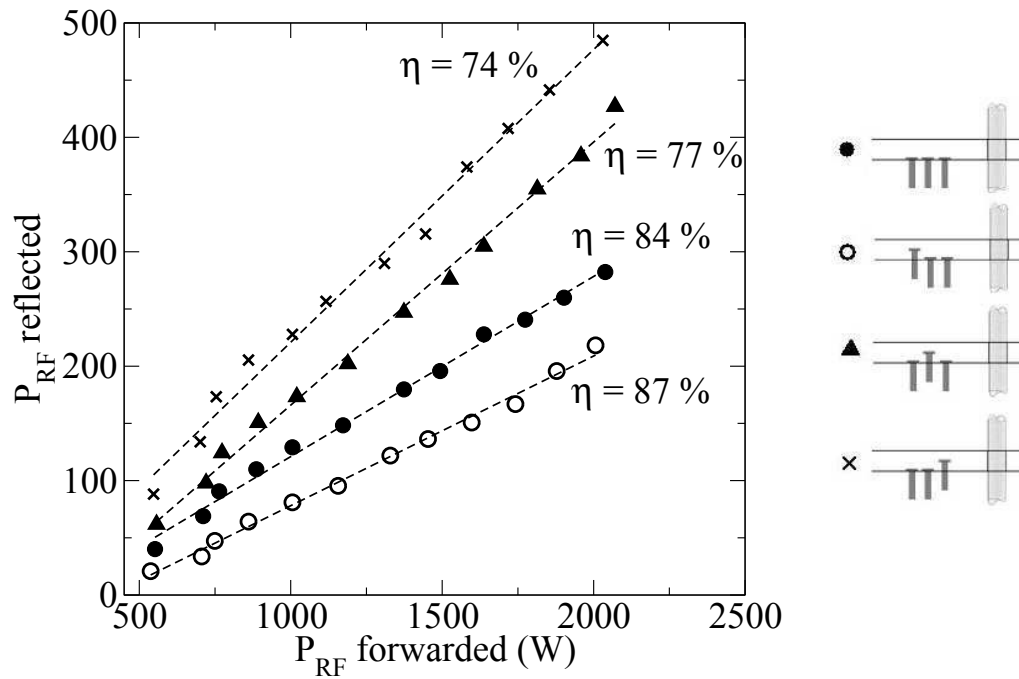


Figure 2.17.: Reflected power versus forwarded power for different configurations of the impedance matching screws.

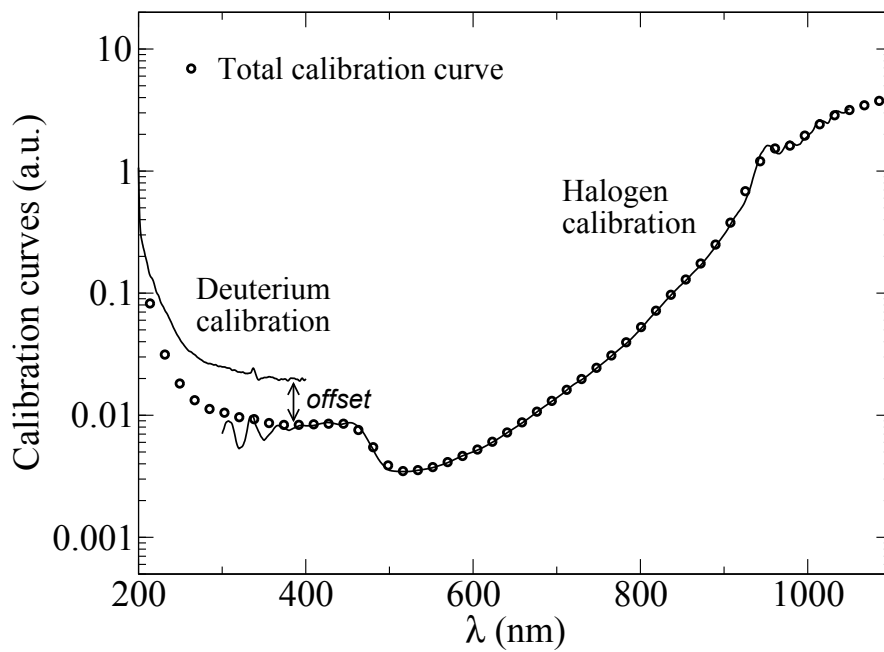


Figure 2.18.: Relative calibration curve using halogen/deuterium source.

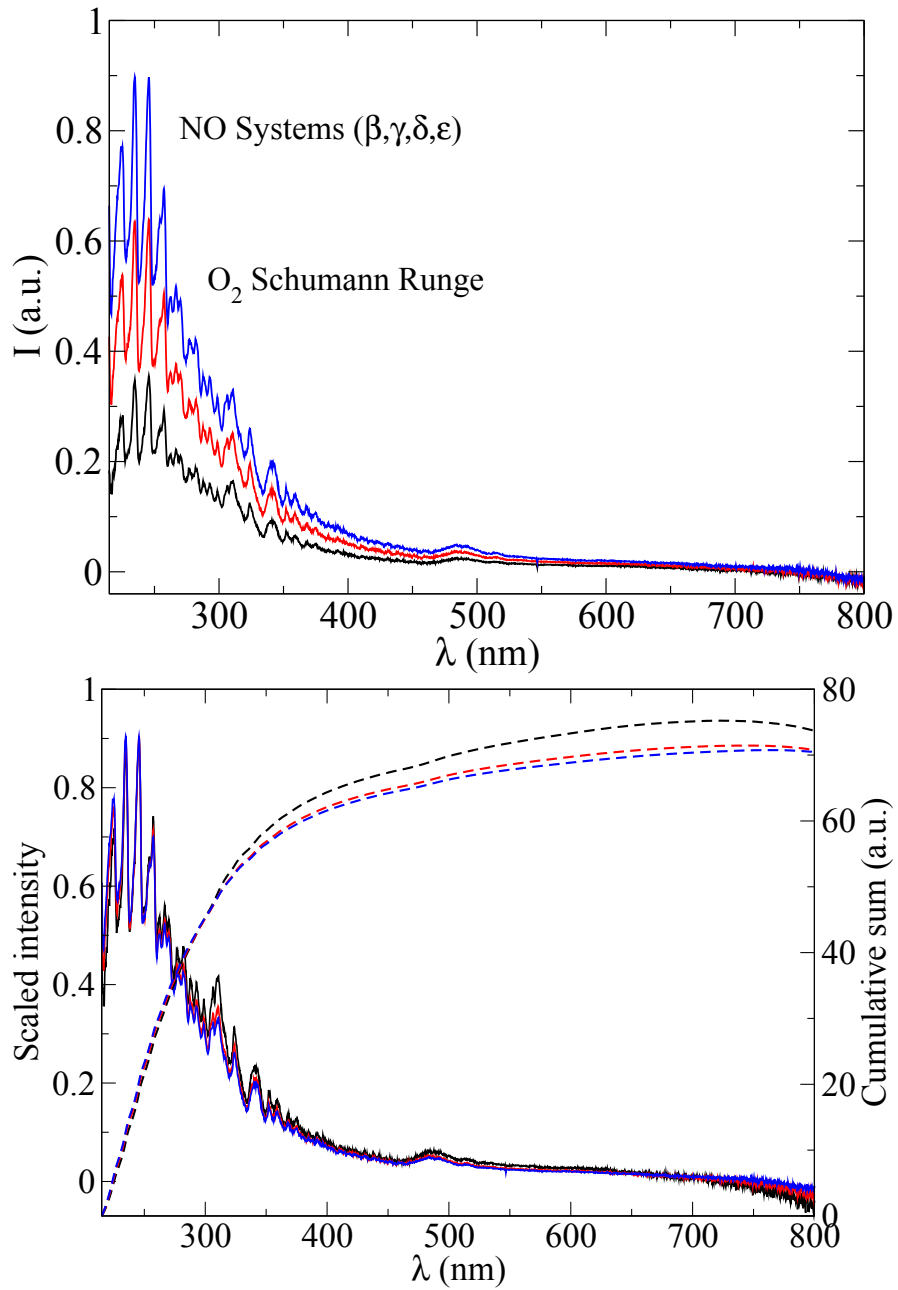


Figure 2.19.: Typical radiative signature of air discharge (top) operated at 0.6 (black), 0.8 (red) and 0.9 kW (blue) and associated scaled spectra (bottom).

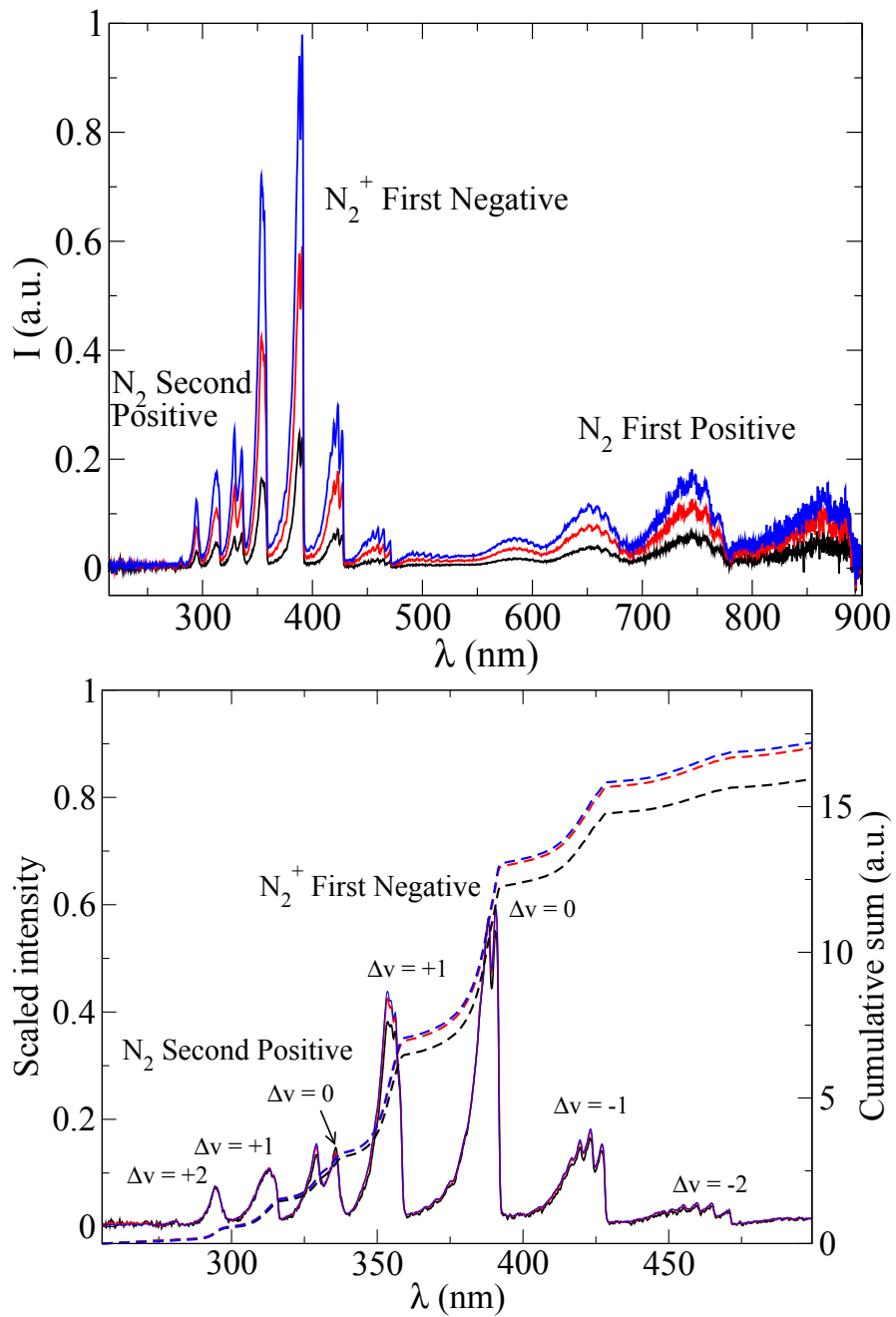


Figure 2.20.: Typical radiative signature of nitrogen discharge (top) operated at 0.6 (black), 0.8 (red) and 0.9 kW (blue) and associated scaled spectra (bottom).

at 250 nm. N_2^+ First Negative and N_2 Second Positive systems are the main contributors in pure N_2 discharge between 290 nm and 450 nm. Displaying scaled spectra for various operating power, we observe that the poor dynamic change in the shape of air and nitrogen spectra allow us to assess for a weak change in temperature. In the visible range, air plasma emission exhibits a weak spectral radiance detrimental for temperature determination. Furthermore, the NO systems lying in the UV can be weakly self absorbed preventing from a direct access to local emission. Weighted average temperature along the line of sight of nitrogen discharge is determined using a simple fitting approach, based on thermal equilibrium assumption detailed in chapter 4. Resulting axial temperature profiles are plotted in Figure 2.21 for various absorbed microwave power. Corresponding scaled axial intensity profiles integrated over the [200-900] nm spectral range are plotted in 2.21. As expected, plasma temperature is only slightly affected by the power variation. Indeed a power increase of 50% results in less than 5% temperature increase. In agreement with previous observation by Timofeev & al. in [62], additional microwave power contributes to expand the plasma volume rather than to heat it to a higher temperature.

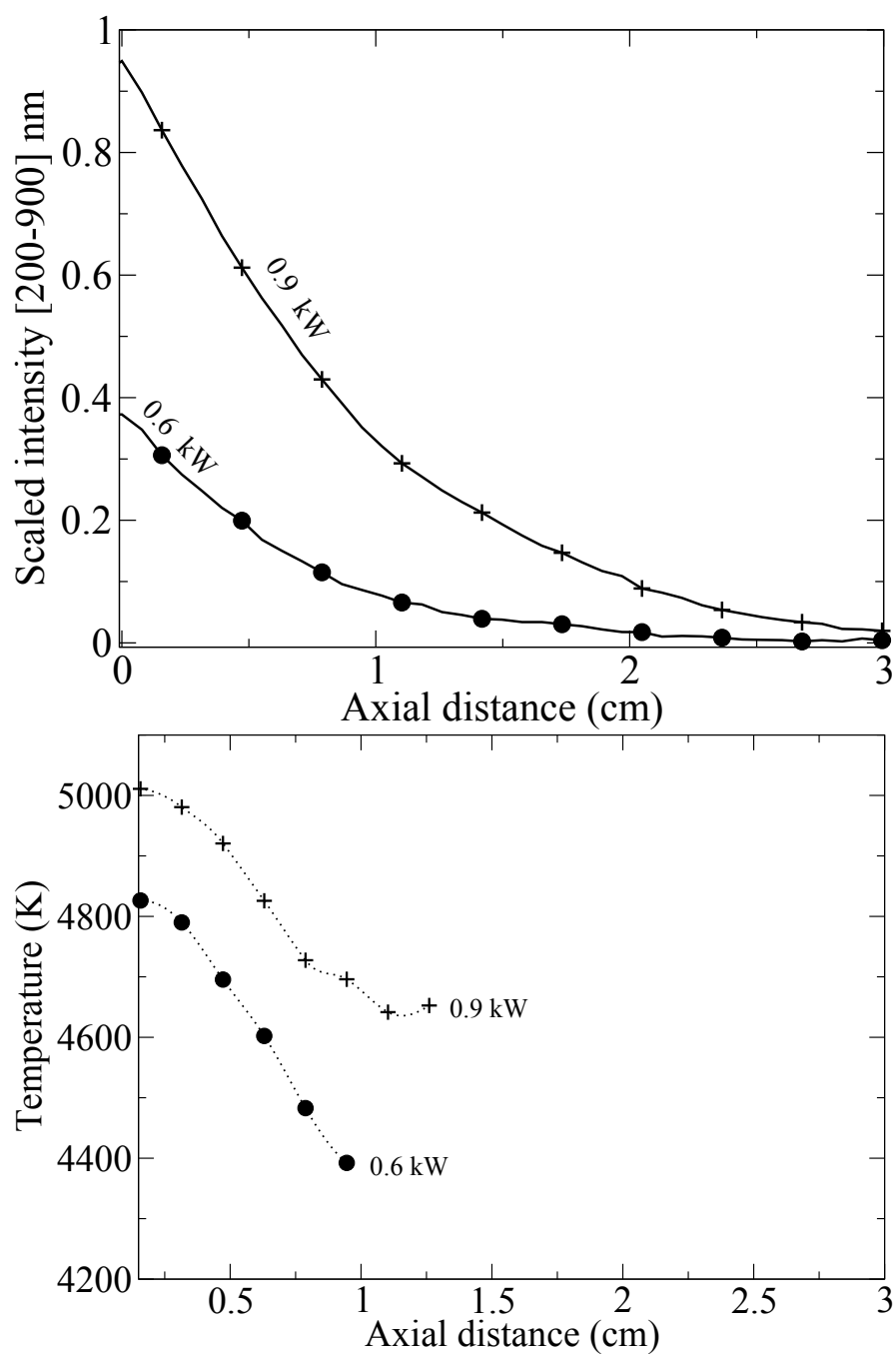


Figure 2.21.: Axial scaled intensity profiles (top) of nitrogen discharge operated at 0.6 (circles) and 0.9 kW (crosses) and associated temperature profiles (bottom).

2.2. Inductively coupled plasma torch: Plasmatron facility

Inductive heating

Plasmatron ICP facility uses a 12-pulses rectifier and a solid state (MOS inverter) RF power generator (400 kHz, 1.2 MW, 11 kV) to feed a single turn flat coil inductor up to several hundreds of kilowatts at nominal operating conditions as illustrated in figure 2.22. The RF cylindrical discharge is generated inside the torch composed of a quartz tube with an internal diameter of 200 mm and 5 mm thickness, and an inserted cold-cage of 160 mm internal diameter consisting of water-cooled copper segments to prevent from overheating. The time-varying electric current flowing through the inductor creates a time-varying magnetic field which sets up an azimuthal oscillating electric currents in the ions and electrons of the support gas. The gas heats up through Joule effect and eventually dissociates and ionizes following similar processes as those described for the microwave discharge. Due to its low breakdown voltage Plasmatron ignition starts with the injection of Argon at low pressure to provide highly energetic free electrons suitable to create an electron avalanche. The overall facility is equipped with a suitable cooling system using closed loop deionized water circuit ($\approx 2 \text{ m}^{-3}/\text{min}$). Pressure chamber is equipped with several optical accesses.

Supersonic regime in Plasmatron facility has been poorly investigated. Supersonic jet operation still need comprehensive characterization. In particular, the operating envelope differs greatly from the subsonic regime. Also, nozzle cooling circuit rapidly heats, giving rise to shortest test duration. The following section will give a brief insight on the supersonic plasma jet unsteadiness.

Supersonic plasma jet unsteadiness

Similarly to the microwave discharge, high speed camera was used to capture unsteady effects within the plasma jet. Results are displayed in figure 2.23. Plasma intensity oscillations that originate from the mixing interaction between the jet and the quiescent surrounding gas are reduced in supersonic regime. Modulated ohmic heating is the main mechanism responsible for supersonic plasma jet unsteadiness at characteristic frequencies defined by the powering circuit (50, 100, 150, 200, 300, 600 and 1200 Hz). Along the centerline, the power spectral density distribution is affected by the coherent oscillation of the power feeding. Amplitude of coherent oscillations are stronger in high density region of the jet whereas small fluctuations are observed in highly expanded regions. Whatever the position of the records, the peak situated at 150 Hz and its harmonics (300 and 600 Hz) are visible. These frequencies are independent of any change in back pressure and originate from the typical characteristic modulation of the power supply. The variation of the reservoir pressure reveals that higher pressure reservoir gives rises to low frequency peaks analogue to a noisy contribution. Deeper investigation on time resolved Electron Energy Distribution Function (EEDF) would give more insight on these instabilities that are due to strongly modulated electron density within an RF cycle.

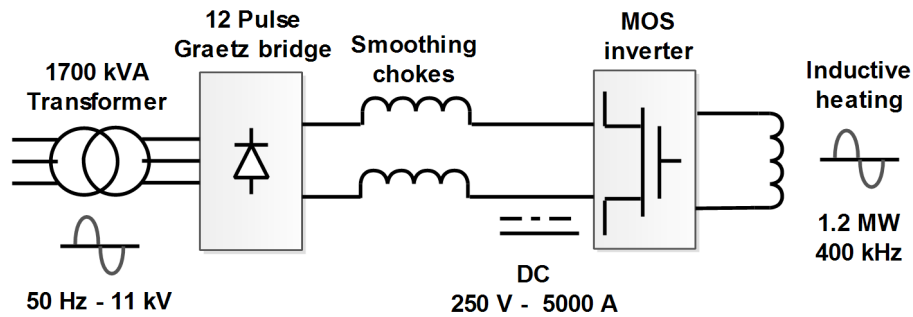


Figure 2.22.: Electrical scheme of VKI Plasmatron facility.

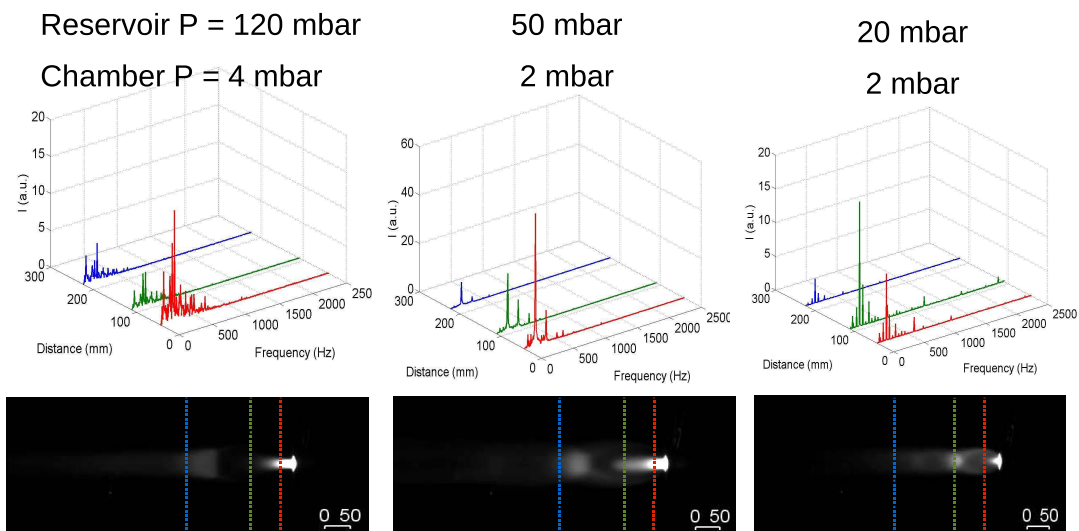


Figure 2.23.: Component frequencies of the emission fluctuation for Plasmatron supersonic plasma flows.

2.3. Nozzle flow and operating map

Isentropic nozzle flow expansion

Supersonic nozzle has been previously designed in VKI for both Plasmatron and small scale plasma facility. Supersonic plasma jets are obtained by expanding high enthalpy reservoir gas through a nozzle into a low-pressure chamber. A converging throat (figure 2.24) is used in Plasmatron facility to choke the flow before the expansion in a chamber. Differently, supersonic jets generated using the microwave plasma source are obtained through a converging diverging nozzle (figure 2.24). Equation 2.5 relates the Mach number M at any point in the expansion to the cross section area ratio A/A^* (where A^* refers to the sonic condition at the throat).

$$\frac{A}{A^*} = \frac{1}{M} \left[\frac{2}{\gamma + 1} \left(1 + \frac{\gamma - 1}{2} M^2 \right) \right]^{\frac{\gamma + 1}{2(\gamma - 1)}} \quad (2.5)$$

Although this relationship does not provide any information on the contour of the expansion duct or the losses that are associated with a multidimensional flow field, it is convenient for a first nozzle design. However, if the nozzle contour is not proper, it might induce shock waves inside the diverging section. Figure 2.25 illustrates hydrodynamic regimes associated to the Plasmatron and the microwave plasma source configurations. Using isentropic relations and knowing the Mach number at any point in the expansion, thermodynamic equilibrium properties can be deduced from the stagnation properties defined in equations 2.8 with the subscript 0.

$$\frac{T}{T_0} = 1 + \frac{\gamma - 1}{2} M^2 \quad (2.6)$$

$$\frac{\rho}{\rho_0} = \left(1 + \frac{\gamma - 1}{2} M^2 \right)^{-\frac{1}{\gamma - 1}} \quad (2.7)$$

$$\frac{p}{p_0} = \left(1 + \frac{\gamma - 1}{2} M^2 \right)^{-\frac{\gamma}{\gamma - 1}} \quad (2.8)$$

Method of characteristics

The expansion waves emanating from the nozzle exit are referred as Prandtl-Meyer expansion waves. Prandtl-Meyer flow is of interest in supersonic flow analysis and contoured nozzle design using the Method Of Characteristics (MOC). The Prandtl-Meyer function is expressed as:

$$\nu(M) = \sqrt{\frac{\gamma + 1}{\gamma - 1}} \arctan \left(\frac{\gamma - 1}{\gamma + 1} (M^2 - 1) \right) - \arctan \left(\sqrt{M^2 - 1} \right) \quad (2.9)$$

The Prandtl-Meyer function represents the angle through which the flow, initially at $M=1$, must be expanded to reach a given supersonic Mach number M . The method of the characteristics allows to design a shock free contoured nozzle for isentropic flow accounting for the multi-dimensional flow inside the duct. It uses the fact that compressible flow is controlled by disturbances that propagate along characteristic wave lines. By tracking how characteristic wave lines propagate at the local Mach angle through a flow, it is possible to solve the entire flow field of perfectly expanding flow. An illustration of the method of characteristics is given in Figure 2.26. Multiple reflections of the characteristics occur from the nozzle wall. We can distinguish between right-running waves C_+ and left-running waves C_- . We can define C_+ and C_- characteristic curves which respect the following algebraic conditions:

$$C_+ = \nu(M) + \theta = \text{constant along right-running characteristics} \quad (2.10)$$

$$C_- = \nu(M) - \theta = \text{constant along left-running characteristics} \quad (2.11)$$

The MOC becomes more accurate as the number of characteristics used in the calculation increases. The accuracy of the solution can be estimated by comparing the exit area ratio of the

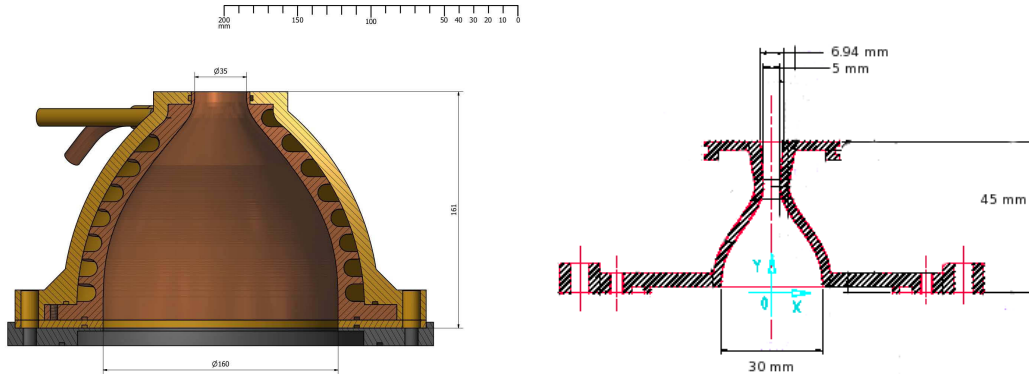


Figure 2.24.: Plasmatron converging throat (right) and MPT converging-diverging nozzle (left) technical drawings.

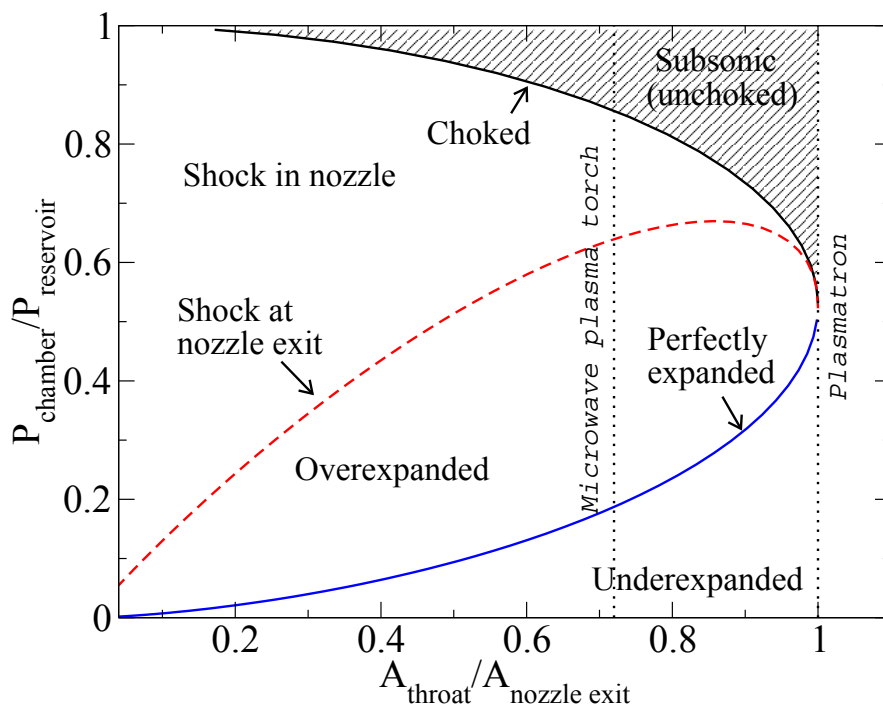


Figure 2.25.: Nozzle operating map ($\gamma = 1.3$) and hydrodynamic regimes associated to experimental configurations of Plasmatron and microwave plasma sources.

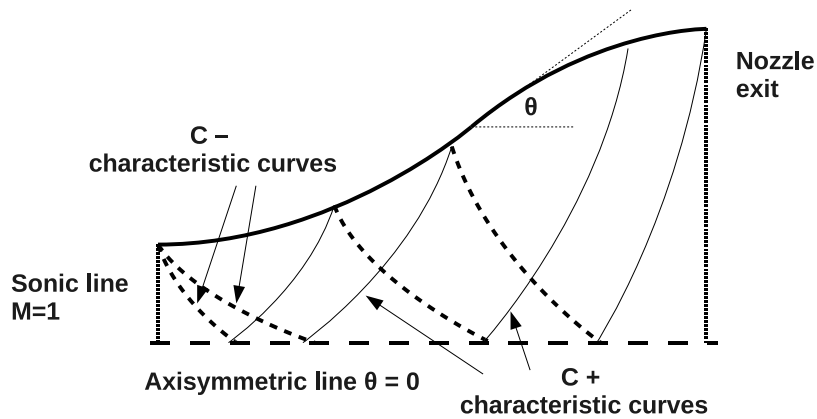


Figure 2.26.: Geometry of contoured nozzle defined by Anderson [63].

calculated nozzle to its ideal isentropic exit area ratio for the desired exit Mach number.

Plasma jet generation

The following figures illustrate the supersonic plasma flows produced in the RF ground test facilities. Pictures in figure 2.27 are related to WMD whereas figure 2.28 illuminates subsonic and supersonic Plasmatron regimes. As mentioned earlier, WMD converging-diverging nozzle operation allow to obtain under-expanded ($P_{chamber} < 45\text{mbar}$) and over-expanded ($P_{chamber} > 45\text{mbar}$) plasma flows whereas Plasmatron sonic throat authorizes only for under-expanded cases.

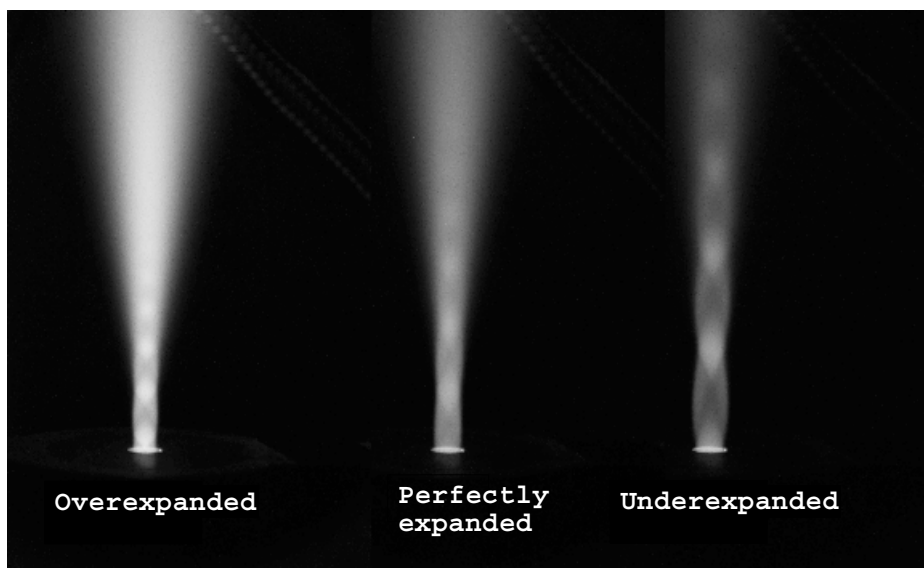
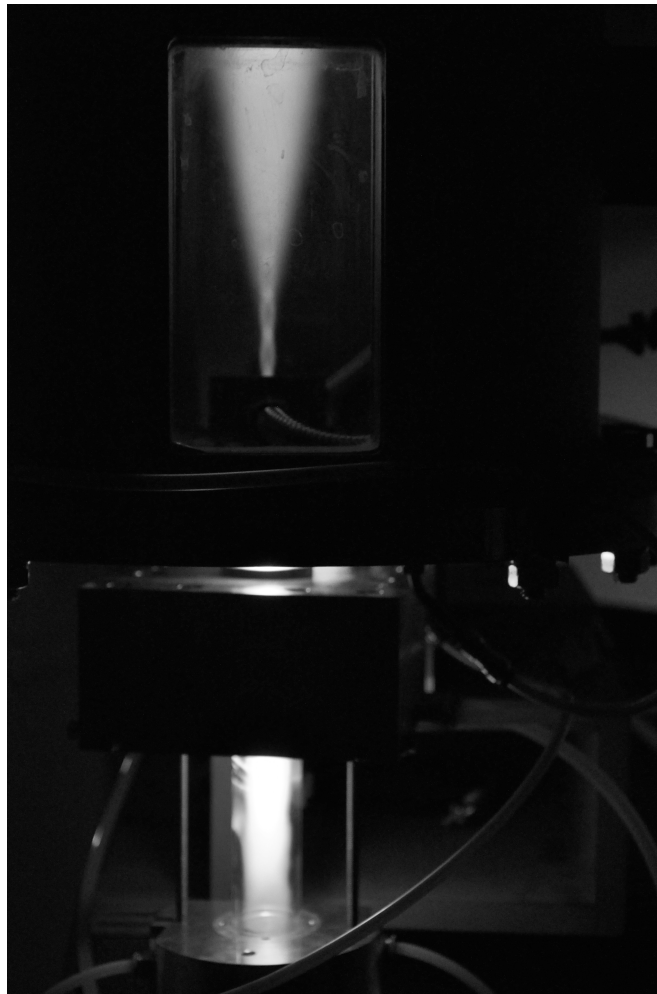


Figure 2.27.: Supersonic microwave discharge system (top) and plasma flow regimes (bottom).

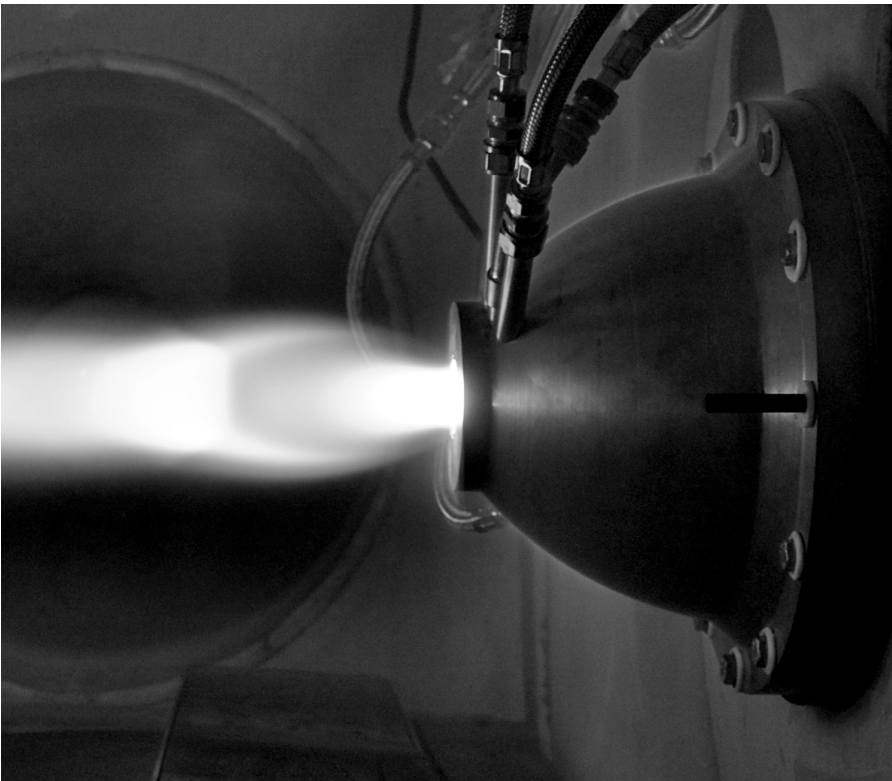
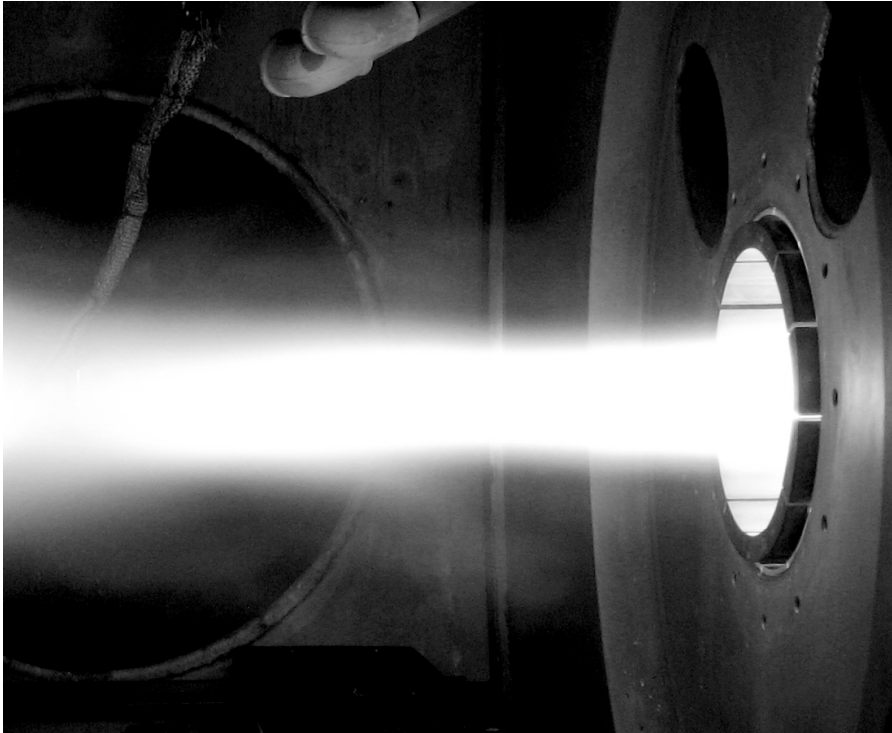


Figure 2.28.: Plasmatron subsonic (top) and supersonic (bottom) plasma jet.

Chapter 3.

Plasma radiation and experimental rebuilding of emission spectra

In RF plasma source facility, electronic excited states are mostly generated during collisions between high energy electron and neutral particle resulting in energy transfer from free electron to bound electron. Spontaneous de-excitation occurs so that radiative transitions between electronic states give rise to a line spectra in the UV and Visible spectral ranges. Exhaustive and accurate spectroscopic databases are required to identify and reproduce plasma radiative signature. In our study, we use two atomic radiative databases ([10], [64]) that cover all observed lines and we use the High Temperature Gas Radiation (HTGR) spectroscopic database elaborated at EM2C-CNRS laboratory [65] to investigate molecular systems. Based on these spectroscopic data, the elaboration of atomic and molecular synthetic spectra is presented, including the formulation of the partition functions and details on spectral broadening. Experimentally, the spectroscopic measurement system are presented. Using a simple approach, we directly measure the line of sight radiation through the use of a fiber optic based setup. We also achieve spectroscopic imaging through the use of a Czerny-Turner monochromator to spectrally resolve one dimension of the jet. We improve existing spectroscopic capacities through the installation of new monochromator with three interchangeable diffraction gratings combined with a new intensified CCD camera. We also adapt the imaging arrangement to a translational motion rail in order to complete a two dimensional spectroscopic description of the jet. Taking advantage of previous work performed at *EM2C* research laboratory [9], we perform signal filtering and Abel inversion to rebuild calibrated local emission spectra. An example of rebuilding procedure is presented.

3.1. Plasma radiation

3.1.1. Atomic line transition.

An atomic level is determined by its orbital, spin, and total angular momenta and also by its parity. Atomic states are described using common spectroscopic notation:

$$\text{electron configuration } {}^{2S+1}L_J^{\text{parity}} \quad (3.1)$$

where L is the total orbital angular momentum, J is the total angular momentum and $2S + 1$ is the spin multiplicity. The electronic statistical weight g_u of the upper electronic energy level of an atomic transition is obtained from the angular momentum quantum number so that $g_u = 2J + 1$.

Emission and absorption coefficients

The total power ϵ_{ul} emitted per unit source volume and per unit solid angle in a spectral line of wavenumber σ_{ul} corresponding to the transition between an upper state u and a lower state l is given by:

$$\epsilon_{ul} = \frac{n_u}{4\pi} A_{ul} h c \sigma_{ul} \quad [\text{W.m}^{-3}.\text{sr}^{-1}], \quad (3.2)$$

where A_{ul} is the atomic transition probability and n_u is the number density of excited atoms in the upper level u . When thermal equilibrium is satisfied, the electronic population density of the upper state with wavenumber σ_u and degeneracy g_u follows a Boltzmann distribution expressed as:

$$n_u = [N] \frac{g_u \exp\left(-\frac{hc\sigma_u}{k_B T}\right)}{Q_{int}} \quad (m^{-3}), \quad (3.3)$$

In practice, we compute species concentration $[N]$ through the use of NASA-CEA equilibrium tool [66]. The statistical weights g_u are obtained from the total angular momentum quantum number J associated to the atomic state u so that $g_u = 2J + 1$. The equilibrium internal partition functions Q_{int} is calculated using a direct summation over a complete set of atomic energy levels as expressed in equation 3.4.

$$Q_{int}(T) = \sum_{i \leq i_{max}} g_i \exp\left(-\frac{E_i}{k_B T}\right) \quad (3.4)$$

where g_i is the statistic weight of level i and E_i is the excitation energy of the level i with respect to the ground state of the atom or ion. The lowering of the ionization potential is accounted to evaluate the cut-off electronic state i_{max} and an extended atomic energy levels tabulation is used similarly to reference [67]. Two databases (NIST [10], Kurucz [64]) are selected for their data concerning radiative transition probability, statistical weight and energy levels in atoms and atomic ions.

Under LTE condition, the absorption coefficient is related to the emission coefficient using Kirchoff law:

$$\frac{\epsilon_\sigma}{\kappa_\sigma} = B_\sigma(T) \quad (3.5)$$

where B_σ is the equilibrium intensity given by the Planck's law:

$$B_\sigma(T) = \frac{2hc^2\sigma^3}{\exp\left(\frac{hc\sigma}{k_B T}\right) - 1} \quad (3.6)$$

Kirchoff' law applies even if the radiation field is not in equilibrium, when the system is said to be in LTE.

Atomic line shape profile

Atomic line shape is affected by natural, Doppler and collisional broadening mechanisms [68]. The line profile resulting from collisions or natural broadening is a lorentzian whereas a gaussian distribution is attributed to Doppler broadening. All three broadening mechanisms that affect line profile can be combined and expressed in terms of the Voigt function. In addition, instrumental effects that include the entrance slit of the spectrometer, the grating, the CCD resolution and the focal length contribute to the line broadening. For our needs we only account for Doppler broadening to solve the radiative transfer equation for atomic lines. More details are presented in section 3.2.4.

Atomic spectroscopic databases

Atomic transitions are identified through the use of NIST [10] and KURUCZ [64] databases. NIST database provides up-to-date access for critically evaluated data on energy levels, wavelengths, and transition probabilities for atoms and atomic ions. Most observed oxygen and nitrogen lines are included in this database. However, to complete the identification, nitrogen transitions which upper energy level is at $106\,477.800\text{ cm}^{-1}$ have been characterized through the use of the larger up-to-date KURUCZ database .

3.1.2. Electronic transition of diatomic molecules.

Similarly to atomic description, electronic states of diatomic molecules are described using common spectroscopic notation:

$$X^{2S+1}\Lambda_{\Omega}^{+/-} \quad (3.7)$$

where Λ is the absolute projection of the total electronic orbital momentum \mathbf{L} on the inter-molecular axis and $2S + 1$ is the spin multiplicity. The absolute value of the projection of the total electronic angular momentum on the inter-nuclear axis is denoted as Ω . Two additional symmetry labels are present. The letters u or g refers to the symmetry with respect to inversion through the center of symmetry for homo-nuclear diatomic molecules. The sign $+$ or $-$ refers to the symmetry with respect to reflection in a plane containing the internuclear axis. To differentiate states with the same S and Λ values, a letter is added to start the spectroscopic notation (X refers to the ground state, then A,B,C... are used). The numerical values (0,1,2, ...) of Λ are replaced by ($\Sigma, \Pi, \Delta, \dots$).

Emission and absorption coefficients

Molecular electronic de-excitation processes are responsible for the emission occurring in the UV and visible spectral ranges. Measured spectral emission ϵ_{σ} issued from multiple rovibronic transitions (ϵ_{ul}) allows a straight probing of the upper (emitting) rovibronic levels population density n_u through the relation (3.8).

$$\begin{aligned} \epsilon_{\sigma} &= \sum_{u \rightarrow l} \epsilon_{ul} f(\sigma - \sigma_{ul}), \\ &= \sum_{u \rightarrow l} n_u \frac{A_{ul}}{4\pi} hc \sigma_{ul} f(\sigma - \sigma_{ul}), \end{aligned} \quad (3.8)$$

Following standard notations, a rovibronic level is characterized by the quantities n, v, J (fine structure quantities being included in the rotational term). The subscript u (resp. l) denotes for the upper state $\|n'v'J'\rangle$ (resp. lower state $\|n''v''J''\rangle$) of the transition. In expression (3.8), ϵ_{ul} is the emission coefficient associated to a transition ($u \rightarrow l$). σ_{ul} is the wavenumber (in cm^{-1}) and A_{ul} is the transition probability (in s^{-1}). h and c are the conventional physical constants. $f(\sigma - \sigma_{ul})$ stands for the spectral profile of a transition due to spontaneous emission. The absorption coefficient is calculated separately from the emission coefficient to account for possible deviation from LTE. We define the absorption coefficient κ_{ul} corrected for stimulated emission so that:

$$\kappa_{ul} = (n_l B_{lu} - n_u B_{ul}) h \sigma_{ul}, \quad (3.9)$$

which leads to the spectral absorption κ_{σ} defined by:

$$\kappa_{\sigma} = \sum_{ul} \kappa_{ul} f(\sigma - \sigma_{ul}), \quad (3.10)$$

where $f(\sigma - \sigma_{ul})$ stands for the spectral profile of an absorption line as defined previously.

Statistical weights

In the Born-Oppenheimer approximation, the total energy of a diatomic molecular state is given by $E_{n,v,J} = hc(E_{el}(n) + G_{vib}^n(v) + F_{rot}^{n,v}(J))$, where E_{el} , G_{vib}^n and $F_{rot}^{n,v}$ are the spectral terms (in cm^{-1}) associated to electronic, vibrational and rotational energies. The total statistical weight associated to each electronic state is determined by the electronic, vibrational, rotational and nuclear spin degeneracy. The electronic statistical weight is expressed as:

$$\begin{aligned} g_n &= 2S + 1 \text{ for } \Sigma \text{ states} \\ g_n &= 2(2S + 1) \text{ for other states } \Lambda > 0 \text{ (}\Lambda \text{ doubling)} \end{aligned}$$

where making use of the Kronecker delta symbol g_e becomes for all states:

$$g_n = (2 - \delta_{0,\Lambda})(2S + 1) \quad (3.11)$$

The electronic statistical weight is the product of a spin multiplicity $2S+1$ and an orbital angular momentum degeneracy. Electronic eigenfunctions of a molecular state are not truly degenerate since they are separated in energy by interaction with the internuclear electrostatic field. The vibrational statistical weight g_v is unity and the rotational statistical weight g_J is $2J+1$. This is a true degeneracy as the eigenfunctions are separated in energy only in the presence of external magnetic field (Zeeman effect). The nuclear spin statistical weight ϕ_P is taken to be $1/2$ for homonuclear molecules and unity for hetero-nuclear molecules.

Partition function

We define the electronic, vibrational and rotational partition function as follows:

$$\begin{aligned} Q_{el}^n(T_{el}) &= g_n \exp\left(-\frac{hcE_{el}(n)}{k_b T_{el}}\right) \\ &= (2 - \delta_{0,\Lambda})(2S + 1) \exp\left(-\frac{hcE_{el}(n)}{k_b T_{el}}\right), \end{aligned} \quad (3.12)$$

$$Q_{vib}^{n,v}(T_{vib}) = \exp\left(-\frac{hcG_{vib}^n(v)}{k_b T_{vib}}\right), \quad (3.13)$$

$$\begin{aligned} Q_{rot}^{n,v,J}(T_{rot}) &= \phi_p g_J \exp\left(-\frac{hcF_{rot}^{n,v}(J)}{k_b T_{rot}}\right) \\ &= \phi_p (2J + 1) \exp\left(-\frac{hcF_{rot}^{n,v}(J)}{k_b T_{rot}}\right), \end{aligned} \quad (3.14)$$

In expression 3.12, S and Λ are the quantum numbers associated with the electronic spin angular momentum and with the projection of the electronic orbital angular momentum, respectively. We assume that electronic motion, molecular vibration and molecular rotation of a diatomic molecules may be regarded as independent. Therefore the internal partition function Q_{int} of a diatomic molecule is related to the rovibronic partition function Q_{mol}^n (resp. $Q_{mol}^{n,v}$) associated to the level $|n\rangle$ (resp. $|nv\rangle$) as defined hereafter:

$$\begin{aligned} Q_{int}(T_{rot}, T_{vib}) &= \sum_n \sum_v \sum_J Q_{el}^n Q_{vib}^{n,v} Q_{rot}^{n,v,J} \\ &= \sum_n \sum_v Q_{el}^n Q_{vib}^{n,v} Q_{mol}^{n,v}(T_{rot}) \\ &= \sum_n Q_{el}^n Q_{mol}^n(T_{rot}, T_{vib}), \end{aligned} \quad (3.15)$$

with,

$$Q_{mol}^{n,v}(T_{rot}) = \sum_J Q_{rot}^{n,v,J}, \quad (3.16)$$

$$Q_{mol}^n(T_{rot}, T_{vib}) = \sum_v \sum_J Q_{vib}^{n,v} Q_{rot}^{n,v,J}, \quad (3.17)$$

The equilibrium internal partition function is expressed by the following expression where Λ -doubling and fine structure are not resolved:

$$Q_{int} = \phi_P \sum_n (2 - \delta_{0,\Lambda})(2S + 1) \sum_v \sum_J (2J + 1) \exp\left(-hc \frac{E_{n,v,J} - E_0}{k_B T}\right), \quad (3.18)$$

where E_0 is the energy of the lowest energy level. The two-temperature approach that considers rotational and vibrational energy terms leads to a different formulation of the internal

partition function due to the rotational-vibrational interaction. In order to decouple the rotational and vibrational contribution, we include an interaction energy term E_{inter} in the rotational energy term, considering that vibrational perturbation affects the rotational mode. The two-temperature formulation of the internal partition function is then given by equation 3.19, similarly to reference [69].

$$Q_{int} = \phi_P \sum_n (2 - \delta_{0,\Lambda})(2S + 1) \exp\left(-hc \frac{E_{el}(n)}{k_B T_{vib}}\right) \sum_v \exp\left(-hc \frac{G_{vib}^n(v) - E_0}{k_B T_{vib}}\right) \sum_J (2J + 1) \exp\left(-hc \frac{F_{rot}^{n,v}(J) + E_{inter}^{n,v,J}}{k_B T_{rot}}\right), \quad (3.19)$$

where T_{rot} and T_{vib} stand respectively for the rotational and vibrational temperature. The maximum summation criteria based on the energy dissociation limit are calculated similarly to reference [70] and internal partition functions are calculated for N_2 and N_2^+ molecules up to 10 000 K. Values of the internal partition function are displayed in figure 3.1 for N_2 and N_2^+ .

Einstein coefficient

Using the High Temperature Gas Radiation (HTGR) database [65] permits to calculate the emission and absorption coefficients associated to bound-bound transitions of molecular systems by using electronic transition moment functions and spectroscopic constants. Einstein coefficients are intrinsic parameters of the radiating particle and satisfy the following relations:

$$A_{ul} = 8\pi hc \sigma_{ul}^3 B_{ul} \quad (3.20)$$

$$g_u B_{ul} = g_l B_{lu} \quad (3.21)$$

$$B_{lu} = \frac{8\pi^3 R_{ul}}{3h^2 c (4\pi\epsilon_0) g_l} \quad (3.22)$$

R_{ul} is the absolute line strength that may be separated into two factors.

$$R_{ul} = \left(R_e^{v'v''}\right)^2 S_{J'J''}^{v'v''} \quad (3.23)$$

$S_{J'J''}^{v'v''}$ stands for the Hönl London factor and $\left(R_e^{v'v''}\right)^2$ stands for the band strength which is the square of the electronic vibrational transition moment. Using SI units, the transition probability A_{ul} is commonly expressed in the form:

$$A_{ul} = \frac{64\pi^4 \sigma_{ul}^3}{3h(4\pi\epsilon_0)} \frac{\left(R_e^{v'v''}\right)^2 S_{J'J''}^{v'v''}}{(2 - \delta_{0,\Lambda'})(2S' + 1)(2J' + 1)}, \quad (3.24)$$

Using the following units $\sigma_{ul}[m^{-1}]$, $\left(R_e^{v'v''}\right)^2 S_{J'J''}^{v'v''}[m^2.C^2]$ and $A_{ul}[s^{-1}]$. The calculation of the emission coefficient is performed expressing the transition probability with the relation 3.24.

Spectral broadening

Assuming that broadening mechanisms can be treated independently, Doppler and collisional processes were accounted for each rovibronic transition. Due to scarce data concerning collisional broadening of diatomic rovibronic lines and following the values obtained by Breene [71] for air molecules, we used typical collisional line half width formula defined by:

$$\gamma_{coll.} = 0.1 \left(\frac{273}{T}\right)^{0.7} [cm^{-1}] \quad (3.25)$$

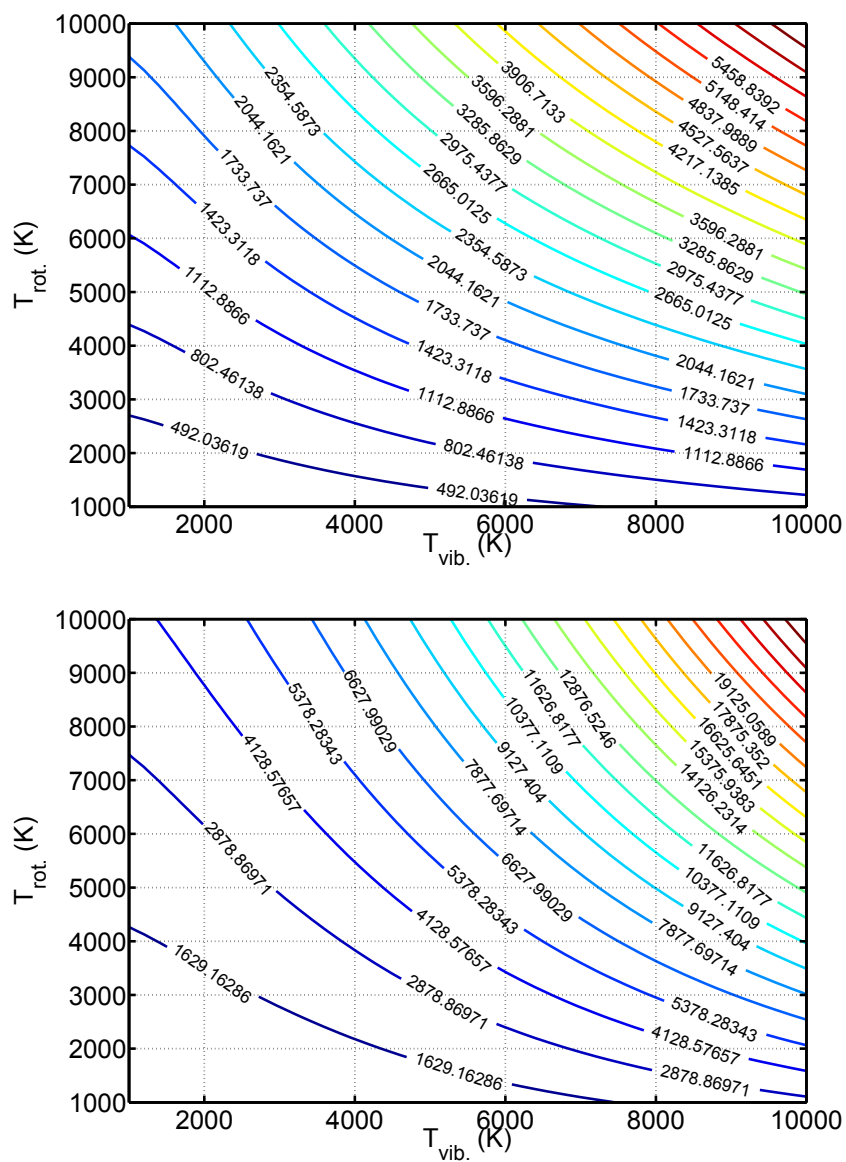


Figure 3.1.: Top: N_2 internal partition function. Bottom: N_2^+ internal partition function.

Collisional broadening is assumed to follow a lorentzian f_L profile of HWHM given by γ_{coll} . so that:

$$f_L(\sigma - \sigma_{ul}) = \frac{1}{\pi} \frac{\gamma_{coll.}}{\gamma_{coll.}^2 + (\sigma - \sigma_{ul})^2} \quad (3.26)$$

We considered that radiating particle velocities have a Maxwellian distribution, so that the Doppler profile is a Gaussian as previously defined in equation 3.36. The total line shape is determined by the convolution of line profile due to each mechanism and leading to the so-called normalized Voigt profile computed by using the Drayson algorithm [72] and defined as:

$$f_V(\sigma - \sigma_{ul}) = \frac{a}{\pi \gamma_{Doppler}} \sqrt{\frac{\ln 2}{\pi}} \int_{-\infty}^{+\infty} \frac{\exp(-y^2)}{a^2 + (\zeta - y)^2} dy \quad (3.27)$$

with,

$$a = \frac{\gamma_{coll.}}{\gamma_{Doppler}} \ln 2 \quad (3.28)$$

$$\zeta = \sqrt{\ln 2} \frac{\sigma - \sigma_{ul}}{\gamma_{Doppler}} \quad (3.29)$$

Each transition profile is calculated over a spectral distance equals to hundred times the half Voigt width $\gamma_V = \left(\gamma_{Doppler}^2 + \gamma_{coll.}^2 \right)^{1/2}$.

HTGR spectroscopic database

High Temperature Gas Radiation (HTGR) database used in this work has been elaborated at EM2C-CNRS laboratory [65]. It includes bound-bound atomic, diatomic and polyatomic transitions, bound-free transitions and free-free transitions covering from the VUV to the far infrared spectral range. We use this database for the elaboration of high resolution emission and absorption spectra of bound-bound diatomic molecular transitions. We use the available diatomic molecules spectroscopic constants which include the main electronic systems that contribute to the radiation in N_2 and air plasmas. The database for diatomic bound-bound radiative transitions is made with up-to-date Electronic Transition Moment Function (ETMF) with vibrational wave functions obtained by means of the Rydberg-Klein-Rees (RKR) method. Through the flexibility of the database and using various formulations, synthetic spectra are elaborated allowing to assess thermal, chemical and optical opacity effects.

3.2. Experimental spectra elaboration

3.2.1. Image acquisition.

The imaging of spectroscopic data are performed on stationary plasma sources by using monochromators which allow to acquire data in the ultraviolet and the visible spectral ranges. The improvement of spectroscopic capacities is executed by adding new optical devices. Therefore, different spectroscopic detection systems corresponding to various experimental campaign have been used and are recalled in table 3.1. Plasma emission is recorded either through the line of sight or through a spatially resolved collection system. In the first case, HR 4000 Ocean optics spectrometer is coupled to an optical fiber through a SMA connector. For spatially resolved measurements, high resolution monochromators are used in combination with CCD cameras. Along the radial direction of the jet, the plasma emission is focused onto the entrance slit of a Czerny-Turner monochromator. The light emitted from the slit is collimated by a concave mirror and then diffracted by a planar grating. Standard groove pattern gratings are used allowing for various spectral resolutions, recalled in table 3.1. The light is then focused by a second concave mirror onto the exit port of the monochromator equipped with a CCD camera. Gratings that disperse the radiation can rotate to produce a serie of monochromatic images of the

LINE OF SIGHT

	<i>Nitrogen WMD subsonic</i>
HR 4000 Ocean optics spectrometer	Toshiba linear CCD array
10.16 cm focal length	3648 pixels array
300 g/mm	$8 \times 200 \mu\text{m}^2$ pixel size

SPATIALLY RESOLVED

	<i>Air Plasmatron subsonic</i>
Jobin Yvon THR 1000	Synapse CCD camera
1 meter focal length	1024×256 pixels array
1200 g/mm	$26 \times 26 \mu\text{m}^2$ pixel size

	<i>Air Plasmatron supersonic</i>
	<i>Nitrogen WMD supersonic</i>
Princeton instruments Acton sp-2750	PI-MAX iCCD camera
75 cm focal length	1024×1024 pixels array
150, 1200 or 3600 g/mm	$12.8 \times 12.8 \mu\text{m}^2$ pixel size

Table 3.1.: Spectroscopic detection systems and associated experimental campaign.

entrance slit. A scheme of the experimental arrangement is displayed in figure 3.2 jointly with typical molecular emission recorded frame. Adjustable slit width provides continuous spectral resolution adjustment and signal-to-noise ratio adaptation. By inserting neutral density filters on the line of sight we are able to record strong emission. Second order filter is added to avoid diffraction orders mixing. The alignment of the optical bench is performed by means of a low power He-Ne laser source. The optical bench is adjusted so that the line of sight is perpendicular to the axial axis of the jet in the horizontal plane. Although optical aberrations degrade spectral and spatial resolutions and weaken the signal, they are not corrected by using achromatic doublet lenses or aspheric optics. In the Plasmatron, using appropriate quartz window apertures, the nearest axial position accessible from direct line-of-sight measurement is located at 18.5 cm (resp. 2.5 cm) from the entrance into the low pressure chamber for subsonic flows (resp. for supersonic flows with additional convergent throat). In the WMD, a straight optical access above the waveguide is available and an additional optical line of sight access inside the cavity was built.

3.2.2. Image processing.**Background signal**

Noisy background of iCCD camera is influenced by several factors. A component of the noise comes from thermally generated electrons from the photocathode and is known as equivalent background illumination (EBI). The EBI could be reduced by cooling the camera with a dry nitrogen cooling circuit. However, relatively high emission from the plasma sources we use, allows to operate with low exposure time, reducing then the contribution of the EBI without external cooling circuit. An other source of noise is the dark current coming from the CCD itself and which is not magnified by the intensifier as it is positioned after the intensifier. The readout noise is generated by the electronic circuit that converts the charge from each pixel into a digitized light-intensity. Also, variation in the number of photons emitted by the plasma is overcome by averaging over typical duration of several milliseconds. Bad pixels are expected

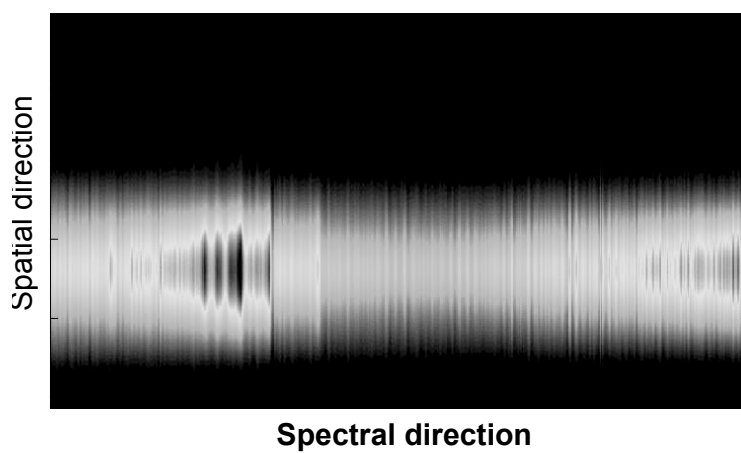
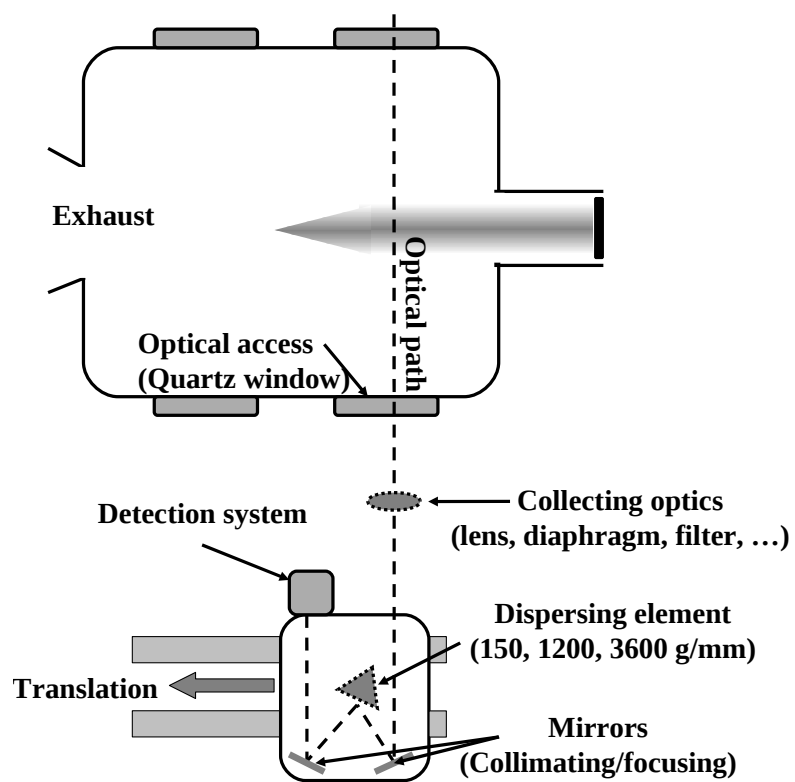


Figure 3.2.: Top: Experimental arrangement for spatially resolved spectroscopic measurements. Bottom: Typical CCD frame.

to affect image quality since approximately 0.5 to 2 % of the detector array may be defective. Since this effect arises from the CCD manufacturing process, each hot-pixel is excluded. Total noisy background is subtracted from the recorded frames.

Calibration procedure

Calibration is performed using a tungsten ribbon-filament lamp chosen with a known spectral radiance [$W.m^{-2}.sr^{-1}.nm^{-1}$] suitable to get spectra calibrated within [350-1200] nm spectral range. The lamp is operated at a single current so that it can produce a stable and reproducible radiance. The optical bench settings for the calibration were identical to those for the experiments except that integration time had to be adjusted so that the signal did not saturate. Compliantly with integration time of interest, the linearity of the CCD camera was assessed by placing a low pressure Hg radiation source (ORIEL 6060 spectral lamp) in the focus point of the collection optics. We also assessed the homogeneous spectral response of the camera so that the calibration procedure can be performed using a single pixel. Defining the spectral radiance I_{σ}^{ref} of the reference tungsten source as the ratio of the spectral irradiance over the solid angle of observation, we can express the calibrated signal I_{σ}^{cal} as:

$$I_{\sigma}^{cal} = I_{\sigma}^{ref} \times \frac{(S_{\sigma}^{mes} - B_{\sigma}^{mes})}{(S_{\sigma}^{tun} - B_{\sigma}^{tun})} \times \frac{t_{tun}}{t_{mes}}, \quad (3.30)$$

where t stands for the integration time of measurements, S stands for the recorded signal and B refers to the measured background. The subscript mes (resp. tun) refers to records performed during experiments (resp. during the calibration with a tungsten lamp). For UV calibration, we used the spectral radiance of a deuterium source (DH-2000 Mikropack) that provides relative calibration in the UV-Visible spectral range by recording along the line of sight of the volumetric source. A correction factor is added with respect to the tungsten calibration curve so that absolute calibration is performed on the UV and visible spectral range.

Spectra corrections

Appropriate corrections should be applied to the theoretical emission spectra generated at high resolution, in order to elaborate synthetic spectra compliant with the experimental data features. The effect of the instrumental broadening is taken into account by convoluting the theoretical spectra with the apparatus function which is found to be in our experiments similar to a gaussian profile. In practice, the instrumental width is obtained by measuring Hg lines from a low pressure source. Correction on theoretical line spectral position is also applied to account for the optical refractive index of air. The refractive index n_{air} accounted in this study is given in reference [73] and is written so that:

$$(n_{air} - 1)TP = (n_{air} - 1)\sigma \frac{0.00138823P}{1 + 0.003671T} \quad (3.31)$$

$$(n_{air} - 1)\sigma = 10^{-8} \left(8342.13 + \frac{2406030}{130 - \sigma^2} + \frac{15997}{38.9 - \sigma^2} \right) \quad (3.32)$$

where σ is expressed in [μm^{-1}], T in [$^{\circ}C$] and P in [torr].

3.2.3. Local emission rebuilding.

The plasma jet being observed in the side-on direction, recorded spectral radiance results from the local emission integrated along the line-of-sight over the entire depth of the source. When the source is cylindrically symmetrical and optically thin, then the radial distribution of the local emission can be rebuilt from the measured spatial distribution of the line of sight integrated signal. After ensuring that measured profiles are symmetrical, spatial filtering procedure is applied for every spectral position. Most of the time, spectral radiance distribution shows symmetrical profiles and local emission rebuilding is performed through the use of Abel transform.

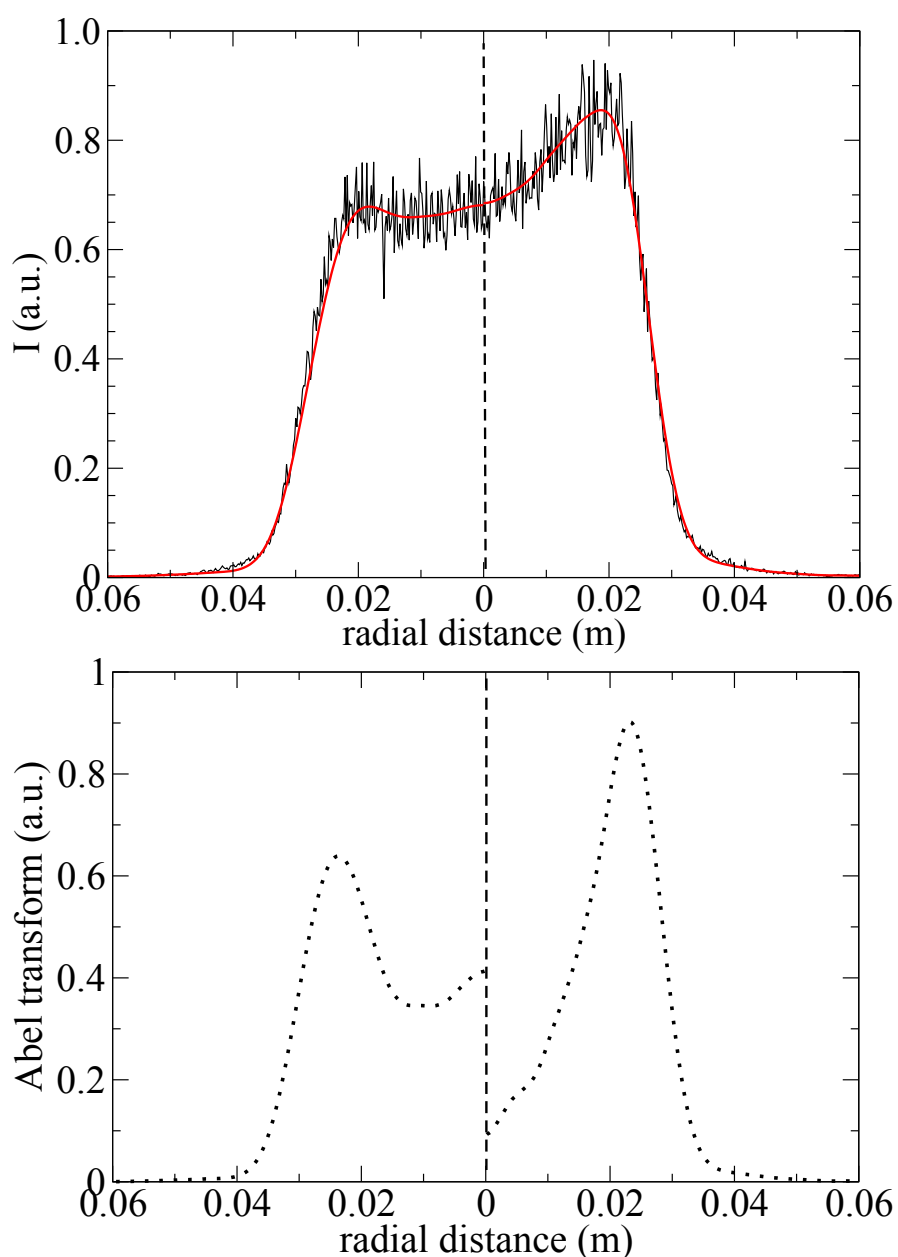


Figure 3.3.: Top: Asymmetric intensity profiles: experimental (black) and filtered (red). Bottom: Corresponding Abel transform.

In supersonic Plasmatron regime, molecular intensity profiles exhibited asymmetrical behavior that may lead to strong uncertainties on rebuilt value as illustrated in figure 3.5. However, this asymmetrical behavior being strictly limited to low intensity light spectral region, we still consider the half profile to perform the Abel transform. Illustrated examples of the rebuilding procedure will be given after a short description of the data processing.

Signal smoothing

A Butterworth low-pass filter is used to cut high frequency components attributed to noise. Its

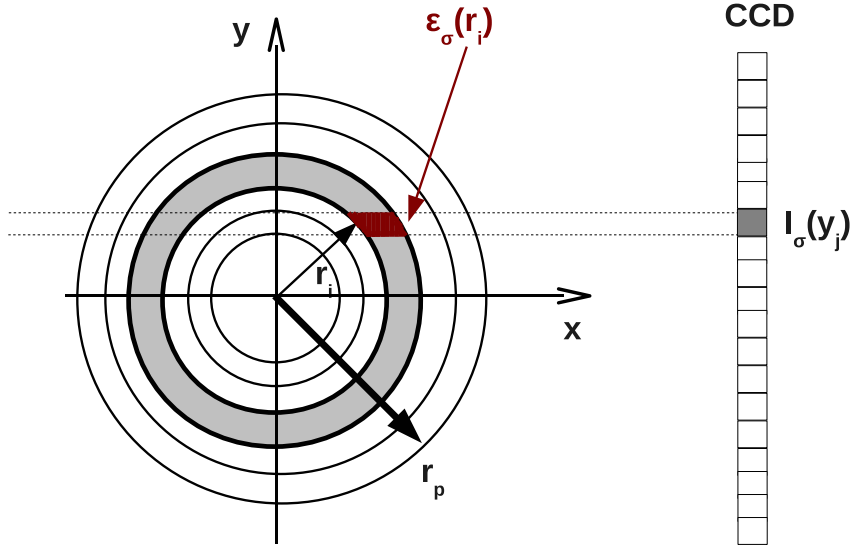


Figure 3.4.: Scheme of radiance I and the local emission ϵ assigned to axisymmetric geometry.

magnitude frequency response function is expressed as:

$$|H(j\omega)|^2 = \frac{1}{1 + \left(\frac{j\omega}{j\omega_c}\right)^{2n}} \quad (3.33)$$

Where ω_c stands for the cutoff frequency and n is the order of the filter. Typical magnification factor employed for imaging the plasma onto the iCCD allows to capture the entire profile using 2/3 of the iCCD height, which corresponds in our case to about 700 pixels. Efficient filtering is obtained empirically by using a 2nd order filter with a corresponding cutoff period ranging from 20 to 30 pixels.

Abel transform

In optically thin media, the relation between the spectral radiance which units are $I[W.m^{-2}.sr^{-1}.nm^{-1}]$ and the local spectral emission which units are $\epsilon_\sigma[W.m^{-3}.sr^{-1}.nm^{-1}]$ (as defined in figure 3.4) is given by the Abel transform expressed as:

$$\epsilon_\sigma(r) = -\frac{1}{\pi} \int_{r=y}^{r=r_p} \frac{dI_\sigma(y)}{dy} \frac{dy}{\sqrt{y^2 - r^2}} \quad (3.34)$$

where r_p stands for the jet radius. Measurements being provided only through a discrete set of values, the equation can be solved in an approximate manner through the use of analytical or numerical methods. The analytical methods fit the experimental data to an analytical function whereas numerically, discretization methods have to be employed. When using analytical methods, polynomial functions are typically used. However, following the work of Deron [67], cubic spline interpolation gives better results. Based on the analytic inverses of Abel equation, the spectral emission is therefore calculated using cubic spline approximation for evaluating the integral of equation 3.34, similarly to Deron [67].

Analytic validation of rebuilt profile.

We test the Abel inversion on the non-monotonic reference function shown in table 3.2 with J_0

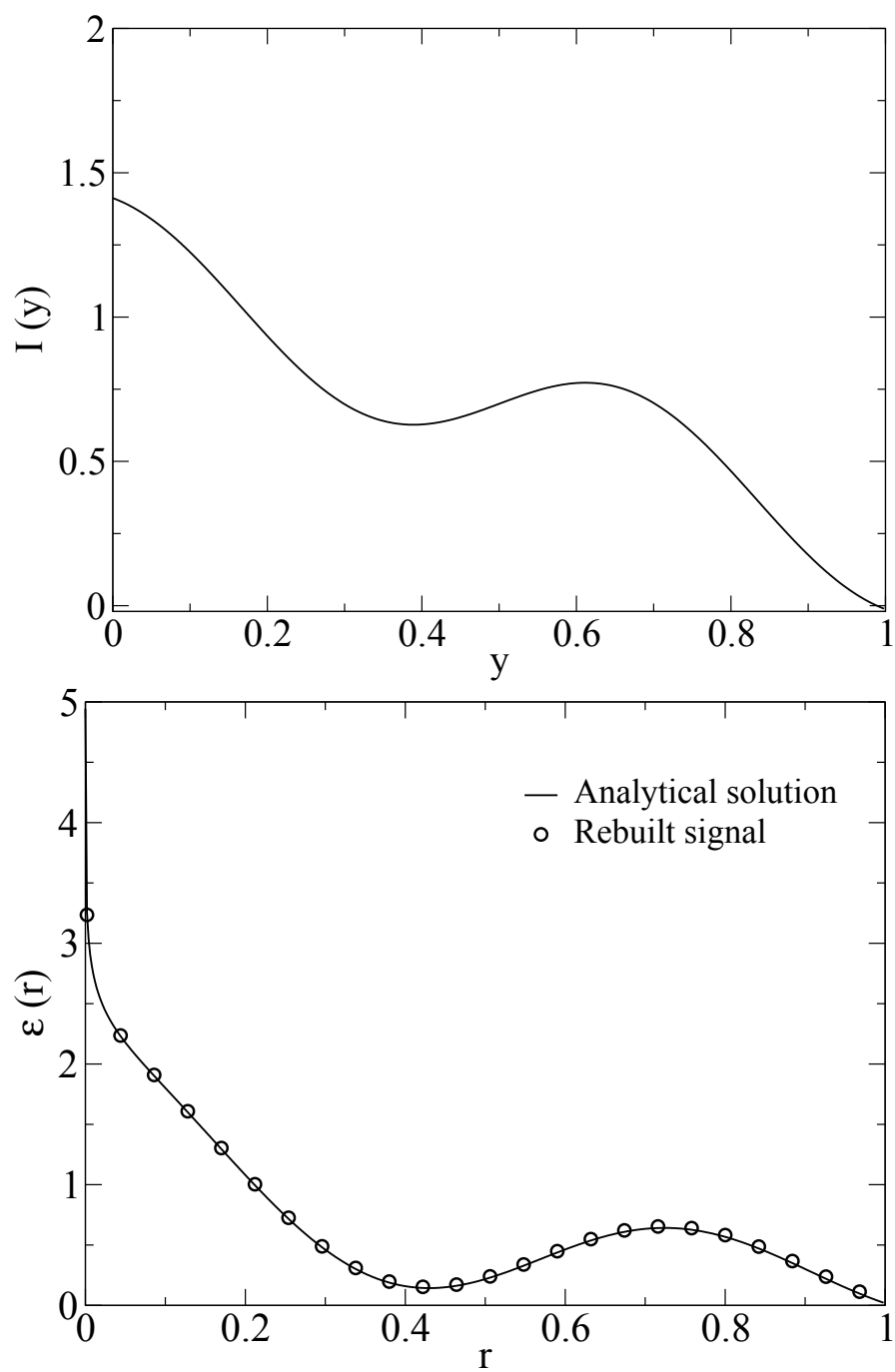


Figure 3.5.: Top: raw profile. Bottom: Abel inversion results

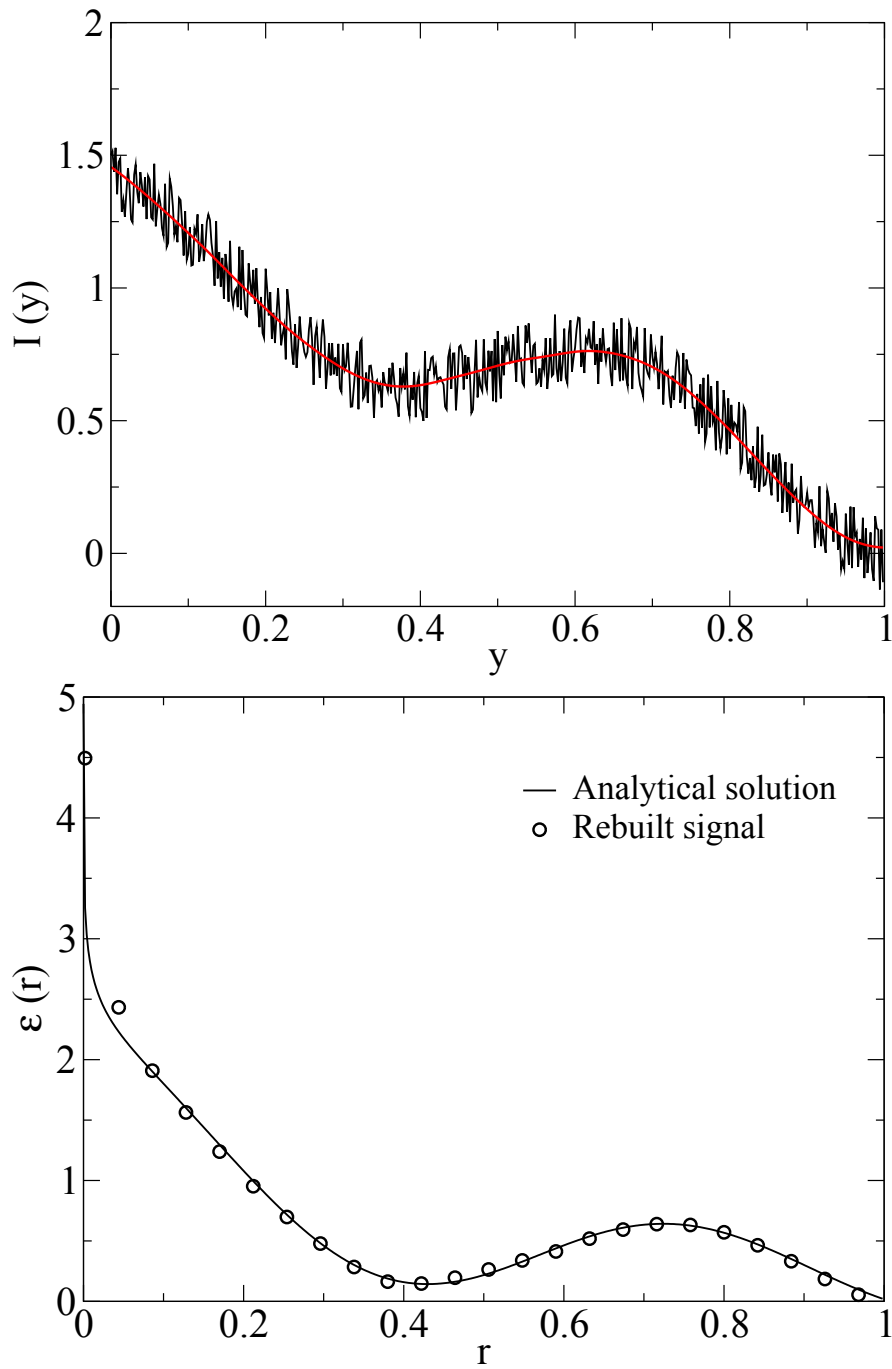


Figure 3.6.: Top: noisy profile and associated filtering. Bottom: Abel inversion results

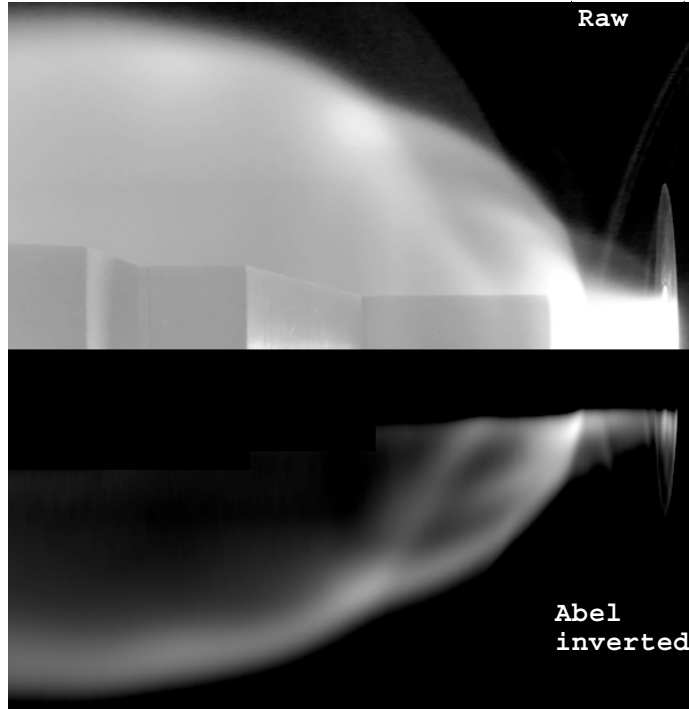


Figure 3.7.: Abel transform of plasma flow emission around heat flux probe.

stands for the Bessel Function, $\omega = 3\pi$ and $\alpha = 1.2$. The filtering procedure and Abel inversion are illustrated in figures 3.5 and 3.6. Similar rebuilt profiles are found with about 5 % error at the center when a noisy background with an amplitude of 20% of the raw signal is added. This problem, due to the filtering process, can be overcome by filtering the entire profile. *Supersonic*

$I(y)$	$\epsilon(r)$
$\frac{2 \cos(\omega y)}{\omega} + (\alpha - y)$	$J_0(\omega r) + \frac{1}{\pi} \cosh^{-1}(\alpha/r)$

Table 3.2.: Synthetic profile used to test the Abel transform.

jet impacting on enthalpy probe.

A picture of a plasma jet impacting an enthalpy probe was Abel inverted. At each axial location, the profile was filtered and Abel inverted. Result is shown in figure 3.7. The front of the probe is not computed due to light saturation. This gives important details on the aerodynamic field, especially on the shock region around the probe.

3.2.4. Radiative transfer calculation.

In order to assess the opacity of the plasma jet, it is useful to solve the radiative transfer equation (RTE). For bound-bound transitions, only spontaneous emission, absorption and stimulated emission have to be accounted for radiative energy transfer applications. Assuming one dimensional geometry where the light is collected along the radial dimension of a plasma jet, neglecting transients and assuming a non-scattering medium, the equation of radiative transport simplifies

as:

$$\frac{dI_{\sigma}(r)}{dr} = \epsilon_{\sigma}(r) - \kappa_{\sigma}(r)I_{\sigma}(r) \quad (3.35)$$

Where ϵ_{σ} (resp. κ_{σ}) designates the spectral emission (resp. absorption) coefficient and I_{σ} is the spectral radiance integrated over the line of sight. Two approaches are considered to solve the radiative transfer. The first concerns the atomic transitions for which the absorption coefficient calculation is based on the emission coefficient using Kirchhoff law that applies under LTE condition. The second concerns radiative transfer calculation for diatomic molecules. In this latest approach, we adopt a formulation where the absorption coefficient is related to the population density of the upper and lower states associated to the rovibronic transition. At LTE, these two approaches are similar.

Atomic case

Deviation from LTE is not considered when solving the RTE for atomic lines. Absorption coefficient is calculated using expression 3.5. Investigated atomic lines being spectrally well separated, the RTE is solved separately for each atomic transition in order to assess the importance of self-absorption. Indeed, all studied atomic lines are spectrally well separated in order to get reliable information on total power emissivity issued from one transition. Furthermore, no overlapping with molecular systems is observed. Therefore we assume that the absorption by other species is not significant. In this context, it is not necessary to compute high spectral resolution line profiles to solve the RTE. Spectral emission and absorption coefficients are computed through a convolution with gaussian distribution f_D which half-width is given by the Doppler half-width γ_D as expressed in equations 3.36 and 3.37.

$$f_D(\sigma - \sigma_{ul}) = \frac{1}{\gamma_D} \sqrt{\frac{\ln 2}{\pi}} \exp\left(-\ln 2 \left(\frac{\sigma - \sigma_{ul}}{\gamma_D}\right)^2\right) \quad (3.36)$$

$$\gamma_D = \sigma_{ul} \sqrt{\frac{2k_B T \ln 2}{mc^2}} \quad (3.37)$$

where T stands for the gas temperature

$$\epsilon_{\sigma} = \int \epsilon_{ul} \times f_D(\sigma - \sigma_{ul}) d\sigma \quad (3.38)$$

The atomic lineshape profile is given by equation 3.38.

Molecular case

For molecular radiative transfer calculation, the radiative transfer analysis is performed through a classical formulation combined with the use of HTGR (High Temperature Gas Radiation) database. The absorption coefficient is calculated separately from the emission coefficient as detailed in equation 3.9. High spectral resolution calculation are performed using spectral broadening described in section 3.1.2.

Chapter 4.

Optical emission spectroscopy diagnostics

Plasmatron facility experiment replicating Stardust re-entry peak heating pressure condition are conducted and will be described in chapter 5. Based on this experiment, we present a spectroscopic diagnostic that uses absolute atomic line intensity to determine the so-called LTE temperature. The sensitivity of this method is discussed. The analysis of the atomic excited states distribution is also described. The determination of the electron density through the characterization of the Stark broadening contribution of hydrogen H_β transition is presented. A fast estimation of the electron density from the half width of the experimental line shape is firstly described. Then, theoretical datasets allowing for a comparison with the entire line shape are introduced. Three different datasets based on the so-called *VCS*, *MMM* and *CS* models are implemented. The latter *CS* model is found to be more suitable to simulate our experiment. This model is described in details. Finally, various formulations of the spectral emission coefficient of a diatomic molecule are detailed. For each formulation referring to a specific equilibrium assumption, the molecular spectra fitting method is detailed and tested.

4.1. Plasma characterization using atomic contribution

4.1.1. Atomic line equilibrium radiation.

Following the equations mentioned in section 3.1.1 of chapter 3, we can express the total power ϵ_{ul} emitted at LTE by an atomic transition which wavenumber is noted σ_{ul} as a function of a single equilibrium temperature T_{LTE} and an equilibrium species concentration $[N]_{LTE}$:

$$\epsilon_{ul} = \frac{1}{4\pi} g_u \frac{[N]_{LTE}}{Q_{int}(T_{LTE})} \exp\left(-\frac{hc\sigma_u}{k_B T_{LTE}}\right) A_{ul} hc \sigma_{ul} \quad (4.1)$$

Knowing the pressure of an isobaric jet, the equilibrium concentration $[N]_{LTE}$ is computed using NASA-CEA equilibrium tool [66]. An iterative procedure is executed to obtain an equilibrium temperature T_{LTE} for which experimental and calculated power are equal. For a plasma at LTE, the resulting equilibrium temperature should be identical for any atomic lines. Temperature sensitivity of the emission of scaled atomic transitions corresponding to arbitrary upper electronic energy levels is displayed in figure 4.1. Equilibrium concentrations are calculated so that they correspond to an air plasma at 273 mbar, similarly to the experiment described in chapter 5. Scaled power of the atomic transitions is obtained by setting to unity the electronic statistical weight and the transition probability. In agreement with Boltzmann distribution, transitions from low lying energy level are stronger than high lying energy level transition. Increasing the temperature of several percents leads to a significant change (about one order of magnitude) in the total power emitted. This diagnostic has a weak sensitivity response and is not adequate to evidence slight departure from equilibrium. However it can be used to evidence strong departure from the equilibrium atomic excited states distribution. In case of significant absorption (in our experiment, it is mostly occurring with transitions from low lying upper energy level), we account also for line self-absorption as introduced by [11]. The radiative transfer equation is solved along the temperature profile obtained under optically thin assumption for each atomic lines. The emission corrected for self-absorption is introduced in a new iterative loop and gives

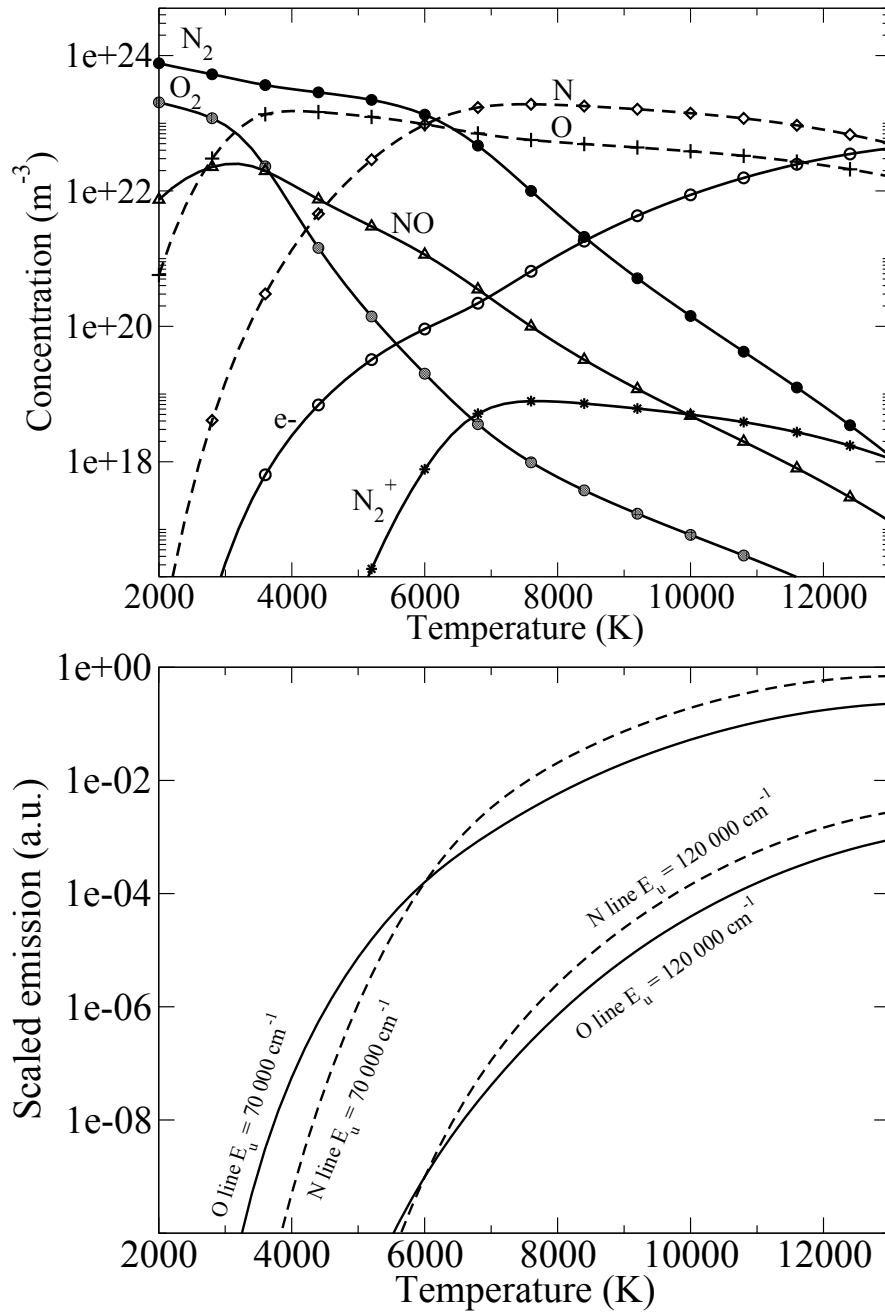


Figure 4.1.: Top: 273 mbar air plasma species concentration. Bottom: Scaled atomic emission.

a new temperature profile. This correction introduces larger changes at the center than at the edges where the optical path is smaller.

4.1.2. Atomic excited states distribution.

Based on measured total power ϵ_{ul} (previously described), we can straightly probe the upper (emitting) level n_u population density of several emitting states. In thermal plasmas, the electronic state distribution function obeys Boltzmann distribution and the excitation temperature of electronic excited states T_{el} can be evaluated on the basis of the Boltzmann diagram method using the following relations:

$$\ln\left(\frac{n_u}{g_u}\right) = \ln\left(\frac{\epsilon_{ul}4\pi}{A_{ul}g_u h c \sigma_{ul}}\right) \quad (4.2)$$

$$= -\left(\frac{hc}{k_b T_{el.}}\right) E_u + \ln\left(\frac{[N]}{Q_{int}}\right) \quad (4.3)$$

This approach is convenient to determine the excitation temperature as no assumption is made concerning the species concentration. Excitation temperature $T_{el.}$ is directly obtained from the slope of a straight line fitted on the set of experimental electronic excited states population logarithm values (left term of Equation 4.3). In our experiment, the equilibrium distribution is measured for electronic states close to the ionization energy and no information is collected concerning the transitions issued from very low energy level. We consider that partial Local Saha equilibrium (pLSE) is prevailing, so that the upper part of atomic energy scheme defined by the excitation temperature $T_{el.}$ complies with the temperature of free electrons T_e . The Saha formula that describes the shape of the atomic states distribution function is therefore expressed as:

$$\frac{n_u}{g_u} = \frac{N_e}{g_e} \frac{n_i}{g_i} \left(\frac{h^2}{2\pi m_e k_B T_e}\right)^{3/2} \exp\left(\frac{I_p}{k_B T_e}\right) \quad (4.4)$$

where n_u is the population density of the atomic excited level u with ionization energy I_p . n_i/g_i (resp. N_e/g_e) is the ion (resp. electron) density per statistical weight. g_i being the degeneracy of the ground state of the ion. Taking the logarithm of equation 4.4, we obtain:

$$\ln\left(\frac{n_u}{g_u}\right) = \frac{I_p}{k_B T_e} + \ln\left(\frac{n_\infty}{g_\infty}\right) \quad (4.5)$$

$$\text{with } \frac{n_\infty}{g_\infty} = \frac{N_e n_i}{2g_0^i} \times \left(\frac{h^2}{2\pi m_e k T_e}\right)^{3/2} \quad (4.6)$$

where, n_∞/g_∞ is called the Saha point in the Boltzmann diagram representation. Non-Boltzmann electronic excitation were not clearly identify in our experiments. However in chapter 7, supersonic air plasma experiment reveals that beyond the ionization energy, an electronic state is underpopulated with respect to the population of the transitions from low-lying energy level. In this case, the atomic scheme can be decoupled in a upper (ruled by pLSE distribution at T_e) and a lower part evidencing over or under population with respect to the Saha distribution. In order to qualitatively express the departure from equilibrium, it can be convenient to defined two temperatures $T_{el.}^{low}$ and $T_{el.}^{high}$ corresponding respectively to the excitation temperature of lower and higher states. However, because we only observed one single state that does not comply with the Boltzmann distribution of lower states, we chose not to define a temperature associated to this state. This state was simply excluded from the linear regression on the Boltzmann plot.

Boltzmann plot linear regression uncertainty

Considering Boltzmann plot, the uncertainty on the fitting of a set of N experimental data points (x_i, y_i) to a straight line model $y = a + bx$ has to be evaluated. We assume that the uncertainty

σ_i associated with each density measurement y_i (standing for $\ln(n_u/g_u)$ in the Boltzmann plot) is fixed at and that the x_i (standing for the energies in the Boltzmann plot) are known exactly. In our experiments σ_i is fixed so that it is equivalent to $\pm 10\%$ uncertainty on the population density. This uncertainty is estimated assuming that major errors are due to the rebuilding procedure that includes the calibration and the Abel transform. To measure how well the linear regression agrees with the data, we use the χ^2 merit function, which in this case is:

$$\chi^2(a, b) = \sum_{i=1}^N \left(\frac{y_i - a - bx_i}{\sigma_i} \right)^2 \quad (4.7)$$

Equation 4.7 is minimized to determine a and b , which gives the following system of equations:

$$\begin{cases} aS + bS_x = S_y \\ aS_x + bS_{xx} = S_{xy} \end{cases} \quad (4.8)$$

where S , S_x , S_y , S_{xx} and S_{xy} are defined by

$$S = \sum_{i=1}^N \frac{1}{\sigma_i^2} \quad S_x = \sum_{i=1}^N \frac{x_i}{\sigma_i^2} \quad S_y = \sum_{i=1}^N \frac{y_i}{\sigma_i^2} \quad S_{xx} = \sum_{i=1}^N \frac{x_i^2}{\sigma_i^2}$$

$$S_{xy} = \sum_{i=1}^N \frac{x_i y_i}{\sigma_i^2}$$

The solutions of 4.8 for the best fit are,

$$a = \frac{S_{xx}S_y - S_xS_{xy}}{\Delta} \quad (4.9)$$

$$b = \frac{SS_{xy} - S_xS_y}{\Delta} \quad (4.10)$$

$$\text{with } \Delta = SS_{xx} - (S_x)^2 \quad (4.11)$$

and the estimated uncertainty on a and b are given by:

$$\sigma_a^2 = \frac{S_{xx}}{\Delta} \quad (4.12)$$

$$\sigma_b^2 = \frac{S}{\Delta} \quad (4.13)$$

4.1.3. Stark broadening of hydrogen lines.

A distinct interest is devoted to the spectral line shape of hydrogen lines belonging to the Balmer serie. There are four lines in the visible region of the hydrogen spectrum that corresponds to the Balmer serie. Spectroscopic constants associated to these lines are detailed in table 4.1. Using Griem's relations [68], broadening contributions of the H_β hydrogen line are illustrated in figure 4.2 for atmospheric pressure condition at LTE. In our temperature and density ranges, Stark and Doppler effects are expected to be the major processes responsible for the line shape broadening. Stark effect results from the combination of the static effect of ions and the collision effect of electrons. Various theoretical models ([68], [74], [75], [76]) are available to determine electron density through the examination of Stark broadening.

Analytical determination of the electron density

By measuring the H_β Stark half width at half maximum γ_{Stark} , the electron density might be evaluated rapidly through the use of an approximate formula [68] which tells:

$$N_e [cm^{-3}] = 10^{16} \left(\frac{\gamma_{Stark}}{4.7333} \right)^{1.49} \quad (4.14)$$

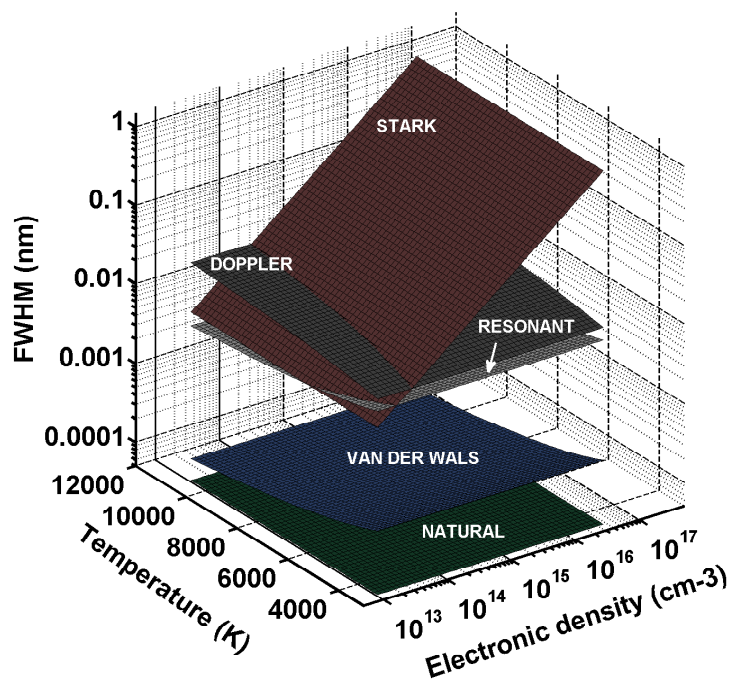


Figure 4.2.: H_{β} line shape broadening contributions as a function of the electron number density and temperature in LTE air plasma at atmospheric pressure.

BALMER SERIE				
Transitions	λ_{air} (Å)	E_l	E_u	A_{ul}
H_{α}	6562.83	82259.163	97492.283	4.4101×10^7
H_{β}	4861.35	82259.163	102 823.904	8.4193×10^6
H_{γ}	4340.47	82259.158	105 291.657	2.5304×10^6
H_{δ}	4101.73	82259.158	106 632.1681	9.7320×10^5

Table 4.1.: Hydrogen Balmer lines spectroscopic data.

where γ_{Stark} is given Angström units. Accounting for the Doppler γ_D and the instrumental broadening γ_I , γ_{Stark} is obtained straightly from the measured half width γ_m according to:

$$\gamma_{Stark} = (\gamma_m^2 - \gamma_{DI}^2)^{1/2} \quad (4.15)$$

$$\text{with } \gamma_D = 1.74 \times 10^{-4} T^{0.5} \quad (4.16)$$

$$\text{and } \gamma_{DI} = (\gamma_{Doppler}^2 + \gamma_{instru.}^2)^{1/2} \quad (4.17)$$

where γ_{DI} refers to the half-width of a gaussian function representing the Doppler and the apparatus broadening contribution.

Hydrogen line shape databases

Theoretical data sets of hydrogen line shape have enabled the use of the whole atomic profile in plasma diagnostics thus reporting a more accurate value of N_e through direct comparison with experiments. Until recently the most accurate line shape calculation method was based on the theory of line broadening developed by Vidal & al. [74]. The so-called *VCS* model evaluates the ionic contribution to the line shape by using quasi-static ion approximation. This assumption gives incorrect results, especially in the central region of Stark broadened lines at low density values. The inclusion of ion dynamics in newer and more elaborate broadening theories has improved the line shape evaluation. Starting from the work of Frisch and Brissaud [77], Seidel [78] obtained theoretical profiles of hydrogen lines which includes ion dynamics effects by means of the so-called *Model Microfield Method (MMM)*. Well known data sets associated to this model are given by Stehle & al. ([79], [76]). Other calculation methods, as the *Computer Simulation (CS)* considered by Gigosos & al. ([80], [75]), also offer the possibility to account for ion dynamics. Comparison between these models are illustrated for H_β line in figure 4.3. These recent sets of data consider the broadening to be produced by the joint action of ions and electrons colliding with the emitting hydrogen particles. Screened field ρ_s and relative reduced mass μ_r parameters defined in equations 4.18 and 4.19 are introduced to characterize the electron and the ion dynamics effects on the broadening.

$$\rho_s = \frac{r_0}{\lambda_D} = \left(\frac{3}{4\pi N_e} \right)^{1/3} \times \left(\frac{q_e^2 N_e}{\epsilon_0 k T_e} \right)^{1/2} \quad (4.18)$$

$$\mu_r = \mu \frac{T_e}{T_i} \quad (4.19)$$

where r_0 is the mean distance between ionic particles of the same kind, λ_D is the Debye length, T_e and T_i are respectively the temperature of electron and ionic particles and μ represents the reduced mass. H_α and H_β Balmer lines are suitable for diagnostic purposes, since their broadening is significant and their line shape is only slightly sensitive to the ion dynamics effects as illustrated at the top of figure 4.4 for H_β line. The use H_β and H_α lines is convenient because of the poor sensitivity to the temperature of electrons as illustrated at the bottom of figure 4.4. Nevertheless, a preliminary investigation reveals that the measured broadening of the H_α line is significantly affected by the Doppler broadening contribution as illustrated in figure 4.5 and 4.6. The determination of electron density through the use H_α line broadening would then suffer greatly from a lack of information on gas temperature. For this purpose, only H_β line broadening will be investigated. H_β line shape can be fitted through the use of only one parameter which is the electron density. The tabulation given by Stehle attributes a constant value of 0.5 to the relative reduce mass (corresponding to hydrogen ion perturbers). Conversely, tabulation from Gigosos is given for various relative reduced mass allowing to model the influence of various ion species. In order to account for the plasma composition, hydrogen line shape calculation are performed by using *CS* tabulation which provide several reduced mass values. Other models are withdrawn from study. The available data selected for H_β theoretical profiles are presented in table 4.2. These data sets are not relevant for high electron density values where asymmetries originate from quadratic Stark effect and quadrupole interaction. The intensity profiles are

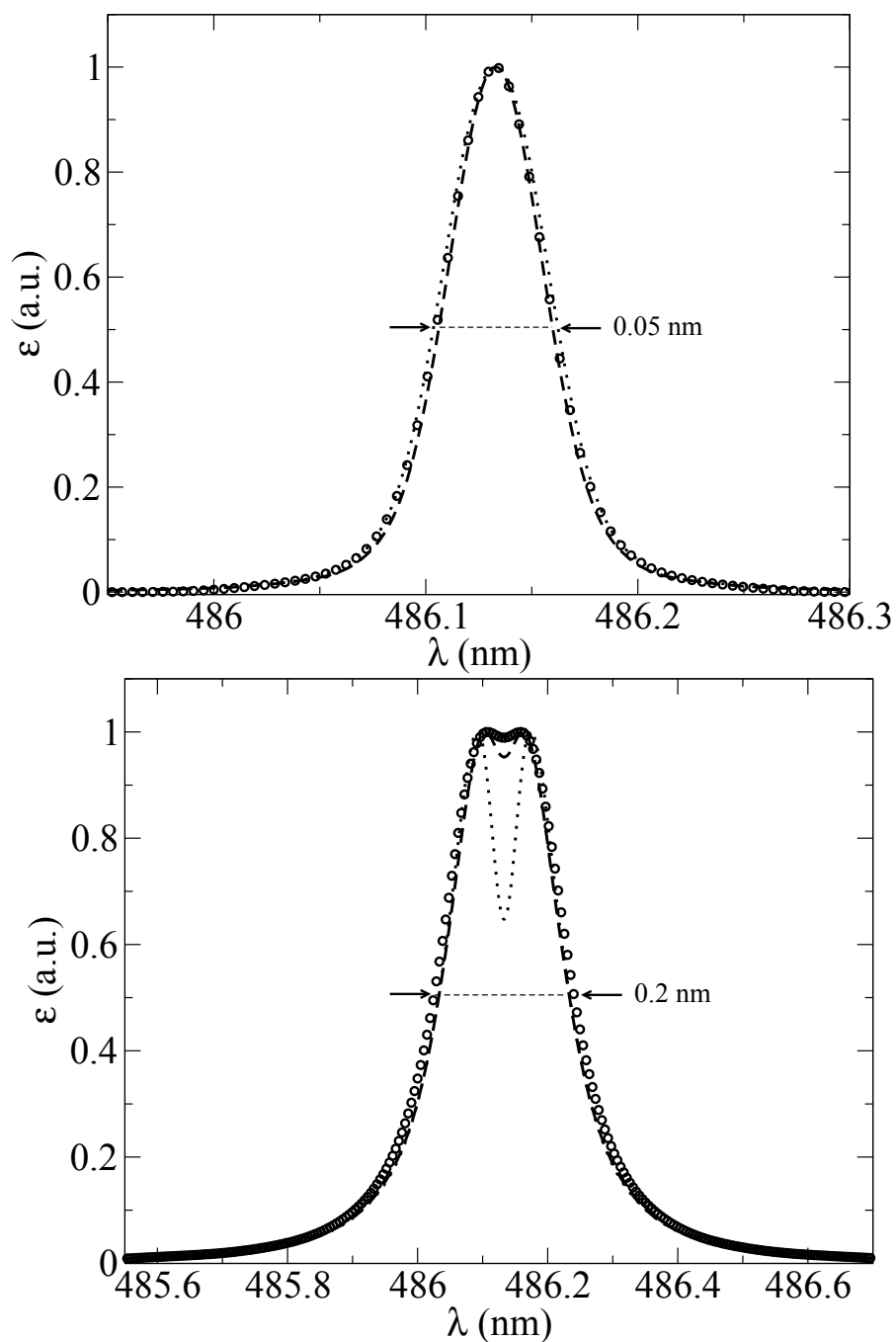


Figure 4.3.: Computations of H_β line shape with Stark and Doppler broadening at 10000 K and 10^{14} (top) and 10^{15} (bottom) cm^{-3} electron density. VCS (dotted), MMM (dashed) and CS (circle)

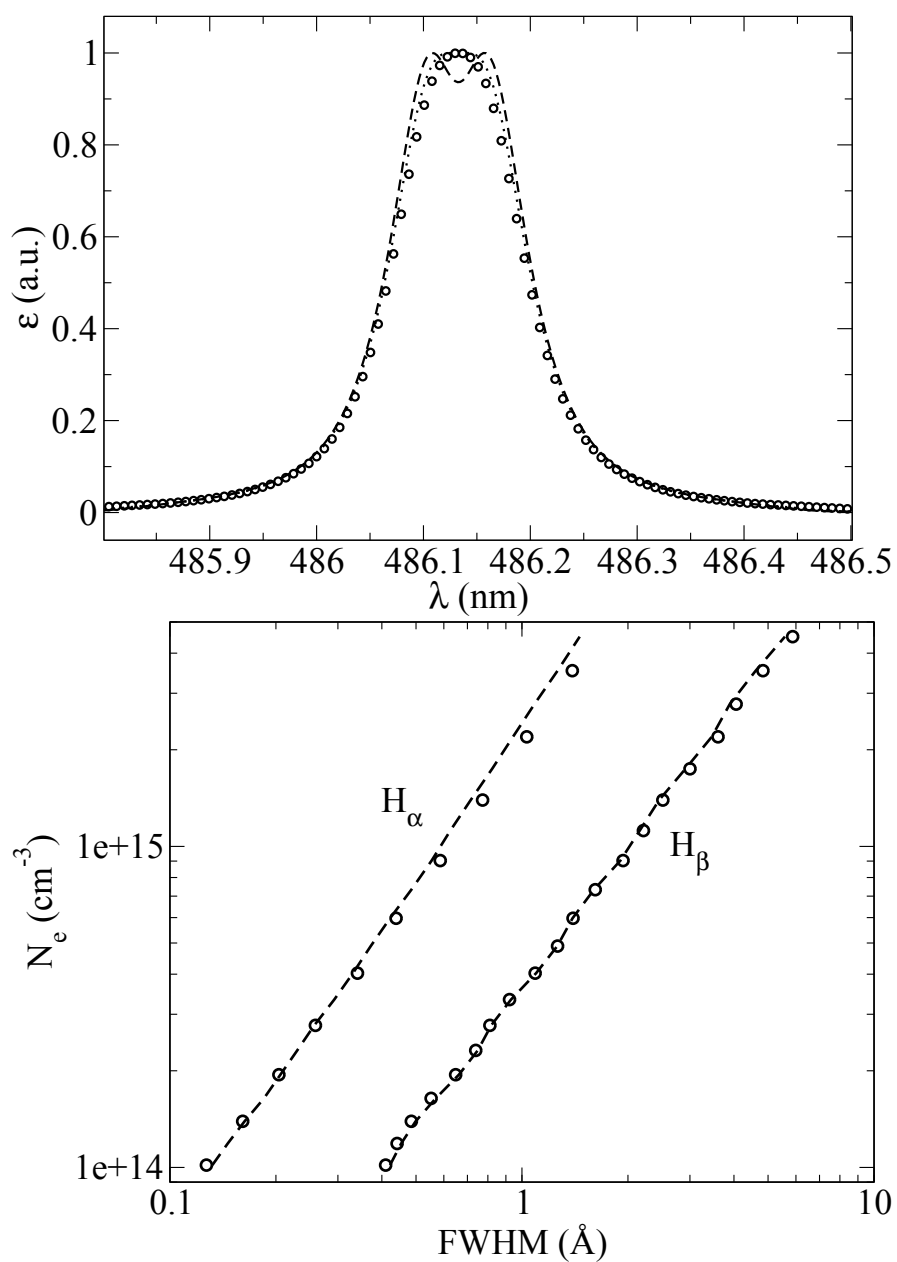


Figure 4.4.: Top: Computations of H_β Stark broadening line shape at 10000 K, $5.0 \times 10^{14} \text{ cm}^{-3}$ electron density for various relative reduced mass $\mu_r = 5.0$ (dashed), 1.0 (dotted), 0.5 (circle). Bottom: Stark broadening FWHM at $T_e = 5000 \text{ K}$ (dashed) and $T_e = 10\,000 \text{ K}$ (circle) using *CS* simulation.

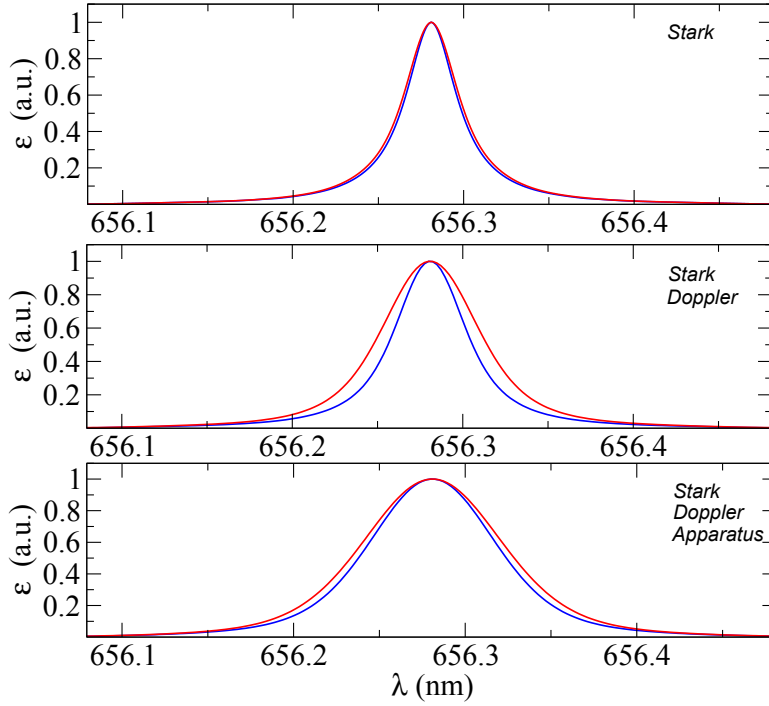


Figure 4.5.: Computed hydrogen H_{α} spectral line shape broadening at $N_e = 5.0 \times 10^{14} \text{ cm}^{-3}$, $T = 5000 \text{ K}$ (blue), 15000 K (red).

$N_e \text{ [m}^{-3}\text{]}$	$T_e \text{ min [K]}$	$T_e \text{ max [K]}$
$10^{20.00}$	1042	37508
$10^{20.33}$	1346	48444
$10^{20.66}$	1738	62568
$10^{21.00}$	2245	80809
$10^{21.33}$	2899	104369
$10^{21.66}$	3744	134798
$10^{22.00}$	4836	174098

Table 4.2.: Electron densities and temperatures selected from *CS* theoretical database for H_{β} line shape calculation.

tabulated against wavelengths for certain values of electron temperature T_e and density N_e . In order to obtain a profile for any couple (T_e, N_e) , a bilinear interpolation is performed from the scattered theoretical data defined by the 2D matrix $(T_e, \log(N_e))$.

Hydrogen spectral line shape fitting

Considering that thermal and Stark effects are independent, the Doppler contribution is accounted using a simple convolution with a gaussian distribution function as defined in chapter 3 by the Doppler half-width $\gamma_{Doppler}$ and using a gas temperature T_g . The theoretical line profile is then convoluted with the instrumental broadening of the apparatus. The spectral profile is finally interpolated to match the spectral grid of the experimental data set and any background in the experimental data is zeroed using linear subtraction so that the experimental line is directly comparable with the theoretical profiles. A minimization routine is called from

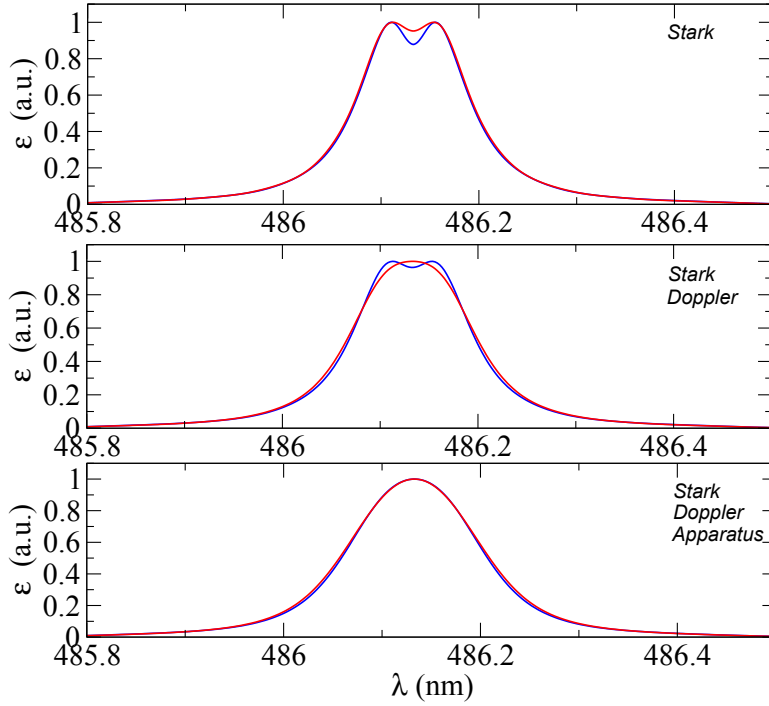


Figure 4.6.: Computed hydrogen H_{β} spectral line shape broadening at $N_e = 5.0 \times 10^{14} \text{ cm}^{-3}$, $T = 5000 \text{ K}$ (blue), 15000 K (red).

a *FORTTRAN* library that reduces the Root Mean Square Error (RMSE) between the experimental and the theoretical scaled line profiles by varying N_e at constant temperature T_e . The iteration corresponding to the lowest RMSE is then reported with the corresponding value of N_e . RMSE distribution during the fitting procedure on a reference H_{β} line is reported in figure 4.7 for a reference density of $1.0 \times 10^{15} \text{ cm}^{-3}$.

4.2. Plasma characterization using molecular contribution

Plasma characterization using molecular spectra is done on the basis of common fitting approaches consisting of the minimization of the RMSE between the experimental spectrum and the spectrum calculated under various equilibrium assumptions. E04JYF *FORTTRAN* minimization routine is well suited to problems that involve several variables function. From starting input conditions involving several bounded independent variables, the estimation of a minimum is achieved through quasi-Newton algorithm which uses the gradient and the Hessian matrix of second derivatives of the function to be minimized. In this section, the reliability of the fitting procedure is tested by computing synthetic spectra of N_2^+ First Negative system under various thermal state assumptions.

Theoretical spectra are calculated on the basis of an advanced tool developed and available at the EM2C laboratory and so-called High Temperature Gas Radiation (HTGR) code described in chapter 3. Assuming that the population of each internal energy mode follows a Boltzmann distribution affected by a distinctive temperature, we can define a rotational temperature T_{rot} , a vibrational temperature T_{vib} and a temperature of electronic excitation T_{el} . Using the expression of the rovibronic partition functions of the internal modes recalled in equations 3.15,

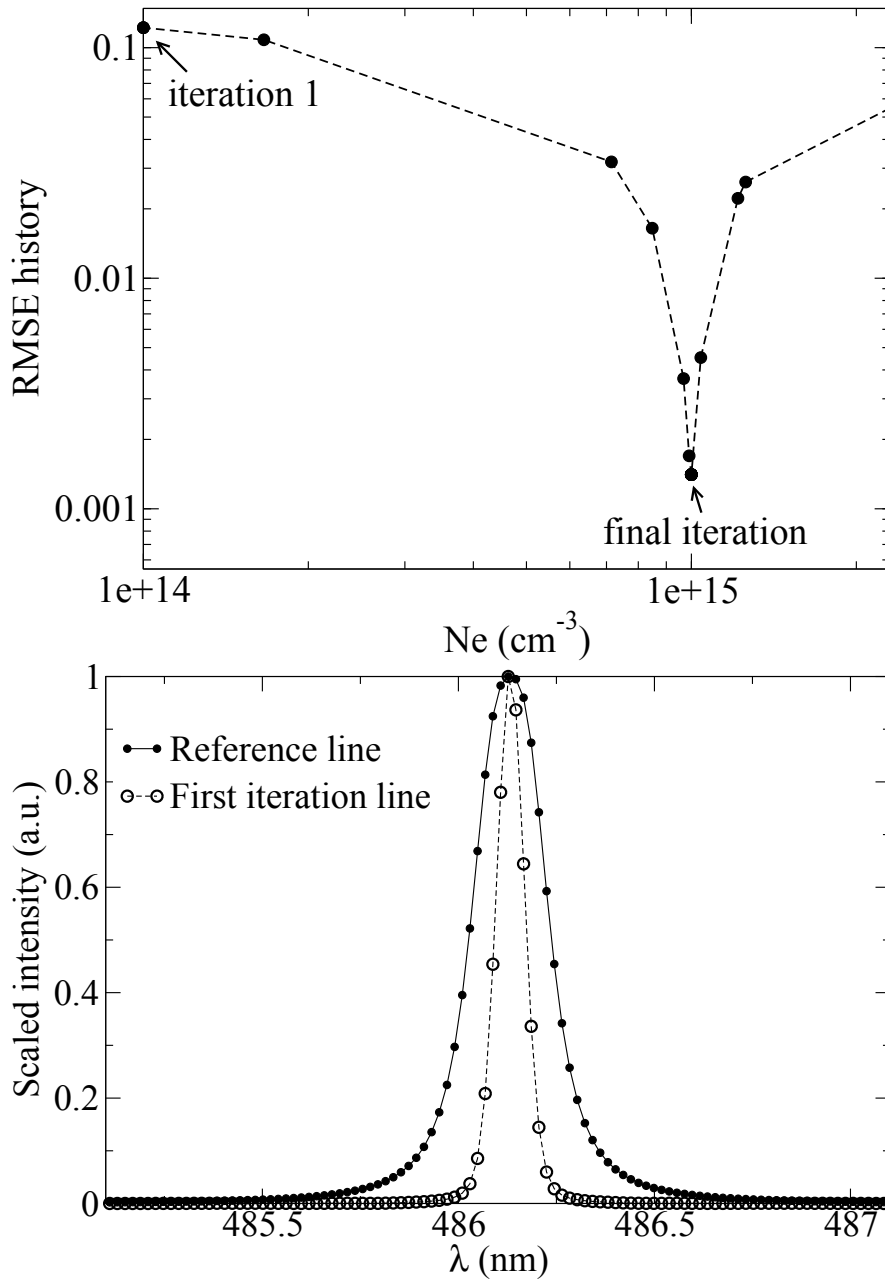


Figure 4.7.: Top: RMSE distribution. Bottom: Reference and computed H_β line at the first iteration

3.16 and 3.17 of chapter 3, the population density associated to each mode is expressed as:

$$N_n = \frac{g_n[N]Q_{mol}^n(T_{rot}, T_{vib})}{Q_{int}(T_{rot}, T_{vib})} \exp\left(-\frac{hcE_{el}(n)}{k_bT_{el}}\right), \quad (4.20)$$

$$N_{n,v} = \frac{N_n Q_{mol}^{n,v}(T_{rot})}{Q_{mol}^n(T_{rot}, T_{vib})} \exp\left(-\frac{hcG_{vib}^n(v)}{k_bT_{vib}}\right), \quad (4.21)$$

$$N_{n,v,J} = \frac{\phi_p(2J+1)N_{n,v}}{Q_{mol}^{n,v}(T_{rot})} \exp\left(-\frac{hcF_{rot}^{n,v}(J)}{k_bT_{rot}}\right), \quad (4.22)$$

where $[N]$ stands for the species concentration, N_n is the population of the n electronic state and $N_{n,v}$ refers to the vibrational populations of the v vibrational level associated to the n electronic state.

4.2.1. Boltzmann population distribution of internal energy modes.

Local thermodynamic equilibrium assumption

Combining equations 3.8 and 3.24 of chapter 3 and equation 4.20 mentioned previously, the spectral emission ϵ_σ from several electronic transitions can be expressed as:

$$\begin{aligned} \epsilon_\sigma &= \frac{16\pi^3 c}{3 \times 4\pi\epsilon_0} \frac{[N]}{Q_{int}(T_{eq})} \\ &\times \sum_{u \rightarrow l} \phi_{p'} \left(R_n^{v'v''} \right)^2 S_{J'J''}^{v'v''} \\ &\times \left(E_{el}(n') + G_{vib}^{n'}(v') + F_{rot}^{n',v'}(J') \right. \\ &\quad \left. - E_{el}(n'') + G_{vib}^{n''}(v'') + F_{rot}^{n'',v''}(J'') \right)^4 \\ &\times \exp\left(-hc \frac{E_{el}(n') + G_{vib}^{n'}(v') + F_{rot}^{n',v'}(J')}{k_bT_{eq}}\right) \\ &\times f(\sigma - \sigma_{ul}), \end{aligned} \quad (4.23)$$

Where $\sum_{u \rightarrow l}$ stands for the sum over all possible electronic transitions ($n'v', J' \rightarrow n''v'', J''$). The equilibrium temperature T_{eq} ($T_{eq} = T_{rot} = T_{vib} = T_{el}$) is obtained by fitting the elaborated spectrum with the experimental spectrum. It consists in the minimization of the function expressed as:

$$RMSE(T_{eq}) = \sqrt{\frac{1}{m} \sum_{i=1}^m (\epsilon_{\sigma_i}^{exp} - \epsilon_{\sigma_i}^{sim}(T_{eq}))^2}, \quad (4.24)$$

m is the number of experimental points in the considered spectral range. For absolute intensity fitting, the knowledge of the concentration of the radiating species should be known. At LTE, chemical equilibrium is accounted in equation (4.23) by setting the value of the species density $[N]$. Knowing the operating pressure and the thermal temperature, the equilibrium concentration for each species is calculated using the NASA Chemical Equilibrium code [66]. Similar fitting can be executed through the use of scaled spectra which allows to neglect any chemical state assumption. In such case, only thermal equilibrium is considered. Similarly to equation 4.24, we define the minimization of the function expressed as:

$$RMSE(T_{eq}) = \sqrt{\frac{1}{m} \sum_{i=1}^m \left(\overline{\epsilon_{\sigma_i}^{exp}} - \overline{\epsilon_{\sigma_i}^{sim}(T_{eq})} \right)^2}, \quad (4.25)$$

Input synthetic spectrum	T = 8000 K, 0.4 nm spectral resolution
First iteration	T = 5000 K
Boundary conditions	[4000-13000] K
Spectral position for scaling	358 nm
Number of iterations [335-360] nm	23
Number of iterations [335-430] nm	23
Output result [335-360] nm	T = 7994.5 K
Output result [335-430] nm	T = 7992.4 K

Table 4.3.: Thermal fitting parameters.

where the normalized spectral emission $\overline{\epsilon_{\sigma}}$ is scaled in reference to a given spectral position σ_{iref} using the following set of equations.

$$\begin{cases} \overline{\epsilon_{\sigma_i}^{exp}} = K_1 \epsilon_{\sigma_i}^{exp} + (K_2 \sigma_i + K_3), \\ \max \left(\overline{\epsilon_{\sigma_{i=iref}}^{exp}} \right) = 1, \end{cases} \quad (4.26)$$

where the over-lined symbols denote for scaled values and K variables are adjustable parameters. Thermal fitting procedure is illustrated in figures 4.8 and 4.9. Input conditions and final result are recalled in table 4.3. The minimization procedure is performed for two different spectral ranges corresponding either to the vibrational band $\Delta v = +1$ or to the vibrational bands $\Delta v = -1, 0$ and $+1$. In figure 4.8, the first iteration scaled spectra are displayed for each case. The black line corresponds to the synthetic spectrum and the red curve is the spectrum calculated using the temperature set through the minimization routine. The vibrational band $\Delta v = +1$ is highly sensitive to the temperature change and both minimization procedures converge with about 0.1% uncertainty on the equilibrium temperature. RMSE distribution displayed in figure 4.9 shows that the wider is the spectral range, the smaller is the finale RMSE value. The convergence speed is similar for both calculations. Best fits are obtained after 23 iterations with a squared correlation coefficient value of 0.99 that demonstrates a very good agreement between the synthetic spectra and the best fit. The squared correlation coefficient R^2 is expressed as:

$$R^2 = 1 - \frac{SS_{res}}{SS_{tot}} \quad (4.27) \quad \text{with } SS_{res} = \sum_i (\epsilon_{\sigma_i}^{exp} - \epsilon_{\sigma_i}^{sim})^2,$$

$$SS_{tot} = \sum_i (\epsilon_{\sigma_i}^{exp} - \epsilon_{\sigma_{mean}}^{exp})^2, \quad \epsilon_{\sigma_{mean}}^{exp} = \frac{1}{m} \sum_{i=1}^m \epsilon_{\sigma_i}^{exp},$$

Chemical non-equilibrium

A multi-species fitting procedure allows to account for several species without any assumption on the relative species concentration. A chemical concentration ratio $R_{ch.} = [N_{species1}] / [N_{species2}]$ is introduced to account for the relative density between the two different species. The spectral emission being defined as previously, the function to be minimized is expressed as:

$$RMSE(T_{eq}, \chi) = \sqrt{\frac{1}{m} \sum_{i=1}^m (\epsilon_{\sigma_i}^{exp} - \epsilon_{\sigma_i}^{sim}(T_{eq}, R_{ch.}))^2}, \quad (4.28)$$

Rotational-vibrational two temperatures assumption

For thermal non-equilibrium, a commonly used model assumes that the plasma can be described by distinct rotational and a vibrational temperatures. Assuming on one hand a Boltzmann distribution for rotation (T_{rot}) and on the other hand a Boltzmann distribution for vibrational energy levels ruled by a single temperature (T_{vib}), the determination of the couple of temperatures (T_{rot}, T_{vib}) consists in the minimization of the functional defined as:

$$RMSE(T_{rot}, T_{vib}) = \sqrt{\frac{1}{m} \sum_{i=1}^m (\overline{\epsilon_{\sigma_i}^{exp}} - \overline{\epsilon_{\sigma_i}^{sim}}(T_{rot}, T_{vib}))^2}, \quad (4.29)$$

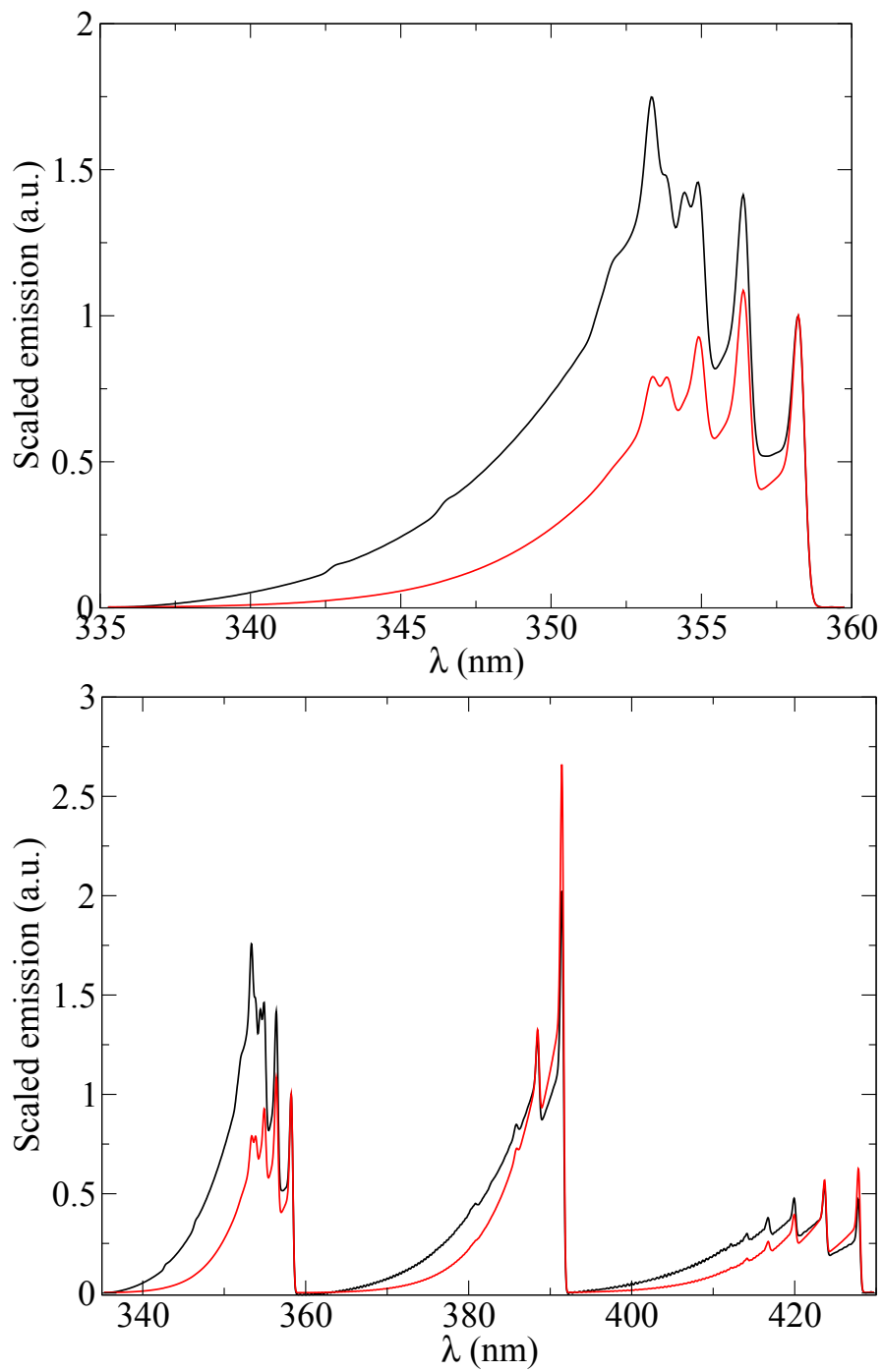


Figure 4.8.: Thermal equilibrium spectra fittings: first iteration [335-360] nm (top) and [335-430] nm (bottom) .

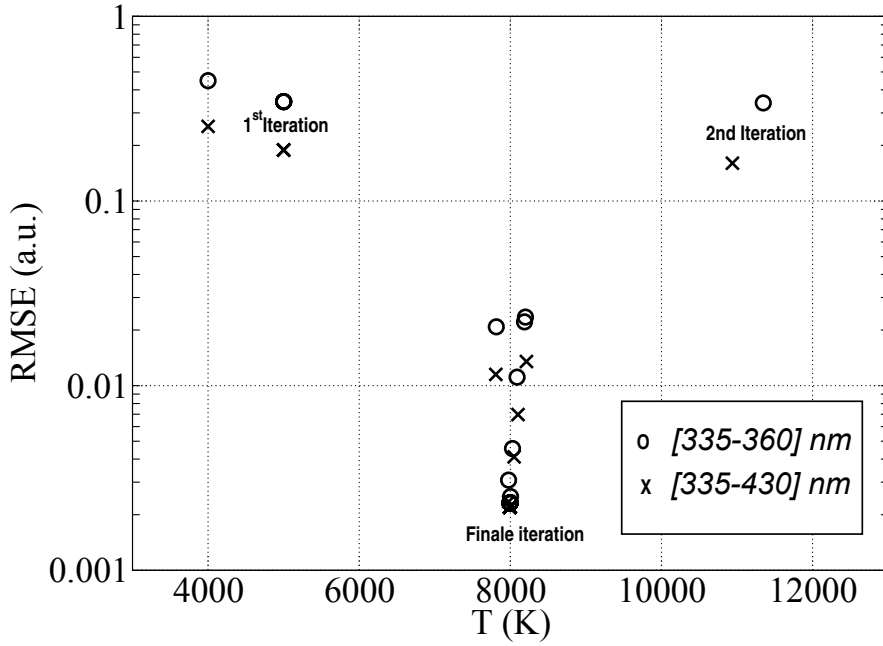


Figure 4.9.: RMSE distribution for various spectral ranges.

The minimization is performed using scaled spectra because species concentration $[N]$ of non-thermal plasmas is not accounted in our model. The overlined symbols are used to mark the scaled parameters. In this case, the spectral emission ϵ_σ is expressed as:

$$\begin{aligned}
 \epsilon_\sigma &= \frac{16\pi^3 c}{3 \times 4\pi\epsilon_0} \frac{[N]}{Q_{int}(T_{rot}, T_{vib})} \\
 &\times \sum_{u \rightarrow l} \phi_{p'} \left(R_n^{v'v''} \right)^2 S_{J',J''}^{v'v''} \\
 &\times \left(E_{el}(n') + G_{vib}^{n'}(v') + F_{rot}^{n',v'}(J') \right. \\
 &\quad \left. - E_{el}(n'') + G_{vib}^{n''}(v'') + F_{rot}^{n'',v''}(J'') \right)^4 \\
 &\times \exp\left(-hc \frac{E_{el}(n') + G_{vib}^{n'}(v')}{k_b T_{vib}} \right) \times \exp\left(-hc \frac{F_{rot}^{n',v'}(J')}{k_b T_{rot}} \right) \\
 &\times f(\sigma - \sigma_{ul}),
 \end{aligned} \tag{4.30}$$

where electronic and vibrational excitations follow a Boltzmann distribution defined by the same temperature T_{vib} . Multi-temperature fitting procedure is illustrated hereafter. Input conditions and final result are recalled in table 4.4. The minimization procedure is performed on the the vibrational bands $\Delta v = -1, 0$ and $+1$. The effect of additional noisy background is examined through the elaboration of noisy synthetic spectrum. In figure 4.10, both synthetic spectra are displayed. The artificial background is set to be linear. In figure 4.11, the first iteration of the minimization procedure is displayed. In the first iteration, the major discrepancy between the spectra is found to rise from the $\Delta v = +1$ vibrational band. The red curve represents again the spectrum calculated using the temperature set through the minimization routine. A slight deterioration on the accuracy of the best fit is found (as illustrated in figures 4.12 and 4.13) when we add superimposed random noise. The minimization procedures converge with a

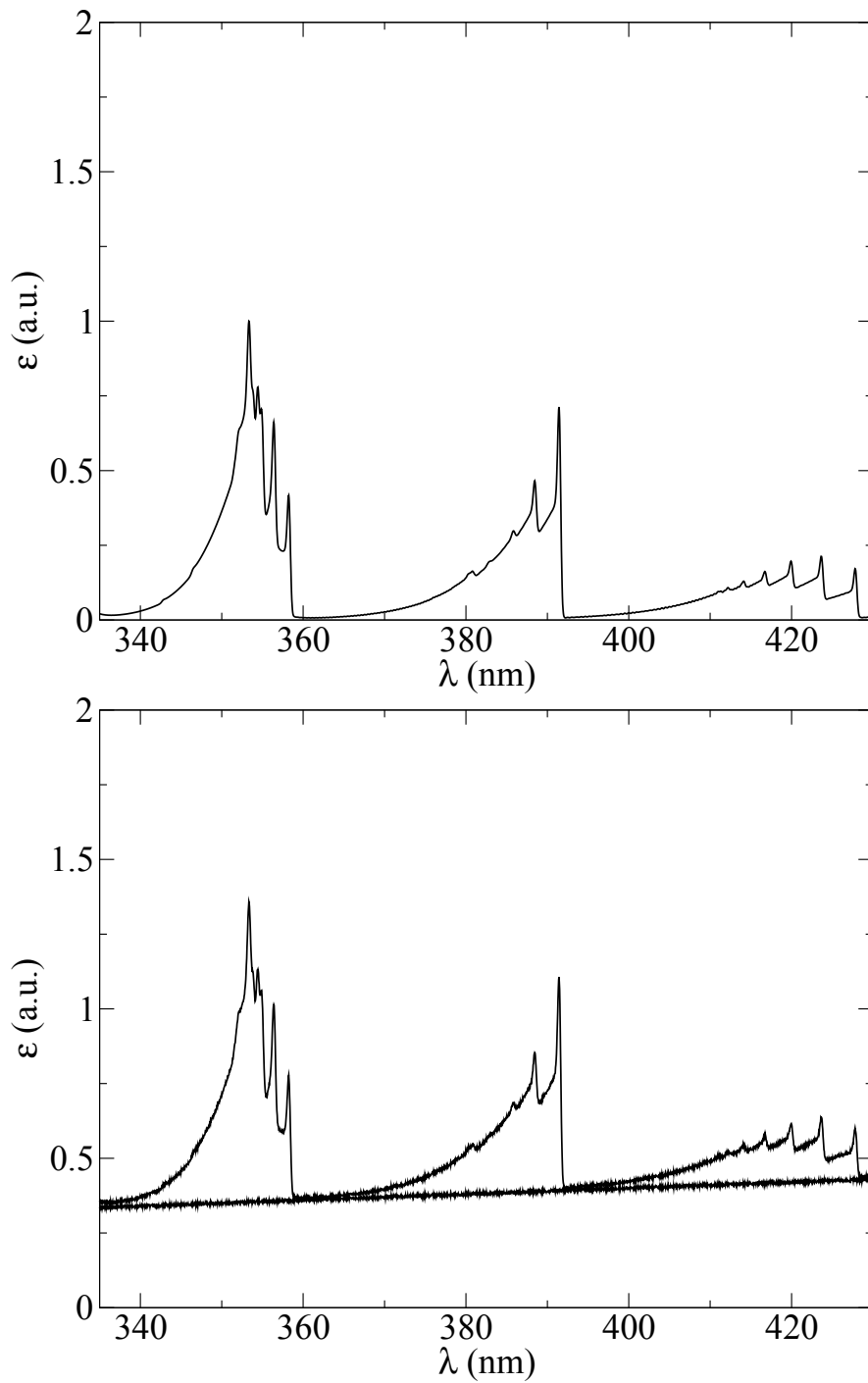


Figure 4.10.: Synthetic spectrum - $T_{rot} = 7000$ K, $T_{vib} = 12000$ K - (top). Synthetic noisy spectrum and additional noisy background (bottom).

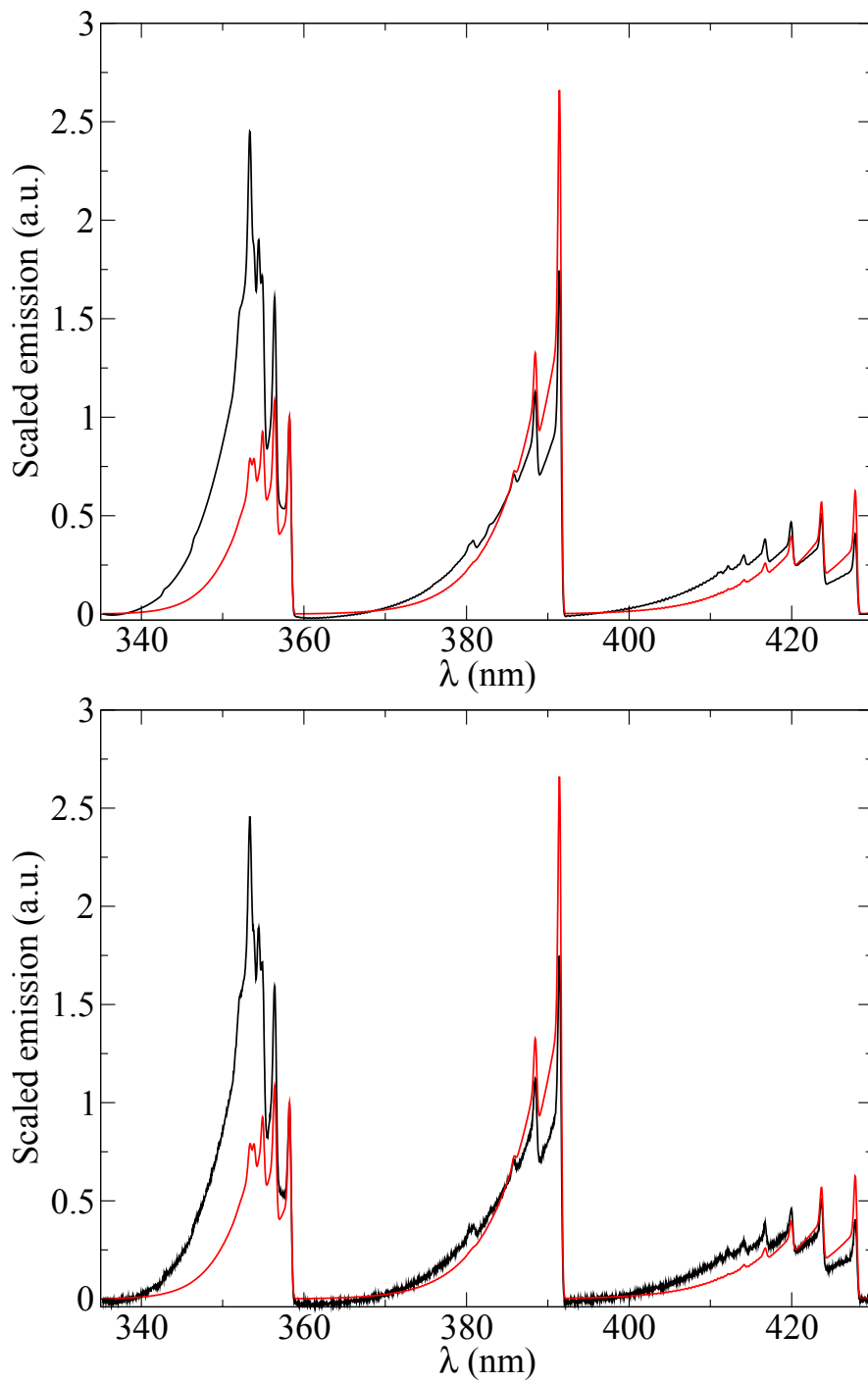


Figure 4.11.: Two-temperature spectra fitting first iteration: synthetic spectrum without background (top) and with noisy contribution (bottom).

Input synthetic spectrum	$T_{rot} = 7000$ K, $T_{vib} = 12000$ K 0.4 nm spectral resolution
First iteration	$T_{rot} = 5000$ K, $T_{vib} = 5000$ K
Boundary conditions	[4000-13000] K
Spectral position for scaling	358 nm
Number of iterations (no background)	99
Number of iterations (noisy background)	83
No background output result	$T_{rot} = 6938.9$ K, $T_{vib} = 12110.2$ K
Noisy background output result	$T_{rot} = 6785.6$ K, $T_{vib} = 12283.3$ K

Table 4.4.: Two-temperature fitting parameters.

squared correlation coefficient value of 0.99 in less than 100 iterations. We obtain 3 % error on both rotational and vibrational temperatures.

4.2.2. Electronic non-equilibrium.

We account for electronic non-equilibrium between electronic states when several electronic systems are fitted together. The amplitude of the emission of a molecular band system is determined mainly by the electronic excitation of the emitting state whereas vibrational and rotational excitations affect the spectral distribution. A population ratio of electronic excited states can be evaluated through fitting procedure by expressing the spectral emission coefficient as a function of the upper electronic population $N_{n'}$ (following the notation introduced in chapter 3). For the two-temperature approach, the calculation of the spectral emission issued from a single electronic state $N_{n'}$ reduces to:

$$\begin{aligned}
\epsilon_{\sigma} = & \frac{16\pi^3 c}{3 \times 4\pi\epsilon_0} \frac{N_{n'}}{g_{n'} Q_{mol}^{n'}(T_{rot}, T_{vib})} \\
& \times \sum_{u \rightarrow l} \phi_{p'} \left(R_n^{v'v''} \right)^2 S_{J'J''}^{v'v''} \\
& \times \left(E_{el}(n') + G_{vib}^{n'}(v') + F_{rot}^{n',v'}(J') \right. \\
& \left. - E_{el}(n'') + G_{vib}^{n''}(v'') + F_{rot}^{n'',v''}(J'') \right)^4 \\
& \times \exp\left(-hc \frac{G_{vib}^{n'}(v')}{k_b T_{vib}}\right) \exp\left(-hc \frac{F_{rot}^{n',v'}(J')}{k_b T_{rot}}\right) \\
& \times f(\sigma - \sigma_{ul}),
\end{aligned} \tag{4.31}$$

Electronic non-equilibrium factor α is introduced to perform the fitting so that no equilibrium assumption is made between the relative population of two electronic levels $N_{n'_1}$ and $N_{n'_2}$.

$$\alpha = \frac{g_{n'_2}}{g_{n'_1}} \times \frac{N_{n'_1}}{N_{n'_2}} \times \frac{Q_{mol}^{n'_2}(T_{rot}^{n'_2}, T_{vib}^{n'_2})}{Q_{mol}^{n'_1}(T_{rot}^{n'_1}, T_{vib}^{n'_1})}, \tag{4.32}$$

A new set of parameters $(T_{rot}^{n'_1}, T_{vib}^{n'_1}, T_{rot}^{n'_2}, T_{vib}^{n'_2}, \alpha)$ is determined by using a classical fitting procedure method characterized by the minimization of $RMSE(T_{rot}^{n'_1}, T_{vib}^{n'_1}, T_{rot}^{n'_2}, T_{vib}^{n'_2}, \alpha)$. An electronic temperature can be determined assuming a Boltzmann distribution between these two electronic states.

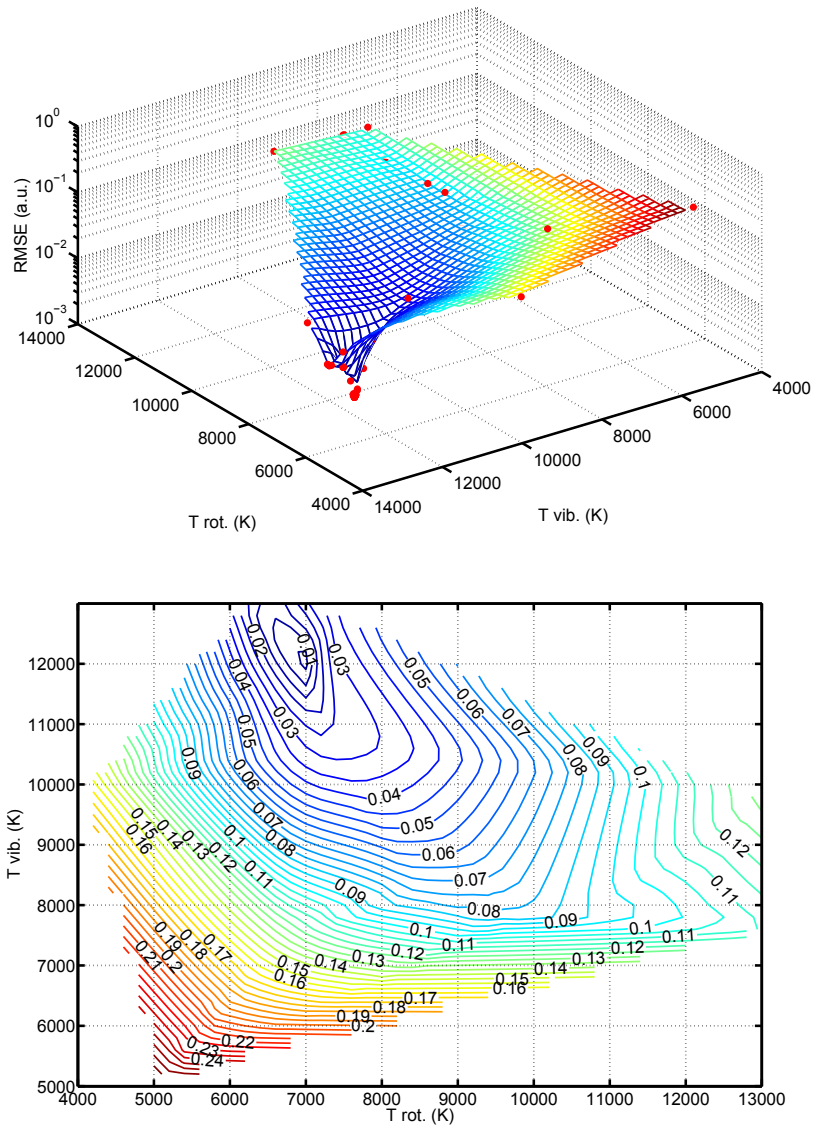


Figure 4.12.: RMSE distribution (top) and RMSE isocontours (bottom).

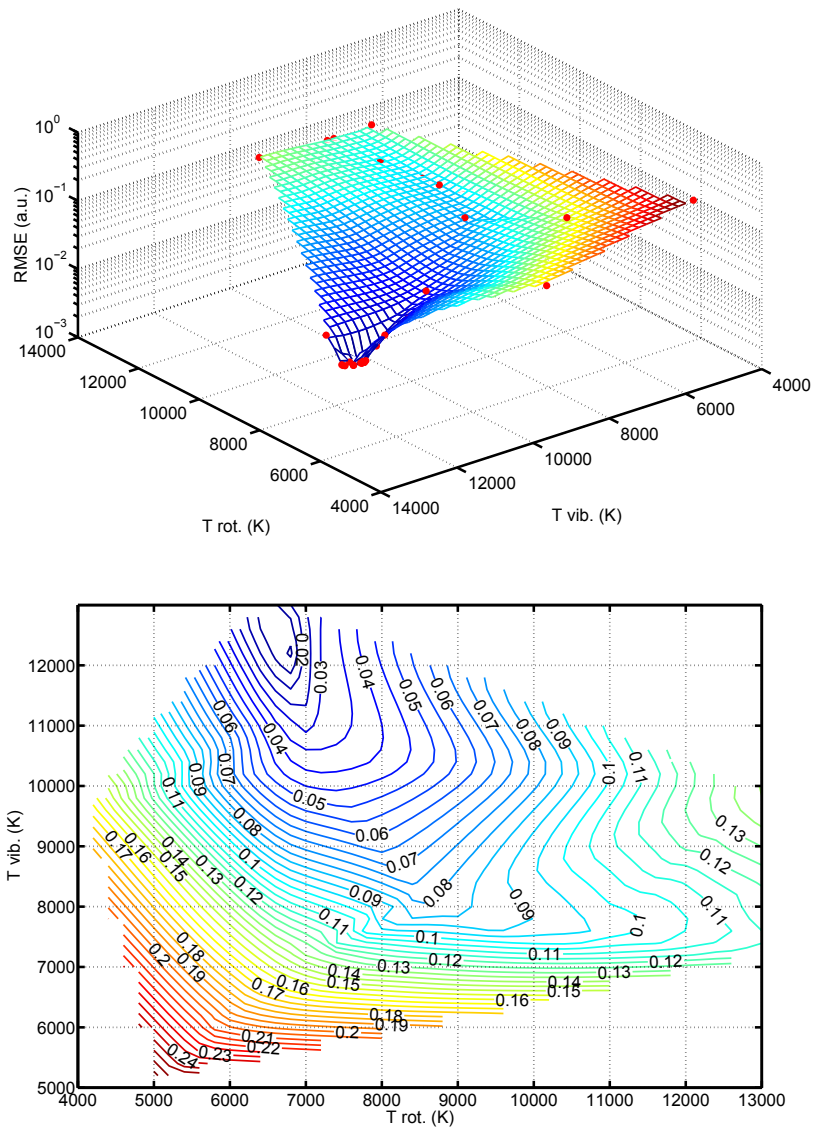


Figure 4.13.: Noisy fitting RMSE distribution (top) and noisy fitting RMSE iso-contours (bottom).

Input synthetic spectrum	$T_{rot} = 7000$ K, 0.4 nm spectral resolution synthetic distribution of vibrational levels
First iteration Boundary conditions Spectral position for scaling	$T_{rot} = 5000$ K, $T_{vib} = 12000$ K [4000-13000] K 358 nm
Number of iterations Output result	690 $T_{rot} = 7053.8$ K synthetic distribution of vibrational levels

Table 4.5.: Vibrational non-equilibrium fitting parameters.

4.2.3. Vibrational non-equilibrium.

Vibrational distribution function can be obtained through molecular fitting. The calculation of the spectral emission issued from a single vibrational state $N_{n'v'}$ reduces to:

$$\begin{aligned}
\epsilon_{\sigma} = & \frac{16\pi^3 c}{3 \times 4\pi\epsilon_0} \frac{N_{n'v'}}{g_{n'} Q_{mol}^{n',v'}(T_{rot})} \\
& \times \sum_{u \rightarrow l} \phi_{p'} \left(R_n^{v'v''} \right)^2 S_{J'J''}^{v'v''} \\
& \times \left(E_{el}(n') + G_{vib}^{n'}(v') + F_{rot}^{n',v'}(J') \right. \\
& \left. - E_{el}(n'') + G_{vib}^{n''}(v'') + F_{rot}^{n'',v''}(J'') \right)^4 \\
& \times \exp \left(-hc \frac{F_{rot}^{n',v'}(J')}{k_b T_{rot}} \right) \\
& \times f(\sigma - \sigma_{ul}),
\end{aligned} \tag{4.33}$$

The minimization of $RMSE(T_{rot}, [N_{n'v'_1}], [N_{n'v'_2}], \dots, [N_{n'v'_{max}}])$ is performed over the relevant vibrational levels ($v' = 1 \rightarrow 8$). The vibrational states accounted in the calculation are chosen so that general features of the spectrum are correctly reproduced in the investigated spectral range. Vibrational population fitting procedure is illustrated hereafter. Input conditions and final result are recalled in table 4.5. The minimization procedure is performed on the the vibrational bands $\Delta v = +1$ using the vibrational levels $v = 1$ to $v = 8$. The synthetic vibrational distribution is arbitrary chosen so that there is an overpopulation of the higher levels in comparison with a 12000 K equilibrium distribution (figure 4.15). In figure 4.14, the synthetic spectrum is displayed with the contribution of each vibrational band. The first iteration is also displayed at the bottom of figure 4.14, showing the large discrepancy between the initial synthetic spectra. The fitted vibrational distribution is in very good agreement with the synthetic distribution (figure 4.15). The rotational temperature is found to agree with less than 1 % with the input conditions. Again, the squared correlation coefficient value is 0.99.

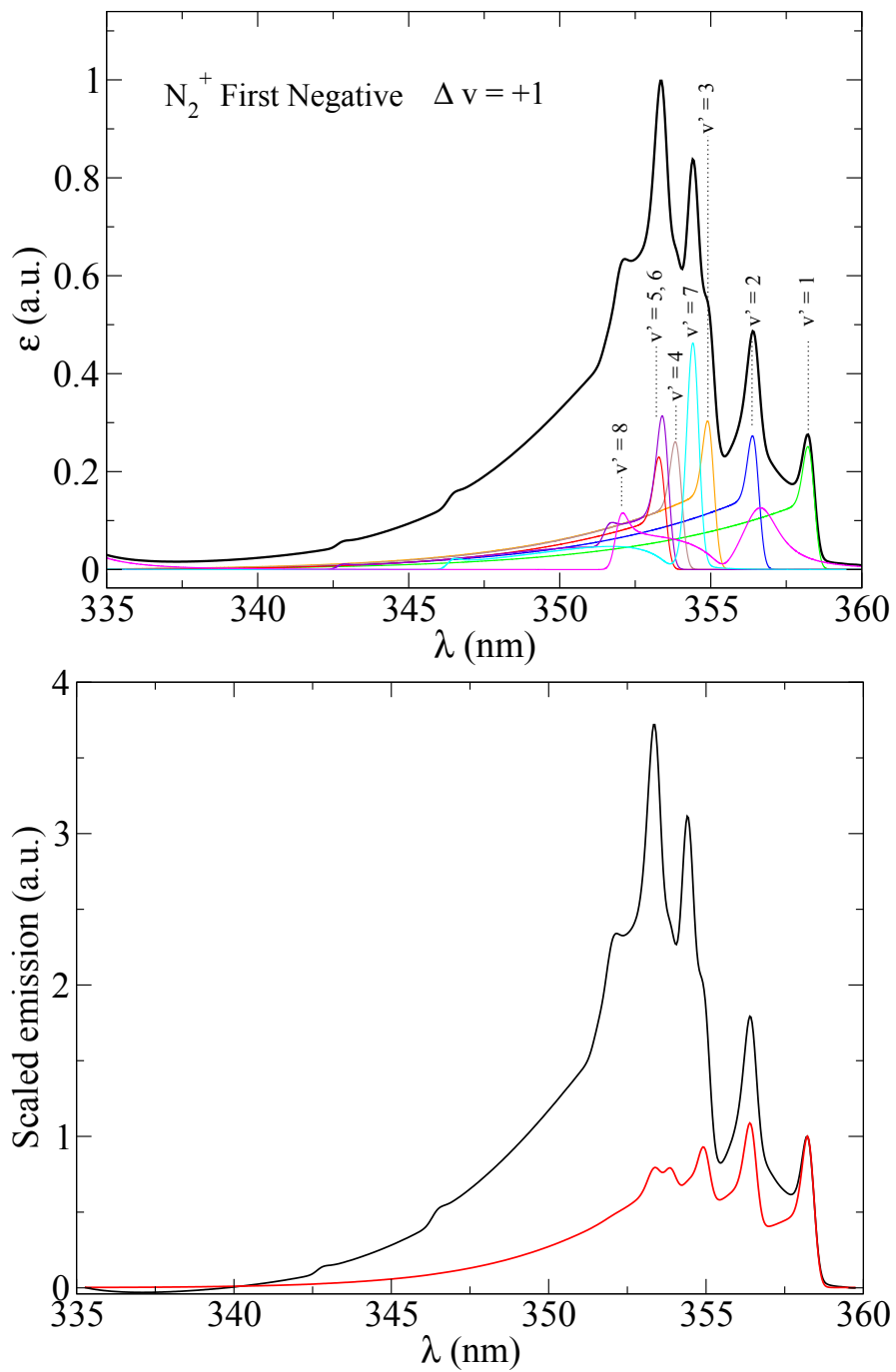


Figure 4.14.: Vibrational non-equilibrium synthetic spectrum and vibrational bands contribution (top) and first fitting iteration (bottom).

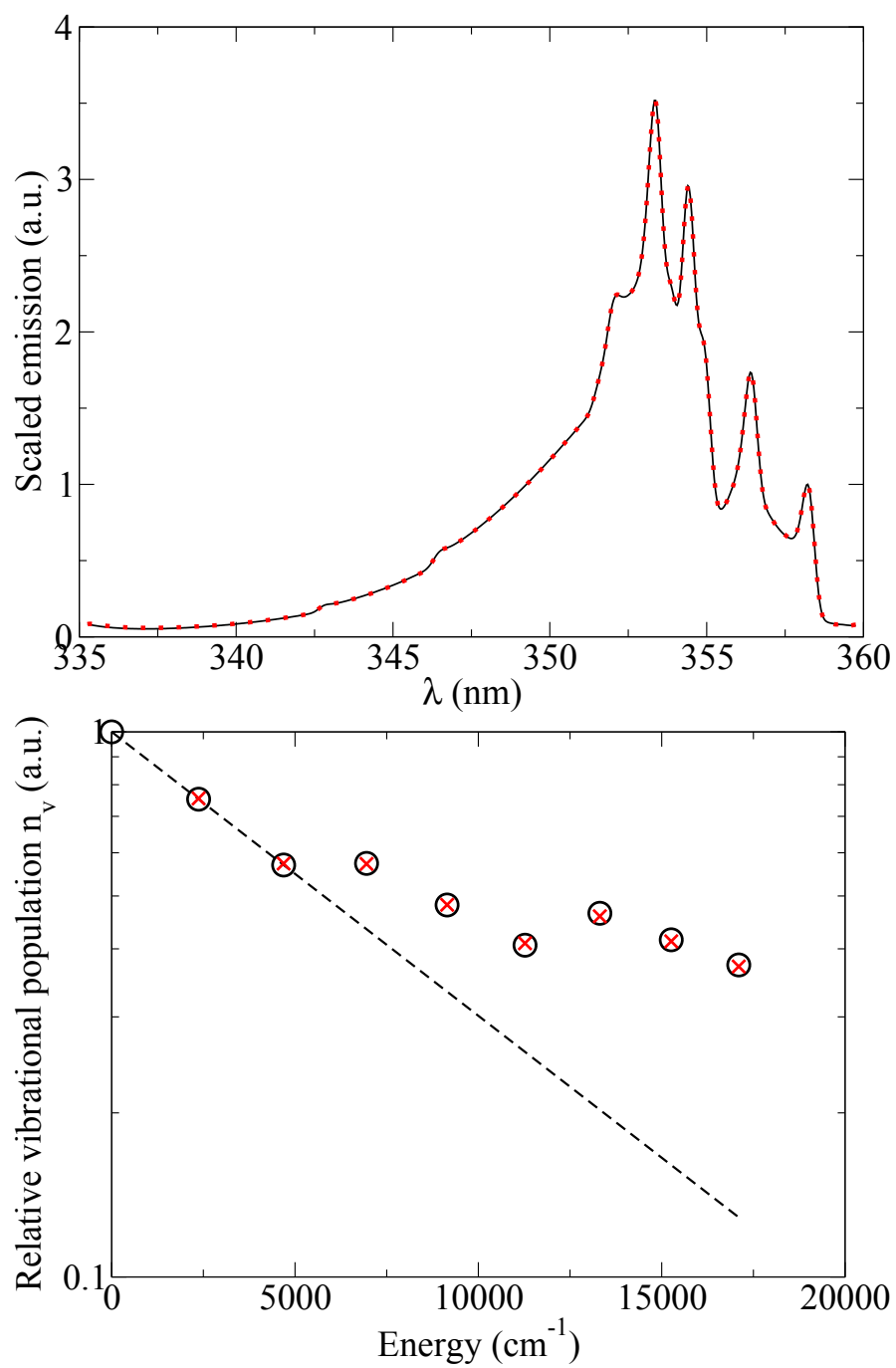


Figure 4.15.: Top: Spectra fitting final iteration. Bottom: Relative population of vibrational levels: 12000 K equilibrium distribution (dashed line), synthetic distribution (circle) and best fit (red cross).

Chapter 5.

Thermodynamic characterization of subsonic plasma flows

Thermal Protection System (TPS) testing requires long duration plasma facilities, suitable to duplicate stagnation point heat flux of real entry flights. In plasma wind tunnels, measured heat flux on the stagnation point is related to the stagnation point heat flux during flights through a classical methodology called Local Heat Transfer Simulation (LHTS). It is used to examine the boundary layer edge conditions and it allows to extrapolate ground testing conditions to heat flux on the stagnation point of re-entry vehicles [35], [81]. This rebuilding procedure is valid under LTE assumption. To assess LTE assumption, the first experimental campaign deals with the characterization of the thermodynamic state of an air subsonic plasma jet produced in VKI ICP Plasmatron facility operating at 500 kW RF-power and 16 g.s^{-1} mass flow rate. The operating pressure is maintained at 273 mbar similarly to the pressure at the peak radiative heat flux of Stardust re-entry.

As stated in chapter 2, WMD was extensively used for the validation of spectroscopic and radiative databases under equilibrium conditions at atmospheric pressure. The objective of the second experimental campaign is to characterize the microwave discharge in a low pressure environment where non-equilibrium thermodynamic processes are expected to prevail.

5.1. ICP air Plasmatron experiment

Optical emission spectroscopy is executed. Specific operating settings are detailed in table 5.1. Although pressure fluctuations are found to be about ± 8.0 mbar, good reproducibility of the spectra is obtained. High-resolution measurements are carried along the radial direction of the jet, 16 cm downstream the exhaust of the jet. The slit aperture of the monochromator is set to $10 \mu\text{m}$, leading to a spectral resolution of about 0.066 nm . Several discrete spectral regions displayed in figure 5.1 are recorded. Spectral scans contain atomic lines (N, O and traces of hydrogen) and molecular systems (N_2^+ 1st Negative and N_2 Second Positive). Also, carbonous contamination is observed, leading to the presence of CN emission on the edge of the jet. All the data are calibrated in absolute units ($\text{W.m}^{-2}.\text{sr}^{-1}.\text{nm}^{-1}$) using a tungsten ribbon-filament lamp combined with deuterium source. Abel transform is used to rebuild local emissivity ($\text{W.m}^{-3}.\text{sr}^{-1}.\text{nm}^{-1}$).

5.1.1. Boltzmann equilibrium of rotational and vibrational energy modes.

In order to account for N_2 and N_2^+ molecular systems lying within $[300-400] \text{ nm}$ spectral range, we adopt a multi-species fitting approach. We observe the presence of CN contaminant affecting the accuracy of the fitting on the edges of the jet beyond 3 cm radial extent. For this purpose 3-species fitting approach is performed under thermal equilibrium. Results of spectra fitting performed assuming a Boltzmann equilibrium of rotational and vibrational energy modes are displayed in figure 5.2. The close agreement between experiments and calculations shows that

Operating conditions	16 g.s ⁻¹ mass flow rate 273 mbar operating pressure 500 kW power
Spectroscopic features	Jobin-Yvon THR1000 monochromator UV-Vis, 0.066 nm spectral resolution Radially resolved measurements (800 μm resolution) Downstream axial location (distance from the exit): 18.5 cm
Radiative transitions of interest	N ₂ ⁺ (B ² Σ _u ⁺ → X ² Σ _g ⁺) 1st Negative System N ₂ (C ³ Π _u → B ³ Π _g) 2nd Positive System Atomic nitrogen Atomic oxygen Atomic hydrogen

Table 5.1.: Experimental operating conditions of subsonic air ICP plasma jet.

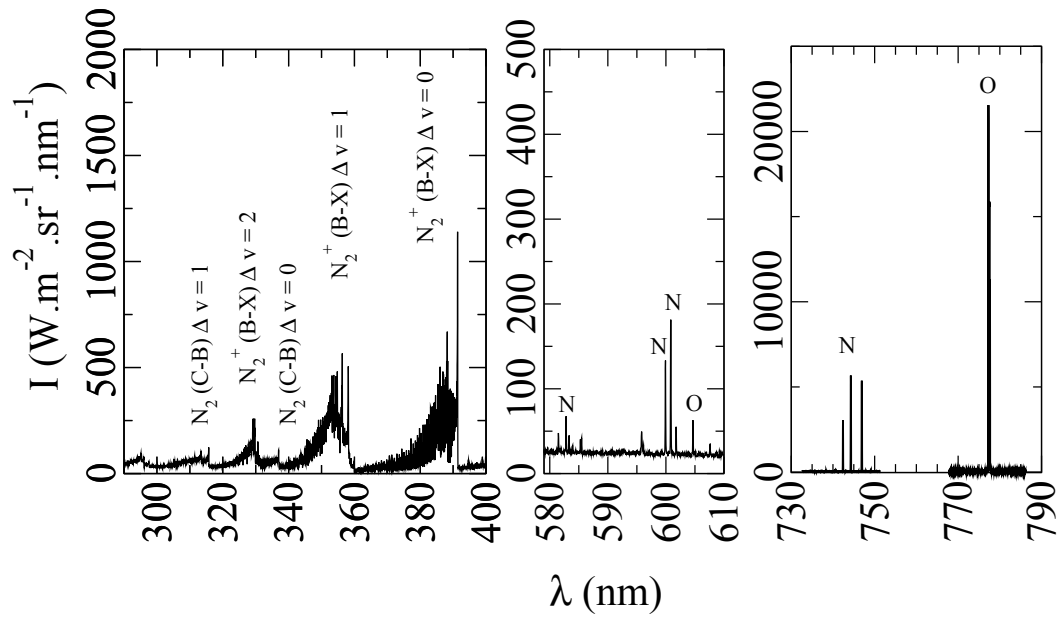


Figure 5.1.: Centerline calibrated spectra.

there is neither rotational nor vibrational departure from Boltzmann distribution. To improve spectra matching, the spectral resolution is degraded to fade possible spectral positions mismatch due to errors on spectral calibration or uncertainties on the position. Spectra fitting correlation coefficient R^2 is displayed in figure 5.3. The squared correlation coefficient R^2 jump from 0.82 (0.066 nm spectral resolution) to 0.97 (0.3 nm spectral resolution) at the jet center, indicating for an improvement of the matching between measured and calculated scaled spectra when decreasing the spectral resolution. On the edges of the jet (at 4 cm), the squared correlation coefficient is respectively 0.85 and 0.94 for raw (0.066 nm) and degraded (0.3 nm) spectral resolution fitting. In figure 5.3, we can observe that temperature profiles obtained for each spectral resolution are in close agreement with less than 2% difference over the whole radial extent. For clarity, we will only use in the following the temperature profile determined using 0.3 nm spectral resolution spectra. Best fits and associated contribution of the molecular systems are displayed in figures 5.4, 5.5 and 5.6 at different radial positions.

The fraction of CN contaminant is evaluated to be about 10^{-5} times smaller than N_2 species fraction. The reliability of molecular spectra fitting rely on the inclusion of the weak contribution of N_2 Second Positive system overlapping the N_2^+ First Negative system. This inclusion allows to assess the relative population associated to $C^3\Pi_u$ electronic state of N_2 Second Positive system and to $B^2\Sigma_u^+$ electronic state of N_2^+ First Negative system. Assuming a Boltzmann distribution of electronic states the relative population between $C^3\Pi_u$ and $B^2\Sigma_u^+$ electronic states can be written as a species concentration ratio N_2^+/N_2 using multi-species fitting procedure described in sub-section 4.2.1 of chapter 4. Measured temperature and species concentration ratio are displayed at the top of figure 5.7. Additionally, LTE concentration are calculated with CEA equilibrium code [66]. N_2 , N_2^+ and electron LTE concentration are plotted at the bottom of figure 5.7. Measured species concentration ratio N_2^+/N_2 is below the computed equilibrium value. It evidences the possibility of unbalanced recombination / ionization processes.

5.1.2. Non-LTE molecular emission.

Taking benefit from the absolute calibration, the molecular emission is examined. The non-LTE situation is identified through a straight comparison between measured and computed spectra. For this purpose, we use a temperature equal to the molecular temperature defined by $T_{rot} = T_{vib}$ previously determined. Figure 5.8 illustrates the non LTE situation which is characterized by a non-equilibrium scaling factor denoted as $\chi = \epsilon^{measured} / \epsilon^{LTE}$. The scaling factor is obtained by direct scaling of the vibrational bandhead (0-0) within $\Delta v=0$ band of the first Negative system of N_2^+ . Figure 5.9 shows the radial evolution of the non-equilibrium factor χ . The non-equilibrium is nearly constant in the central part of the jet with a value of about 4.5. It slightly decreases to reach unity on the edge indicating for equilibrium. Molecular spectra radiative transfer calculation permits to evaluate the effect of the local non-equilibrium emission on the spectral radiance. Figure 5.10 displays the comparison between line of sight recorded spectra and the rebuilt spectral radiance obtained by solving the radiative transfer equation. The very good agreement between optically thin and optically thick radiative transfer calculation confirms that the jet can be considered as optically thin within [300-400] nm spectral window. At the top of figure 5.10, the temperature profile used to compute equilibrium radiative transfer calculation is recalled. Obtained non-equilibrium factor of 3.7 is close to the non-equilibrium factor previously determined locally at the center of the jet with a value of 4.5. This in accordance with the statement that the line of sight emission is strongly dominated by the emission issued from the central core of the jet.

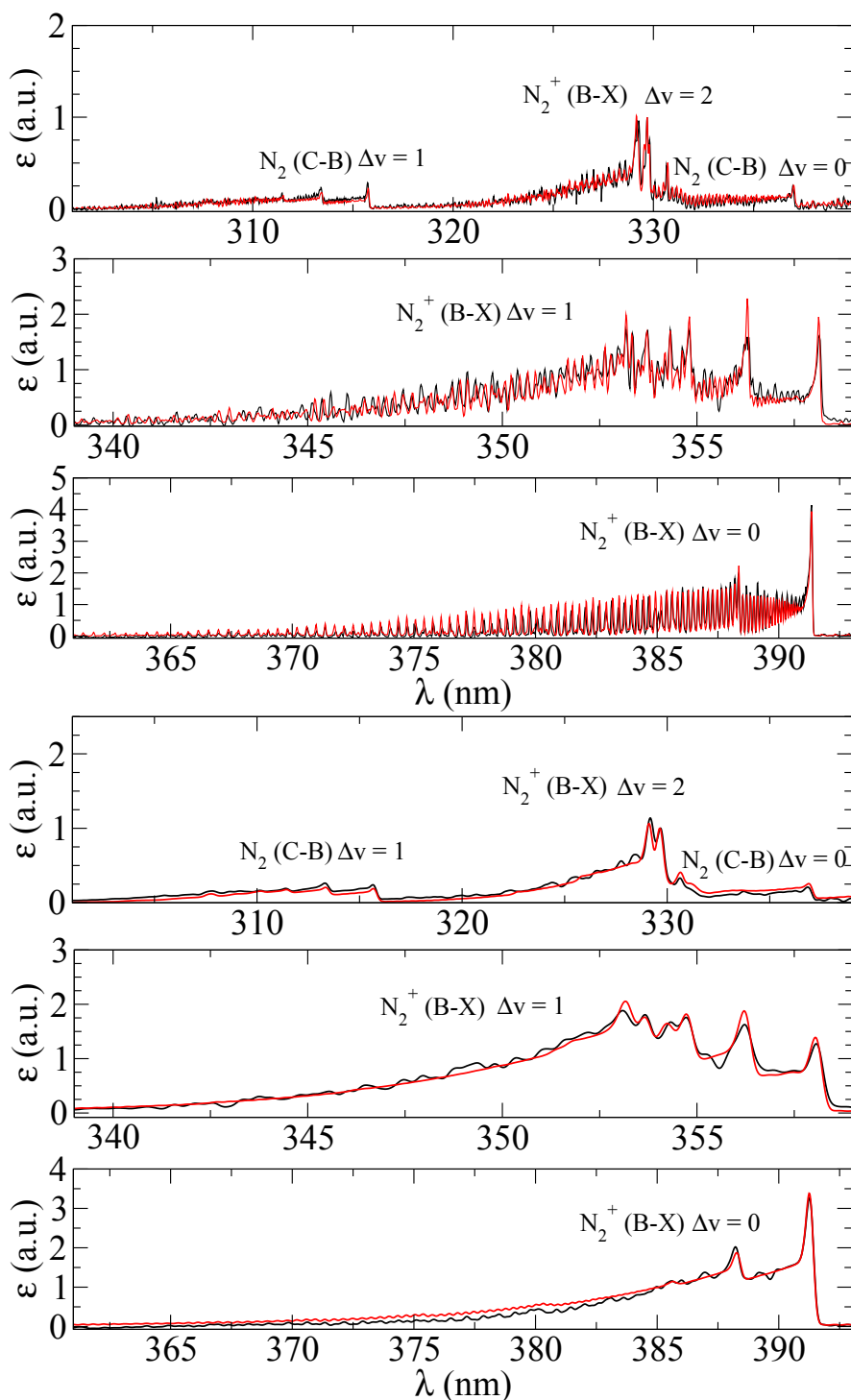


Figure 5.2.: Best fits executed at 0.066 nm (first three figures) and 0.3 nm (last three figures) spectral resolution. Experimental (black) and computed equilibrium (red) spectra on the jet centerline.

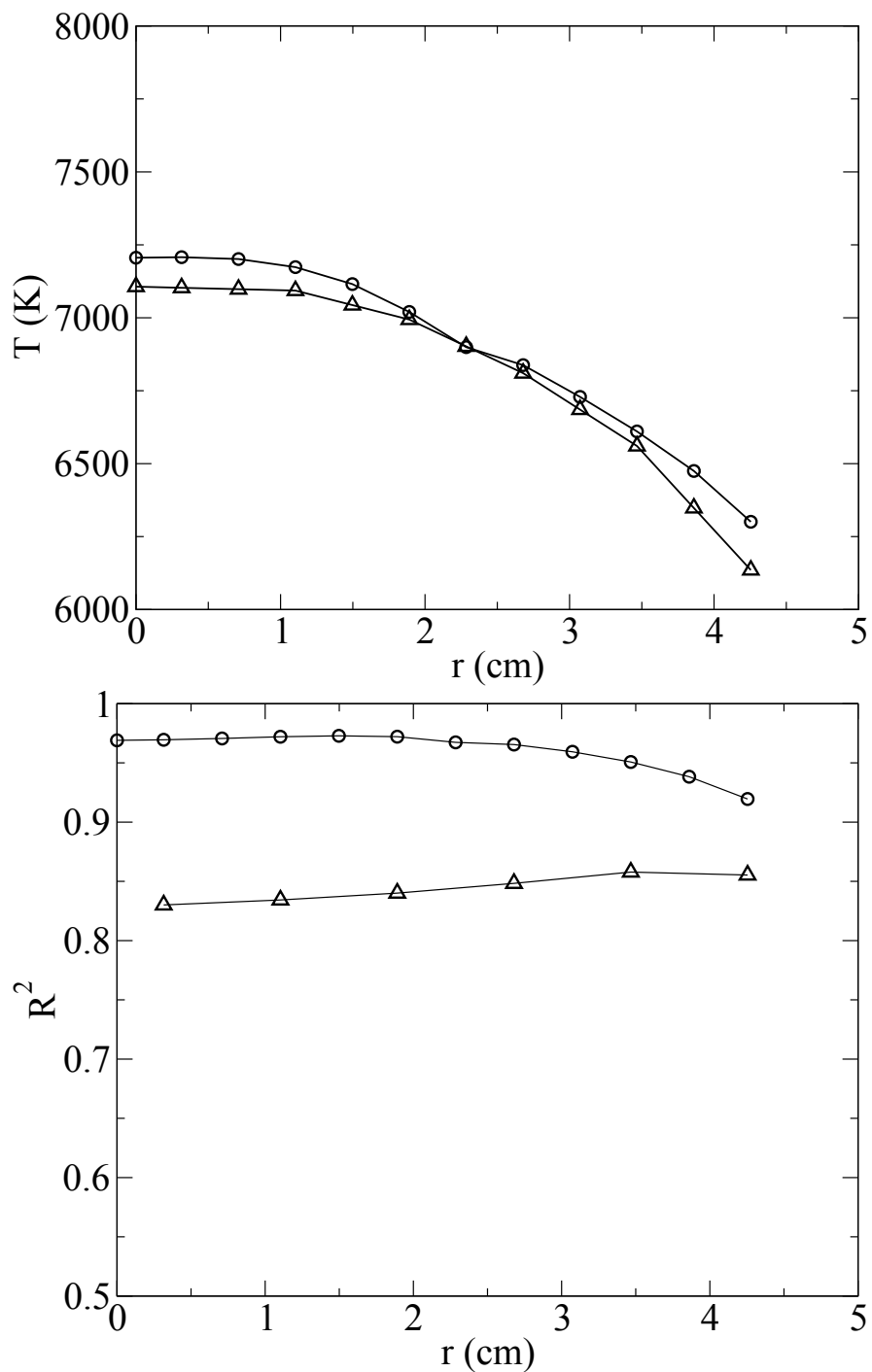


Figure 5.3.: Top: Radial temperature profiles associated to 0.066 nm (triangle) and 0.3 nm (circle) spectral resolution fitting. Bottom: Squared correlation coefficient associated to 0.066 nm (triangle) and 0.3 nm (circle) spectral resolution fitting.

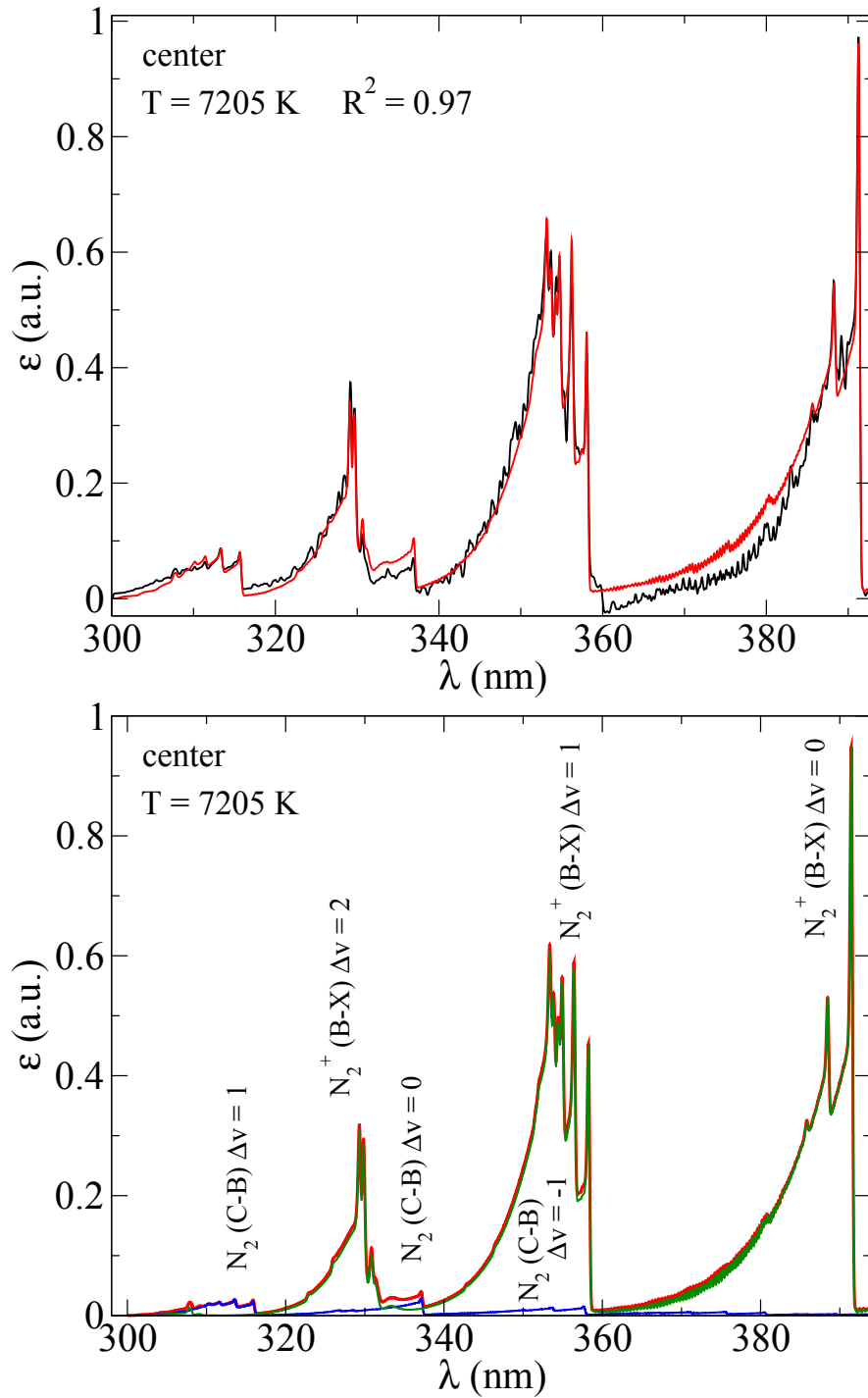


Figure 5.4.: Top: Best fit accounting for N_2^+ , N_2 and CN molecular systems. Bottom: Synthetic representation of the relative contribution of each system.

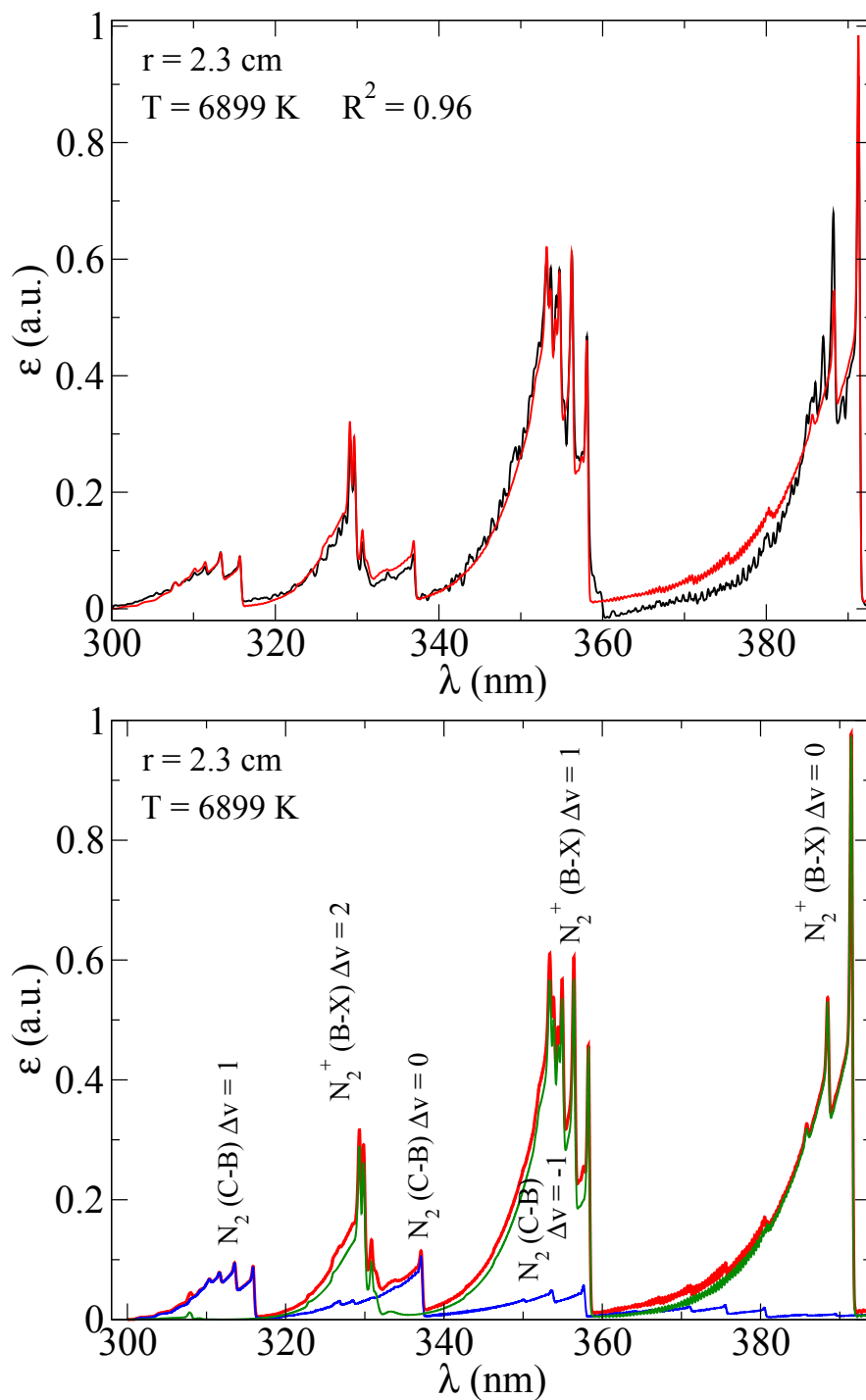


Figure 5.5.: Top: Best fit accounting for N_2^+ , N_2 and CN molecular systems. Bottom: Synthetic representation of the relative contribution of each system.

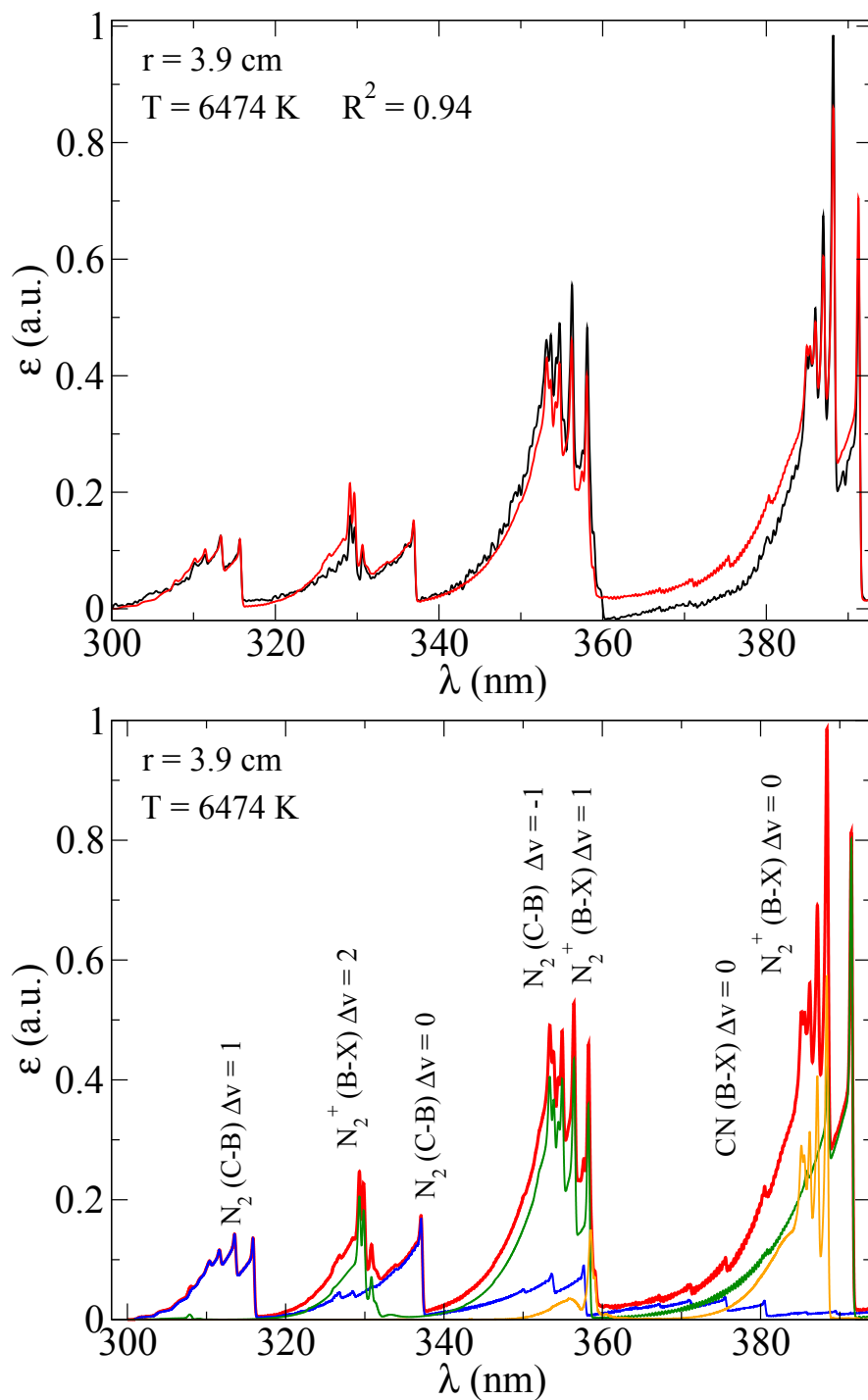


Figure 5.6.: Top: Best fit accounting for N_2^+ , N_2 and CN molecular systems. Bottom: Synthetic representation of the relative contribution of each system.

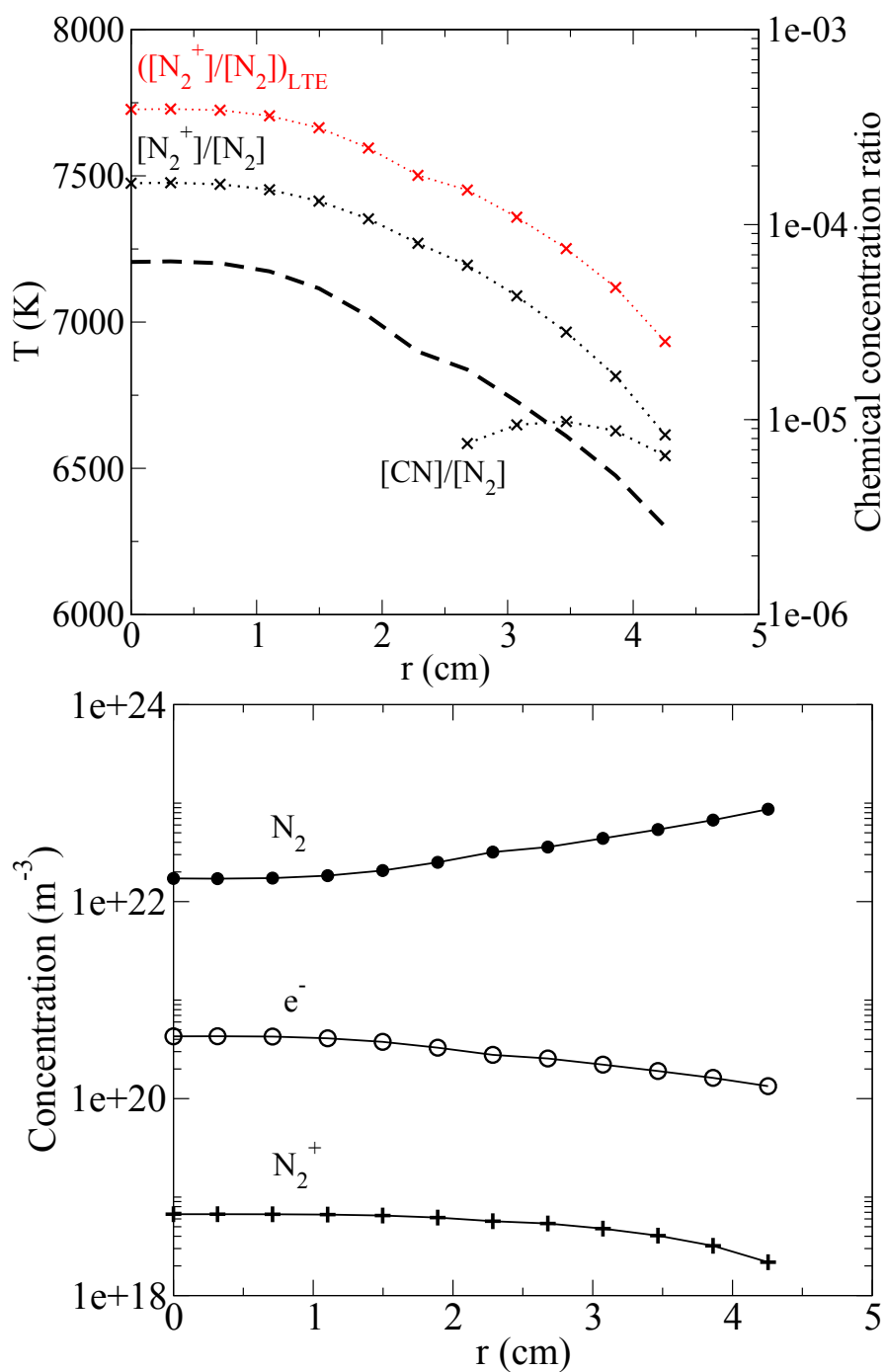


Figure 5.7.: Top: Temperature (dashed line) and species concentration ratio N_2^+/N_2 (cross) radial profiles. Bottom: Radial LTE concentration computed using CEA equilibrium tool [66].

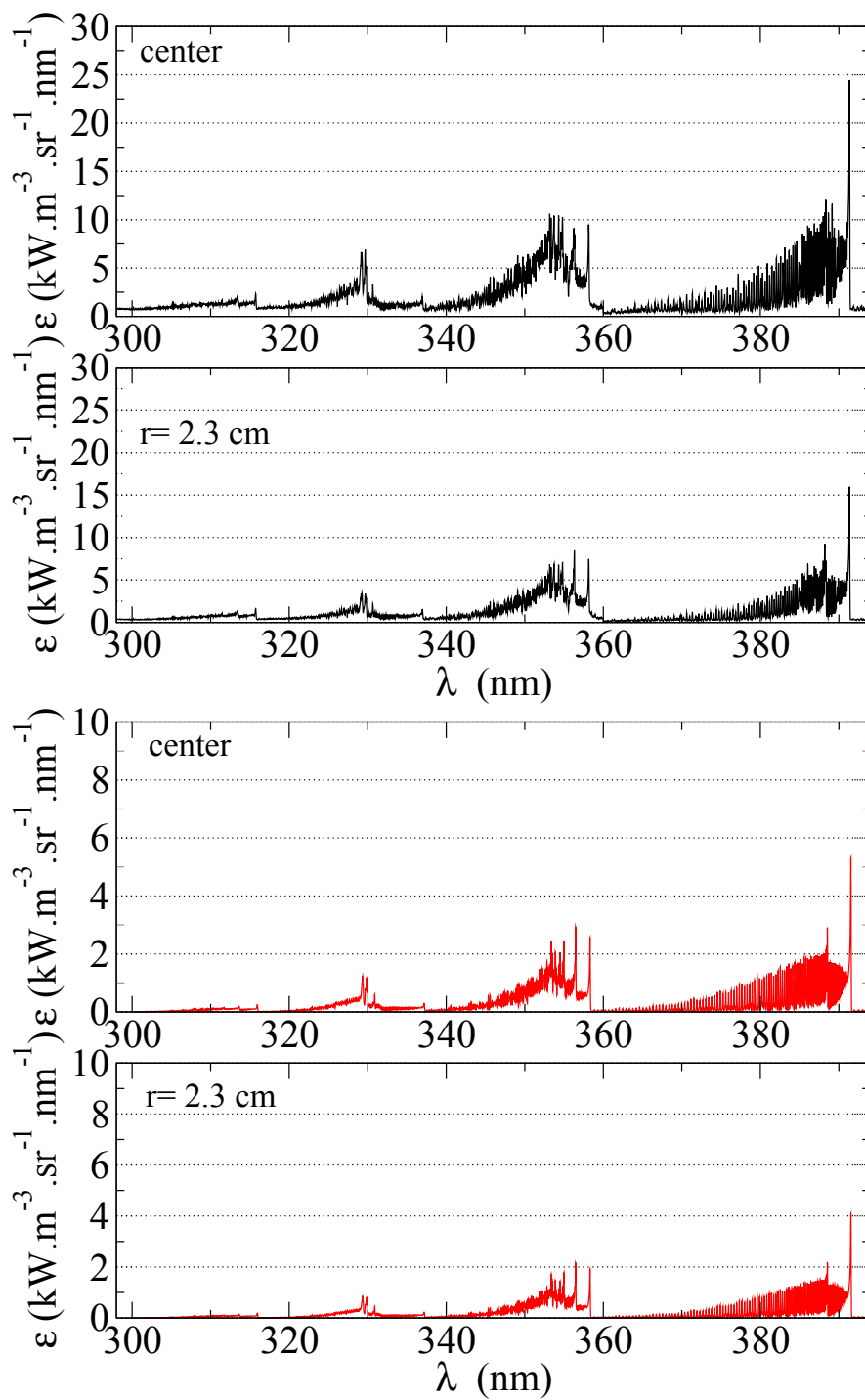


Figure 5.8.: Experimental spectra (top) and calculated LTE spectra (bottom).

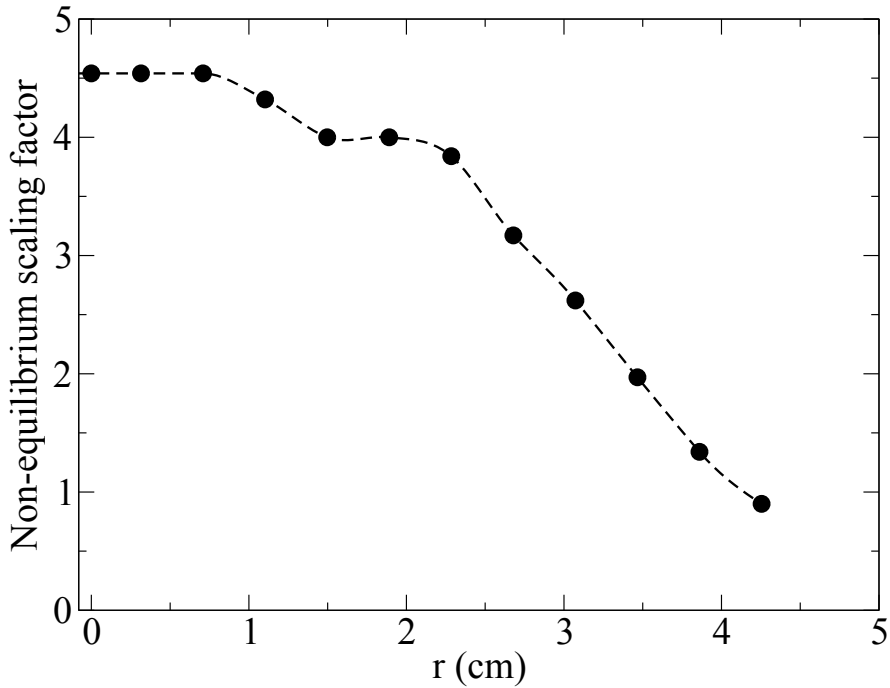


Figure 5.9.: Radial evolution of the non-equilibrium scaling factor

5.1.3. Atomic LTE radiation.

Taking advantage of nitrogen and oxygen atomic lines listed in table 5.2, we determine the electronic temperature T_{el} , associated to the electronic excited states. Selected lines offer strong and distinctive peaks allowing an accurate determination of line total emission over a large radial extent. Highly valuable atomic transitions from high excited states of nitrogen are observed and displayed in figure 5.11. NIST database [10] miss information on these lines. We rely therefore only on KURUCZ database [64] to characterize these transitions. The energy level corresponding to these lines being weakly populated, most of these atomic transitions rapidly fade along the radial extent. Among all lines referenced in KURUCZ, we select only one transition, at 582.954 nm, which gives reliable information on the total emission. We account for self absorption following the procedure described in subsection 4.1.1 of chapter 4. Measured emission and LTE emission are compared for nitrogen atomic line at 742 nm (resp. oxygen atomic lines at 777 nm) in figure 5.12 (resp 5.13) in order to determine the LTE temperature associated to each line. Admitting a severe error of $\pm 10\%$ on rebuilt emission, uncertainties on the equilibrium temperature are estimated by taking the logarithm and differentiating equation 4.1 in chapter 4. We obtain less than 2 % error on the rebuilt temperature. The oxygen triplet line at 777 nm suffers from significant self-absorption. Accounting for optically thick medium, the corrected emission radial profile differs significantly from the recorded raw emission profile with 50 % emission increase at the center of the jet. The correction for self-absorption is therefore impacting on the determination of LTE temperature which leads to a correction of about 4 % at the center of the jet. The overall LTE temperature profiles are displayed in figure 5.14. Apart from the oxygen triplet, the overall LTE temperature profiles are in close agreement. LTE temperature profiles good agreement allows us to state that thermal and chemical equilibrium is likely to prevail in the jet. However, as displayed in figure 4.1, N and O species concentrations are weakly affected by the temperature between 7000 and 12000 K. The statement concerning

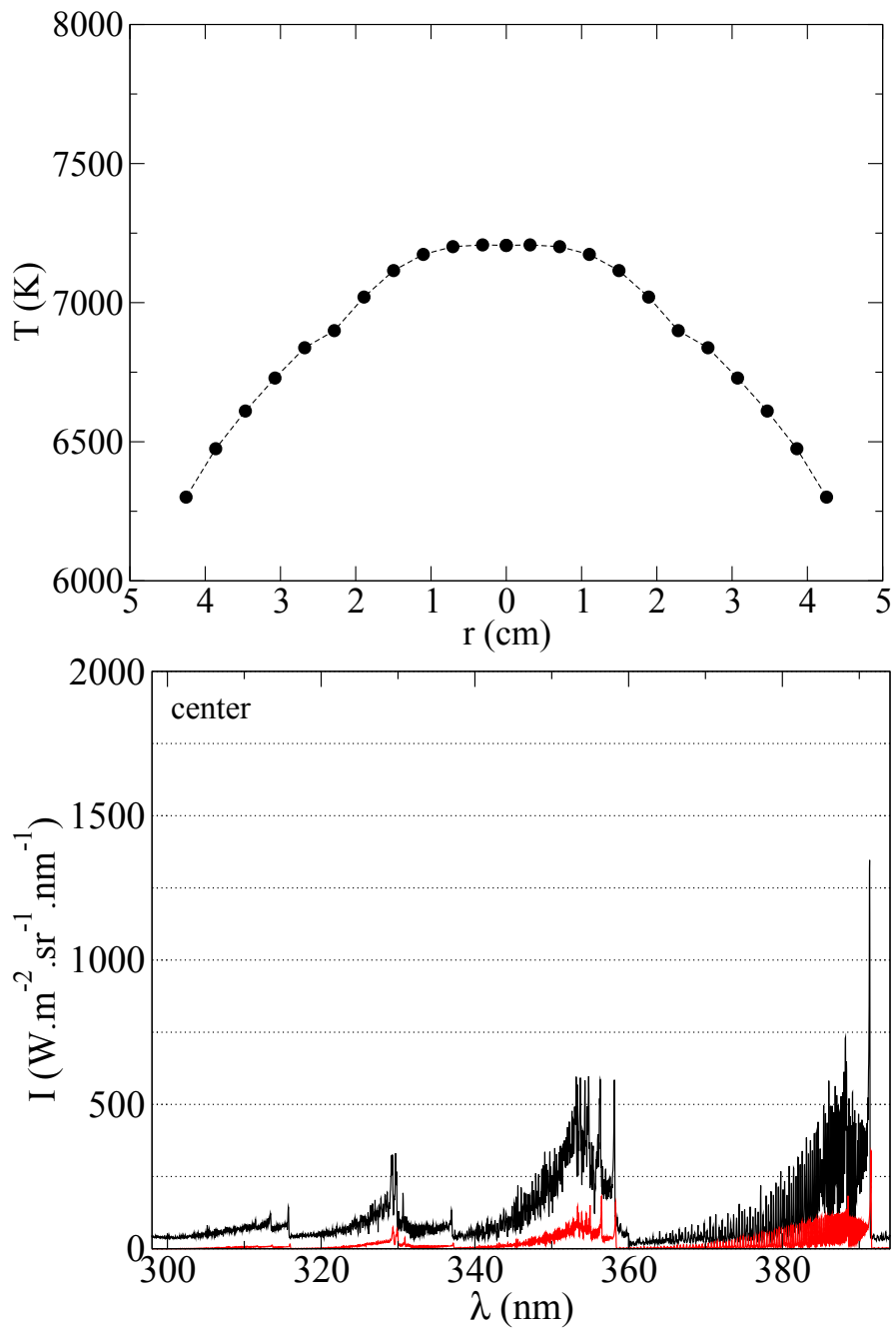


Figure 5.10.: Top: Temperature profile used for radiative transfer calculation. Bottom: Experimental (black) and synthetic equilibrium (red) line of sight spectra (non-equilibrium factor at the centerline $\chi = 3.7$).

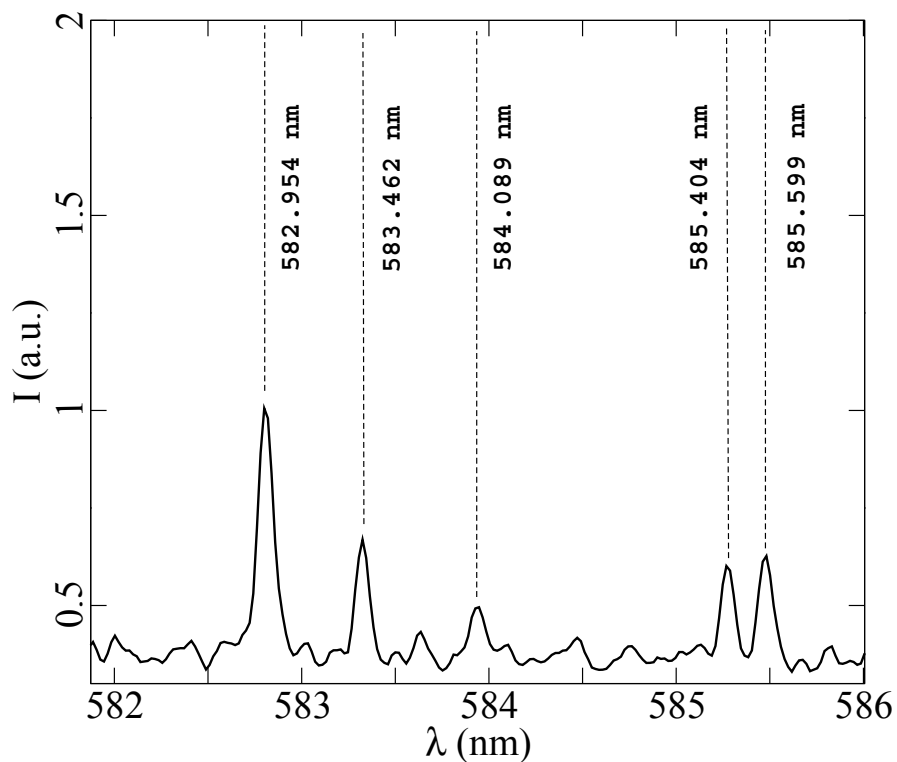


Figure 5.11.: Measured nitrogen atomic lines available from KURUCZ database [64]

$\lambda_{air}(nm)$	$A_{ul}(s^{-1})$	$E_l(cm^{-1})$	$E_u(cm^{-1})$	g_l	g_u
N lines		$D_e = 117225.7cm^{-1}$			
491.494	$8.08 \cdot 10^5$	86137.350	106477.800	2	2
493.512	$1.76 \cdot 10^6$	86220.510	106477.800	4	2
582.954 *	$6.375 \cdot 10^5$	95532.150	112681.389	6	6
599.943	$3.64 \cdot 10^6$	93581.550	110245.183	2	2
600.847	$3.58 \cdot 10^6$	93581.550	110220.107	2	4
742.364	$5.95 \cdot 10^6$	83284.070	96750.840	2	4
744.229	$1.19 \cdot 10^7$	83317.830	96750.840	4	4
O lines		$D_e = 109837.02cm^{-1}$			
604.623	$1.05 \cdot 10^6$	88630.587	105165.232	3	3
604.644	$1.75 \cdot 10^6$	88631.146	105165.232	5	3
604.649	$3.50 \cdot 10^5$	88631.303	105165.232	1	3
777.194	$3.69 \cdot 10^7$	73768.200	86631.454	5	7
777.417	$3.69 \cdot 10^7$	73768.200	86627.778	5	5
777.539	$3.69 \cdot 10^7$	73768.200	86625.757	5	3

Table 5.2.: Spectroscopic data of the considered O and N emission lines taken from [10] and [64] (indicated by a star).

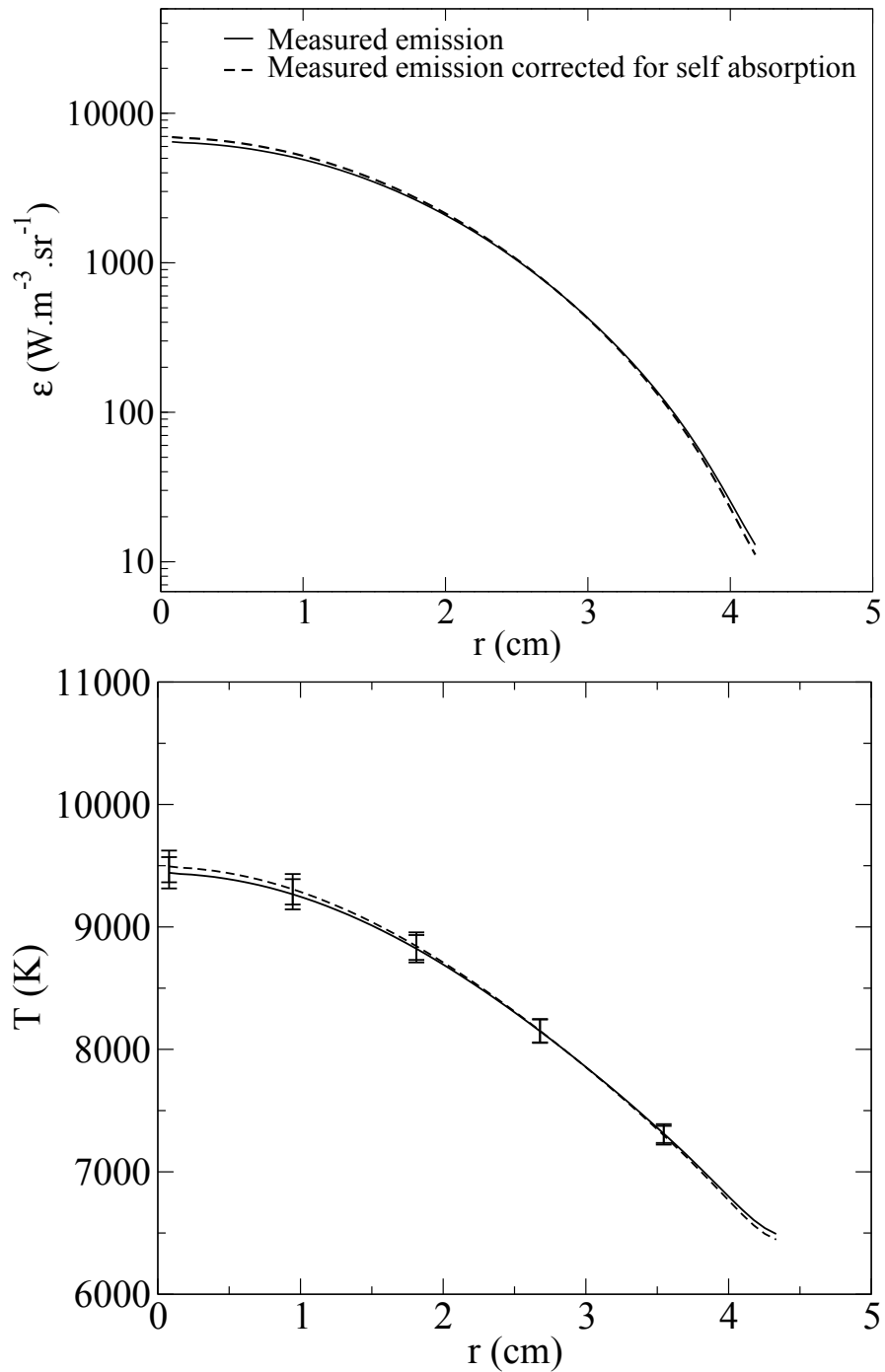


Figure 5.12.: Top: Measured (black) and theoretical (red) emission for nitrogen line at 742 nm. Bottom: LTE temperature profile (solid line) and temperature profile corrected for self absorption (dashed line).

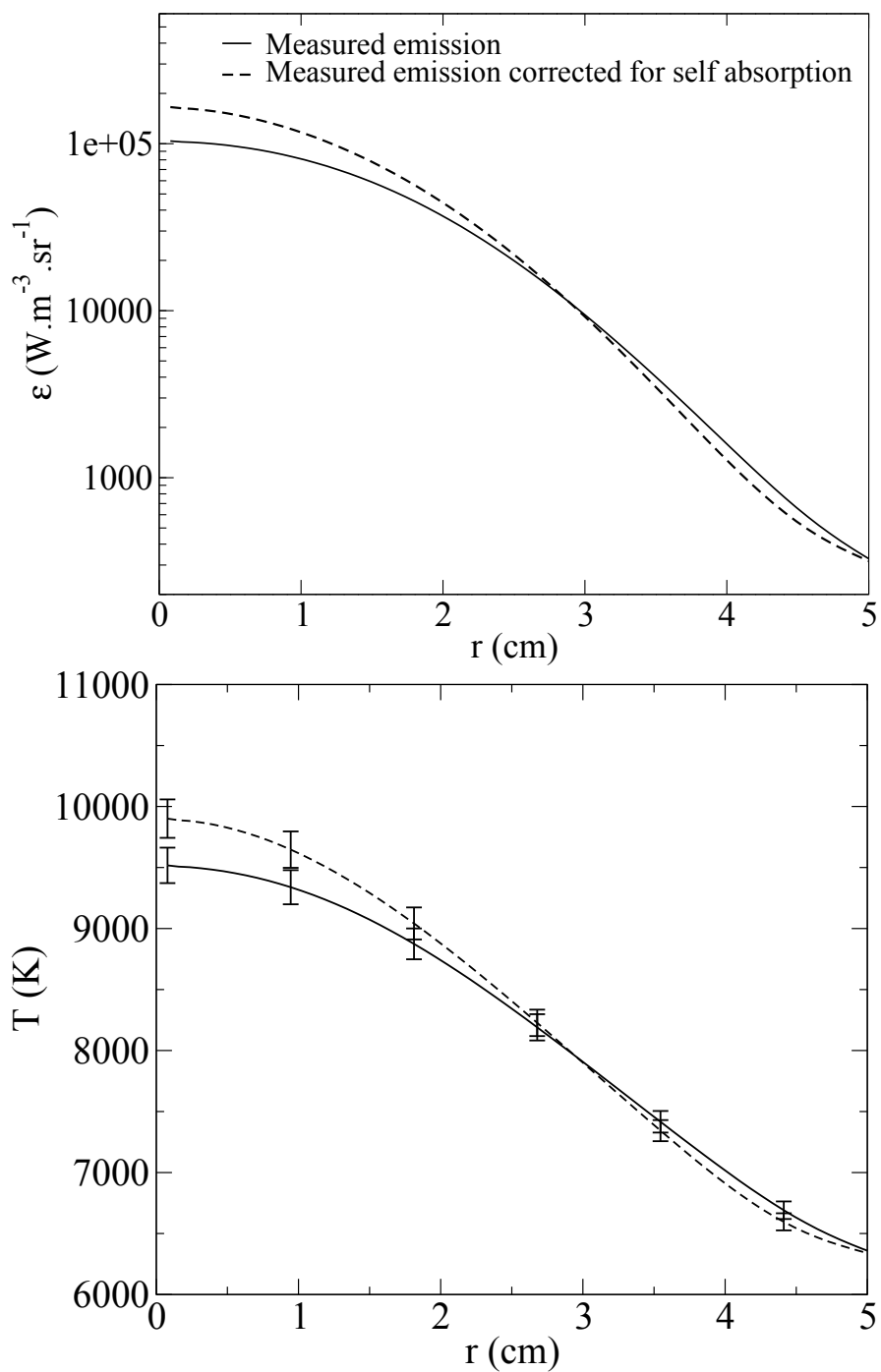


Figure 5.13.: Top: Measured (black) and theoretical (red) emission for oxygen triplet line at 777 nm. Bottom: LTE temperature profile (solid line) and temperature profile corrected for self absorption (dashed line).

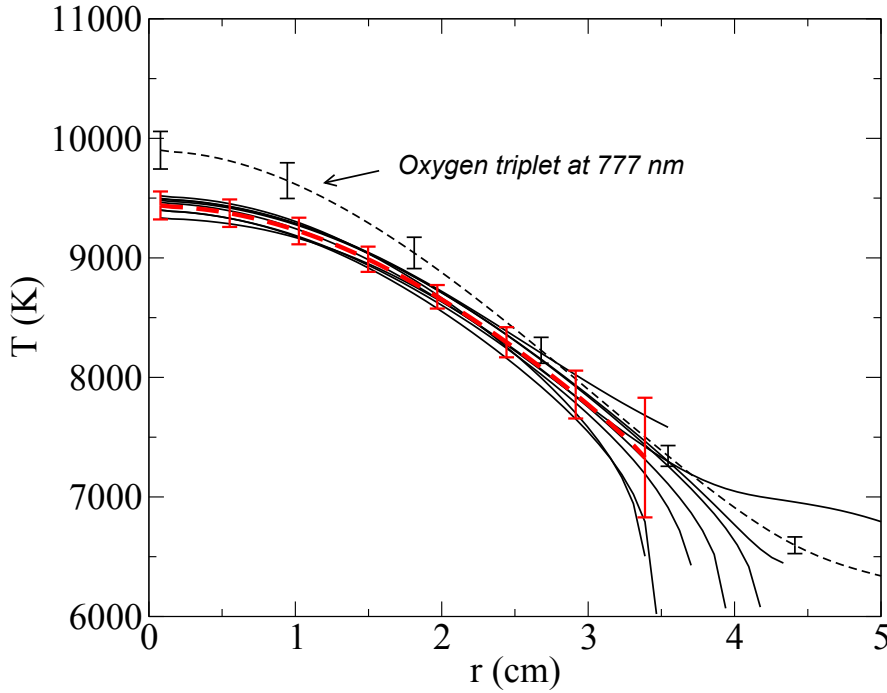


Figure 5.14.: LTE temperature profiles (black) and mean LTE temperature profile (red) excluding the oxygen line at 777 nm.

chemical equilibrium is therefore questionable. A mean atomic LTE temperature profile is used to rebuild the optically thick line of sight spectral radiance through the resolution of radiative transfer assuming LTE. Reconstructed atomic lines are illustrated in figure 5.15 and compared with line of sight calibrated measurements. Reconstructions are performed either using LTE temperature profiles or LTE temperature profiles corrected for self absorption. It comes that the inclusion of self absorption allows to better replicate the recorded spectral radiance. Reconstructed local spectral emission and measured line of sight spectral radiance are therefore found to be consistent and in agreement with LTE assumption. The temperature profile of oxygen triplet deviate slightly from the other profiles. In the lowest part of the atomic energy scheme, the population associated to oxygen triplet therefore deviate from the rest of the energy distribution scheme. The lack of measured oxygen lines prevents from using Boltzmann diagram method to define an electronic temperature from the oxygen excited states distribution. In the following, we will define an electronic temperature associated to the atomic energy distribution of nitrogen lines which proximity to thermal equilibrium is expected.

Atomic excited states distribution of nitrogen lines will permit to define an electronic temperature without any assumptions concerning the chemical state. The number of lines accounted is ruled by an intensity threshold that excludes weak lines drown in a noisy background. Boltzmann plots are displayed in figure 5.16. The small dispersion of experimental points compared to the linear regression ensures an uncertainty of less than 10 % on the temperature, assuming an error of $\pm 10\%$ on the weighted population value. In figure 5.16, Boltzmann diagram accounting for the optical thickness of the jet is presented. Experimental points are associated with distribution calculated under LTE assumption at 273 mbar. The good agreement between measured and LTE weighted population confirms the thermal and chemical equilibrium state mentioned earlier.

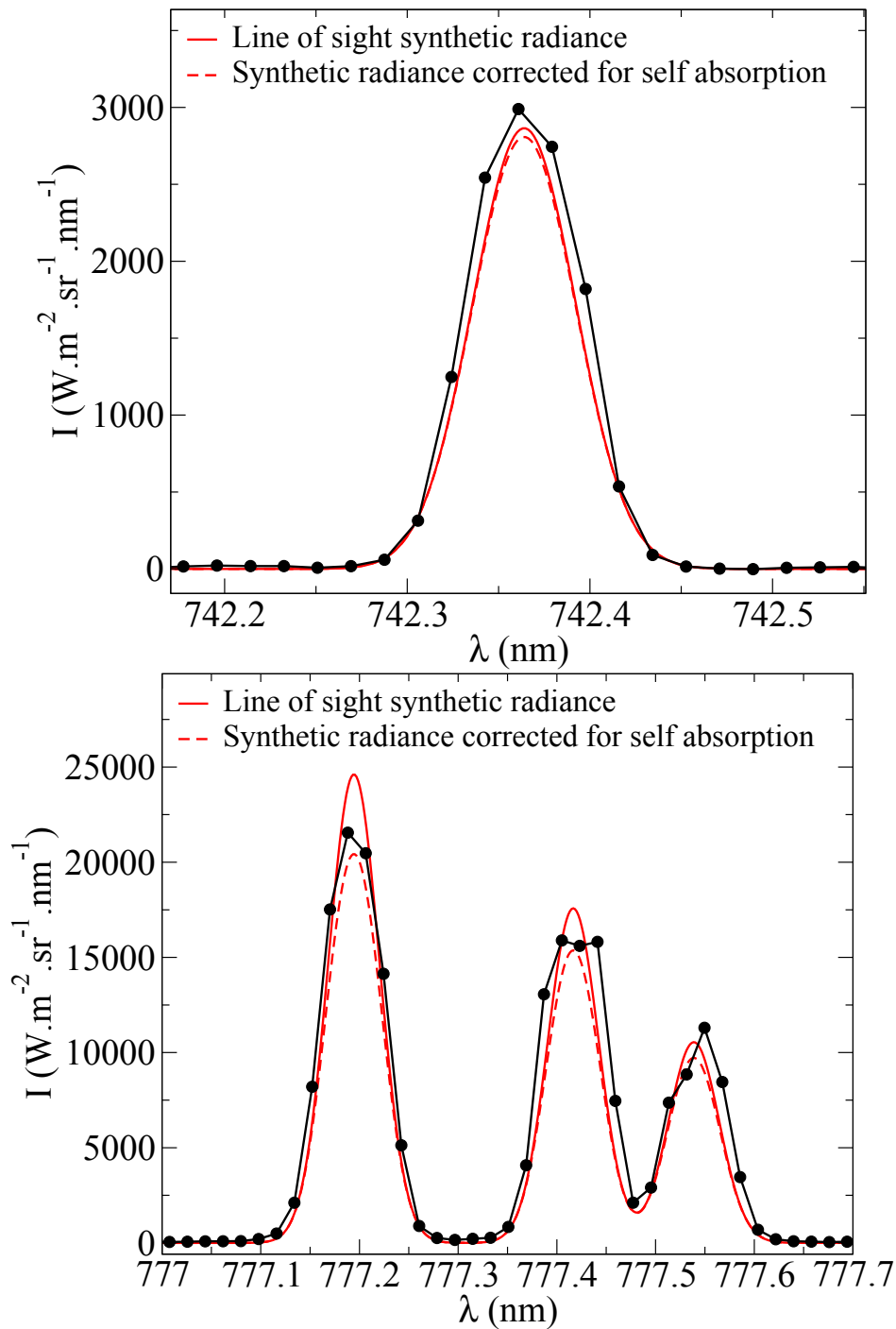


Figure 5.15.: Line of sight reconstructed spectral radiance using optically thin (red line) or optically thick (dashed red line) LTE temperature profile and line of sight measurements of atomic lines (black circles).

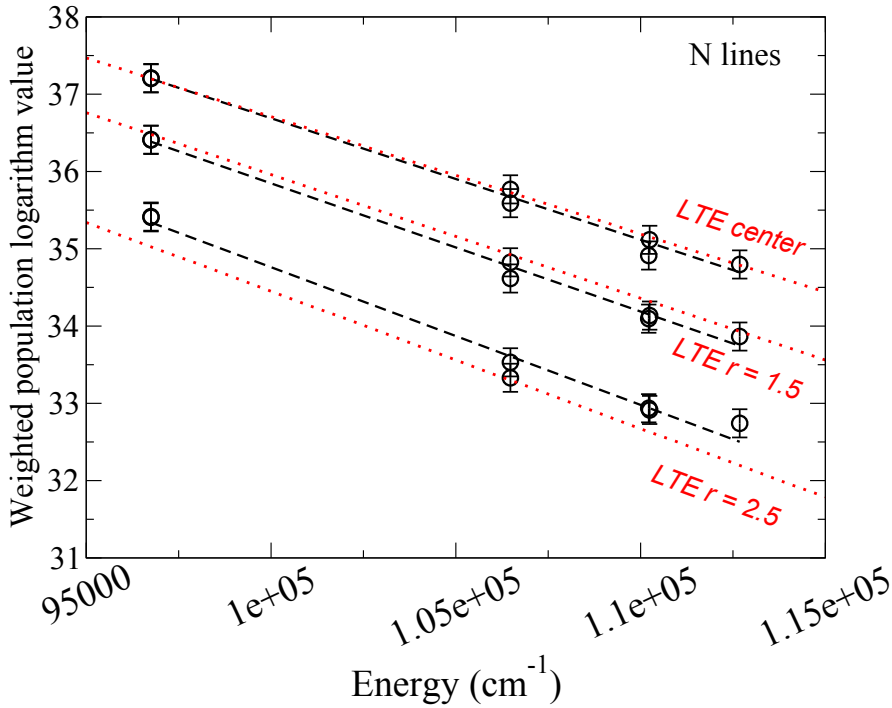


Figure 5.16.: Boltzmann diagrams at various radial positions (black) and associated LTE distributions (red).

5.1.4. Unbalanced recombining / ionizing processes.

The energy distribution is described by several temperatures such as the electronic temperature $T_{el.}$, the vibrational $T_{vib.}$ and the rotational temperature $T_{rot.}$. Confrontation between LTE temperature, electronic temperature and equilibrium temperature of rotational and vibrational modes is displayed in figure 5.17. A good agreement is observed between LTE and electronic temperature profiles, whereas the temperature profile related to the rotational and vibrational energy modes is found to be much lower. Kinetic models would help to identify the main energy exchange processes responsible for this non-equilibrium situation. Atomic excited states agree with LTE situation, whereas emission of molecular excited states is higher than expected in LTE situation. The equilibrium electron density will be estimated and compared with experiments to evaluate the ionization/recombination equilibrium.

H_{β} line at the jet centerline is displayed in figure 5.18 with its associated best fit. The Doppler contribution is calculated assuming that $T_{rot} = T_{vib} = T_{gas}$ and the electron density is determined from the analytical formula 4.14 at the jet centerline. It gives an electron density of about $1.5 \times 10^{21} \text{ m}^{-3}$ which is in good agreement with line shape fitting solution which density profile is displayed in figure 5.19. According to Wilson's criterion [12] (more stringent than Griem's criterion, it should be used when low excited states exist), the required electron density for complete LTE is about $3.0 \times 10^{17} \text{ cm}^{-3}$, taking $\Delta^0 E = 15.6 \text{ eV}$ which is the ionization potential for the N_2 molecule. This value is well above the measured electron density, therefore, based on this criterion, departure from complete LTE state can be expected. Electron density profile determined from line shape fitting (*CS* model) is displayed in figure 5.19. We assume $T_{el.} = T_e$. Giving an arbitrary large uncertainty (+/- 50 %) on the gas temperature, the error induced on electron density is only +/- 1 % at the center and increases towards the edge to reach +/- 15 % at 3.5 cm. Computed equilibrium densities calculated using CEA

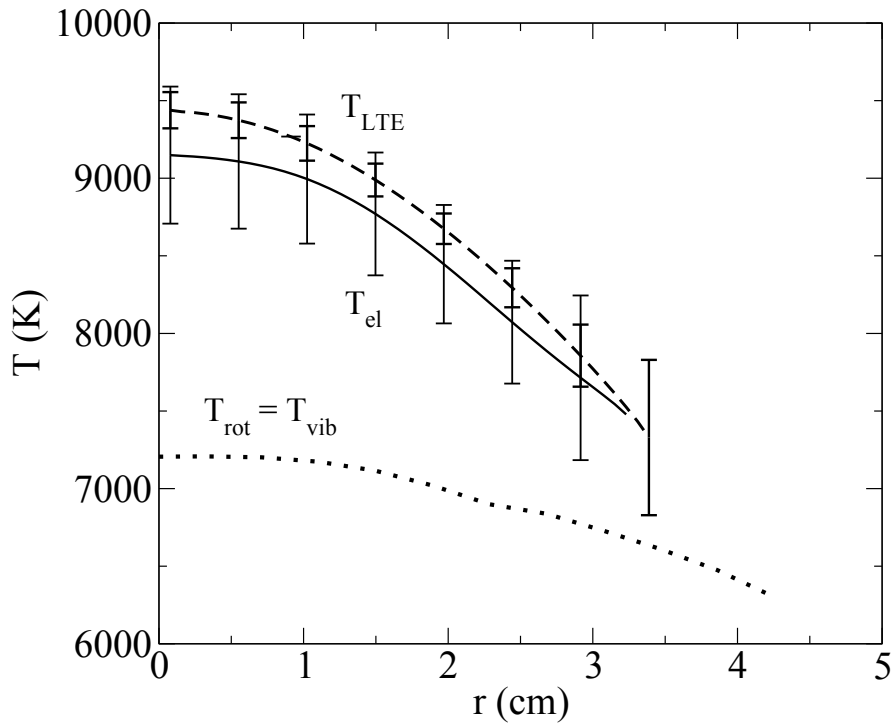


Figure 5.17.: Mean LTE (dashed line), electronic (solid line), molecular rotational and vibrational (dotted line) temperature profiles.

equilibrium tool [66] are displayed on the same figure using various temperature profiles. Two approaches consider either the rotational temperature T_{rot} or the electronic temperature T_{el} as input. In a third approach, electron density is calculated at equilibrium using an average temperature $T_{av} = \sqrt{T_{rot} T_{el}}$, similarly to the geometric average temperature proposed by Park [82]. This third approach fit better with measured densities whereas using the rotational (resp. electronic) temperature leads to underestimated (resp. overestimated) electron density. Park's average temperature reproduce well the equilibrium electron density of the plasma. The difference between rotational and electronic temperature affects the equilibrium concentrations of the plasma. Assuming that mostly the translational temperature (close to the rotational temperature) rules the species concentration, measured electron density is found to be higher than the LTE value, which states the recombining / ionizing non-equilibrium processes.

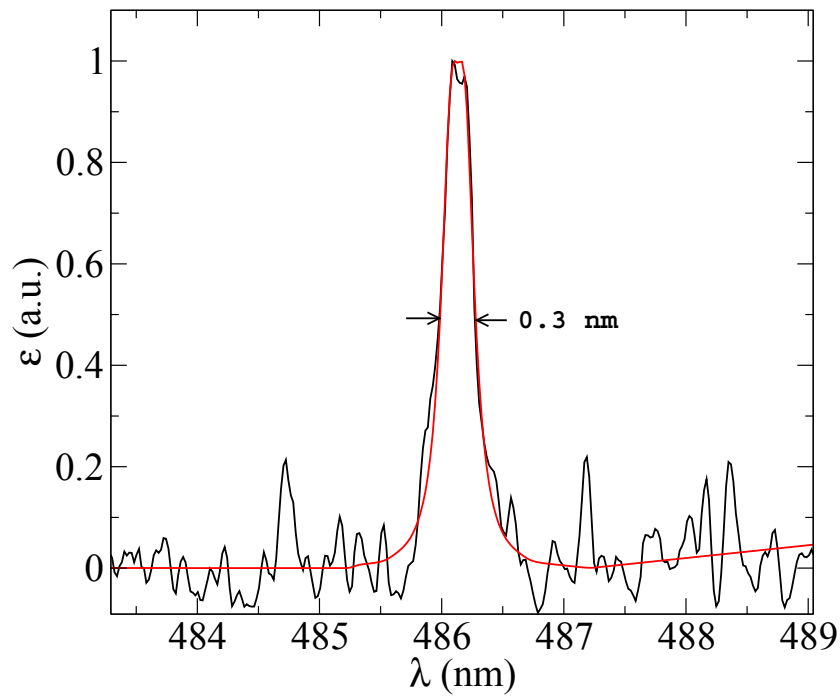


Figure 5.18.: H_β line measured at the center of the jet (black) and best fit (red).

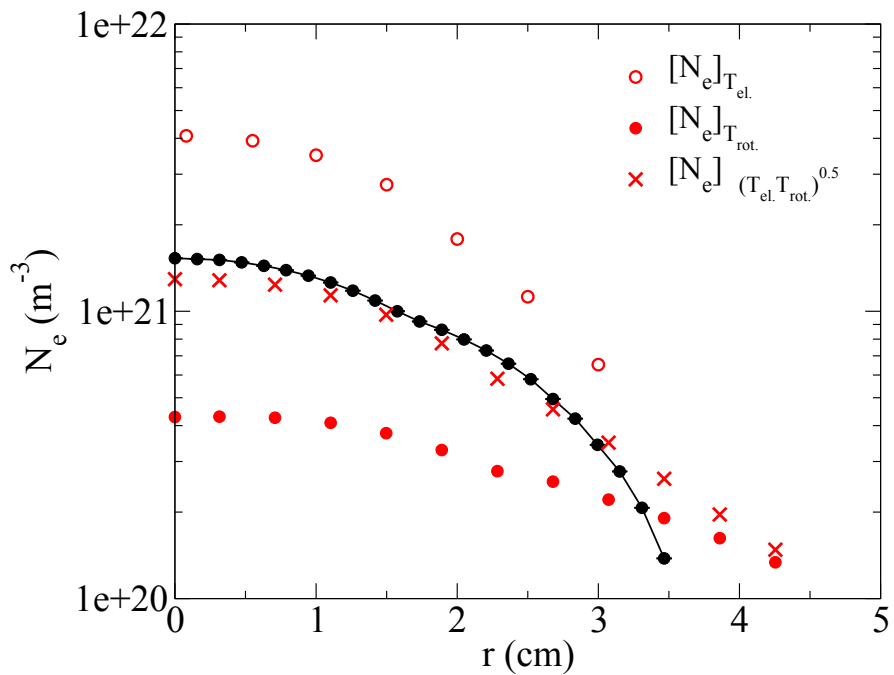


Figure 5.19.: Measured electronic density profile (black) and density computed at equilibrium (red).

5.2. Microwave sustained nitrogen discharge in the ignition region

Nitrogen microwave induced plasma discharge operating at various pressures ranging from 10 mbar to 1 bar is characterized. The setup is illustrated in figure 5.20 and operating settings are detailed in table 5.3. Spectroscopic measurements are executed in the ignition region of a steady state discharge. Measurements are integrated along the line of sight in the microwave cavity. Records of N_2^+ and N_2 bound molecular systems lying in the UV and visible spectral ranges are analyzed. Relative calibration is performed in this spectral range. A preliminary investigation of light oscillation dynamics ensures the absence of incoherent dynamics in the low frequency range which could be detrimental to the reliability of time integrated measurements. Only coherent peaks at 50, 150 and 300 Hz are observed for both light and microwave power oscillations. The performance of the vacuum system is not entirely satisfactory as the presence of CN violet system emission is detected for operating pressure above 150 mbar. An evaluation of the CN contaminant concentration is performed through molecular fitting procedure (figure 5.21). CN contaminant mole fraction is evaluate to be, at most, of the order of 1.0×10^{-7} . Regarding the small amount of contaminant, it is considered that CN species has a negligible impact on the thermodynamic state of the nitrogen discharge. For better accuracy, the spectral band ranging from 380 to 400 nm is excluded from the molecular fitting procedure in order not to account for the strong peak of CN violet system $\Delta v=0$.

Two-temperature approach is adopted to estimate the rotational and vibrational temperatures associated to $C^3\Pi_u$ and $B^3\Pi_g$ electronic states of N_2 and $B^2\Sigma_u^+$ state of N_2^+ . Typical best fits are presented in figure 5.22 for two pressure cases, showing good agreement between measured and computed spectra (correlation coefficient > 0.9). At the bottom of figure 5.22, synthetic spectra point out the relative contribution of the molecular systems for each pressure case within [290-430] nm spectral window.

5.2.1. Assessment of radiative transfer along the line of sight.

The line of sight plasma jet emission is collected in the ignition region through a 1 mm diameter aperture (acting as a collimator) coupled to an optical fiber through SMA connector. The relative contribution of N_2^+ and N_2 bound molecular systems depends on the operating conditions. First and second positive systems of N_2 contribute mostly at low pressure whereas the first negative system of N_2^+ contribution increases as the pressure is increased. The optical access inside the waveguide termination, where the ignition starts, allows to get strong signal regardless of the operating conditions. Local spectral emission rebuilding through Abel inversion is not possible because of the unique line of sight. The influence of thermal and chemical gradients along the line of sight is therefore estimated through straight comparison between synthetic line of sight integrated spectra and synthetic local emission spectra. The effect of light integration over non homogeneous and non isothermal plasma column is estimated by using synthetic temperature profiles and their associated LTE species concentration. Radiative transfer of nitrogen plasma column is investigated using synthetic temperature profiles displayed in figure 5.23 combined with the associated equilibrium concentration of N_2 and N_2^+ species. The investigation is performed over [275 - 475] nm spectral range. 1D finite difference method is used to solve the radiative transfer equation. An appropriate spatial step in the radial direction of the jet is used for the calculation. Boundary conditions are set so that the temperature at the quartz boundary is 1300 K (melting point 1400 K). On figure 5.23, scaled local emission spectrum and line of sight scaled spectral radiance spectrum are compared for the *profile 1* condition that corresponds to an extreme case with the highest gradients. Slight discrepancies between line of sight integrated and local spectra arise between 300 and 375 nm spectral positions. The estimation of the temperature through equilibrium spectra fitting method (described in subsection

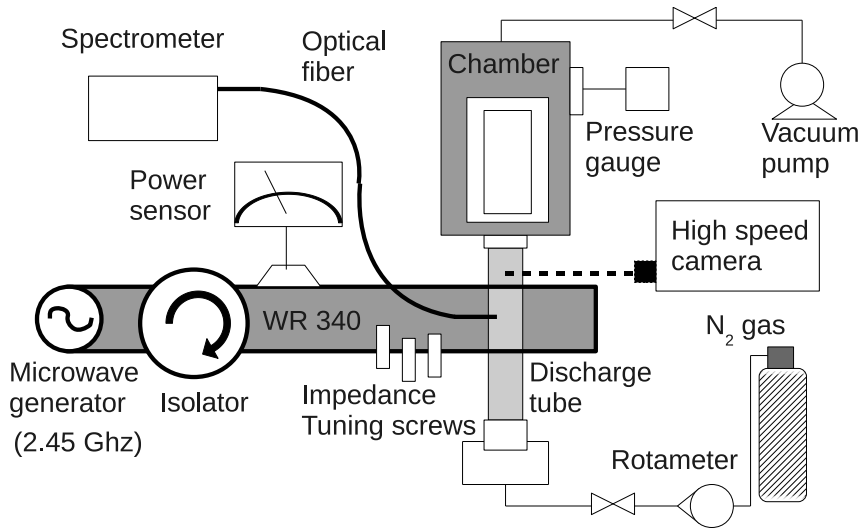


Figure 5.20.: Schematic of the setup.

Operating conditions	0.15 g.s ⁻¹ mass flow rate [10 - 10 ³] mbar operating pressure range [0.3 - 1.2] kW absorbed microwave power range
Spectroscopic features	Ocean Optics HR 4000 / optical fiber UV-Vis, 1.7 nm spectral resolution
Radiative transitions of interest	Line of sight measurements in the ignition region $N_2 (B^3\Pi_g \rightarrow A^3\Sigma_u^+)$ 1st Positive System $N_2 (C^3\Pi_u \rightarrow B^3\Pi_g)$ 2nd Positive System $N_2^+ (B^2\Sigma_u^+ \rightarrow X^2\Sigma_g^+)$ 1st Negative System

Table 5.3.: Experimental operating conditions of subsonic microwave nitrogen discharge.

4.2.1) gives an error of about 1% between these two cases at the jet centerline (figure 5.23). This error is decreasing on the edge as the length of line sight integration is reduced. Regarding the slight mismatch between local and integrated spectra, we assume that the line of sight integrated measurements can be reasonably used to evaluate the temperature at the center. This is notably permitted because cold layer on the outer of the discharge hardly contribute to the whole signal spatially integrated.

5.2.2. Effect of microwave power on rotational and vibrational energy modes.

The effect of microwave power on the excitation of equilibrium discharges has been extensively discussed ([62], [83]). Several authors have reported that additional microwave power contributes to expand the plasma volume rather than heating the plasma to a higher temperature. At atmospheric pressure we mentioned that gas temperature is slightly affected by power variation. Indeed, 50% power increase results in less than 5% temperature elevation.

Thermal non-equilibrium is investigated as a function of absorbed microwave power for two operating pressures at 10 and 100 mbar. Results are displayed in figures 5.25. At low pressure, rotational and vibrational temperatures are not affected by power variation. Rotational

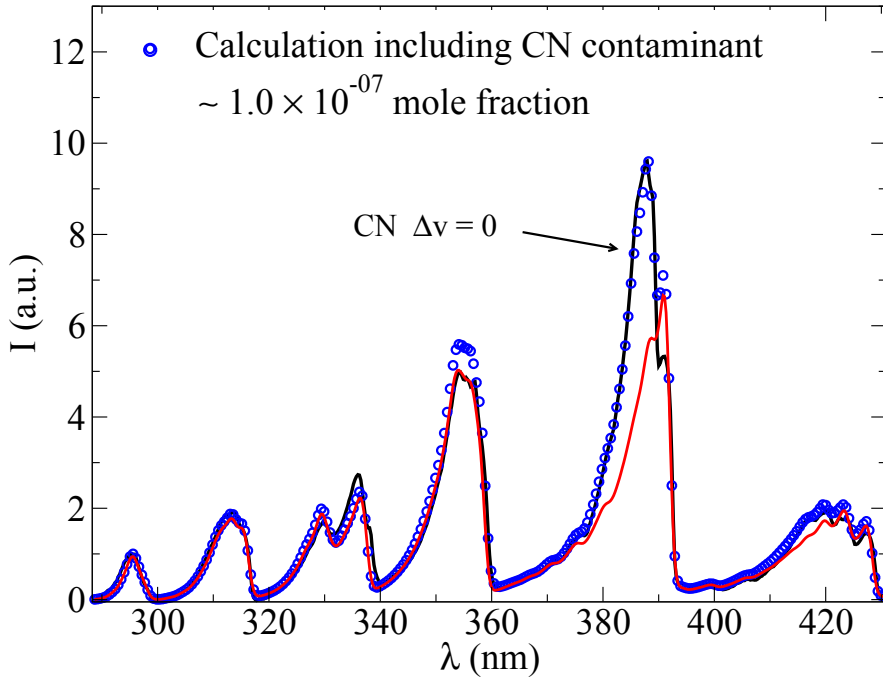


Figure 5.21.: Experimental spectra (black) and associated best fits without CN contaminant (red) and with CN contaminant (blue circles).

temperatures of the electronic excited states $C^3\Pi_u$ and $B^3\Pi_g$ are fairly similar, indicating for identical population and depopulation processes. Small rotational constants (1.63772 for $B^3\Pi_g$ and 1.82680 for $C^3\Pi_u$ [84]) suggest that rotational excited levels exchange kinetic energy with translational motion of molecules. Therefore the energy distribution of rotational mode tends to equilibrate with translation motion of heavy particles. Vibrational temperatures associated to $C^3\Pi_u$ and $B^3\Pi_g$ states of N_2 are higher than the corresponding rotational temperatures. Oppositely to rotational kinetics, vibrational kinetics would then be mostly affected by electron impact excitation. Vibrational temperature of $B^3\Pi_g$ is much higher than $C^3\Pi_u$ electronic level indicating for different kinetic mechanisms. At higher pressure (100 mbar), the thermodynamic state of the discharge is not significantly affected by the microwave power although vibrational and rotational temperatures of $C^3\Pi_u$ tend to equilibrate.

5.2.3. Effect of operating pressure on rotational and vibrational energy modes.

In the following, the power density is maintained at approximately $6 \text{ MW}\cdot\text{m}^{-3}$. Relaxation mechanism through collision processes is greatly influenced by the pressure. Assuming on one hand a Boltzmann distribution for rotation (T_{rot}) and on the other hand a Boltzmann distribution for vibrational energy levels ruled by a single temperature (T_{vib}), the determination of the couple of temperatures (T_{rot} , T_{vib}) is performed for large pressure range. Figure 5.25 displays the excitation temperatures of rotational and vibrational modes as a function of the operating pressure. At the bottom of figure 5.25, average temperatures \bar{T} defined by $\bar{T} = \left(T_{B^3\Pi_g}^2 \times T_{C^3\Pi_u}^2\right)^{0.5}$ are plotted. For nitrogen molecule neutral species, below 100 mbar, vibrational temperatures decrease with increasing the discharge operating pressure whereas ro-

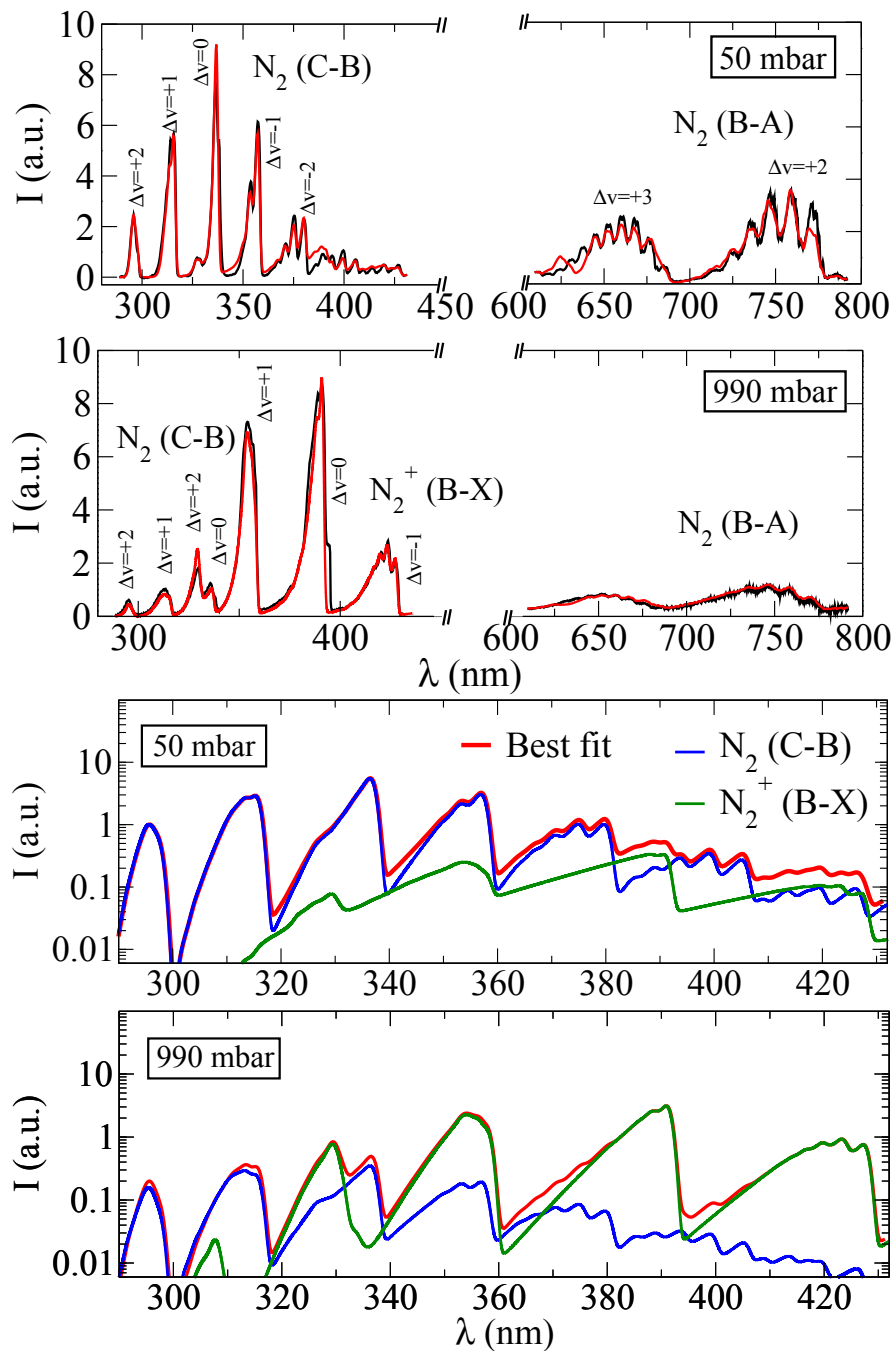


Figure 5.22.: Top: Experimental spectra (black) and their associated best fits (red). Bottom: Best fits (red) and resolved contribution of N_2 2nd Positive (C-B) (blue) and N_2^+ First Negative (B-X) (green) systems.

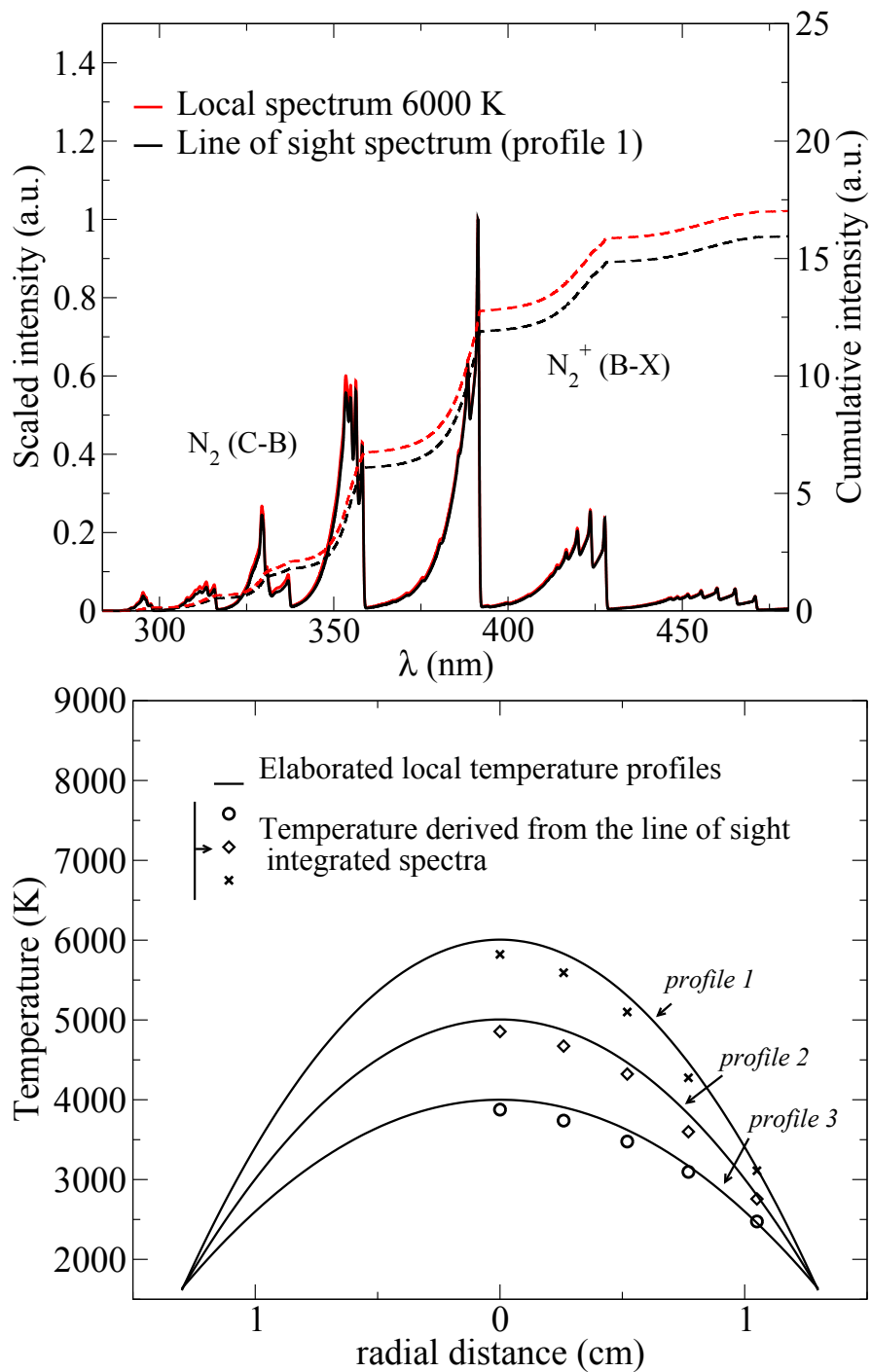


Figure 5.23.: Top: Synthetic centerline spectra corresponding to *profile 1* - Line of sight (black), local (red). Bottom: Synthetic temperature profiles.

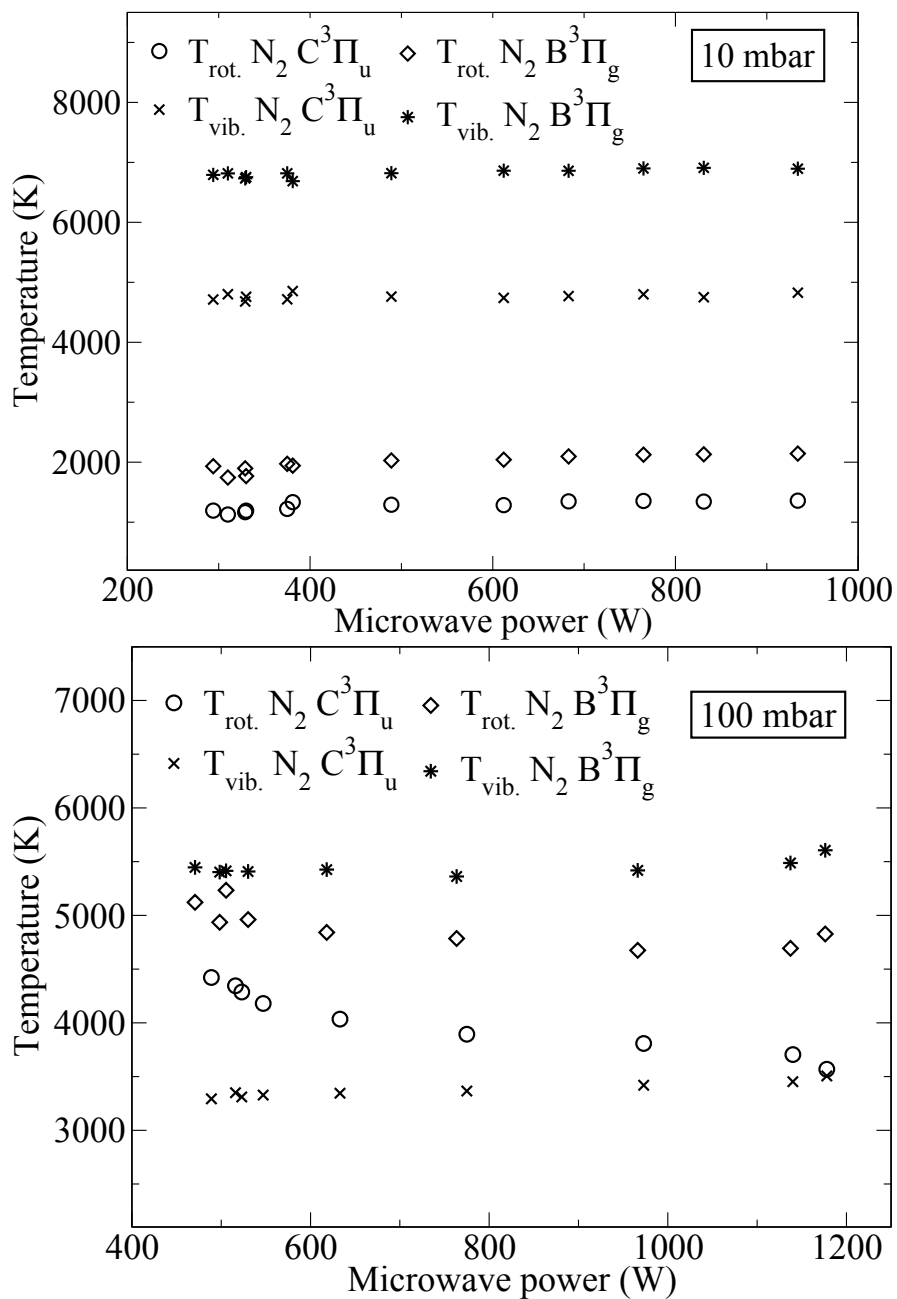


Figure 5.24.: Rotational and vibrational temperatures of $C^3\Pi_u$ and $B^3\Pi_g$ states of N_2 at 10 mbar (top) and 100 mbar (bottom) operating pressure.

tational temperatures increase. Increasing the pressure reduces the mean free path of electrons leading to lower vibrational excitation through electronic impact excitation. Conversely, heavy particles collision rate is increased, leading to fastest relaxation of rotational states. Above 100 mbar, rotational and vibrational temperatures associated to the electronic states of N_2 tend to equilibrate. In order to assess the uncertainty of the fitting procedure, temperature sensitivity of scaled total emission \bar{S}_R is investigated. To obtain the scaled total emission, calculated spectra are scaled and band intensities are integrated over the spectral extent of interest. The resulting scaled total emission is correlated to the rotational and vibrational temperatures. Following the expressions 5.1, uncertainties on the temperatures are determined assuming a relative error of +/-10 % on the measured total emission $\Delta\bar{S}_R$.

$$\Delta T_{rot} = \Delta\bar{S}_R \left[\left(\frac{\partial\bar{S}_R}{\partial T_{rot}} \right)_{T_{vib}} \right]^{-1}, \quad \Delta T_{vib} = \Delta\bar{S}_R \left[\left(\frac{\partial\bar{S}_R}{\partial T_{vib}} \right)_{T_{rot}} \right]^{-1}, \quad (5.1)$$

The normalized total emission associated to $B^2\Sigma_u^+$ state is found to exhibit a low sensitivity to the rotational temperature denoting for a large uncertainty. Rotational temperature of $B^2\Sigma_u^+$ state is therefore not displayed in figure 5.25.

5.2.4. Electronic excited states of N_2 and N_2^+ molecular system.

Calculated population ratios of electronic excited states are derived from equations 5.2 and 5.3. Computed population of electronic states were calculated assuming a Boltzmann distribution of the electronic mode defined by an electronic temperature T_{el} . Comparisons between analytical electronic population ratio and experiments are displayed in figure 5.26.

$$\frac{N_{B^3\Pi_g}}{N_{C^3\Pi_u}} = \frac{Q_{mol}^{B^3\Pi_g}(\bar{T})}{Q_{mol}^{C^3\Pi_u}(\bar{T})} \times \exp\left(-hc \frac{T_{el}(B^3\Pi_g) - T_{el}(C^3\Pi_u)}{k\bar{T}_{el}}\right), \quad (5.2)$$

$$\frac{N_{B^2\Sigma_u^+}}{N_{C^3\Pi_u}} = \frac{Q_{mol}^{B^2\Sigma_u^+}(\bar{T}) Q_{int}^{N_2}(\bar{T}) [N_2^+]}{3Q_{mol}^{C^3\Pi_u}(\bar{T}) Q_{int}^{N_2^+}(\bar{T}) [N_2]} \times \exp\left(-hc \frac{T_{el}(B^2\Sigma_u^+) - T_{el}(C^3\Pi_u)}{k\bar{T}_{el}}\right), \quad (5.3)$$

At the top of figure 5.26 population density ratio $N_{B^3\Pi_g}/N_{C^3\Pi_u}$ measured through fitting and calculated population ratio are displayed. By comparing calculations with experiment, it comes that the electronic excitation is described by a temperature close to the rotational and vibrational temperature above 100 mbar.

Theoretical calculation of $N_{B^2\Sigma_u^+}/N_{C^3\Pi_u}$ electronic population density ratio are displayed at the bottom of figure 5.26. In this case, species density should be known in order to solve equation 5.3. LTE species concentrations $[N_2]$ and $[N_2^+]$ are calculated using previously determined temperature. Above 100 mbar, the electronic population ratio $N_{B^2\Sigma_u^+}/N_{C^3\Pi_u}$ is significantly over-predicted by equilibrium calculations similarly to what is encountered during recombining/ionizing unbalanced processes.

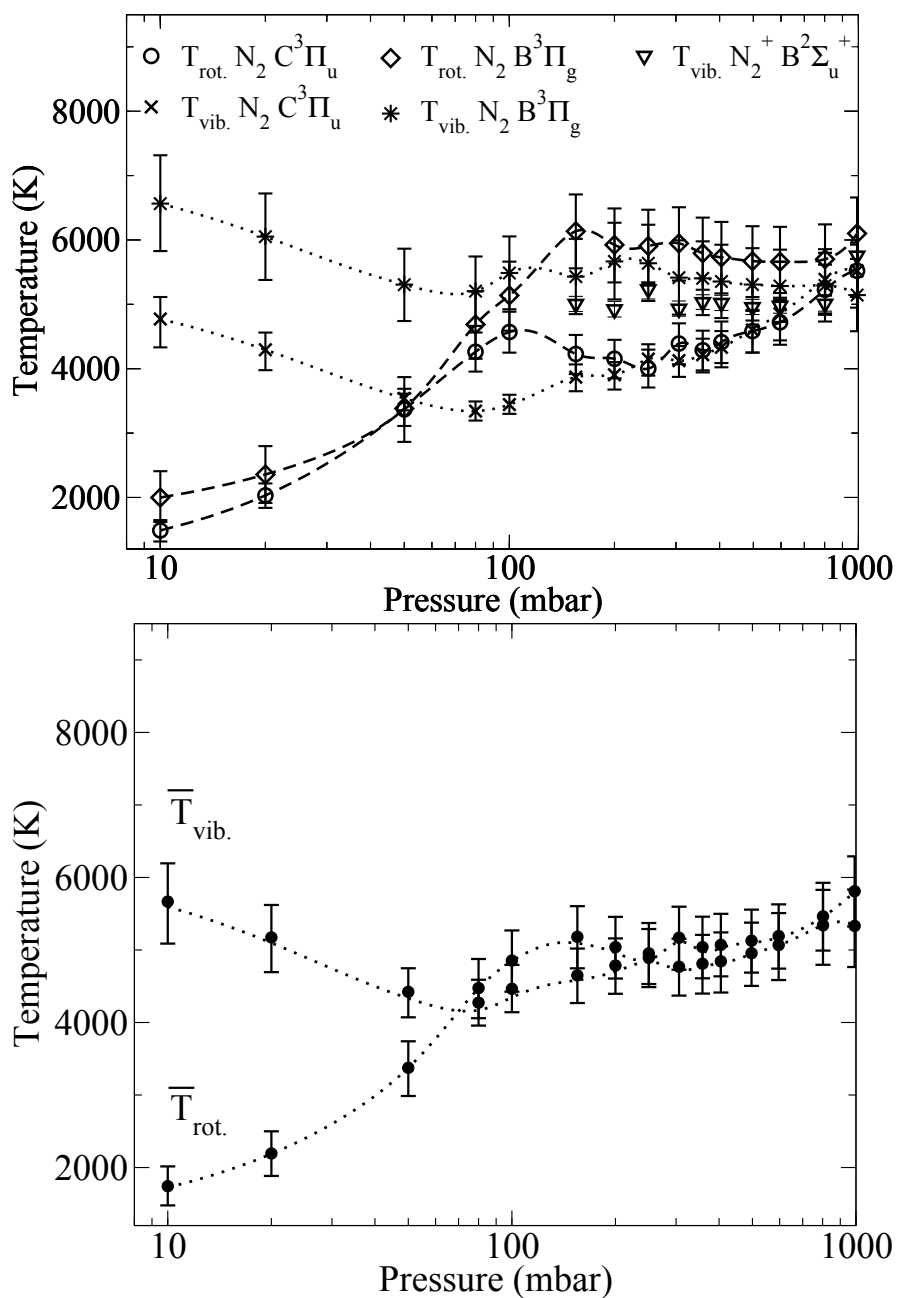


Figure 5.25.: Top: Rotational and vibrational temperatures of $C^3\Pi_u$ and $B^3\Pi_g$ states of N_2 and vibrational temperature associated to $B^2\Sigma_u^+$ state of N_2^+ . Bottom: Corresponding geometric average temperatures.

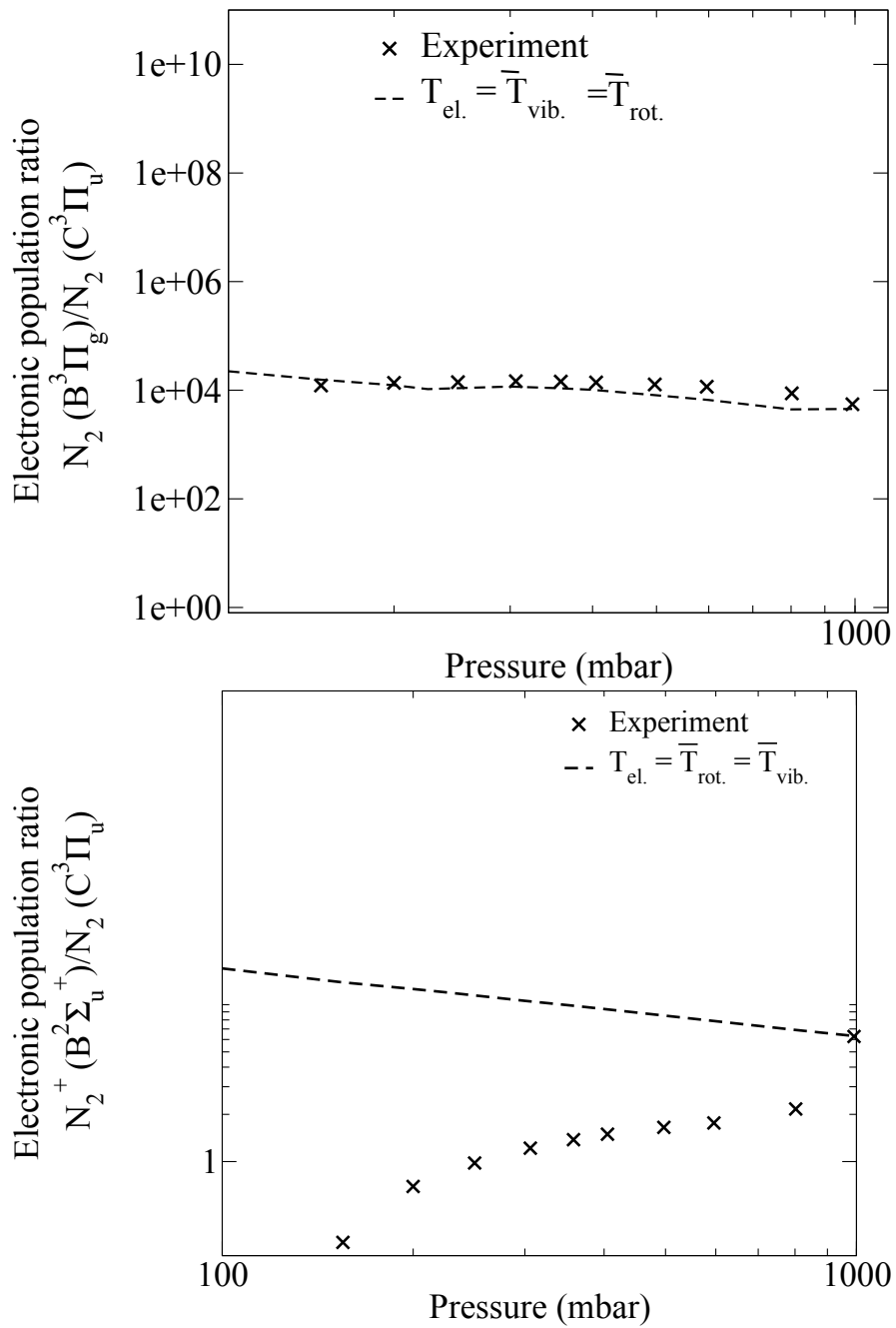


Figure 5.26.: Top: Electronic population density ratio $N_{B^3\Pi_g}/N_{C^3\Pi_u}$. Bottom: Electronic population density ratio $N_{B^2\Sigma_u^+}/N_{C^3\Pi_u}$. Experiment (cross) and theoretical calculation (red).

Chapter 6.

Preliminary description of supersonic plasma flows

6.1. Topology

Supersonic expansion through a steep pressure ratio between a high pressure reservoir and a low pressure chamber leads to the formation of periodic cells barrel-shaped structure. When the flow exits the nozzle with a pressure difference with the ambient atmosphere, it leads to the formation of compression-expansion structures. Different regimes are possible, ranging from under- to over-expanded and passing by the adapted nearly shock free supersonic expansion. Most experiments take benefit of the strong expansion and the Mach disk prevailing in under-expanded supersonic plasma jet to investigate the aerothermochemical properties.

Wave structures that create shock diamonds pattern in supersonic jets are illustrated in figures 6.1 and 6.2. Pressure waves propagate inside the jet so that on the jet boundary reflected waves are adjusted to match pressure conditions. Type of reflected wave will depend on whether pressure must drop or rise. The interaction between similar waves on the jet axis leads to a reflection of the same type of waves towards the edges of the jet. The description of choked flows corresponding to under-expanded and over-expanded situations are detailed hereafter.

In under-expanded jets, the sequence of compression and expansion begins with the creation of an expansion fan. Expansion waves are created from the edge of the nozzle and direct the flow out of the jet axis. These waves are reflected on the jet axis that leads to an axial expansion of the flow where pressure is reduced. A compression zone is then created from oblique shock waves reflected at the edges of the jet and results in a high density plasma zone. A part of kinetic energy from the expansion zone is then converted into thermal energy in this compression zone. This process repeats until the jet static pressure equilibrate with the surrounding gas. Taking a close look at the first expansion region, pressure waves reflected from the free shear layer which bounds the jet laterally are members of the same family of characteristics which coalesce to form the barrel shock. The edges of the expansion zone are therefore brighter than on the axis because of the reflection of expanding flow by the cold dense surrounding gas. Also, a bright plasma plume is visible in the first expansion zone. Immediately in front of the nozzle orifice, there is a zone of silence, which is not disturbed by shock waves. In case of high under-expansion, oblique compression waves coalescence leads to the formation of a Mach disk at the end of strong expansion. In case of strong rarefaction phenomenon, the validity of this continuum description is not valid anymore and the shock structure vanishes because of scarce collision events.

Similar process occurs in an over-expanded jet (figure 6.2). Starting from oblique shock waves created from the edge of the nozzle, the flow is turned towards the axis of the jet. It leads to a local compression. Shock waves are reflected on the jet axis toward the edges of the plasma jet and the flow turns parallel to the jet axis. A Mach reflection might occur in the jet if the angle between the incident compression waves and the jet axis is sufficiently large (incident angle being pressure dependent). Compression waves are then reflected on the plasma jet boundary where expansion fan is created. The flow is then turned out of the jet axis.

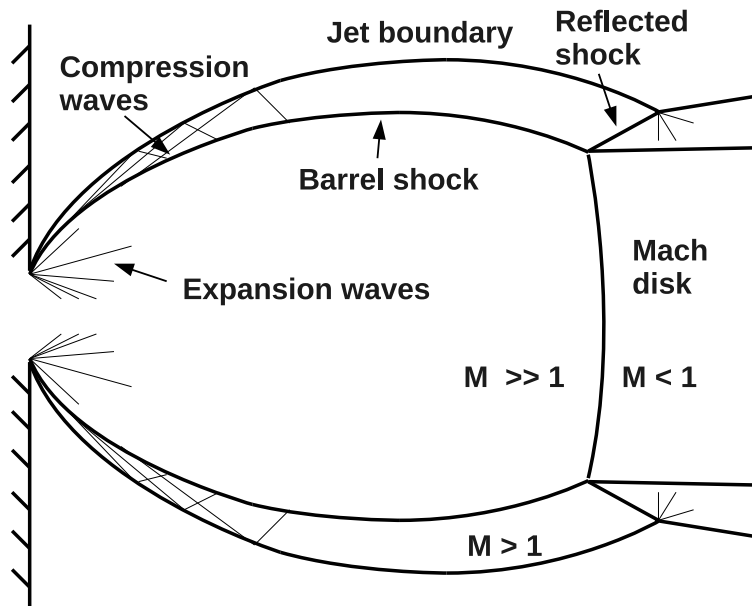


Figure 6.1.: Wave structures that create the first expansion cell in under-expanded flow.

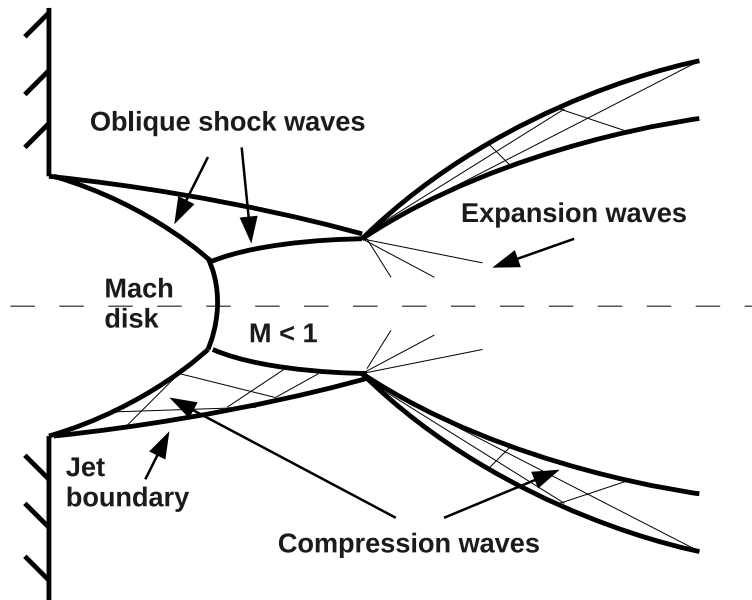


Figure 6.2.: Oblique shocks that create the first compression cell in over-expanded flow.

6.2. Experimental studies overview

Supersonic plasma jets are largely employed over a wide range of applications and research fields. Numerous studies related to the replication of natural phenomena or the optimization of industrial processes rely on supersonic plasma jet technology. Non-equilibrium mathematical models are often carried jointly with experimental characterization of supersonic plasma flows ([85], [86]). Investigations of thermodynamics and transport properties of supersonic plasma jets have benefited from the large interest put on the optimization of industrial material processes. Indeed, expanding thermal plasmas supersonically are convenient to study deposition mechanisms. Plasma chemistry aspects of expanding thermal arc plasma have been studied extensively by Sanden & al. [87]. Non-equilibrium state of supersonic expansion can be favorable for efficient plasma chemical processes. Standard thermal spray equipments are designed to obtain expanded plasma jets allowing accurate deposition. In the frame of fusion energy research, the investigation of supersonic plasma jets merging is also of interest [88]. The reproduction of the dynamics of astrophysical flows have promoted the use of scaled supersonic laboratory plasma jets where the radiative energy flux plays an essential role in the dynamics of radiative shocks ([89], [90]). Conversely to astrophysical problems, entry shocks occur in environments from which the radiation escapes and in which the radiative energy carried by line radiation is important. The development of supersonic plasma jet technologies to investigate collisional and radiative processes occurring during atmospheric entries is still not yet well developed [91].

Supersonic acceleration techniques

Various technologies are used to obtain supersonic plasma jets. Plasma acceleration is usually obtained by expanding the gas into a low pressure chamber using either a converging-diverging nozzle or a sonic orifice. Sonic throat experiments are considered as valuable alternative to conventional nozzle-confined expansion experiments to study the dynamics of supersonic free jets. However, this technique allows only for under-expanded jet operation. More recently, magnetic nozzles have been largely employed in plasma thruster technology ([92], [93], [94], [95], [96]) or material processing applications ([97], [98]). A magnetic nozzle consists in an axisymmetric divergent magnetic field providing high thrust efficiency through ambipolar electric field produced by electron pressure gradient and resulting in axial ions acceleration. In such configuration, the power loss occurring in solid nozzles is reduced because the wall-plasma contact is avoided. An easy handling of the field geometry and intensity permits a suitable control of the thrust for plasma propulsion devices. However, complex downstream detachment and acceleration mechanisms make the modeling complicated. A Mach 3 wind tunnel with integrated microwave plasma generating capability has been designed by McAndrew [99]. In this case, the acceleration was provided through a converging-diverging nozzle integrated to the microwave waveguide structure.

Rarefaction effect

Although several studies have been devoted to supersonic expansion of gas jets in low pressure environment, it is still not clear how important is the rarefaction effects on the flow field. An issue concerns the incursion of background molecules passing through the barrel shock in the supersonic part of the flow. This phenomenon predicted in the 60's by Fenn and Anderson [100] and Campargue [101] has been extensively studied in the thesis of Abbate [102] and Mazouffre [103] through numerical and experimental investigations. Due to rarefaction effects, the invasion occurs in the regions of the jet where the density in the expansion is lower than in the background gas. Accounting for rarefaction, the expansion is found to be stronger, moving the shock downstream. Particles and collisions tracking in the supersonic region proves the presence of background particles which explains the thermodynamic non-equilibrium, thus influencing also the flow field. Vankan & al. [104] evidenced the bimodal character of the velocity distribution function in the expansion and in the shock regions. It is interpreted in terms of a component expanding from the source and a component flowing into the plasma expansion from the periphery.

Pulsed / continuous operations

Although it is not of interest in our study, a large amount of investigation on pulsed supersonic plasma jet can be found in the literature. These experimental arrangements give rise to transient phenomena of importance for the establishment of equilibrium state. Under certain conditions and electrode geometries, electrical pulse discharges are accompanied by the formation of supersonic plasma jets [105]. Low pressure pulsed RF supersonic plasma jet systems are suitable for thin film plasma deposition ([106], [105]) and pulsed plasma thruster technology which is of interest for small satellites guidance applications [107].

Effect of swirl on the shock structure

In our experiments, supersonic microwave discharge is created using a tangential gas injection accelerated through a convergent-divergent nozzle. The rotation of swirling flows plays a significant role in determining the shock structure. The application of swirl always results in a reduction in axial Mach number component that weakens the Mach disk strength of under-expanded jet. The degree of flow rotation is characterized by the swirl number, defined as the ratio of the mean axial and rotational momenta of the flow. Abdelhafez & al. [108] examined the slight increase of the swirl number within the shock. According to the fundamentals of gas dynamics, the velocity component parallel to the plane of a shock wave is preserved through the shock and experiences no change. Conversely, the axial velocity is perpendicular to the Mach disk and undergoes significant reduction through the shock structure.

Characterization techniques

Experimental characterization of supersonic non reactive flows have been extensively investigated in order to identify the structure and the dynamical properties of supersonic jets. To some extent, hydrodynamic phenomena of weakly ionized under-expanded supersonic plasma jets can be described by using the adiabatic supersonic expansion and shock wave structure theory in the continuum regime [109]. This aspect is addressed in section 6.3. Some of the earliest data on free jet structure were obtained by interferometric techniques by Landenburg & al. [110] in 1949. Impact pressure, mass flow probe measurements ([111], [112], [109]) and electron beam method [113] have also been performed to characterize the dynamical structure of cold supersonic jets. The use of electrostatic probes allows not to rely on the assumption of local thermodynamic equilibrium. It is an appropriate diagnostic to study low pressure plasma jets which are known to be non-LTE. For this reason, Gindrat & al. have used double Langmuir probes and Mach probes [114]. The perturbation coming from the shock layer formed upstream of the sensor should then be accounted to obtain reliable intrusive measurements. Non-intrusive optical techniques are rather preferred in order not to alter fluid dynamics and chemical kinetics in the jet.

Schlieren flow visualization based on the deflection of the optical path length in the jet is largely used to assess the structure of neutral supersonic plasma jet. A source light propagating through the jet is bent as a result of the gradient of its refractive index. Schlieren visualization technique has permitted to perform qualitative analysis of the spatial structure of axisymmetric supersonic jets [115]. The emission from supersonic plasma jet can provide a direct insight on the jet structure. Even if the emission is not an accurate monitor of the flow thermodynamic properties, it reflects quite well the electron temperature and density changes.

Various laser-based spectroscopic techniques have been developed to characterize the flow field properties of supersonic jets with high spatial resolution. Two-photon absorption laser induced fluorescence allows for the spatially resolved determination of density, temperature and velocity. In high speed compressible flows with large velocity gradients, particle-based techniques might suffer from the large inertia of the seed particles. Velocity distribution of particles can be obtained by means of resonant laser induced fluorescence spectroscopy ([91], [116]). High resolution absolute densities, rotational temperature and velocity maps were obtained from measurements in a steady axisymmetric supersonic jet using diagnostics based on linear Raman spectroscopy [117], Laser Doppler Velocimetry [118] and Rayleigh scattering [119]. A complete

density and thermal mapping of CO₂ cold supersonic jet was performed by Mate & al. using Raman spectroscopy technique [117]. In case of low temperature, low density flows, investigation of rotational temperatures require special instrumentation at any point in non-radiating flows. For this purpose electron beam fluorescence technique is often used to excite the gas and predict the temperature using relative intensities in the rotational structure of the emission spectra or by measuring the Doppler broadening of a single rotational line.

Detailed kinetic characterization of supersonic plasma flows of Ar, H₂, CO₂, N₂ and Air mixtures at static pressures ranging from of 1 to 10 mbar was performed by Drake & al. ([120], [121]) using spectroscopic diagnostics. Emission spectroscopic study of a low pressure supersonic Ar-H₂ DC plasma jet for pressure ranging from 200 mbar to 1 bar was performed by Sabsabi & al. [122]. Important deviations from LTE were noticed at 200 mbar chamber pressure. Axial variations of electron density was coinciding with the observed diamond shock wave in the plasma jet [122]. A brief overview of previous experimental investigations dedicated to the characterization of thermo-chemical processes in supersonic plasma is given below. Since the literature is full of various descriptions in this area, the review will therefore be mostly limited to optical measurement techniques performed in continuous ground facilities operating with a stationary supersonic plasma jet.

6.3. Aerothermochemical processes

Fully ionized plasma description is relevant to discuss astrophysical phenomena, while it is more realistic to consider weakly ionized plasmas in the frame of re-entry physics and related laboratory experiments. The following discussion about aerothermochemical processes in supersonic plasma jets will be therefore limited to partially ionized gases.

In weakly ionized plasmas, processes involving electrons, ions and excited species do not couple strongly to neutral particles because of the low degree of ionization. In a preliminary approach we can therefore consider that the classical aerodynamic field is unaffected by collisional and radiative processes. Inviscid flow solution for under-expanded free jet was obtained by Ashkenas and Sherman [109] by the method of characteristics. The gas dynamic theory of Prandtl-Meyer flows can be used as a guide to get approximate understanding of expanding plasma flows. However, if the plasma is substantially ionized in the compression regions, a modified pressure and density ratio formula across the shock has to be introduced. In reactive flows, the effect of radiation, elastic and inelastic species collisions, unequal electron and heavy species temperature and the effect of electron heat conduction should be assessed.

6.3.1. Weakly ionized plasma expansion

Van de Sanden has extensively explored the fundamental investigation of supersonically expanding plasma jets [123]. Inert species in the plasma expansion expand just like free jet normal gas expansion [109]. However, the expansion of the reactive species is influenced by inelastic collisions, chemical reactions and diffusion phenomena that affect the flow field thermodynamic state. A close look to the internal energy of excited species and electron energy might reveal non Maxwell-Boltzmann distributions. At the nozzle exit, the electron density rapidly falls, diminishing the number of collisions. One may expect non-thermal plasma. Previous studies of electron-ion recombination in expanding plasma flows have evidenced significant thermodynamic non-equilibrium such as thermal non-equilibrium between electrons and heavy particles, non-equilibrium electron density and excitation non-equilibrium ([124], [125], [126]).

In literature, supersonic plasma molecular expansion are poorly investigated in favor of atomic gases. Supersonically expanding argon cascaded arc plasma was investigated by Meeusen & al. for sub-atmospheric pressure at about 100 mbar and temperature of 10 000K. The role of

charge exchange and dissociative recombination in the expansion was identified to be the dominant process in the formation of excited states [98].

Meulenbroeks & al. [127] observed significant associative charge exchange reaction in the expanding argon cascaded arc plasma, supplied with additional amount of hydrogen.

Yano & al. [128] have developed a facility to generate a supersonic high pressure glow discharge. In such facility, the expansion of the plasma is accompanied by a rapid cooling and recombination which results in kinetic non-equilibrium between electrons and heavy particles. In this situation, the plasma is recombining by collisional processes and a departure from Saha-Boltzmann equilibrium is observed.

Selezneva & al. have reported the effect of chamber pressure on the deviation from LTE in direct current argon supersonic plasma jets for pressure lying between 60 and 400 mbar [129]. In the divergent part of the nozzle, the electron number density has been found to be close to the frozen value where the hydrodynamic timescale is much lower than recombination and ionization timescale. In this region, electron density was rather convective flux controlled than ionization-recombination reaction controlled.

Spectroscopic study of a supersonic argon/hydrogen plasma jet generated by an ICP torch with a convergent-divergent nozzle has been conducted by Sember & al. [130] at about 18 mbar and 10 000 K plasma environment. Jet in pure argon appeared to be chemically frozen and populations of excited states deviate from Boltzmann distribution. However, Saha equilibrium was prevailing at the ionization limit. The jets in the mixture of argon and hydrogen was less frozen and with increasing the hydrogen amount, the flow became strongly recombining. The departure from Boltzmann equilibrium varies along the centerline, which is apparently caused mainly by changes in population of low-lying levels. Increasing the hydrogen content was leading to the under-population of all the argon atomic states with respect to Saha equilibrium.

Engeln & al. gave an overview of the way macroscopic parameters (density, velocity and temperature) behave in an expanding thermal plasma [131]. Argon thermal plasma expansion is found to be similar to the expansion of a hot neutral gas with a minor modification in the adiabatic exponent. However, the addition of hydrogen or nitrogen change drastically the behavior of radical in the expansion. In supersonic expansion, a drop in the electron temperature T_e lags the drop in the temperature of the gas. The electron concentration N_e becomes frozen being much greater than the equilibrium electron density. In the same time the distribution of electrons over the excited states is at variance with Boltzmann equilibrium distribution.

Spectroscopic studies of vibrational non-equilibrium in nitrogen supersonic nozzle flows were conducted in excited but not dissociated nitrogen flow [132] for reservoir temperatures and pressures in 2800-4600 K and 24 to 82 bar range. The rapid monotonic decrease in pressure and kinetic temperature in the expansion caused fairly small departure from equilibrium in the vibrational degree of freedom. This departure was dictated primarily by the efficiency of vibrational de-excitation.

Macroscopic description of weakly ionized plasma expansion

In the case of supersonic weakly ionized plasma expansion, transport of particles tends to follow the quasi-adiabatic expansion behavior of a free jet despite possible microscopic non-equilibrium processes. Flow field calculation by Ashkenas and Sherman [109] is helpful for determining flow quantities within an expansion. The expansion can be described using a density rarefaction model, as suggested by Schram & al. [133]. Under the assumption that particles originate from a flowing point source of density n_0 , the axial dependence of the density in a supersonic expansion can be written as:

$$n(z) = n_0 \times \frac{1}{1 + z^2/z_0^2} \quad (6.1)$$

where z_0 is the position of the virtual point source. For an adiabatic process, the Poisson adiabatic formula reads as:

$$\left(\frac{n}{n_0}\right)^{\gamma-1} = \frac{T}{T_0} \quad (6.2)$$

where γ is the value of the specific heat ratio.

In neutral gas expansion, the flow can be considered as isentropic (equation 6.2) and the axial temperature profile can thus be described by the relation:

$$T(z) = T_0 \times \left(\frac{1}{1 + z^2/z_0^2} \right)^{\gamma-1} \quad (6.3)$$

Starting from an initial sonic axial velocity c_0 at the nozzle exit, and under the assumption of an adiabatic inviscid expansion, the axial flow velocity w can be retrieved from the momentum balance. Using the axial dependence of density and temperature. The velocity along the jet axis is then given by the following equation:

$$w(z) = \frac{c_0}{(\gamma-1)^{1/2}} \left[\gamma + 1 - 2 \left(\frac{n(z)}{n_0} \right)^{(\gamma-1)} \right]^{1/2} \quad (6.4)$$

Anomalous transport of radicals in plasma expansion were experimentally observed. Mazouffre [103] has studied the decoupling between the H atom and argon carrier gas during the plasma expansion. A significant amount of H atoms escape from the supersonic expansion by a diffusion process due to strong density gradients between the core of the jet and its vicinity. This anomalous transport is largely influenced by wall surface recombination process.

6.3.2. Weakly ionized stationary shock front

Internal energy relaxation in compression regions are not well documented experimentally but rather benefits from numerous analytical and numerical investigations that use kinetic models including the effect of radiation, elastic and inelastic species collisions in thermo-chemical non-equilibrium plasmas. For example, vibrational kinetics, dissociation, translational and rotational relaxation in a strong shock wave of nitrogen were investigated by Bruno & al. using Direct Simulation Monte Carlo simulation [134]. A self-consistent modeling of translational, rotational and vibrational kinetics of a diatomic gas undergoing dissociation in the shock wave revealed non-equilibrium distributions.

An aspect of the shock front in plasma is the presence of recombination processes which acts mainly on heating the electrons. High electron temperature are found in compression region where electron can gain energy through three particle recombination. Sanden & al. [135] investigated highly under-expanded argon flow produced in a cascaded arc at temperature of about 10 000 K and pressures ranging from 10^{-1} to 1 mbar. The importance of three-particle recombination in the heating of electrons was evidenced.

Macroscopic description of weakly ionized stationary shock front

Plasma expansion ends with a stationary shock front resulting from the coalescence of compression waves. Throughout the stationary shock front, of which the thickness is of the order of one local momentum exchange mean free path, the velocity decreases, and the temperature rises, due to collisions with the background gas. Highly under-expanded plasma jets give rise to the formation of a Mach disk located at a distance z_M front the nozzle exit. For a given specific heat ratio, the distance z_M is determined by the pressure ratio across the nozzle (equation 6.5). From compressible flow theory, Witte [136] derived analytically a relation for z_M which depends also on the sonic nozzle diameter D_{exit} , whereas Ashkenas [109] found experimentally a similar relation holding for argon, nitrogen and air mixtures.

$$\frac{z_M}{D_{exit}} = \frac{1}{\sqrt{2}} \left(\frac{2}{\gamma+1} \right)^{\frac{1}{2} \left(\frac{1}{2} + \frac{1}{\gamma-1} \right)} \left(\frac{\gamma^2}{2(\gamma-1)} \right)^{0.25} \left(\frac{p_0}{p_b} \right)^{0.5} \quad (6.5)$$

which becomes for $\gamma = 5/3$:

$$\frac{z_M}{D_{exit}} = 0.64 \left(\frac{p_0}{p_b} \right)^{0.5} \quad (6.6)$$

and for $\gamma = 7/5$

$$\frac{z_M}{D_{exit}} = 0.67 \left(\frac{p_0}{p_b} \right)^{0.5} \quad (6.7)$$

where p_0 is the stagnation pressure in the reservoir and p_b refers to background pressure in the chamber. Classically, the shock is treated as a discontinuity across which mass, momentum and energy are conserved. The jump relations for the pressure p , the density ρ and the temperature ratio for an adiabatic normal shock front can be expressed using the Rankine-Hugoniot relations and the Mach number magnitude ahead of the shock wave M_1 :

$$\frac{p_2}{p_1} = \frac{2\gamma M_1^2 - (\gamma - 1)}{\gamma + 1} \quad (6.8)$$

$$\frac{\rho_2}{\rho_1} = \frac{(\gamma + 1)M_1^2}{(\gamma - 1)M_1^2 + 2} \quad (6.9)$$

$$\frac{T_2}{T_1} = \frac{(2\gamma M_1^2 - \gamma + 1)((\gamma - 1)M_1^2 + 2)}{(\gamma + 1)^2 M_1^2} \quad (6.10)$$

The downstream Mach number M_2 is expressed as:

$$M_2 = \left(\frac{2 + (\gamma - 1)M_1^2}{2\gamma M_1^2 - (\gamma - 1)} \right)^{0.5} \quad (6.11)$$

where the subscripts 1 and 2 refer respectively to the upstream and downstream quantities. The shock front has a finite thickness. Shock front width is typically a few neutral-neutral collision mean free paths. Based on kinetic theory, a theoretical profile, the so-called Mott-Smith profile, has been proposed to describe the shape of a shock front [137]. The ratio densities across the shock can be evaluated through kinetic models and is defined as:

$$y = y_1 + \frac{y_2 - y_1}{1 + \exp(-4z/L)} \quad (6.12)$$

where y stands for the considered property, y_1 is the value of y far away ahead the shock, y_2 the post-shock equilibrium value and L is the shock thickness that can be approximated from the maximum slope as follows:

$$L \approx \frac{y_2 - y_1}{\left| \frac{\partial y}{\partial z} \right|_{max}} \quad (6.13)$$

Using the continuum theory the shock thickness can also be expressed as a function of the mean free path $\bar{\lambda}$ and Mach number ahead of the shock front M_1 :

$$L \approx \frac{\bar{\lambda}}{3(M_1 - 1)} \quad (6.14)$$

Due to slow energy exchange between the electrons and the heavy particles and to the charge separation within the shock, the Mach disk of a weakly ionized plasma should be considered differently from neutral gas shock front. Experimental anomalies of shocks in weakly ionized plasmas have been commonly observed [138]. In a weakly ionized shock, the position of the ion shock front might differ from the one of neutral shock front. The ion shock thickness is also expected to be also larger than that of neutral gas. Conversely to neutral shocks, weakly

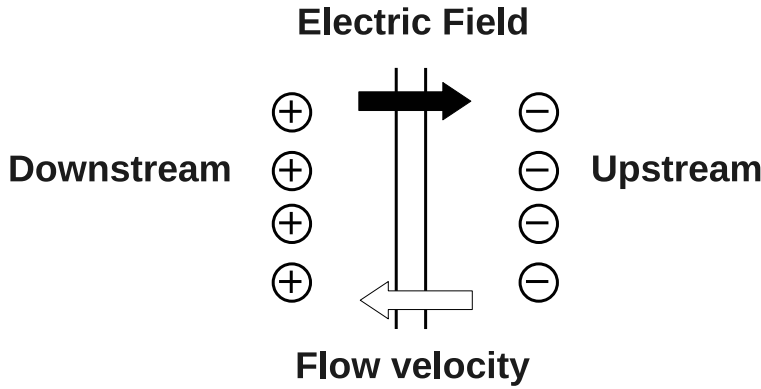


Figure 6.3.: Schematic of electronic double layer at a stationary shock front in weakly ionized gas.

ionized shocks exhibit charge separation due to the mobility of the electrons which diffuse faster than heavy particles. Under ambipolar condition, the diffusion of ions and electrons is highly correlated because of the formation of space-charge electric field. The formation of an electrical double layer, as illustrated in figure 6.3, equilibrates the fluxes of ions and electrons. A thermal layer of elevated electron temperature is formed ahead of the shock. An excess of negative charge density is present ahead of the shock. An electron preheating ahead of the ion density shock is commonly observed. This charged particle precursor may be able to interact with the neutral flow in front of the shock and significantly affect flow parameters before crossing the neutral shock itself. Van de Sanden [123] proposed an explanation where the current density formed in the expansion region would be responsible for ohmic dissipation ahead of the shock. Large electron heat conduction and possible recombination mechanism would then contribute to the electron preheating ahead of the shock. In the shock wave, ions do not behave adiabatically due to electric field created by charge separation. This phenomenon contributes to the alteration of classical aerodynamic field. When the ratio of the Debye length λ_D to the shock thickness L is small, then particles cross the shock without undergoing the effect of the macroscopic electric field. In such a case it is expected that charged particle effects would be very small in comparison to neutral interactions. In ground plasma sources under investigation, the ratio λ_D/L can be approximated to range between 0.01 and 1. Additionally to energy transfer process through momentum, the conduction, the radiation and the electric field are responsible for significant energy transfer across the shock. Van de Sanden propose to rewrite the jump relation for ions front by substituting in equations 6.8, 6.9 and 6.10 the upstream Mach number M_1 by an equivalent electron-ion Mach number M_1^{e-i} defined by:

$$M_1^{e-i} = \left(\frac{v_d^2}{\gamma R_g (T_i + T_e)} \right)^{1/2} \quad (6.15)$$

where v_d is the drift velocity and R_g the gas constant. An analytical model for the property ratios across weakly ionized shock with ionization process was developed by Saeks & al. [139]

and is expressed in term of upstream Mach number M_1 as:

$$\frac{p_2^i}{p_1} = \frac{\gamma M_1^2 + 1}{\gamma + 1} \quad (6.16)$$

$$\frac{\rho_2^i}{\rho_1} = \frac{(\gamma + 1)M_1^2}{\gamma M_1^2 + 1} \quad (6.17)$$

$$\frac{T_2^i}{T_1} = \left(\frac{\gamma M_1^2 + 1}{(\gamma + 1)M_1} \right)^2 \quad (6.18)$$

where the superscript i refers to the modified downstream properties accounting for ionization. We can notice that pressure and density ratios across a normal shock wave are always reduced with ionization. However, the downstream temperature ratio across a normal shock wave is increased with ionization. In the planetary entry flow regime of interest, pressure and thermal diffusion effects are generally negligible compared to mass diffusion due to concentration gradients.

Chapter 7.

Thermodynamic characterization of supersonic plasma flows

7.1. ICP air Plasmatron experiment

7.1.1. Preliminary observations.

Experimental arrangement and topology of the flow

In the present experiment, the Plasmatron is operated at 490 kW power and 4.5 g/s air mass flow rate settings. Supersonic plasma jets are obtained by expanding the plasma through a strictly convergent nozzle (sonic nozzle) of 35 mm throat exit diameter into a test chamber where a low pressure is maintained. The pressure in the reservoir P_0 is maintained at 120 mbar and the back pressure P_b in the chamber is set either to 6 (*case 1*) or 12 (*case 2*) mbar, both cases corresponding to under-expanded situation characterized by the presence of a Mach disk. Pictures of the jet corresponding to these two cases are displayed in figure 7.1. When the back pressure is reduced to 6 mbar in the chamber, the plasma jet is highly under-expanded. The jet expands faster and appears to be less luminous due to the flow rarefaction. Following the definition given by Muntz & al. [113] and using computed nozzle exit parameters given in table 7.2, the continuum regime holds if the back pressure is maintained higher than 2.6 mbar. In our experiment the continuum regime is then always valid. In figure 7.1, vertical lines show the axial locations of the spectroscopic measurements, covering the first expansion and the first compression zones. Abel inverted pictures 7.2 illustrate the complex structures of compression and expansion zones in the jet caused by multiple reflections of expansion and shock waves. In particular Abel inverted pictures evidence bright zones in the compression region mainly located on the edges. A conventional OES technique is set up and applied within a large spectral range in the first expansion zone (starting at 2.5 cm from the throat exit) and in the compression region. In figure 7.1, vertical lines correspond to 2.5, 3.5, 4.5, 8.5, 10.5, 11.5, 12.5, 13.5, 15.5, 17.5 cm (resp. 2.5, 3.5, 4.5, 6.5, 7.5, 8.5, 9.5, 10.5, 11.5, 12.5 cm) axial locations for 6 mbar (resp. 12 mbar) back pressure case. At each axial location, the line of sight plasma jet emission is collected through an aperture and then focused with a fused silica lens onto the entry of a Acton Series monochromator of 75 cm focal lengths. The spectrometer is combined with a ICCD PI-MAX camera with a frame of 1024×1024 pixels of $12.8 \mu\text{m}$ side. Emission issued from the jet is spatially resolved in the radial direction. A radial slice of about 19 cm height was optically conjugated using a 100 mm focal lens onto an image with a magnification factor of 0.07. It allows to capture the whole radial profile of the jet onto the CCD screen of the camera with a spatial resolution of about 180 microns. We focus our investigation on the visible spectral domain that includes mainly atomic contribution of oxygen and nitrogen atomic lines, the small contribution of N_2^+ First negative system and H_β hydrogen line. The radiation from oxygen and nitrogen atomic lines and the N_2^+ First negative system are recorded using a 150 grooves/mm grating whereas the hydrogen lines was measured improving the spectral resolution by using a 1200 grooves/mm grating in order to resolve the Stark broadening. The corresponding spectral resolutions are measured to be respectively 0.5 nm and 0.06 nm, setting the entrance slit of the monochromator to 3 microns. The recorded spectra are calibrated in absolute radiance. Calibrated spectra at the plasma jet center line are shown in figure 7.3. At the conditions reported here, the air mixture is assumed to be optically thin and proper Abel

Operating conditions	<p>4.5 g.s⁻¹ mass flow rate reservoir pressure $p_0 = 120$ mbar 490 kW power (standard coupling efficiency 50%) 35 mm sonic throat</p> <p>Back pressure in the chamber - case 1 $p_{back.} = 6$ mbar - case 2 $p_{back.} = 12$ mbar</p>
Spectroscopic features	<p>Acton Series monochromator (75 cm focal length) 0.5 nm (UV-Vis) and 0.06 nm (hydrogen line) spectral resolution</p> <p>Radially resolved measurements (180 μm resolution) Downstream axial location (distance from nozzle exit): -case 1: [2.5, 3.5, 4.5, 8.5, 10.5, 11.5, 12.5, 13.5, 15.5, 17.5] cm -case 2: [2.5, 3.5, 4.5, 6.5, 7.5, 8.5, 9.5, 10.5, 11.5, 12.5] cm</p>
Radiative transitions of interest	<p>N_2^+ ($B^2\Sigma_u^+ \rightarrow X^2\Sigma_g^+$) 1st Negative System N_2 ($C^3\Pi_u \rightarrow B^3\Pi_g$) 2nd Positive System Atomic nitrogen lines Atomic oxygen lines Atomic hydrogen lines</p>

Table 7.1.: Characteristics of experimental ICP supersonic air plasma jet experiments.

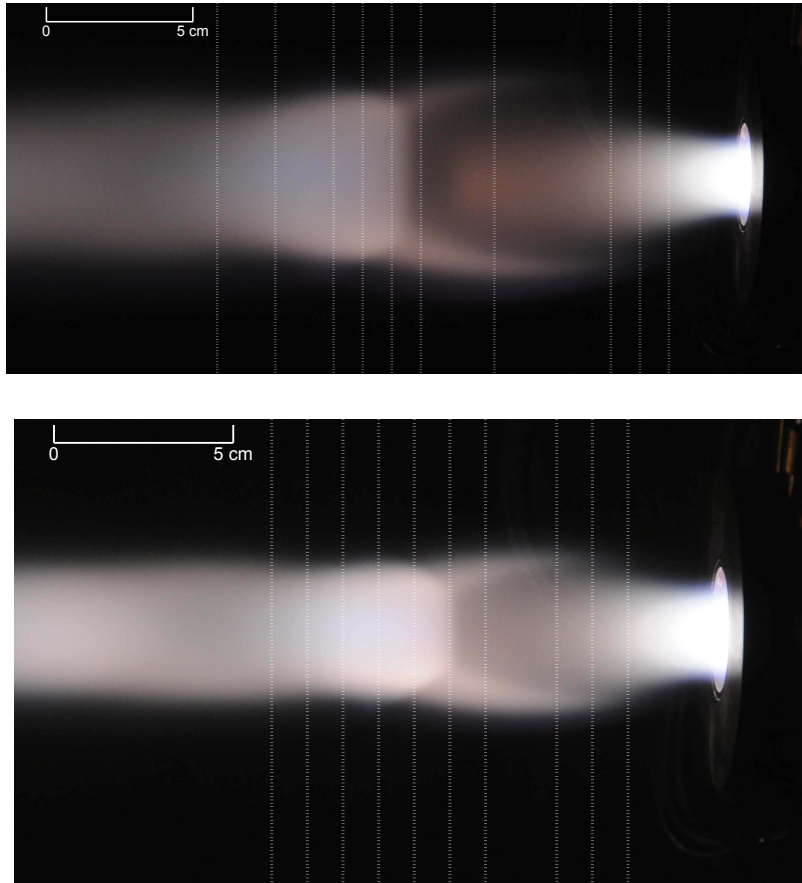


Figure 7.1.: Locations of line of sight measurements in supersonic air plasma jets at 6 mbar (top) and 12 mbar (bottom) back pressure conditions.

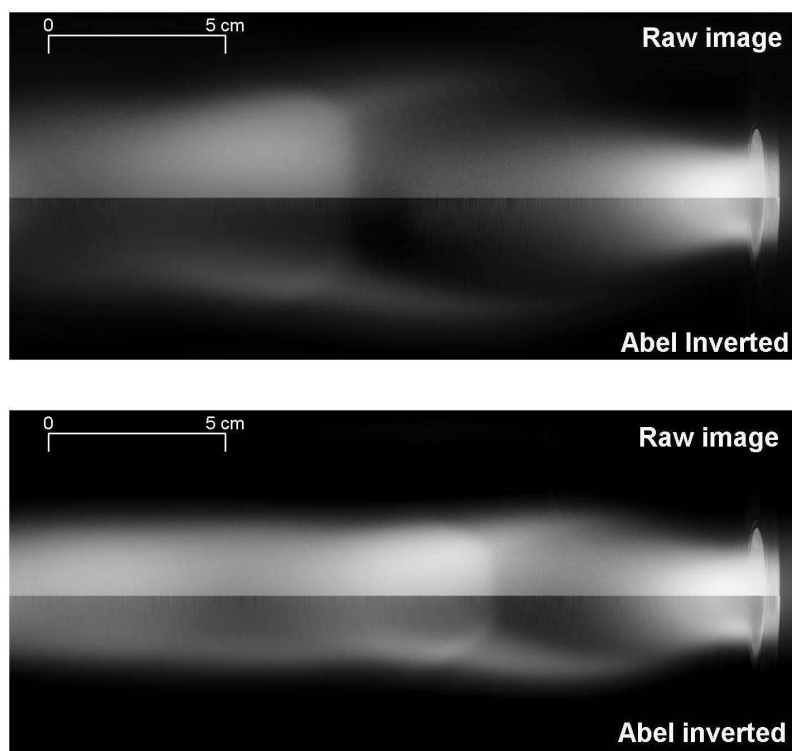


Figure 7.2.: Raw and Abel inverted pictures of supersonic air plasma jets at 6 mbar (top) and 12 mbar (bottom) back pressure.

inversion is applied on measured spectra allowing to rebuild local spectral emission. Using camera recorded line of sight light intensity, raw and Abel inverted light intensity profiles on the symmetry axis are plotted in figure 7.4. Abel inverted profiles exhibit significant change in the relative light intensity compared to raw profile. The non monotonic profile of light intensity along the axis exhibits synchronous variations for raw and Abel inverted profiles. In a first crude approximation, neglecting temperature effects, light intensity variation can be related to the excited species concentration and Mott-Smith profile (using equation 6.12) can then be used to assess shock thickness. The supersonic flow adapts to the downstream conditions over a finite length. In figure 7.4, Mott-Smith profiles (red) are built using $L=2$ cm (*case 1*) and $L=1.8$ cm (*case 2*) shock thickness value.

Spectroscopic records

Spectroscopic records of the spectral radiance and associated local emission are used to estimate 2D light intensity distribution. For this purpose, radiative records are integrated over [400-900] nm spectral range. Resulting iso-contours are displayed in figure 7.5 and 7.6 for *case 1* and 2 respectively. Abel inverted iso-contours reveal an emission peak located nearby the triple point where the barrel shock, the Mach disk and the reflected shock intersect ($r=2.5$ cm, $z=13.0$ cm). This feature can be retrieved from the pictures displayed in figure 7.2. Starting from the 2D emission distribution, the Mach disk location is roughly gauged at the end of the first expansion at the start of the shock. The estimated Mach disk position is $z_M \approx 10.5$ cm for $p_b = 6$ mbar (*case 1*) and $z_M \approx 6.7$ cm for $p_b = 12$ mbar (*case 2*). Using the well-known empirical correlation proposed in [140] in the case of an ideal gas expansion, the Mach disk position is

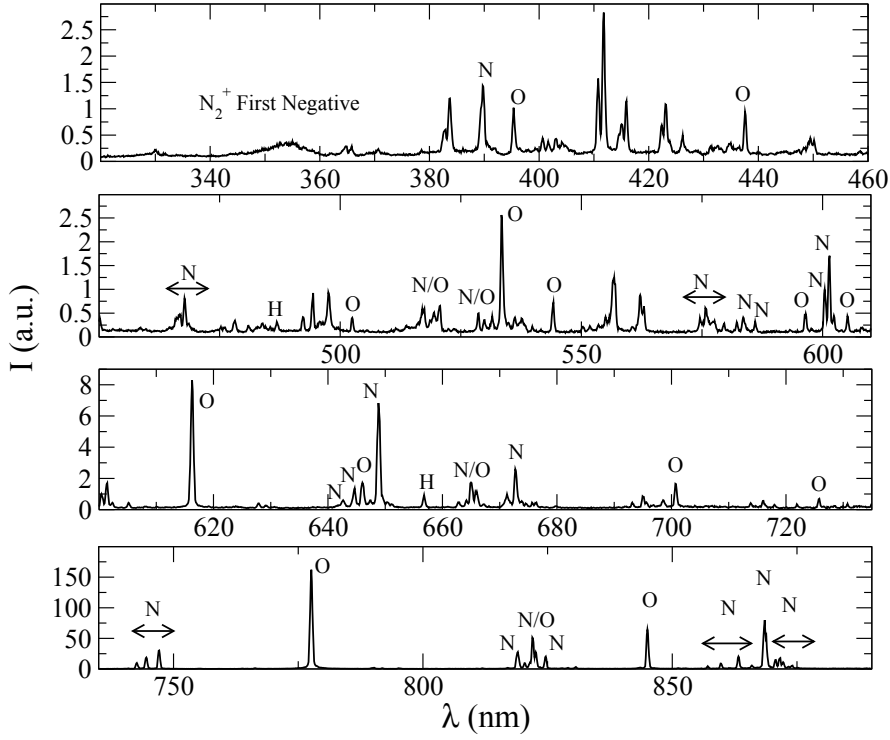


Figure 7.3.: Typical radiative signature of supersonic air plasma jet in the first expansion zone ($r = 0$ cm, $z = 2.5$ cm).

expressed as:

$$z_M^{6\text{mbar}} = 3.00 \times D_0 \quad (7.1)$$

$$z_M^{12\text{mbar}} = 2.12 \times D_0 \quad (7.2)$$

yielding to $z_M = 10.5$ cm at $P_b = 6$ mbar and $z_M = 7.4$ cm at $p_b = 12$ mbar for a 3.5 cm sonic throat diameter. The experimental estimations and the empirical values are in good agreement, revealing that non ideal gas effects do not impact significantly the hydrodynamic behavior of the jet for the Mach position.

7.1.2. Quasi 1D isentropic approximation.

In a preliminary approach, simple quasi 1D calculations to describe qualitatively plasma properties in the first expansion cell and downstream the shock. We evaluate the Mach number in the expansion region before the shock using the expansion angle and assuming ideal air. The Mach number is straightly related to the cross section area of the jet. Mach number profiles determined on the symmetry axis using the jet radial extent and assuming isentropic flow expansion are displayed in figure 7.7. From the reservoir pressure and the mass flow rate, the

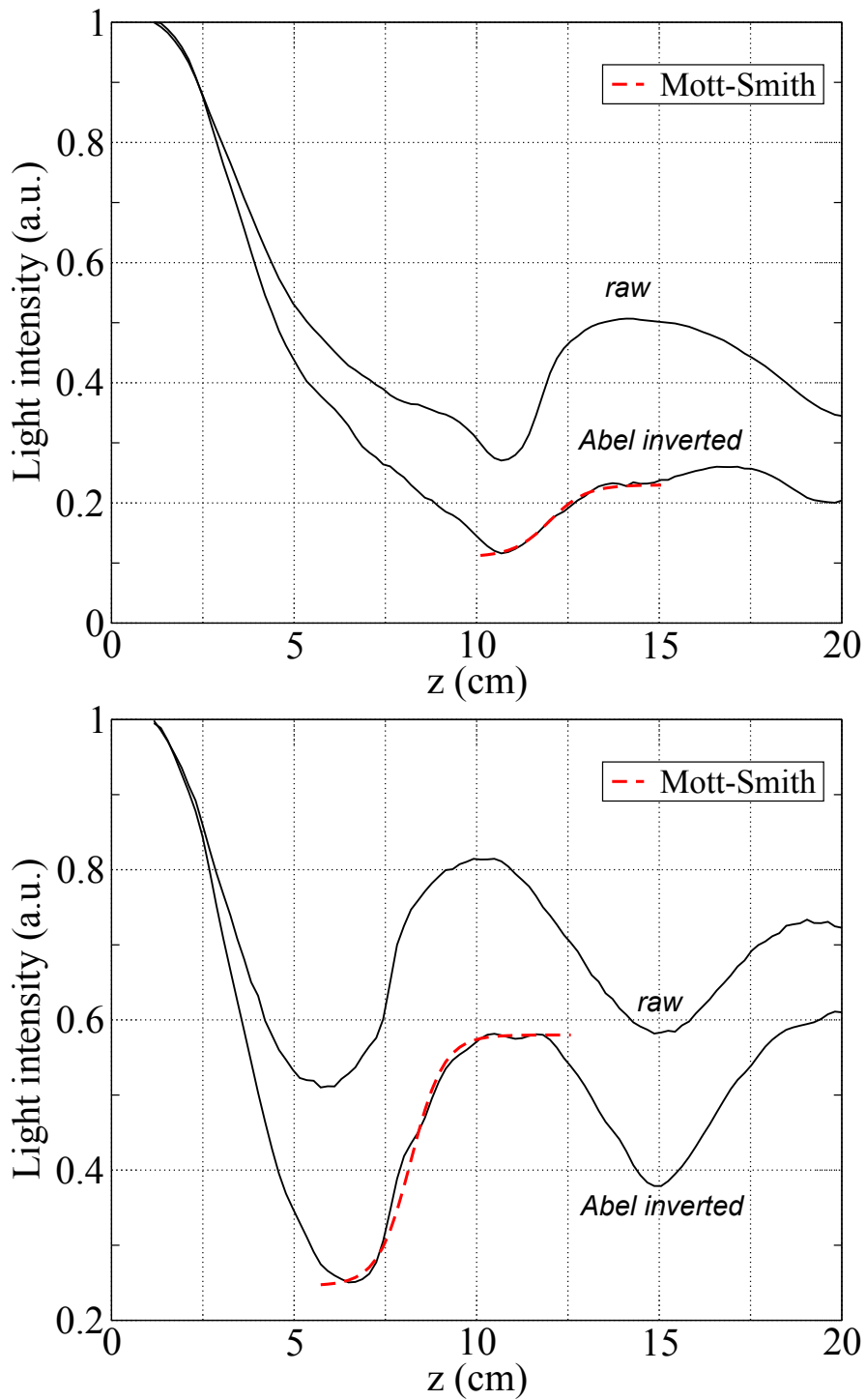


Figure 7.4.: Light intensity axial profiles for 6 mbar (top) and 12 mbar (bottom) back pressure conditions.

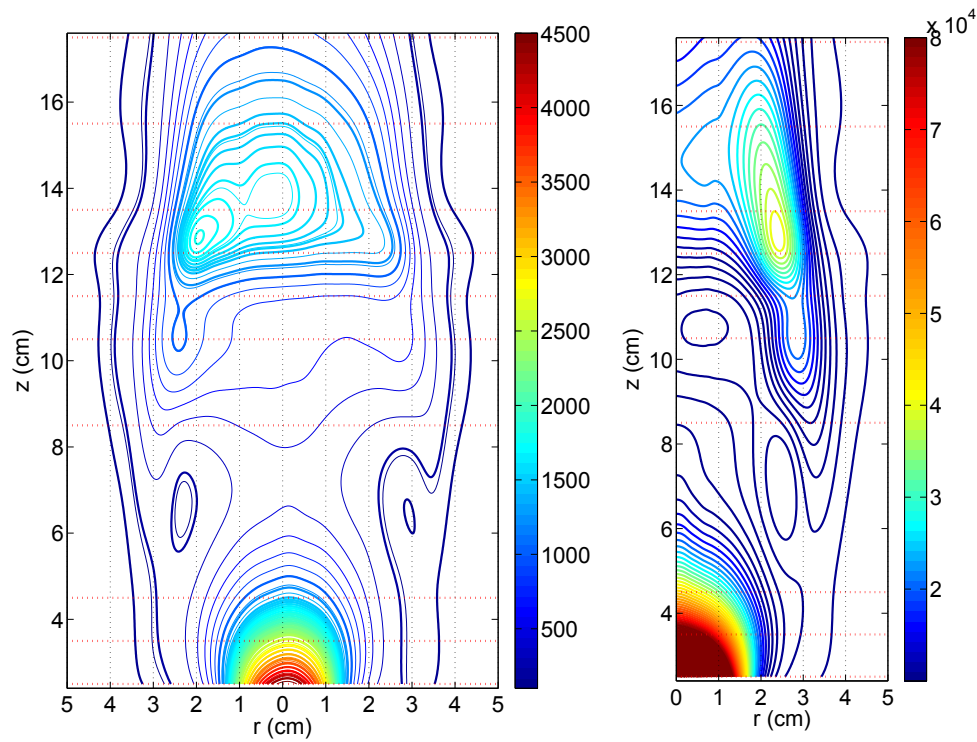


Figure 7.5.: *Case 1* ($p_b = 6$ mbar): Spectrally integrated radiance [$\text{W}\cdot\text{m}^{-2}\cdot\text{sr}^{-1}$] over [400-900] nm spectral range (left) and associated local emission [$\text{W}\cdot\text{m}^{-3}\cdot\text{sr}^{-1}$] (right).

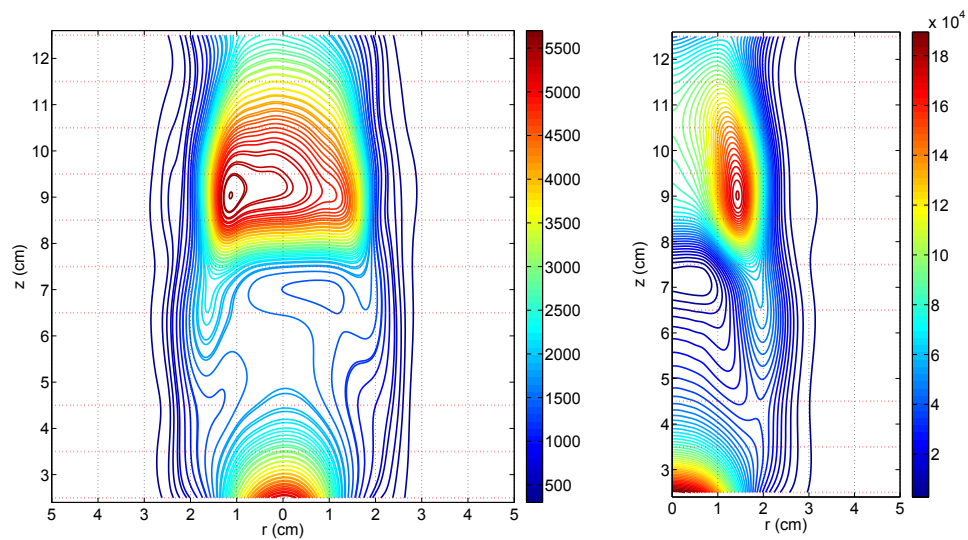


Figure 7.6.: *Case 2* ($p_b = 12$ mbar): Spectrally integrated radiance [$\text{W}\cdot\text{m}^{-2}\cdot\text{sr}^{-1}$] over [400-900] nm spectral range (left) and associated local emission [$\text{W}\cdot\text{m}^{-3}\cdot\text{sr}^{-1}$] (right).

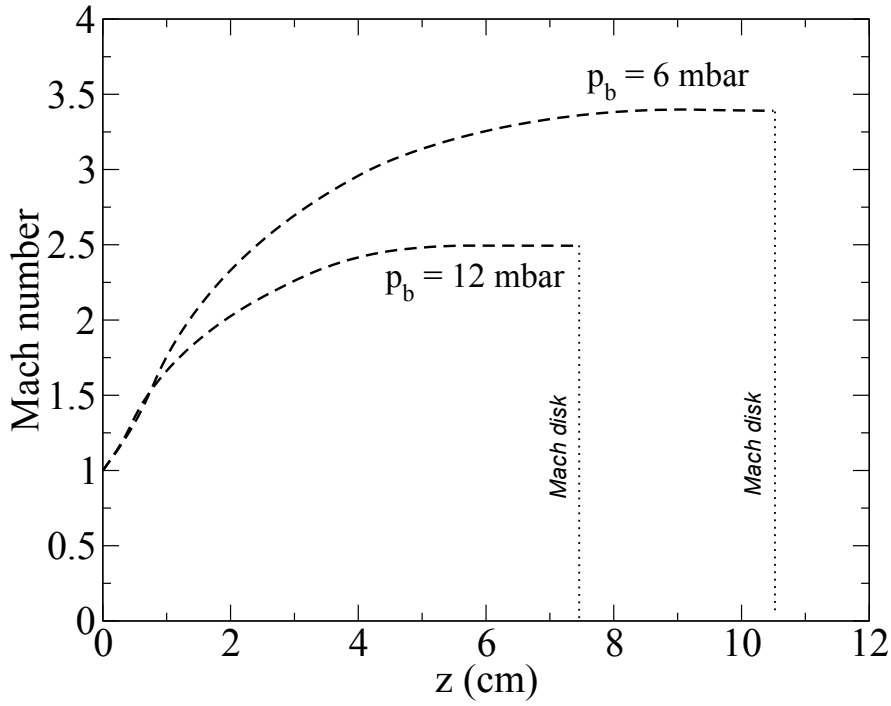


Figure 7.7.: Mach number axial profiles in the first expansion cell before the Mach disk.

Mach	1.0
p_{exit} [mbar]	63.0
ρ_{exit} [$\text{kg}\cdot\text{m}^{-3}$]	2.5×10^{-3}
T_{exit} [K]	8950

Table 7.2.: Nozzle exit computed parameters value.

nozzle exit conditions listed in table 7.2 are computed using the following relations:

$$p_{exit} = p_{res} \left(1 + \frac{\gamma - 1}{2} \times M_{exit}^2 \right)^{-\frac{\gamma}{\gamma - 1}} \quad (7.3)$$

$$\rho_{exit} = \frac{\dot{m}^2}{\gamma \times p_{exit} \times M_{exit}^2 \times A^2} \quad (7.4)$$

$$T_{exit} = \frac{p_{exit}}{\rho_{exit} \times R_g} \quad (7.5)$$

where $M_{exit} = 1$, R_g is the gas constant and A is the section of the jet. Following similar method, one dimensional computation is performed to rebuild axial expansion pressure and temperature profiles from the observed jet cross section. Results are displayed in figure 7.8. Equilibrium calculations of species concentration are presented in figure 7.9, using previous one dimensional calculations. Finally, the conditions downstream the shock are computed and reported in table 7.3.

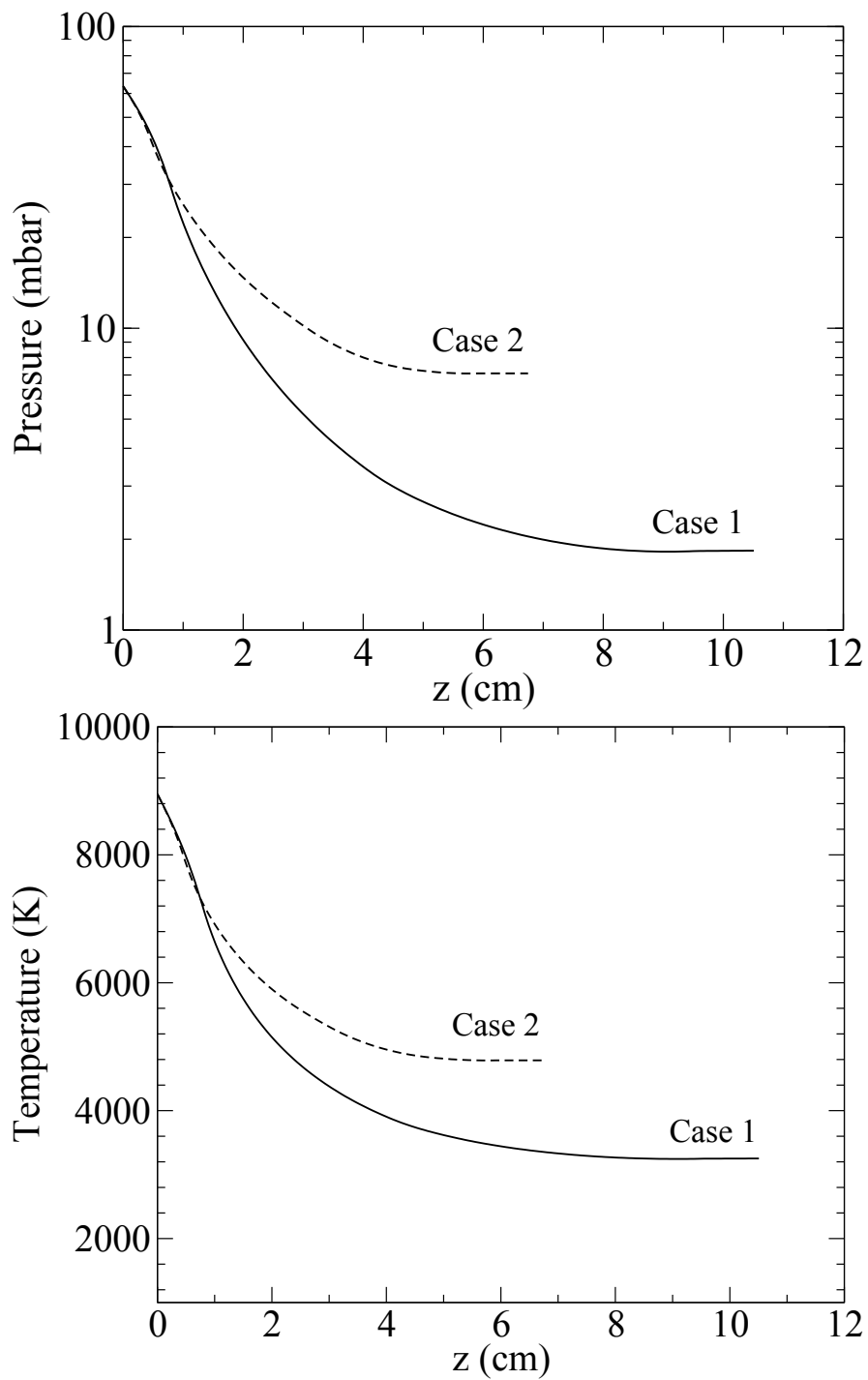


Figure 7.8.: Computed axial expansion pressure (top) and temperature (bottom) profiles.

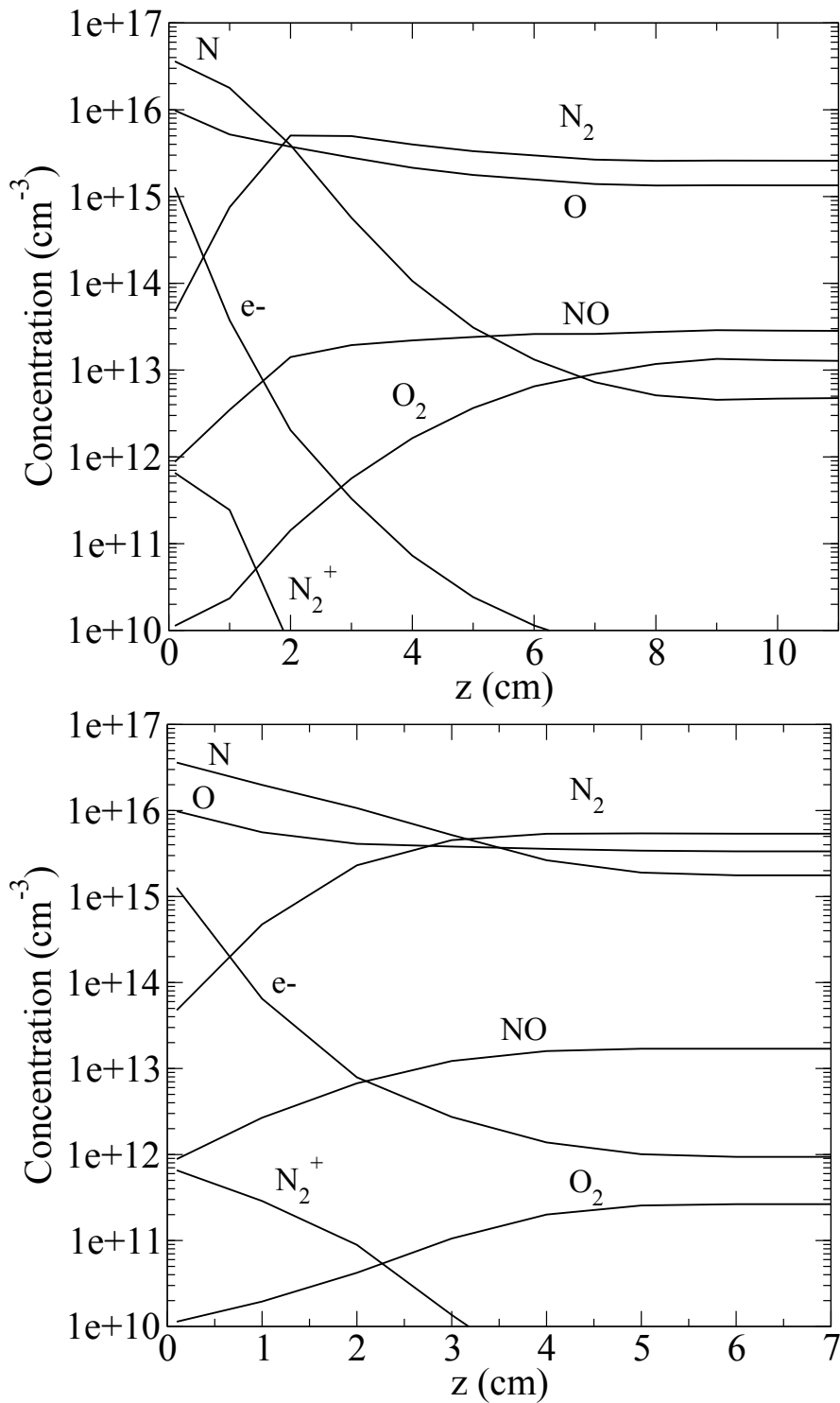


Figure 7.9.: LTE computation of species density profiles. Case 1 (top), case 2 (bottom).

Case 1		
Upstream	Downstream adiabatic normal shock	Downstream weakly ionized shock
$M_1 = 3.40$	$M_2 = 0.45$	
$p_1 = 1.8 \text{ mbar}$	$p_2 = 24.4 \text{ mbar}$	$p_2^i = 13.1 \text{ mbar}$
$T_1 = 3256 \text{ K}$	$T_2 = 10312 \text{ K}$	$T_2^i = 14366 \text{ K}$
$\rho_1 = 2.0 \times 10^{-4} \text{ kg.m}^{-3}$	$\rho_2 = 8.2 \times 10^{-4} \text{ kg.m}^{-3}$	$\rho_2^i = 3.2 \times 10^{-4} \text{ kg.m}^{-3}$
Case 2		
Upstream	Downstream adiabatic normal shock	Downstream weakly ionized shock
$M_1 = 2.50$	$M_2 = 0.51$	
$p_1 = 7.0 \text{ mbar}$	$p_2 = 50.3 \text{ mbar}$	$p_2^i = 28.7 \text{ mbar}$
$T_1 = 4786 \text{ K}$	$T_2 = 10202 \text{ K}$	$T_2^i = 12590 \text{ K}$
$\rho_1 = 5.0 \times 10^{-4} \text{ kg.m}^{-3}$	$\rho_2 = 1.7 \times 10^{-3} \text{ kg.m}^{-3}$	$\rho_2^i = 7.9 \times 10^{-4} \text{ kg.m}^{-3}$

Table 7.3.: Flow properties calculated across the shock for adiabatic normal shock front and weakly ionized shock.

7.1.3. Two dimensional thermodynamic characterization.

Based on bilinear interpolation, a microscopic description of two dimensional supersonic flow is proposed. It includes a thermal non-equilibrium description through the use of an electronic temperature T_{el} that differ from the temperature defined by $T_{rot} = T_{vib}$ which characterize the vibrational and rotational energy levels distribution. Rotational and vibrational temperatures are derived from classical spectra fitting of N_2^+ First Negative system considering thermal equilibrium assumption. As mentioned in chapter 5, this molecular system is overlapped with N_2 2nd Positive. The fitting is therefore performed using the contribution of N_2 2nd Positive and N_2^+ First Negative systems. No CN contamination are depicted. As illustrated in figure 7.10, the presence of atomic lines, not accounted in the computed spectra prevent from using the entire spectral range to perform the fitting. For this purpose, when required, several spectral ranges are excluded from the RMSE calculation (in particular, the atomic lines between 380 and 400 nm). Spectra fitting results are presented in figure 7.11. The good agreement between experimental and synthetic spectra (with a correlation coefficient above 0.9) confirms the thermal equilibrium state. The high spectral resolution reached through the use of a 1200 grooves/mm grating allows to capture the Stark broadening of H_β hydrogen line. The benefit of using highly resolved optical bench to capture H_β line broadening is illustrated at the top of figure 7.12. At the bottom of figure 7.12, despite weak atomic contamination, a good agreement between experimental and computed H_β line shape is observed. Density lower than $1.10 \times 10^{14} \text{ cm}^{-3}$ are not measured with respect to the available tabulated data of H_β spectral line shape in reference [75]. Because of the low spectral resolution, several atomic lines are merged together and few lines are relevant for diagnostics. However, we take benefit of the large energy range of the upper atomic states of several oxygen lines to evaluate the plasma electronic temperature. Oxygen atomic transitions accounted in this study are listed in table 7.4. Atomic oxygen lines taken into account can be classified into three groups of transitions which electronic configuration and electron coupling term are recalled in table 7.5. *Group I* contains lines which upper energy level is below 90000 cm^{-1} . *Group II* is characterized by upper energy level E_u ranging from 98000 to 107000 cm^{-1} . *Group III* contains the line located at 715.67 nm with an upper energy level $E_u = 116631.094 \text{ cm}^{-1}$ above the first ionization energy $E_i = 109837.02 \text{ cm}^{-1}$.

Typical Boltzmann diagram plots in expansion and compression regions, presented in figure 7.13, show that excited state population densities are slightly scattered and fairly distributed along a straight line. However the entire atomic energy distribution scheme shows that the distribution might deviate significantly from a strict Boltzmann distribution. In particular the population of the highest upper energy levels, located beyond the first ionization energy, was found to be systematically slightly underpopulated. This underpopulation is amplified behind

$\lambda_{air}(nm)$	$A_{ul}(s^{-1})$	$E_l(cm^{-1})$	$E_u(cm^{-1})$	g_l	g_u
O lines		$D_e = 109837.02cm^{-1}$			
394.7295	4.9110 ⁵	73768.200	99094.837	5	7
394.7481	4.8810 ⁵	73768.200	99093.641	5	5
394.7586	4.8710 ⁵	73768.200	99092.968	5	3
436.8258	7.5810 ⁵	76794.978	99680.968	3	3
436.8193	7.5610 ⁵	76794.978	99681.309	3	1
436.8242	7.5910 ⁵	76794.978	99681.049	3	5
501.8782	4.2810 ⁵	86 625.757	106 545.354	3	5
501.9291	7.1310 ⁵	86 627.778	106 545.354	5	5
543.5178	7.74 10 ⁵	86625.757	105019.307	3	5
543.5775	1.29 10 ⁶	86627.778	105019.307	5	5
543.6862	1.80 10 ⁶	86631.454	105019.307	7	5
595.8386	6.80 10 ⁵	88630.587	105409.008	3	5
595.8386	3.78 10 ⁵	88630.587	105409.008	3	3
595.8584	2.27 10 ⁵	88631.146	105409.008	5	5
595.8584	2.52 10 ⁴	88631.146	105409.008	5	3
595.8584	9.06 10 ⁵	88631.146	105409.008	5	7
604.6233	1.05 10 ⁶	88630.587	105165.232	3	3
604.6438	1.75 10 ⁶	88631.146	105165.232	5	3
604.6495	3.50 10 ⁶	88631.303	105165.232	1	3
615.5971	5.72 10 ⁶	86625.757	102865.655	3	3
615.6778	5.08 10 ⁶	86627.778	102865.547	5	7
615.8187	7.62 10 ⁶	86631.454	102865.506	7	9
645.360	1.6510 ⁶	86625.757	102116.698	3	5
645.444	2.7510 ⁶	86627.778	102116.698	5	5
645.598	3.8510 ⁶	86631.454	102116.698	7	5
700.1899	1.4710 ⁶	88630.587	102908.489	3	3
700.1922	2.6510 ⁶	88630.587	102908.443	3	5
700.2173	9.8310 ⁴	88631.146	102908.489	5	3
700.2196	8.8310 ⁵	88631.146	102908.443	5	5
700.2230	3.5310 ⁶	88631.146	102908.374	5	7
700.2250	1.9610 ⁶	88631.303	102908.489	1	3
715.670	5.0510 ⁷	102662.026	116631.094	5	5
725.4154	2.2410 ⁶	88630.587	102411.995	3	3
725.4448	3.7310 ⁶	88631.146	102411.995	5	3
725.4531	7.4510 ⁵	88631.303	102411.995	1	3
777.1944	3.69 10 ⁷	73768.200	86631.454	5	7
777.4166	3.69 10 ⁷	73768.200	86627.778	5	5
777.5388	3.69 10 ⁷	73768.200	86625.757	5	3
844.6247	3.22 10 ⁷	76794.978	88631.303	3	1
844.6359	3.22 10 ⁷	76794.978	88631.146	3	5
844.6758	3.22 10 ⁷	76794.978	88630.587	3	3

Table 7.4.: Spectroscopic data of the considered O emission lines taken from [10].

Label	Lower level electronic configuration	Upper level electronic configuration	Energy range (cm-1)
Group I	2s ² 2p ³ (⁴ S ⁰) 3s	2s ² 2p ³ (⁴ S ⁰) 3p	< 90000
Group II	2s ² 2p ³ (⁴ S ⁰) 3p	2s ² 2p ³ (⁴ S ⁰) 5s/4d/6s/5d/7s	98000 to 107000
Group III	2s ² 2p ³ (² D ⁰) 3s	2s ² 2p ³ (² D ⁰) 3p	116631

Table 7.5.: Electron configuration and level identification associated to oxygen transitions.

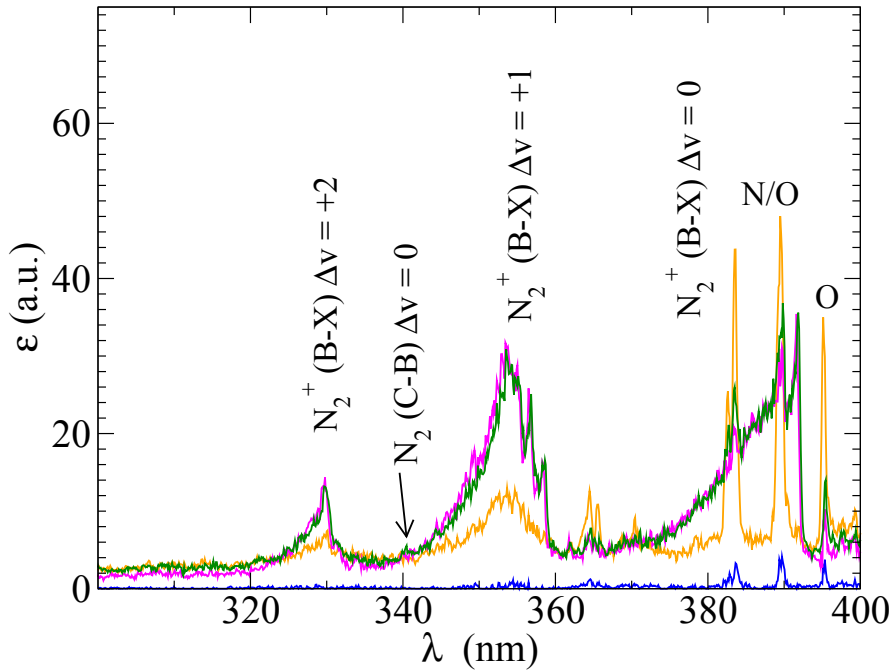


Figure 7.10.: *Case 2* spectral emission at various axial locations on the symmetry axis [2.5 cm (orange), 6.5 cm (blue), 8.5 cm (pink) and 11.5 cm (green)].

the Mach disk. The determination of the electronic temperature is therefore performed with the exclusion of the line at 715 nm. In regions with low intensity level, the temperature reliability is affected by the decrease of the signal to noise ratio and the vanishing of lines with higher upper energy level. Despite such detrimental situation, the temperature estimation is found to be sufficiently reliable because of the large energy range over which the linear regression is performed. Radial distribution of plasma properties are processed using bi-cubic spline interpolation yielding to a two dimensional distribution description of the jet. Mappings are presented in figures 7.14 and 7.15 for the *case 1* and *2* respectively. The scattered data used for the interpolation are symbolized by black circles. Large spatial steps in the axial direction prevent from accurate interpolation in the low density, in the region before the shock in particular. Although such inconvenience exists, the distribution remain fully reliable in regions where measurements are performed. Although affected by low level of emission in the central regions (consecutive to the pressure drop), resulting mappings provide valuable information to assess 2D plasma flow computations. The detailed analysis of the measured quantities provide a qualitative description of the jet structure. The topology of under-expanded plasma jet match pretty well with the mappings, in particular the reflected shock and the expansion are well depicted by the iso-contours. In the expansion region, measured electron density variation suggests that the adiabatic expansion model can be used to describe faithfully the plasma expansion (figure 7.16). Therefore, we can state that the recombination or ionization can be neglected in comparison with the density change due to expansion. In table 7.6, the parameters n_0 and z_0 corresponding to the best fit among an adiabatic profile are reported together with the corresponding plots displayed in figure 7.16. For both *cases 1* and *2*, the parameters n_0 is of the order of 10^{15} cm^{-3} with a virtual point source z_0 close to the nozzle exit. A difference between temperature obtained through molecular fitting approach and electronic temperature is observed, specially when electronic population densities are largely scattered around the linear

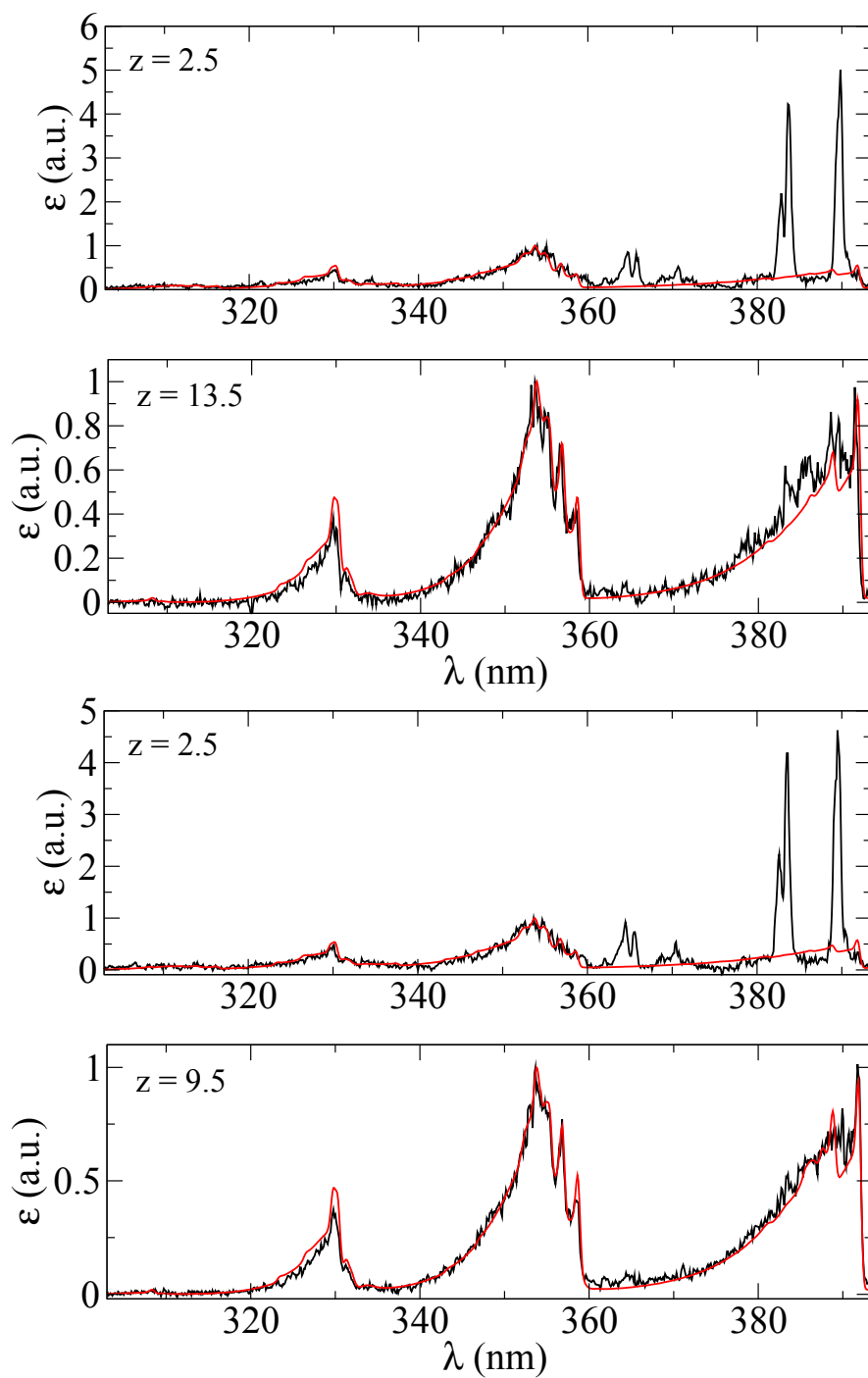


Figure 7.11.: Best fit (red) and experimental spectra (black) at various axial locations on the symmetry axis. *case 1* (top), *case 2* (bottom)

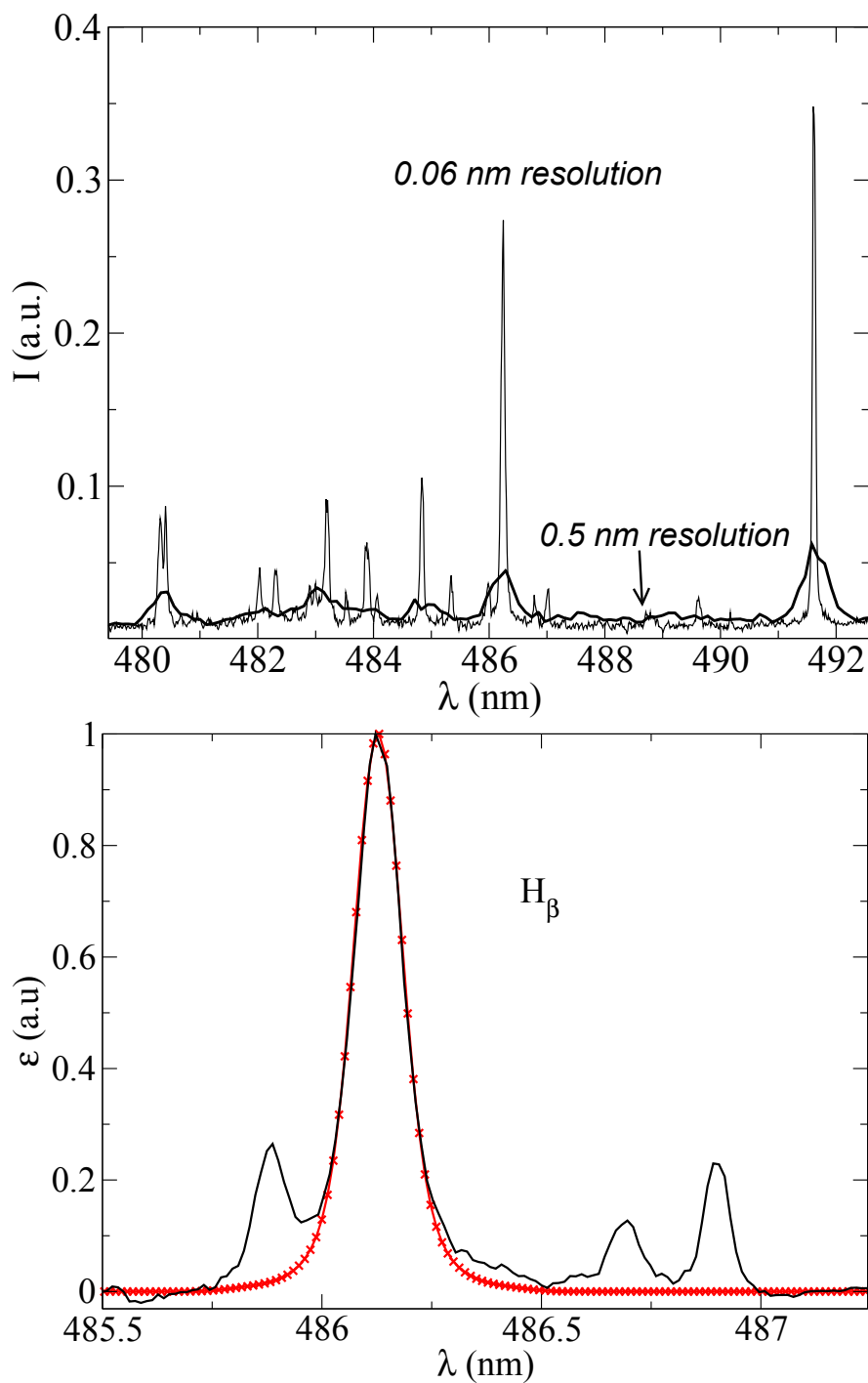


Figure 7.12.: Top: Calibrated spectra at 0.06 nm and 0.5 nm spectral resolution. Bottom: Typical best fit (red) and experimental H_β line

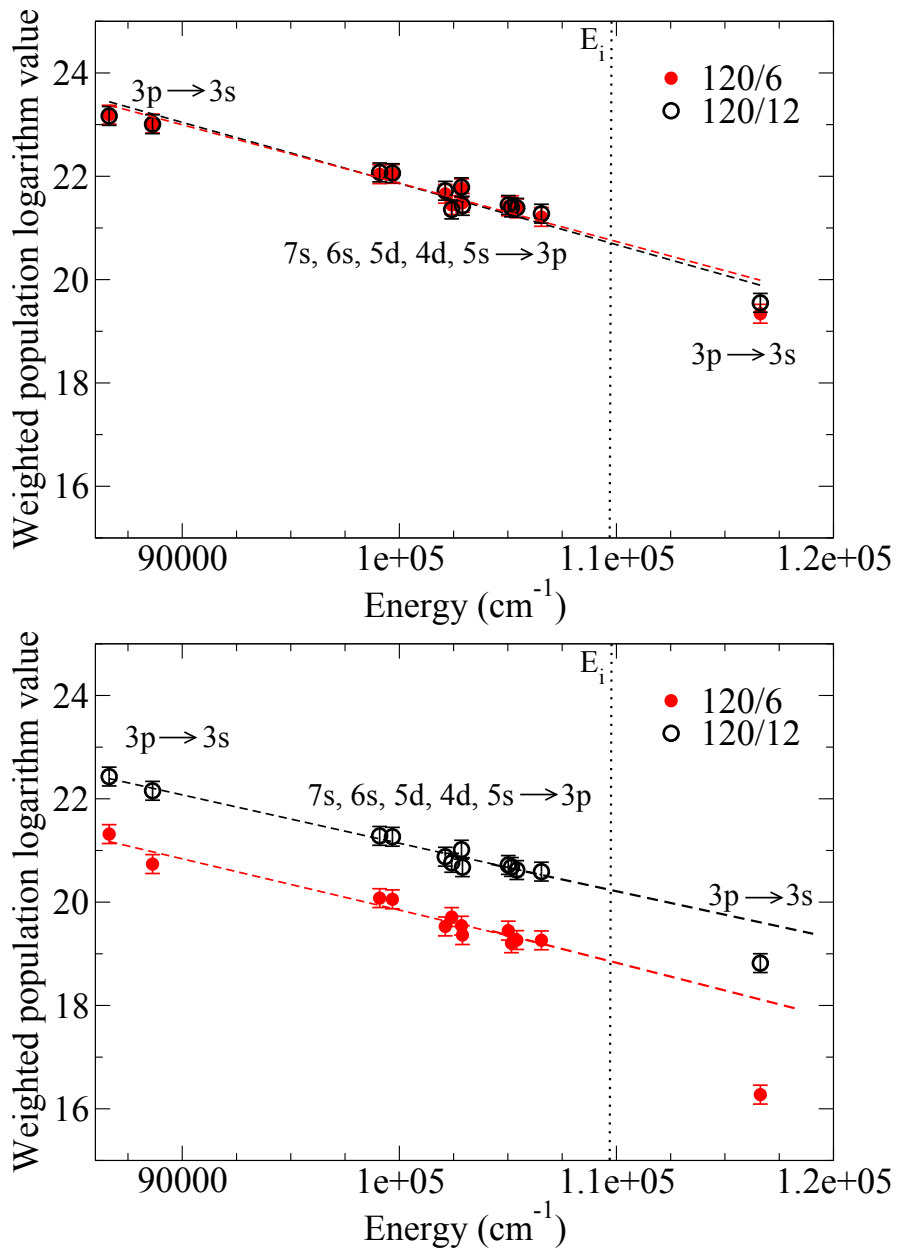


Figure 7.13.: Typical Boltzmann plot at $z = 2.5$, $r = 1.0$ cm (top) and $z = 12.5$, $r = 2.0$ cm (bottom).

Adiabatic expansion	
Case 1 $n_0 = 1.4 \times 10^{15} \text{ cm}^{-3}$ $z_0 = 1.7$ cm	Case 2 $n_0 = 6.3 \times 10^{15} \text{ cm}^{-3}$ $z_0 = 0.7$ cm
Mott-Smith shock profile thickness	
Case 1 $L = 0.9$ cm	Case 2 $L = 1.1$ cm

Table 7.6.: Analytical profiles parameters.

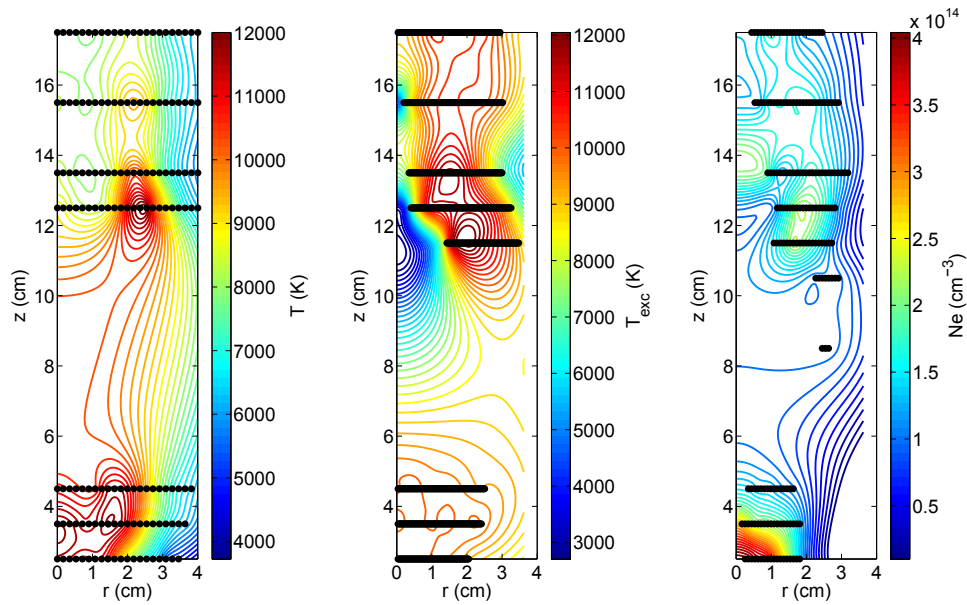


Figure 7.14.: *Case 1* ($p_b = 6$ mbar): Interpolated temperatures and electron density iso-contours.

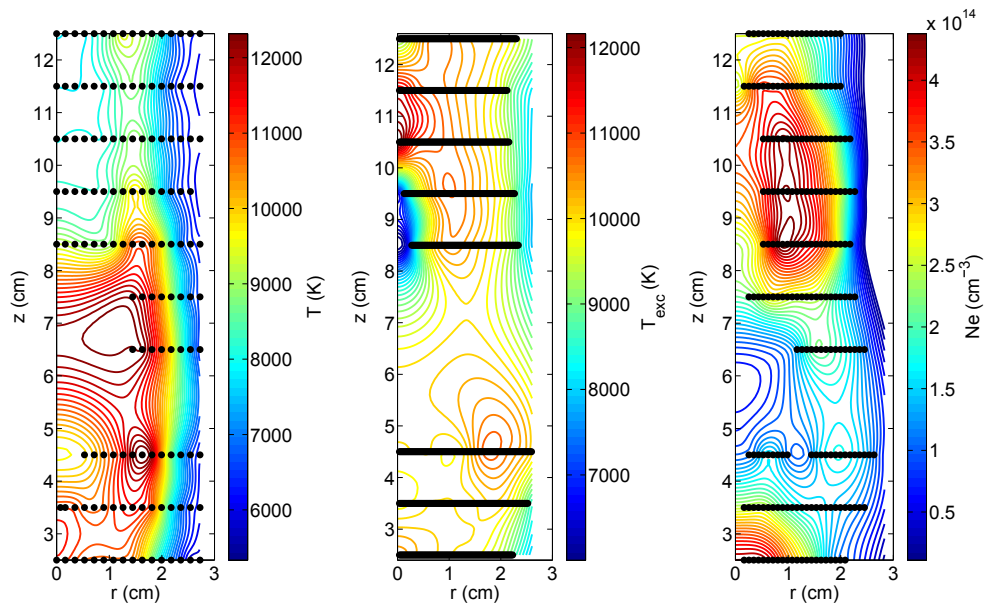


Figure 7.15.: *Case 2* ($p_b = 12$ mbar): Interpolated temperatures and electron density isocontours.

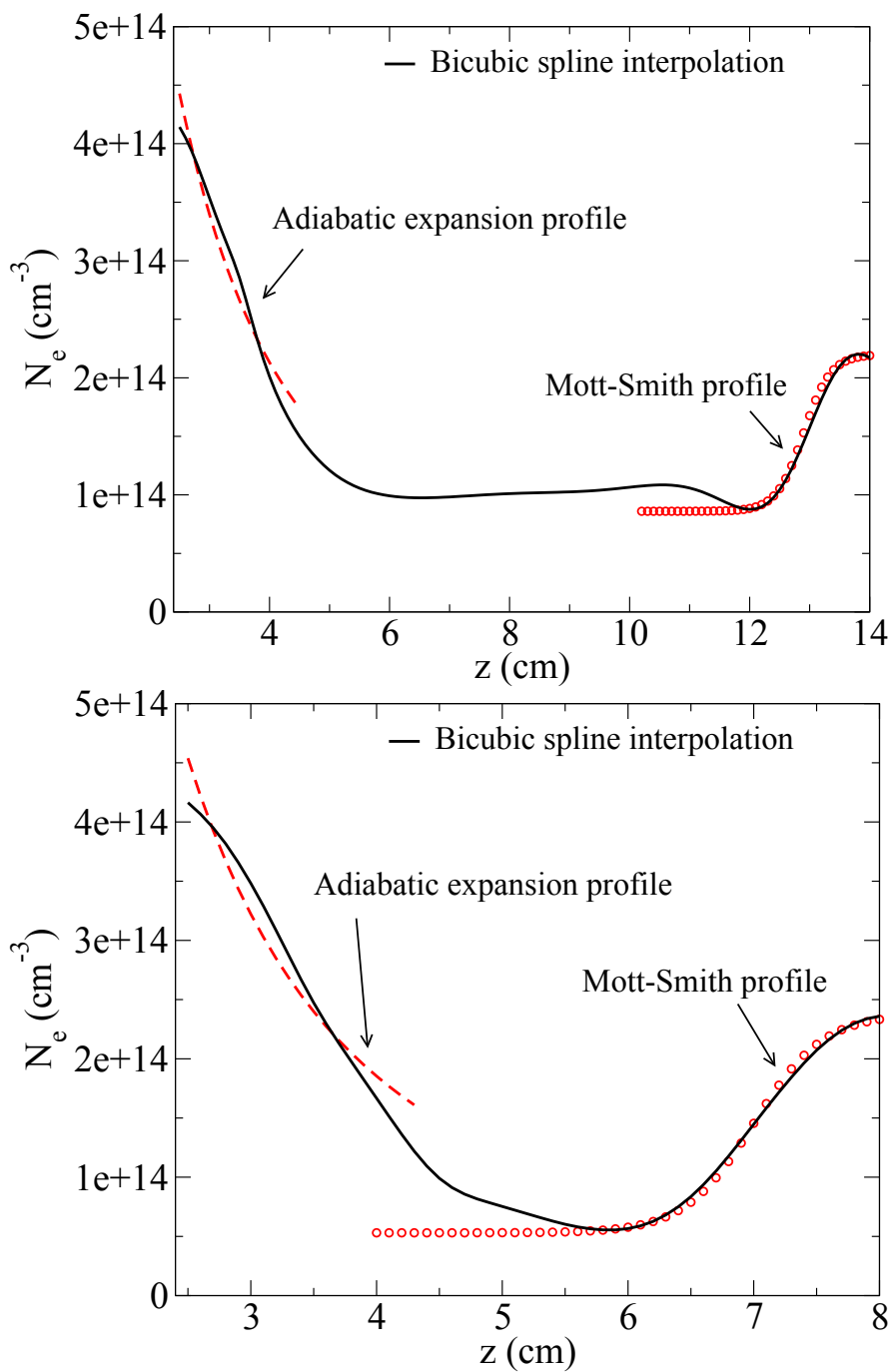


Figure 7.16.: Electron density interpolated profile on the symmetry axis (black). Analytical expansion and shock profiles (red). Case 1 $p_b = 6$ mbar (top), Case 2 $p_b = 12$ mbar (bottom).

regression, giving rise to larger uncertainties on the electronic temperature. In this case, the use of a linear regression by parts applied to the energy distribution scheme helps to identify the behavior of the atomic excited states distribution. However, because spectroscopy was only applied in the visible spectral range for atomic transitions, we miss some information on the population of lower energy state that could have been measured in the infra-red domain.

7.2. Microwave sustained nitrogen post discharge

The WMD is operated in supersonic regime with nitrogen gas. The quartz tube is inserted into a vacuum chamber and is ended with a convergent-divergent nozzle described in chapter 2. A set of mirrors enables to radially record the jet emission through a periscope-like arrangement as the jet exits vertically. The power generator is operated so that the forwarded power is about 1 kW and the impedance matching is set to ensure less than 5 % reflected power. Swirl injection is maintained at constant mass flow rate of 1 g/s controlled by a rotameter. Supersonic plasma regimes are obtained by expanding the plasma through a convergent-divergent nozzle of 6.94 mm exit diameter. The pressure in the reservoir P_0 is maintained at 410 mbar and the back pressure P_b in the chamber is arbitrary set either to 35 mbar (under-expanded), 45 mbar (quasi perfectly expanded) or 90 mbar (over-expanded) as illustrated in the pictures of section 2.3. At several axial positions, the line of sight plasma jet emission is collected through an aperture and then focused with a fused silica lens onto the entry of a Acton Series monochromator of 75 cm focal lengths. The spectrometer is combined with a ICCD PI-MAX camera with a frame of 1024×1024 pixels of $12.8 \mu\text{m}$ side. Emission issued from the jet is spatially resolved in the radial direction. A radial slice of about 16 mm height was optically conjugated using a 200 mm focal lens onto an image with a magnification factor of 0.8. It allows to capture the whole radial profile of the jet onto the CCD screen of the camera with a spatial resolution of about 16 microns. The same optical arrangement is used to record spectra emission in the reservoir. In the reservoir, only line of sight measurements is performed. We focus our investigation on the visible spectral domain that includes mainly the contribution of N_2^+ First negative system in the reservoir and the contribution of N_2 First positive system in the jet. Plasma emission is recorded using a 150 grooves/mm grating and the entrance slit of the monochromator is set to $18 \mu\text{m}$ in order to get sufficient light intensity. The measured spectral resolution is 1.7 nm. The plasma is assumed to be optically thin and proper Abel inversion is applied on measured spectra along the supersonic jet. Resulting spectra are shown in figure 7.17 for various axial positions. From this figure, it comes that spectra changes result mostly from a density change (indeed scaled spectra are overlapped). The chemistry is frozen and is not influenced by compression and expansion zones which only affect the magnitude of the emission. For this purpose, thermodynamic characterization will be executed at only one location for the over-expanded case.

We evaluate the nozzle exit properties assuming ideal gas and using isentropic relations. The Mach number is straightly related to the cross section area of the nozzle exit and the pressure exit is derived from isentropic expression. Nozzle exit conditions are listed in expressions 7.7 and 7.8. These results are in agreement with what is found experimentally: Below (resp. above) 41 mbar, the jet is under-expanded (resp. over-expanded) and the perfect expansion occur around 41 mbar. The reactivity in the nozzle does not strongly affect the aerodynamic regime in the expansion region.

$$A_{exit} = 1.926 \times A^* \quad (7.6)$$

$$\text{which gives } M_{exit} = 2.1 \quad (7.7)$$

$$\text{and } p_{exit} = 41\text{mbar} \quad (7.8)$$

7.2.1. Reservoir thermal equilibrium state.

In the reservoir, the thermodynamic state is assessed through line of sight records at the center of the jet. The thermal equilibrium is assessed through molecular fitting of N_2^+ First negative system, accounting for the vibrational bands $\Delta v = -1, 0$ and $+1$ in order to get high sensitivity.

Vibrational non-equilibrium fitting is performed so that the RMSE is determined through six parameters: $T_{rot.}$, $[N_{nv=0}]$, $[N_{nv=1}]$, $[N_{nv=2}]$, $[N_{nv=3}]$, $[N_{nv=4}]$. The vibrational levels are chosen so that their contributions are significant at equilibrium as illustrated at the top of figure 7.18. Convergence is reached when the vibrational population is following a Boltzmann distri-

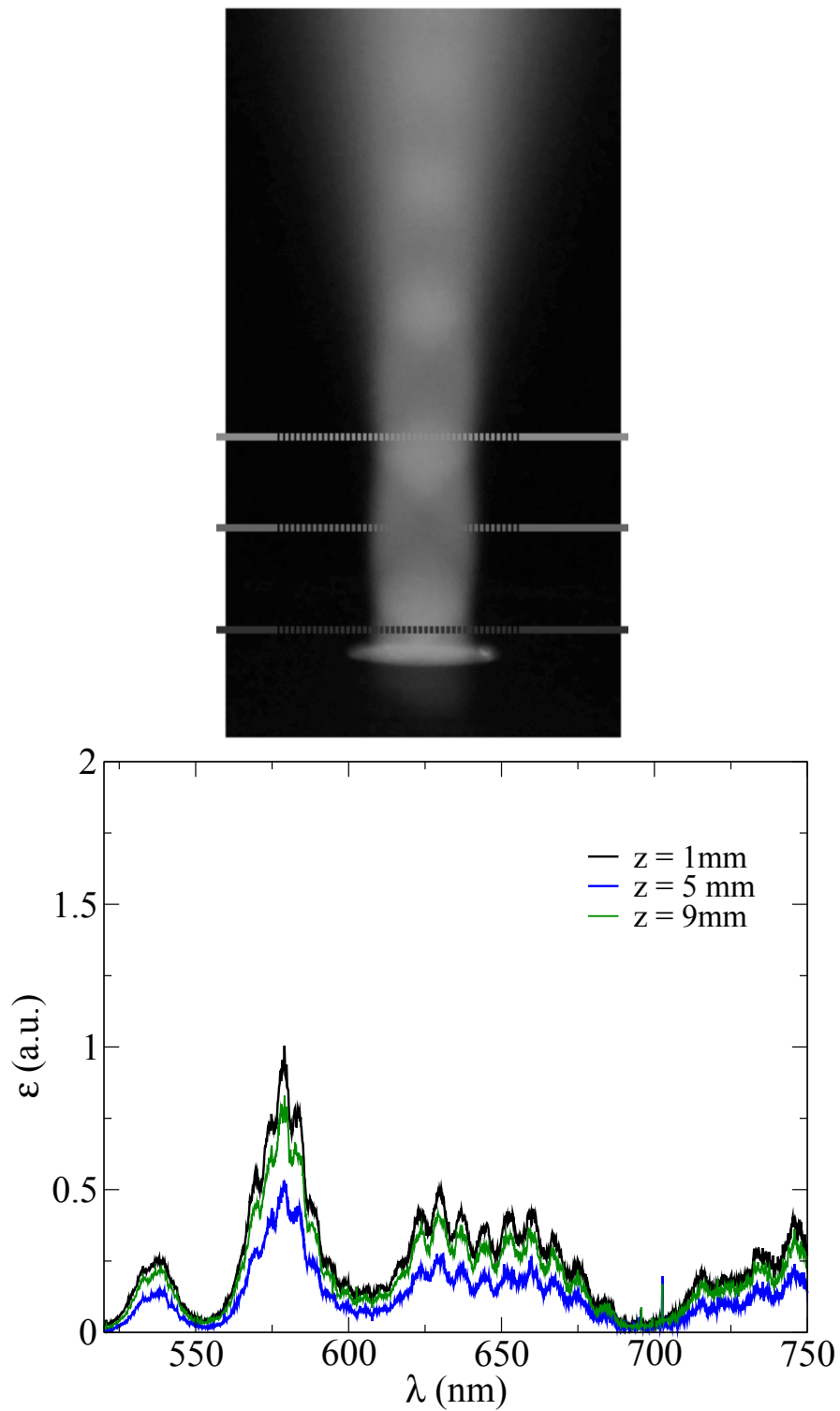


Figure 7.17.: Top: Over-expanded jet. Bottom: N₂ First Positive spectra along the axis of the over-expanded jet.

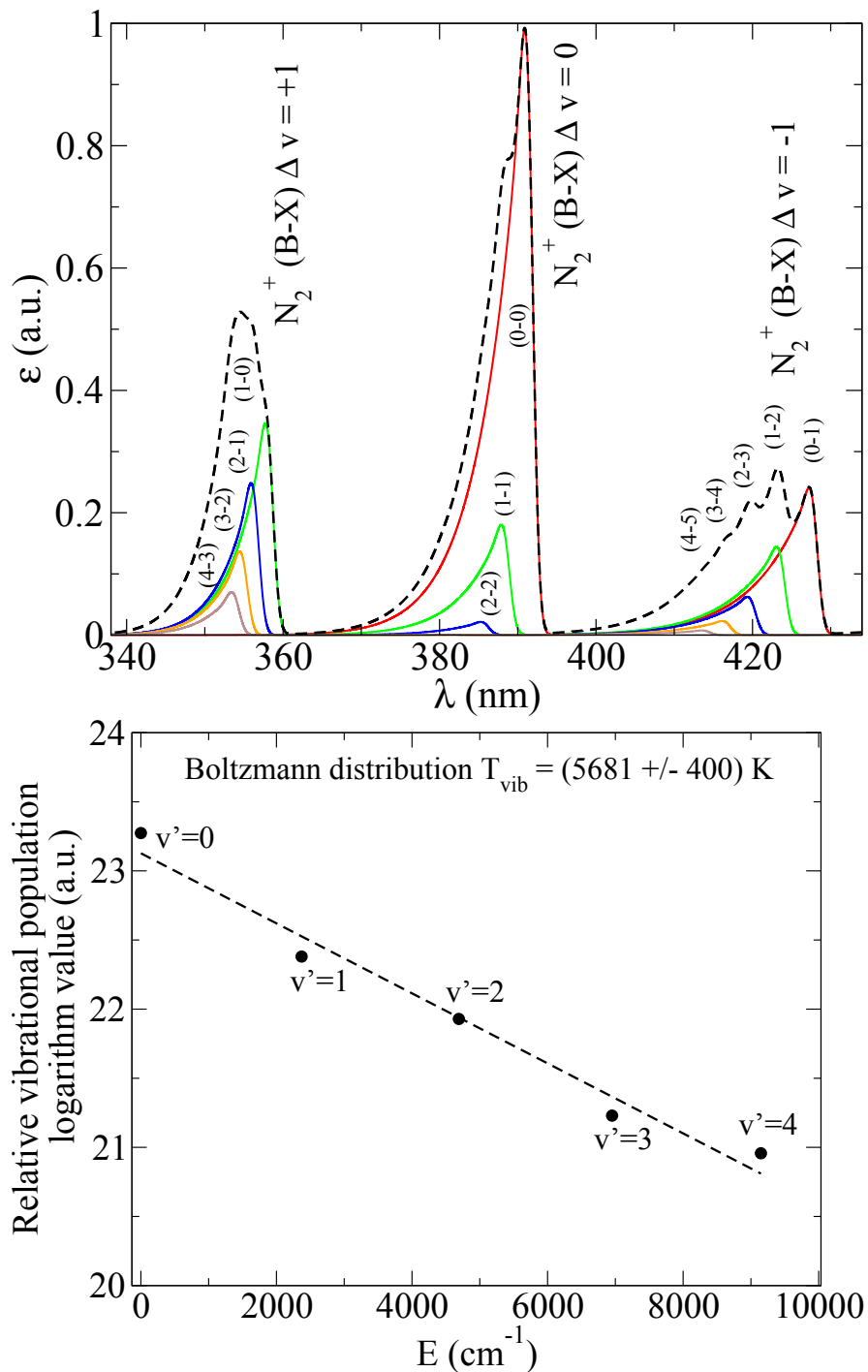


Figure 7.18.: Vibrational equilibrium synthetic spectrum and corresponding vibrational bands contribution (top). Measured vibrational distribution (bottom).

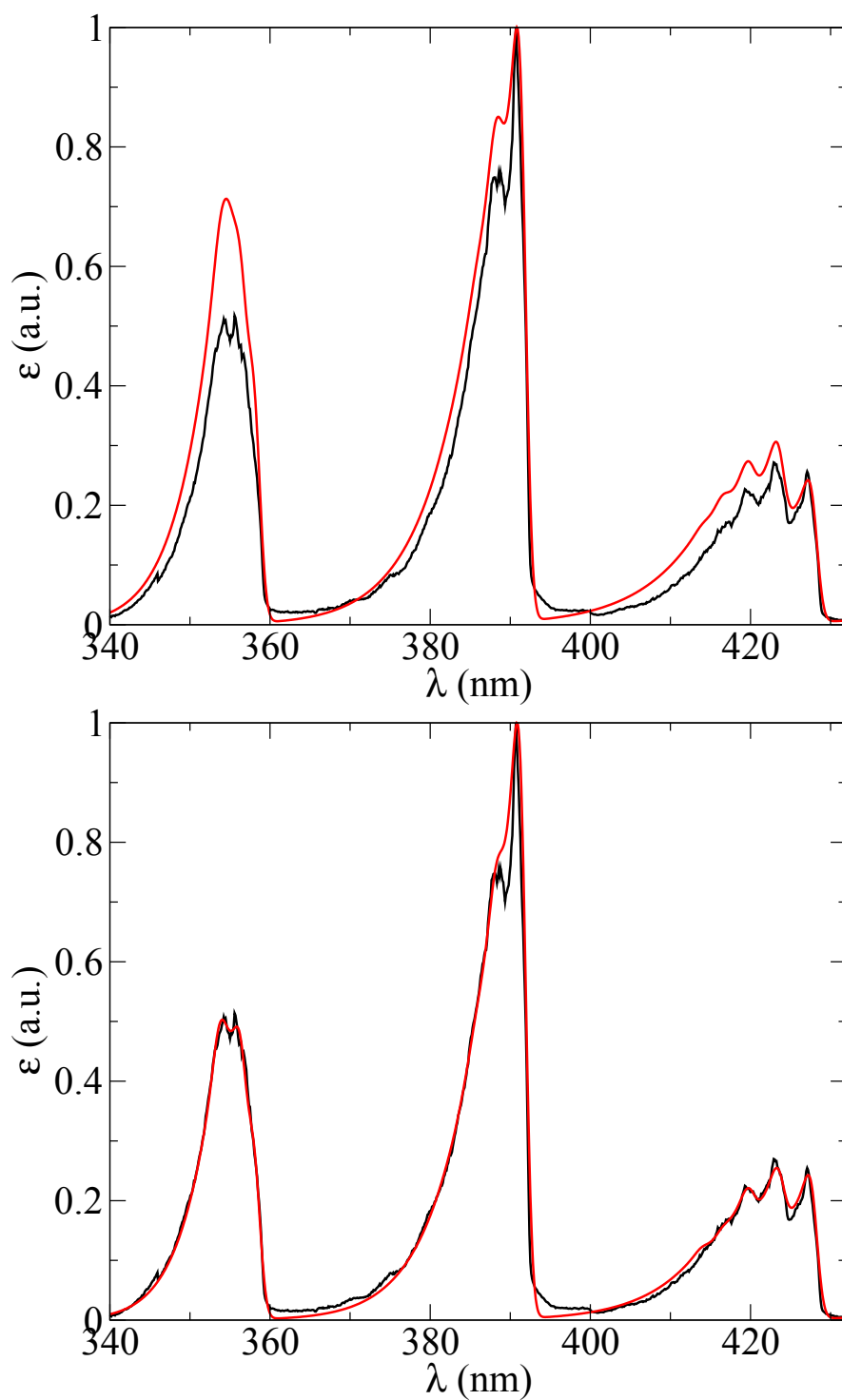


Figure 7.19.: Top: Initial fitting condition at $T_{rot.} = T_{vib.} = 6000$ K (right). Bottom: Best fit obtained for $T_{rot.} = 5354$ K and $T_{vib.} = 5681$ K

Operating conditions	1.0 g.s ⁻¹ mass flow rate reservoir pressure p ₀ = 410 mbar 1 kW absorbed RF power 6.94 mm nozzle exit Back pressure in the chamber: - Under-expanded case = 35 mbar - Perfectly expanded case ≈ 45 mbar - Over-expanded case = 90 mbar
Spectroscopic features	Acton Series monochromator (75 cm focal length) 1.7 nm spectral resolution Radially resolved measurements (≈ 16 μm resolution)
Radiative transitions of interest	N ₂ ⁺ (B ² Σ _u ⁺ → X ² Σ _g ⁺) 1st Negative System N ₂ (B ³ Π _g → A ³ Σ _u ⁺) 1st Positive System

Table 7.7.: Characteristics of supersonic microwave nitrogen plasma jet experiment.

bution described by a temperature $T_{vib.} = 5681$ K and the rotational temperature $T_{rot.}$ is 5354 K. At the bottom of figure 7.18, the vibrational distribution is displayed together with the linear regression. Synthetic spectra (red) and experimental spectra (black) are displayed in figure 7.19 for the initial fitting conditions and the final iteration conditions. The good agreement between rotational and vibrational temperature validate the thermal equilibrium assumption.

7.2.2. Post discharge frozen non-equilibrium state.

In the jet, vibrational non-equilibrium fitting is performed to account for strong vibrational non-equilibrium. Additionally to a rotational temperature, vibrational levels are accounted in the fitting procedure. Given a non-equilibrium distribution, it is difficult to estimate the number of vibrational levels needed to reproduce the spectrum. Accounting for a large number of vibrational states can lead to low residual between experimental and calculated spectra but high lying levels population density value can become meaningless. Furthermore, giving the spectral resolution of our experiment (1.7 nm), all vibrational band are not well separated and the overlapping between different vibrational contributions leads to uncertainties on the vibrational distribution obtained through the fitting. Vibrational levels selection is based on the calculation of vibrational bands contribution at equilibrium. In order to reproduce N₂ First Positive spectrum at LTE between 520 nm and 750 nm, six levels ($v'=2$ to 7) are required at 2000 K whereas twelve levels ($v'=2$ to 13) should be accounted at 5000 K as illustrated in figure 7.20. The contribution of the first two vibrational levels ($v'=0$ and $v'=1$) is very weak and can be neglected for equilibrium spectra computation within the [420-750] nm spectral window. As expected, the contribution of high-lying levels decreases with decreasing the rotational temperature. Non-equilibrium fitting is performed by accounting twelve levels ($v'=2$ to 13), starting with a Boltzmann distribution at 4000 K (figure 7.21). In figures 7.22 and 7.23, intermediate steps of the fitting are displayed.

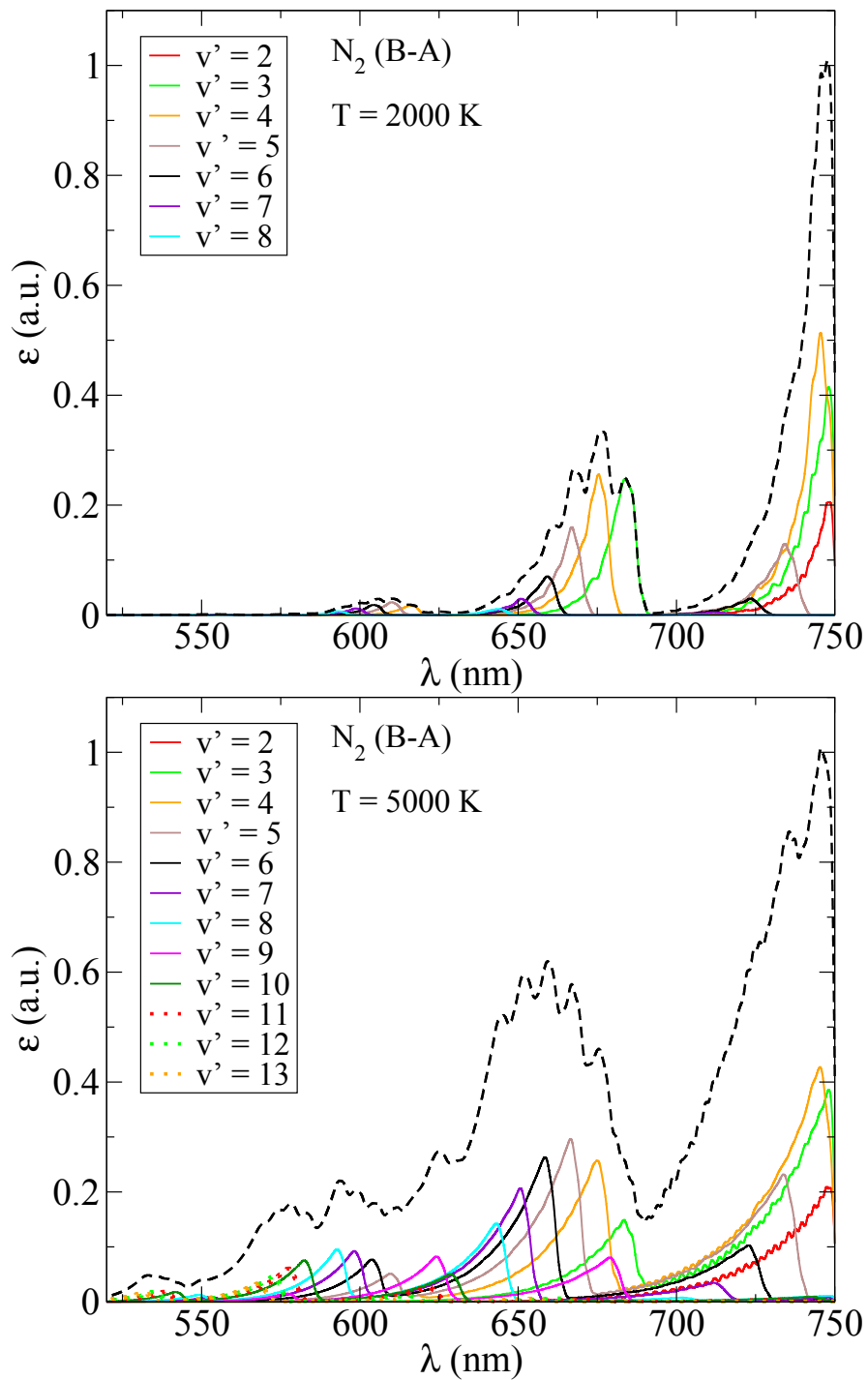


Figure 7.20.: Equilibrium synthetic spectrum (black) and corresponding vibrational bands contribution at 2000 K (top) and 5000 K (bottom).

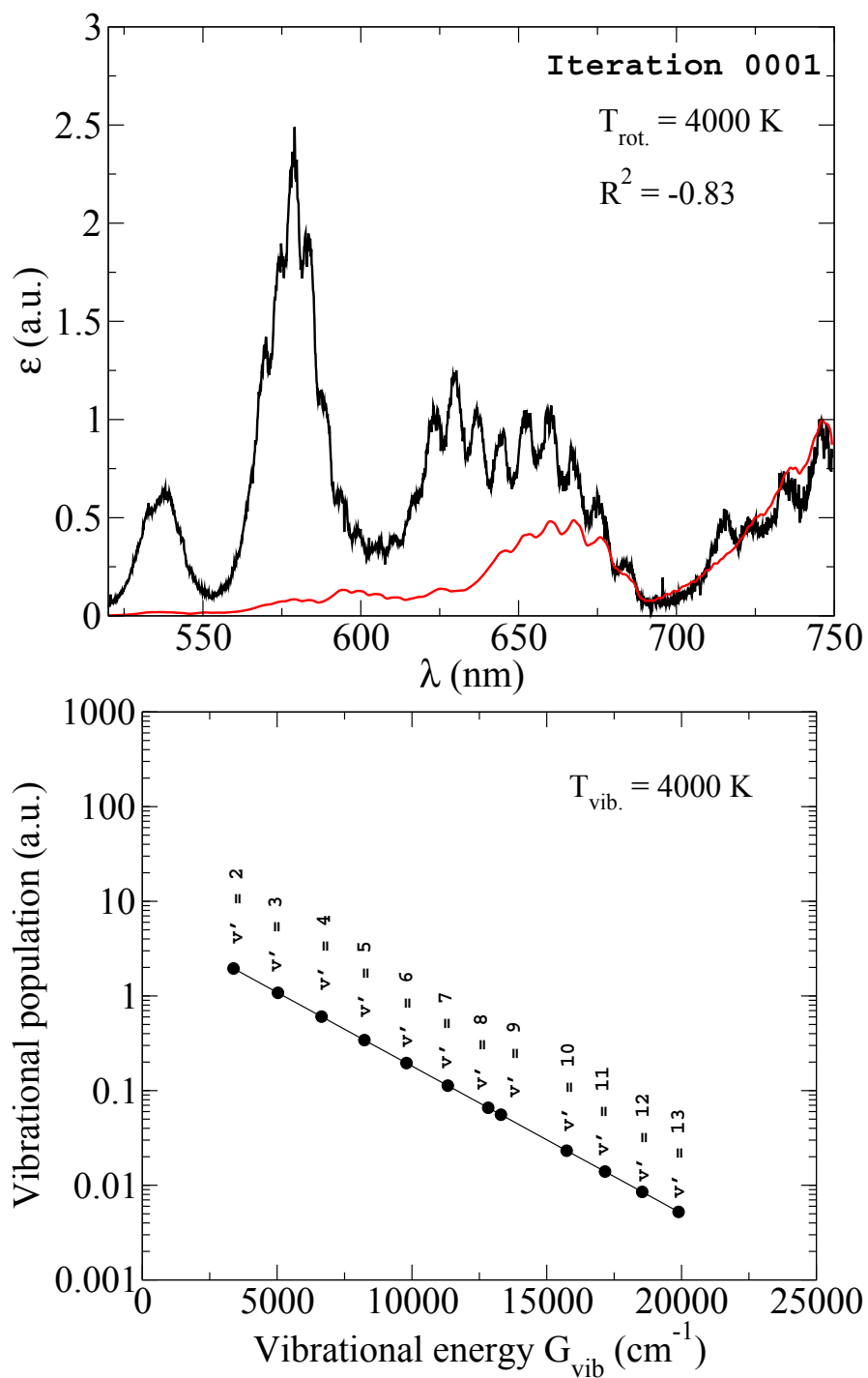


Figure 7.21.: Spectra fitting initial conditions. Top: Measured spectrum (black) and synthetic spectrum (red). Bottom: Synthetic vibrational population distribution.

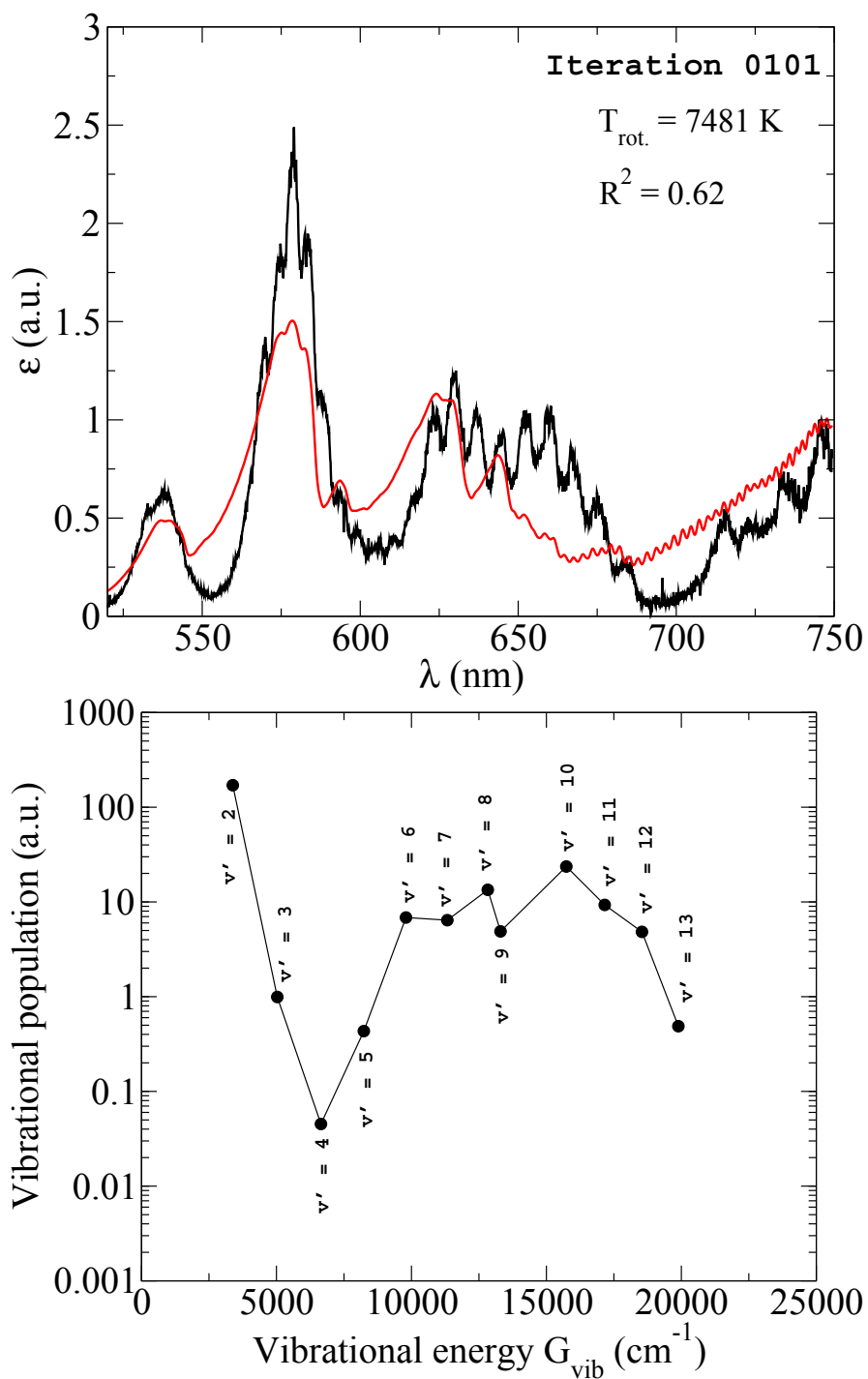


Figure 7.22.: Spectra fitting iteration 101. Top: Measured spectrum (black) and synthetic spectrum (red). Bottom: Synthetic vibrational population distribution.

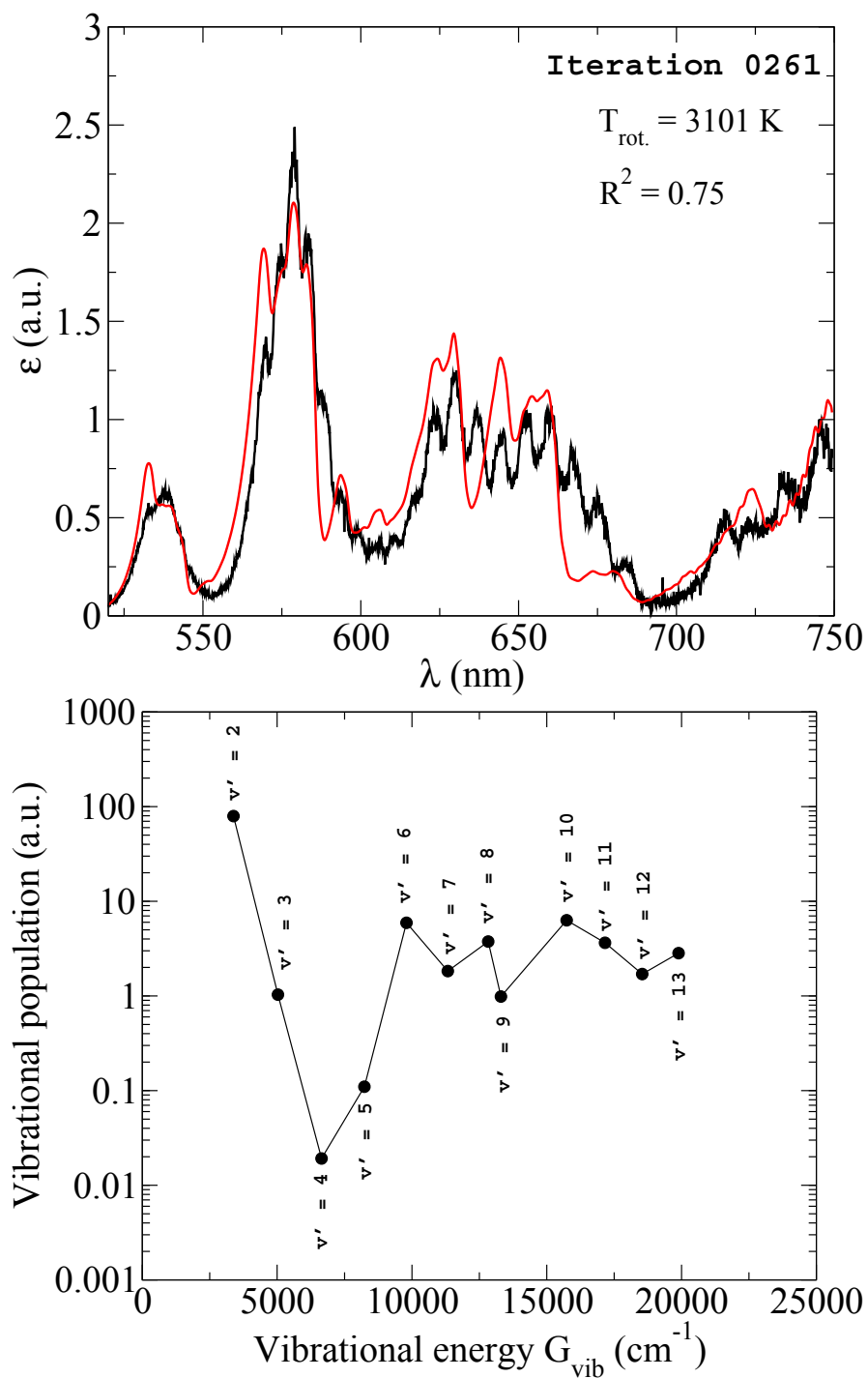


Figure 7.23.: Spectra fitting iteration 261. Top: Measured spectrum (black) and synthetic spectrum (red). Bottom: Synthetic vibrational population distribution.

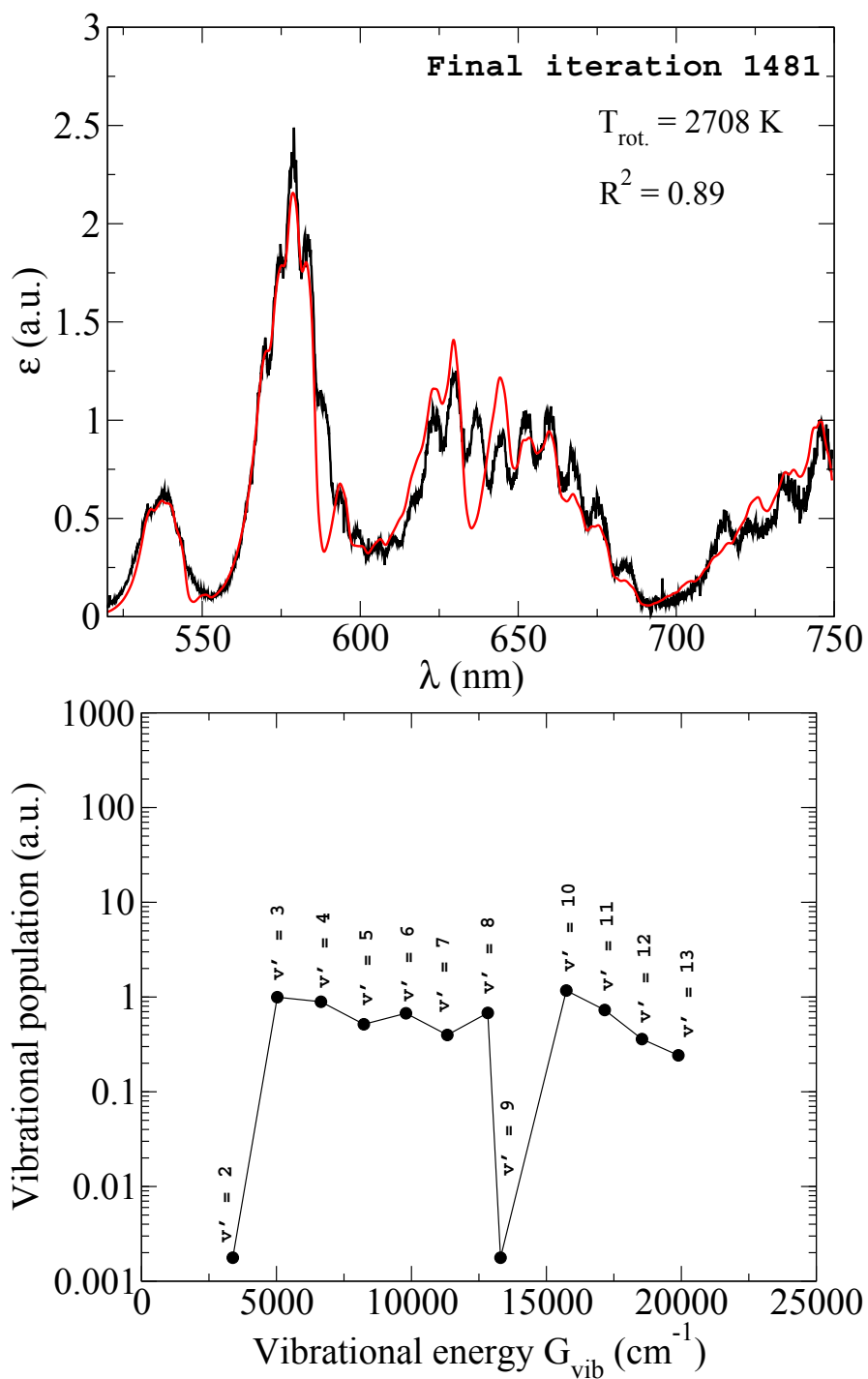


Figure 7.24.: Spectra fitting converged solution. Top: Measured spectrum (black) and synthetic spectrum (red). Bottom: Synthetic vibrational population distribution.

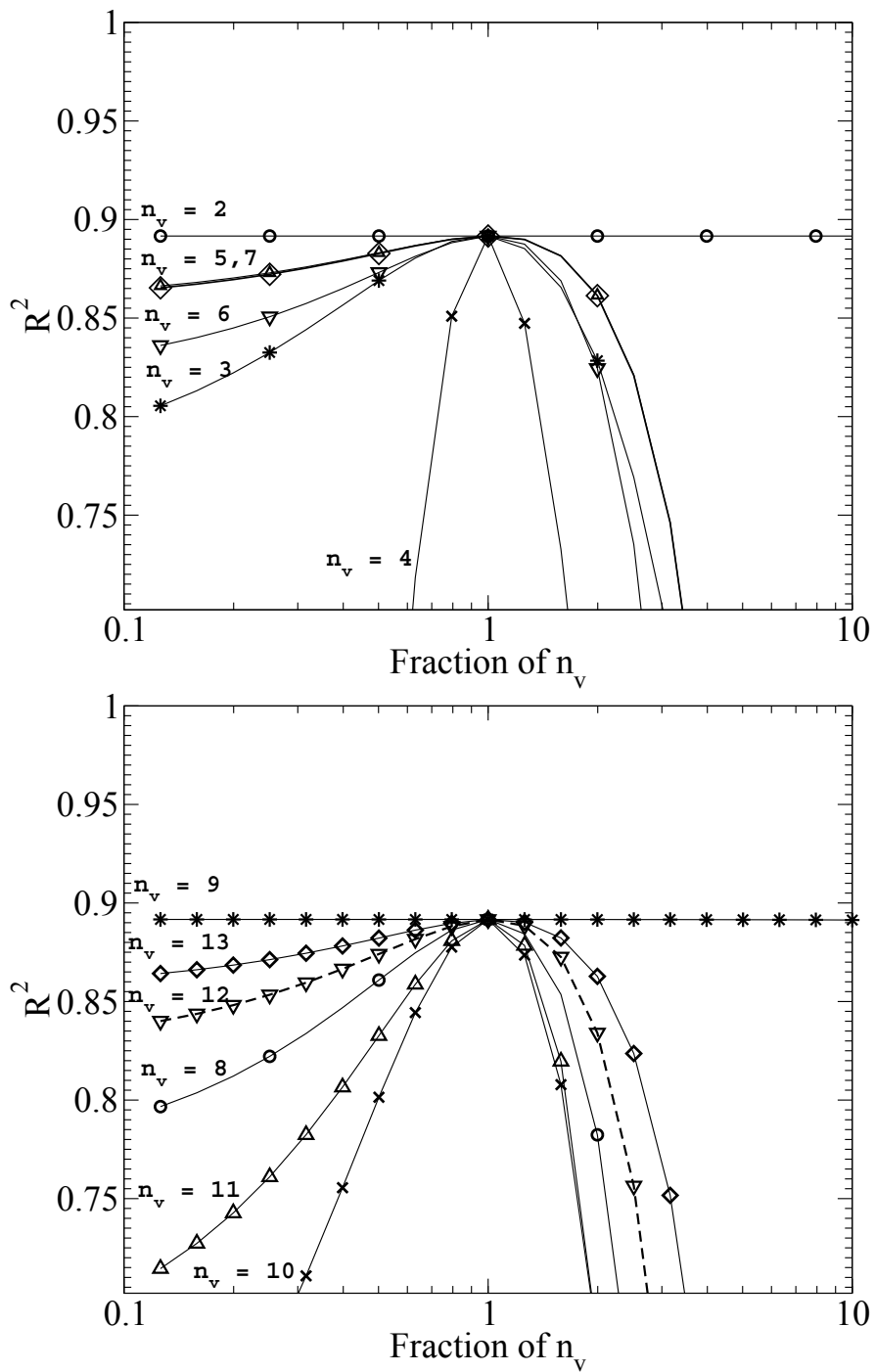


Figure 7.25.: Sensitivity of the correlation coefficient R^2 relative to the fraction of the vibrational population at $T_{rot.} = 2708$ K.

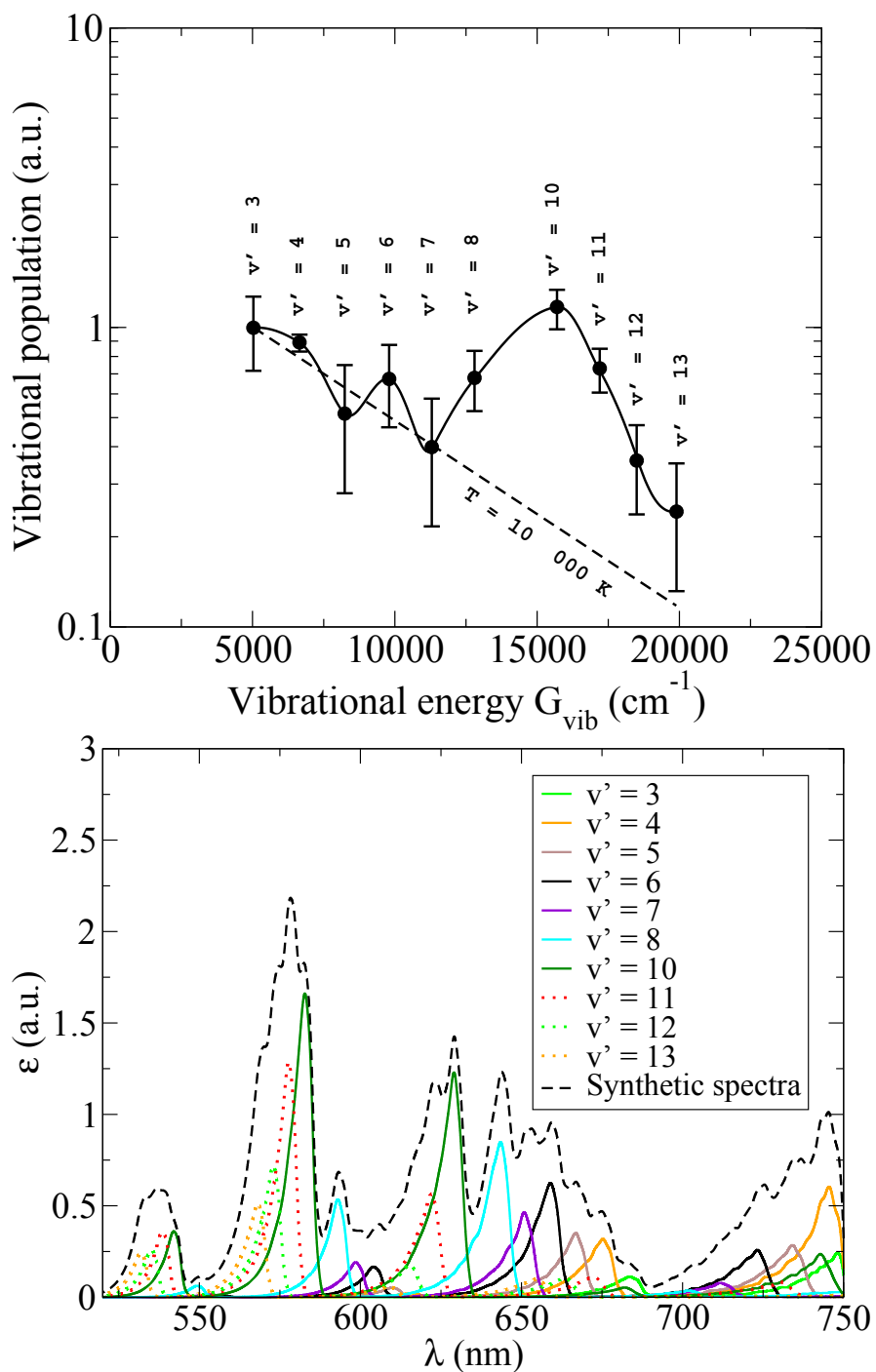


Figure 7.26.: Meaningful synthetic vibrational population distribution (top) and corresponding vibrational band spectra contribution (bottom).

When the convergence is reached, a good agreement is obtained between experimental and synthetic spectra with a correlation coefficient of 0.89 (figure 7.24). Although the synthetic spectra match pretty well with the measured spectral emission, the non-continuity of the derived vibrational distribution is doubtful. Uncertainties on each vibrational population density is therefore estimated. For this purpose, we examine the sensitivity of the correlation coefficient to the population of each vibrational level. Taking the converged solution at $T_{rot.} = 2708$ K, the vibrational population density is varied so that we evaluate the effect on the residual. For each vibrational level, the correlation coefficient which gives the quality of the least square fitting to the experimental spectrum is plotted in figure 7.24. The vibrational levels $v'=2$ and $v'=9$ are excluded from the distribution because of their very low sensitivity. We consider that above 0.87 value for R^2 , we obtain reliable solution of the least square minimization procedure. Uncertainties on population density plotted in figure 7.26 are based on this threshold value of R^2 . In figure 7.26, the contribution of the vibrational bands of the converged solution is displayed. A significant departure from Boltzmann distribution is clearly observed. The non-equilibrium distribution evidences that high lying levels (> 7) are over-populated with respect to the equilibrium distribution defined by the low-lying levels (3, 4, 5, 6 and 7) with a temperature of 10000 K.

Chapter 8.

Conclusion

8.1. Contribution of the thesis

In the Introduction, we stated that the objective of the thesis was to assess the possibility of producing non-equilibrium flows relevant to atmospheric re-entry investigation using stationary plasma jets. In particular, we were interested in generating and characterizing vibrational non-equilibrium high enthalpy flow suitable for the validation of non-equilibrium kinetic models adopted for re-entry simulation. We have used a radio-frequency ICP source, commonly employed to duplicate large heat flux, in order to generate stationary non-equilibrium flows. Also we have installed and characterized a new microwave plasma facility operating at lower enthalpy. Both sources were operated in subsonic and supersonic regimes. Measurements demonstrate that non-equilibrium stationary plasma sources can be used to test collisional-radiative models.

Subsonic air plasma experiment was performed using ICP facility operating at 273 mbar, similarly to Stardust peak radiative heating pressure. The profuse amount of atomic transitions enabled to identify atomic lines from KURUCZ [64] database which are not presented in the NIST [10] database. In agreement with Wilson criterion, a departure from complete LTE was observed. Measured electron density ($\approx 1.0 \times 10^{21} \text{ m}^{-3}$) higher than LTE condition complied with recombining/ionizing unbalanced processes. Rotational and vibrational temperatures were found to be lower than the electronic temperature with about 25 % difference at the jet centerline which reduces at about 5 % difference at 4 cm radial extent on the edges of the jet. Population of atomic excited states were compliant with LTE assumption whereas the emission of molecular excited states was found to be higher than expected in LTE condition. Molecular non equilibrium radiation was assessed through direct comparison between radiative transfer calculation and recorded spectral radiance. Locally, measured molecular non-equilibrium emission is about 4.5 times higher than LTE emission at the center of the jet and reduces to unity on the edge where equilibrium radiation prevails. Average temperature proposed by Park using two-temperature kinetic model [82] allows to reproduce the measured equilibrium electron density using LTE computation. Given these results, VKI experimental studies on stagnation point duplication should account for non-LTE conditions.

Conventional equilibrium microwave plasma source operating at atmospheric pressure was adapted for low pressure environment. Equilibrium state of subsonic nitrogen microwave plasma operating within 10 mbar to 1 bar pressure range was investigated in the ignition region of the discharge. Thermal equilibrium state was uncovered at relatively high pressure whereas two-temperature model was successfully used to characterize the thermal departure from equilibrium at low pressure. Rotational and vibrational temperatures associated to $C^3\Pi_u$ and $B^3\Pi_g$ electronic states of N_2 and $B^2\Sigma_u^+$ state of N_2^+ were investigated. At low pressure, significant thermal non-equilibrium was found with 50 % discrepancy between rotational and vibrational temperature. There was no effect of the microwave power on the equilibrium state. Measured N_2^+ electronic state population was found to be underpopulated in comparison to LTE calculations which is related to the recombining/ionizing unbalanced processes in the discharge.

Under-expanded high enthalpy air plasma jets were investigated using ICP facility operating at

different back pressure conditions. Air plasma reactivity did not affect the aerodynamics of the diamond-shaped jets and simple isentropic expansion model were used to estimate flow topology features in the expansion. The highest observable atomic excited state was found to be away from the equilibrium distribution defined by the lower part of the atomic excited states distribution scheme. The determination of the electronic temperature was therefore performed over limited atomic states corresponding to low energy range in the Boltzmann diagram representation. Vibrational and rotational energy modes were characterized by a common temperature and electron density was measured using Stark broadening of hydrogen line. Based on bilinear interpolation of spectroscopic measurements, two dimensional macroscopic description of supersonic flows is proposed.

Supersonic nitrogen plasma jet was investigated in the post discharge of the microwave facility at relatively low temperature (2700 K). In the reservoir thermal equilibrium state was estimated at 5500 K. After the nozzle, in the post-discharge, a chemically frozen state associated with a strong non-equilibrium distribution of the vibrational energy states was observed. Proper description was adopted to characterize the non-equilibrium vibrational population distribution of $B^3\Pi_g$ electronic state of N_2 .

In summary, this thesis was successful in achieving the thermodynamic description of non-equilibrium high enthalpy flows. Although, duplication with re-entry flow kinetics was not achieved through these experiments, we have characterized several departure from thermodynamic equilibrium. A complete set of data is provided for further comparison with non-equilibrium kinetic computations.

Plasmatron supersonic experiments suggest that the expansion is too weak to get strong departure from Boltzmann equilibrium of atomic and molecular excited states. Highly under-expanded jet operation would therefore be useful to reach lower Damköhler number and observe strong non-equilibrium.

The influence of plasma sources power feeding oscillations on time integrated measurements is currently an important area of investigation in VKI. The development of dual wavelength high speed imaging would allow to assess the importance of the fluctuation in term of temperature. Deeper uncertainty and sensitivity analysis applied to molecular spectra fitting are needed to assess non-equilibrium situation with better accuracy.

Finally, non-equilibrium kinetics studies relevant for atmospheric re-entry investigation would be greatly improved through the investigation of non-stationary phenomena occurring during the ignition phase of the facility.

Appendix A.

Waveguide based microwave device: cavity technical drawings

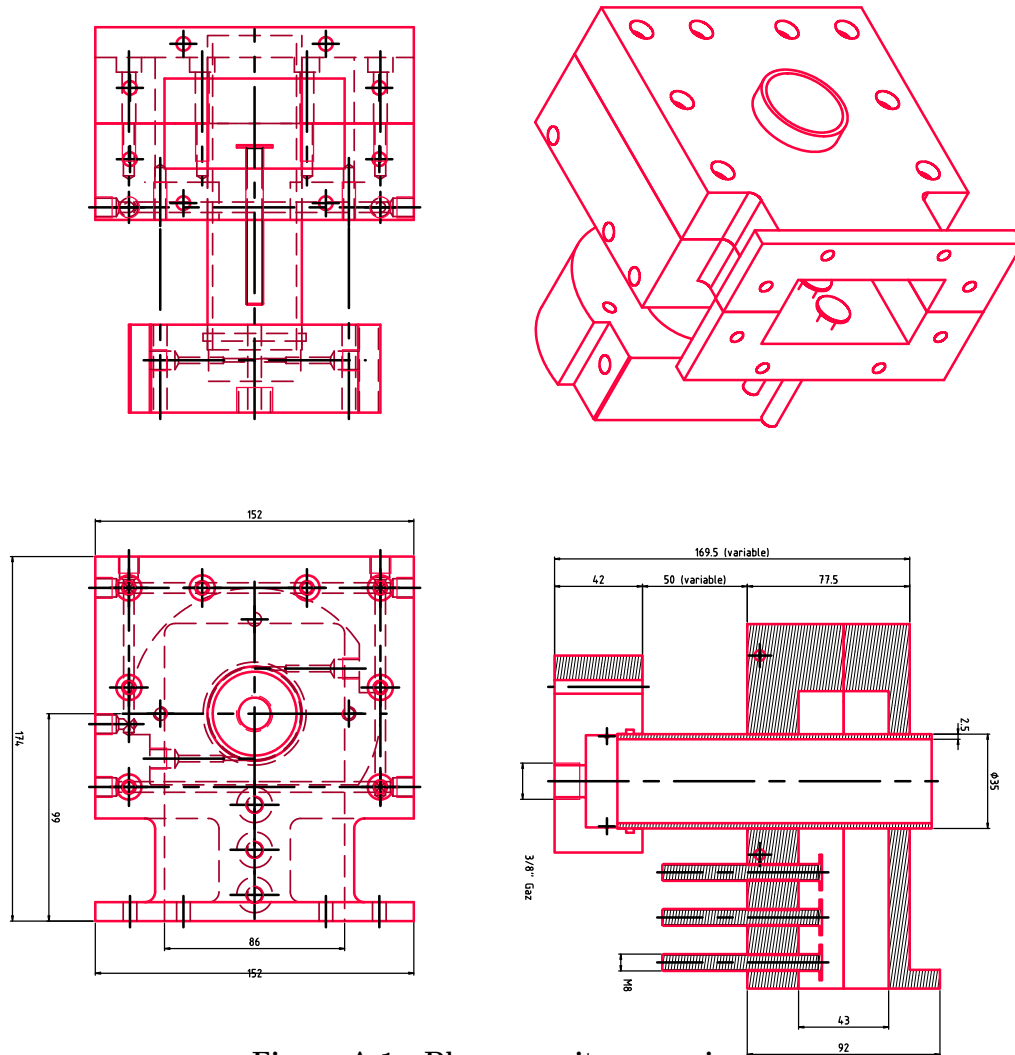
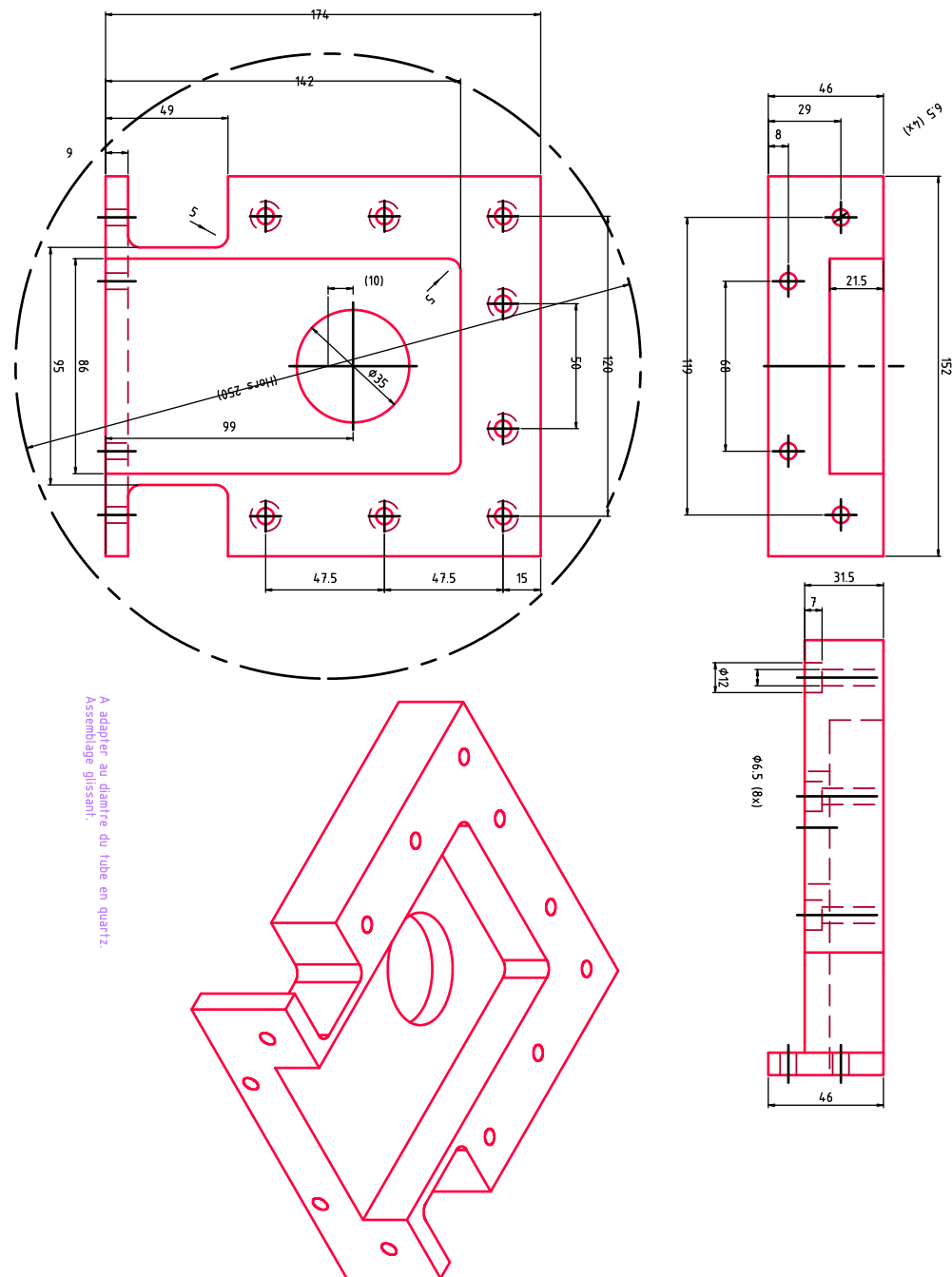


Figure A.1.: Plasma cavity: overview.



A adapter au diamètre du tube en quartz.
 Assemblage glissant.

Figure A.2.: Plasma cavity: upper part.

Bibliography

Each reference is followed by the list of the pages where it is cited.

- [1] M. E. Tauber, K. Sutton. Stagnation point radiative heating relations for Earth and Mars entries. *Journal of Spacecraft and Rockets*, 28(1), pp. 40-42, 1991. 1
- [2] M. Panesi, Y. Babou and O. Chazot. Prediction of non-equilibrium radiation: Analysis and comparison with EAST experiments. *AIAA-2008-3812*, 2008. 2, 169
- [3] P. Rivière, M-Y Perrin, A. Soufiani. Line-by-line and statistical narrow-band calculations of radiative transfer in some atmospheric entry problems. *Proceedings of the first international workshop on radiation of high temperature gases in atmospheric entry*, ESA SP-533, pp. 189-196, 2003. 1
- [4] J. O. Johnston. Nonequilibrium Shock-Layer Radiative Heating for Earth and Titan Entry. *Virginia Polytechnic Institute and State University, PhD thesis*, 2006. 1
- [5] M. Panesi. Physical models for nonequilibrium plasma flow simulations at high speed re-entry conditions. *von Karman Institute for fluid dynamics/ Università degli studi di Pisa, PhD thesis*, 2009. 1
- [6] A. Bultel, J. Annaloro. Elaboration of collisional-radiative models for flows related to planetary entries into the earth and mars atmospheres. *Plasma Sources Sci. Technol.* 22, 2013. 1
- [7] S. Paris, D. Charbonnier, D. Tran. Experimental and Numerical Investigation of Aerothermal Characteristics of the IXV Hypersonic Vehicle. *Proceedings of the 7th European Symposium on Aerothermodynamics*, 2011. 3, 169
- [8] C. Park. Nonequilibrium hypersonic aerothermodynamics. *John Wiley and Sons*, 1989. 4
- [9] S. Chauveau. Constitution de bases de données spectroscopiques relatives a un plasma d'air. *Laboratoire d'Enèrgétique Moléculaire et Macroscopique, Combustion (EM2C) du CNRS et de l'ECP, Paris*, 2001. 5, 39, 167
- [10] Kramida, A., Ralchenko, Yu., Reader, J. and NIST ASD Team (2013). NIST Atomic Spectra Database (version 5.1). National Institute of Standards and Technology, Gaithersburg, MD. URL <http://physics.nist.gov/PhysRefData/ASD/index.html>. 5, 39, 40, 89, 91, 129, 151, 167
- [11] H.R. Griem. Plasma spectroscopy. *Mcgraw-Hill, New York*, 1964. 5, 6, 55
- [12] R. Wilson. *J. Quant. Spectr. Rad. Transf.*, 2, 477, 1962. 5, 96
- [13] M.G. Tomasko & al. The Descent Imager/Spectral Radiometer (DISR) aboard Huygens. *ESA SP 1177, pp. 109-138*, 1997. 6
- [14] M. R. Patel, J. C. Zarnecki and D. C. Catling. Ultraviolet radiation on the surface of Mars and the Beagle 2 ultraviolet sensor. *Planetary and Space Science*, 50, pp. 915-927, 2002. 6

- [15] D. C. Slater, S. A. Stern, T. Booker, J. Scherrer, M. F. A'Hearn, J.L. Bertaux, P. D. Feldman, M. C. Festou and O. H. W. Siegmund . Radiometric and calibration performance results of the Rosetta UV imaging spectrometer ALICE. *Proc. SPIE 4498 UV/EUV and Visible Space Instrumentation for Astronomy and Solar Physics*, 239, 2001. 6
- [16] N. Ignatiev & al. Water vapour in the middle atmosphere of Venus:An improved treatment of the Venera 15 IR spectra. *Planetary and Space Science*, 47, Issue 8-9, p. 1061-1075, 99. 6
- [17] D. L. Cauchon. Project Fire Flight 1 Radiative Heating Experiment. *NASA TM X-1222*, 1966. 6
- [18] D. L. Cauchon. Radiative Heating Results from the FIRE II Flight Experiment at Reentry Velocity 11.4 Kilometers per Second. *NASA TM X-1402*, 1967. 6
- [19] D.B. Lee, W.D. Goodrich. The Aerothermodynamic Environment of the Apollo Command Module During Superorbital Entry. *NASA TN D-6792*, April 1972. 7
- [20] R. C. Ried, .C. Rochelle and J.D. Milhoan. Radiative Heating to the Apollo Command Module: Engineering Prediction and Flight Measurement. *NASA TM X-58091*, 1972. 7
- [21] A. Seiff, D. E. Reese, S. C. Sommer, D. B. Kirk, E. E. Whiting, H. B. Niemann. PAET, An Entry Probe Experiment in the Earth's Atmosphere. *Icarus*, 18, Issue 4, pp. 525-563, 1973. 7
- [22] R. I. Sammonds, R. L. Kruse. Aerodynamic characteristics of the planetary atmosphere experiments test entry probe. *Journal of Spacecraft and Rockets*, 12, No. 1, pp. 22-27, 1975. 7
- [23] P.W. Erdman, E. C. Zipf, P. Epsy, C. Howlett, D. A. Levin, R. Loda, R. J. Collins, and G. V. Candler. Flight Measurements Of Low-Velocity Bow Shock Ultraviolet Radiation. *J. Therm. & Heat Trans.*, 7, pp. 37-41, 1993. 7
- [24] P. W. Erdman, E. C. Zipf, P. Epsy, C. Howlett, C. Christou, D. A. Levin, R. J. Collins, and G. V. Candler. In Situ Plume Radiance From Bow-Shock Ultraviolet 2 Rocket Flight. *J. Therm. & Heat Trans.*, 7, pp.704-708, 1993. 7
- [25] Erdman & Al. Radiation from a 5-km/s Bow Shock. *Journal of Thermo-physics and Heat Transfer*, 9, No. 3, 1994. 7
- [26] C. B. Phillips, P. W. Erdman, C. Howlett, D. A. Levin, M. G. Lovern. Multi-Spectral Shock-Layer Radiance Flight Experiment Plan. *10th AIAA/BMDO Technology Conference*, 1, 2001. 7
- [27] K. A. Trumble, I. Cozmuta, S. Sepka, P. Jenniskens, M. Winter. Postflight Aerothermal Analysis of Stardust Sample Return Capsule. *Journal of Spacecraft and Rockets*, 47, issue 5, pp. 765-774, 2010. 7
- [28] S. Löhle, R. Wernitz, G. Herdrich, M. Fertig, H. P. Röser, H. Ritter. Airborne re-entry observation experiment SLIT: UV spectroscopy during stardust and ATV-1 re-entry. *CEAS Space Journal*, 1, issue 1-4, pp. 59-69, 2011. 7
- [29] J. H. Grinstead, P. Jenniskens, A. M. Cassell, J. Albers, M. W. Winter . Airborne Observation of the Hayabusa Sample Return Capsule Re-entry. *42nd AIAA Thermophysics Conference*, 2011. 7
- [30] T. J. Kowal. Orion flight test-1 thermal protection system instrumentation. *International planetary probe workshop*, 2011. 7

- [31] G. Herdrich, M. Auweter-Kurtz, M. Fertig, S. Löhle, S. Pidan and M. Winter. Present design of the flight instrumentations PYREX, PHLUX and RESPECT for the capsule EXPERT. *Proceedings of the fifth European Symposium on Aerothermodynamics for Space Vehicles*, ESA SP-563, 2004. 7
- [32] R. Savajano, O. Joshi and P. Leyland. Aerothermal analysis of the Phoebus capsule with radiative heating on the back body. *50th AIAA Aerospace Science Meeting*, AIAA 2012-1281, 2012. 7
- [33] G. Bailet, C.O. Asma, J. Muylaert and T. Magin. Feasibility analysis and preliminary design of an atmospheric re-entry cubesat demonstrator. *Proceedings of the 7th European Symposium on Aerothermodynamics*, 2011. 7
- [34] D. M. Bushnell. Scaling: Wind tunnel to flight. *Annual Review of Fluid Mechanics*, 38, pp. 11-128, 2006. 8
- [35] A. Kolesnikov. Extrapolation from high enthalpy tests to flight based on the concept of LHTS. *RTO-VKI Special course. Measurement Techniques for High Enthalpy and Plasma Flows*, 1999. 8, 79
- [36] J. R. Maus. Aerodynamic and aerothermal facilities II. Short-duration high enthalpy facilities. *Description and Flow Characterization of Hypersonic Facilities Final Report*, AEDC TR-94-8, 1994. 8, 169
- [37] D. W. Bogdanoff. Shock tube experiments for Earth and Mars entry conditions. *Technical Report*, RTO-EN-AVT-162, NATO, 2007. 9
- [38] A. M. Brandis. Experimental study and modelling of non-equilibrium radiation during Titan and martian entry. *PhD thesis, The University of Queensland, Australia*, 2009. 9
- [39] T. Hideyuki, M. KODERA, K. Tomoyuki, S. Kazuo, T. Masahiro and I. Katsuhiko. Aero-heating measurements on a reentry capsule model in free-piston shock tunnel HIEST. *48th AIAA Aerospace Sciences Meeting Including the New Horizons Forum and Aerospace Exposition*, 2010. 9
- [40] Y. Gouji, T. Hiroki, S. Toshiyuki, F. Kazuhisa. Shock Layer Radiation Analysis using a Hypervelocity Shock Tube (HVST). *Transactions of the Japan Society for Aeronautical and Space Sciences*, Vol. 55, pp. 37-43, 2012. 9
- [41] R. Parker, M. MacLean, M. Holden, T. Wakeman. Shock Front Radiation Studies at CUBRC. *48th AIAA Aerospace Sciences Meeting Including the New Horizons Forum and Aerospace Exposition*, 2010. 9
- [42] <http://esther.ist.utl.pt/>. 9
- [43] F. Panerai. Aerothermochemistry Characterization of Thermal Protection Systems. *PhD thesis Università degli Studi di Perugia*, 2011. 9
- [44] D. Lequang, Y. Babou, P. André. Investigations of a microwave plasma source operating with air, N₂, CO₂ and argon gases. *IOP Conf. Ser.: Mater. Sci. Eng.*, 29, 2012. 9
- [45] D. Vacher, M. Dudeck, P. André, M. Lino da Silva, G. Faure, M. Dubois, A. Hamwi, S. Ménéciér and D. Rochette. Radiation from an ICP plasma TORCH in the near-UV to near-IR spectral region for a Titan-type N₂-CH₄ Mixture. *Journal of Technical Physics*, 2010. 9

- [46] Y. Babou. Transferts radiatifs dans les plasmas de mélange $\text{CO}_2\text{-N}_2$: base de données spectroscopiques, étude expérimentale et application aux rentrées atmosphériques. *Laboratoire d'Énergétique Moléculaire et Macroscopique, Combustion (EM2C) du CNRS et de l'ECP, Paris*, 2007. 13
- [47] S. Depraz, M.Y. Perrin, Ph. Riviere, A. Soufiani. Infrared emission spectroscopy of CO_2 at high temperature. Part II : Experimental results and comparisons with spectroscopic databases. *JQSRT*, 113,14-25, 2012. 13
- [48] S. Depraz, M.Y. Perrin, A. Soufiani. Infrared emission spectroscopy of CO_2 at high temperature. Part I : Experimental setup and source characterization. *JQSRT*, 113, 1-13, 2012. 13
- [49] B. Bottin, M. Carbonaro, S. Zemsch and G. Degrez. Aerothermodynamic design of an inductively coupled plasma wind tunnel. *32nd AIAA Thermophysics Conference, Atlanta, USA*, AIAA paper 97-2498, June 23-25 1997. 13
- [50] M. Moisan and Z. Zakrzewski. Plasma sources based on the propagation of electromagnetic surface waves. *J. Phys. D: Appl. Phys.*, Vol. 24, 1991. 13, 15
- [51] T. Fleisch, Y. Kabouzi, M. Moisan, J. Pollak, E. Castanos-Martinez, H. Nowakowska and Z. Zakrzewski. Designing an efficient microwave-plasma source, independent of operating conditions, at atmospheric pressure. *Plasma Sources Sci. Technol.*, Vol. 16, 173-182, 2007. 15
- [52] A.W. Trivelpiece, R. W. Gould. Space charge waves in cylindrical plasma columns. *Journal of Applied Physics*, Vol. 30, Issue 11, 1959. 16
- [53] M. Moisan, Z. Zakrzewski and R. Pantel. The theory and characteristics of an efficient surface wave launcher (surfatron) producing long plasma columns. *Journal of Physics D: Applied Physics*, 12 Number 2, 1979. 16
- [54] H. Nowakowska, D. Czyilkowski, Z. Zakrzewski. Surface wave sustained discharge in Argon: Two temperature collisional radiative model and experimental verification. *Journal of Optoelectronics and Advanced Materials*, Vol. 7, No. 5, p. 2427 - 2434, October 2005. 16
- [55] V. M. M. Glaude, M. Moisan, R. Pantel, P. Leprince, and J. Mare. Axial electron density and wave power distributions along a plasma column sustained by the propagation of a surface microwave. *J. Appl. Phys.*, 51, 5693, 1980. 16
- [56] Itakawa et al. *J. Phys. Chem. Ref. Data*, 15, 1986. 17
- [57] J. Margot Chaker, M. Moisan, V. M. M. Glaude, P. Lauque, J. Paraszczak and G. Sauve. Tube diameter and wave frequency limitations when using the electromagnetic surface wave in the $m=1$ (dipolar) mode to sustain a plasma column. *J. Appl. Phys.*, 66-9, 4134, 1989. 17
- [58] M. Moisan and J. Pelletier. Microwave excited plasmas Plasma Technology 4. *Elsevier science BV*, 1992. 17
- [59] G. L. Brown, J. M. Lopez. Axisymmetric vortex breakdown part I, Physical mechanisms. *Journal of Fluid Mechanics*, 1990. 17
- [60] Y. C. Hong, H. S. Uhm, S. C. Cho. Argon Microwave Discharges Sustained at Atmospheric Pressure: Suppression of Plasma Filaments with Molecular Gases. *Journal of the Korean Physical Society*, Vol. 53, No. 6, pp. 3220-3223, 2008. 18

- [61] Y. Babou, F. Canat, D. Le Quang. Tomography of thermal plasma flows by mean of single camera. *International Workshop on Radiation of High Temperature Gases in Atmospheric Entry*, 2012. 21
- [62] A. V. Timofeev. Theory of microwave discharges at atmospheric pressures. *Plasma Physics Reports*, Vol. 23, no. 72, pp. 158-164, 1997. 30, 100
- [63] J. D. Anderson. *Modern Compressible Flow: With Historical Perspective*. 1982. 36, 169
- [64] R.L. Kurucz and B. Bell. Kurucz CD-ROM No. 23. Cambridge, Mass. *Smithsonian Astrophysical Observatory*, 1995. 39, 40, 89, 91, 151, 167, 171
- [65] M. Y. Perrin, P. Rivière, A. Soufiani. Radiation database for Earth and Mars entry. *Von Karman Lecture Series*, RTO-EN-AVT-162, 2008. 39, 43, 45
- [66] B. J. McBride, S. Gordon. Computer program for calculation of complex chemical equilibrium compositions and application. II User manual and program description. *NASA Lewis Research Center, Cleveland, OH*, Reference publication 1311, 1996. 40, 55, 66, 81, 87, 97, 171
- [67] C. Deron. Rayonnement thermique des plasmas d'air et d'argon: modelisation des propriétés radiatives et étude expérimentale. *Laboratoire d'Énergétique Moléculaire et Macroscopique, Combustion (EM2C) du CNRS et de l'ECP, Paris*, 2003. 40, 50
- [68] H.R. Griem. Spectral Line Broadening by Plasmas. *Academic Press, New York and London*, 1974. 40, 58
- [69] R.L. Jaffe. *AIAA paper in Proc. 22nd AIAA Thermophys. Conf., Honolulu*, 1987. 43
- [70] Y. Babou, P. Rivière, M. Y. Perrin, A. Soufiani. High Temperature and Nonequilibrium Partition Function and Thermodynamic Data of Diatomic Molecules. *Int J Thermophys*, 30, pp. 416-438, 2009. 43
- [71] R. G. Breene. Spectral line broadening in air molecule systems. *Applied Optics*, 6, pp. 141-147, 1967. 43
- [72] S.R. DRAYSON. Rapid computation of the Voigt profile. *J. Quant. Spectrosc. Radiat. Transfer*, 16, pp.611-614, 1976. 45
- [73] B. Edlen. The refractive index of air. *Metrologia*, 2, pp. 71-80, 1966. 48
- [74] C. R. Vidal, J. Cooper, E. W. Smith. Hydrogen Stark-Broadening Tables. *The Astrophysical Journal supplement*, Vol. 214, 1973. 58, 60
- [75] M. A. Gigosos, V. Cardenoso. New plasma diagnosis tables of hydrogen Stark broadening including ions dynamics. *J. Phys. B:At. Mol. Opt. Phys.*, 29:4795-4838, 1996. 58, 60, 128
- [76] B. W. Acon, C. Stehle, H. Zhang, A. Montaser. Stark-broadened hydrogen line profiles predicted by the model microfield method for calculating electron number densities. *Spectrochimica Acta Part B*, Vol. 56:pp. 527-539, 2001. 58, 60
- [77] U. Frisch and A. Brissaud. *J. Quant. Spectrosc. Radiat. Transfer*, 11:1753, 1971. 60
- [78] J. Seidel. *Z. Naturf.*, 32 a:1195, 1977. 60
- [79] C. Stehle. Stark broadening of H lines (Stehle 1995). *VizieR Online Data Catalog*, 6082, sep 1995. 60

- [80] M. A. Gigosos, M. A. Gonzalez, V. Cardenoso. Computer simulated Balmer-alpha, -beta and -gamma Stark line profiles for non-equilibrium plasmas diagnostics. *Spectrochimica Acta Part B*, Vol. 58:pp. 1489–1504, 2003. 60
- [81] G. Degrez, P. Barbante, M. de la Llave, T. Magin, and O. Chazot. Determination of the Catalytic Properties of TPS Materials in the VKI ICP Facilities. *European Congress on Computational Methods in Applied Sciences and Engineering, ECCOMAS Computational Fluid Dynamics Conference*, 2001. 79
- [82] C. Park. *J. Thermophys. and Heat Transfer* 7, 385, 1993. 97, 151
- [83] K. Green, M. C. Borrás, P. P. Woskov, G. J. Flores III, K. Hadidi, and P. Thomas. Electronic Excitation Temperature Profiles in an Air Microwave Torch. *Transactions on Plasma Science*, Vol. 29, 2001. 100
- [84] S. Chauveau. Constitution de bases de données spectroscopiques relatives a un plasma d'air. *Laboratoire d'Énergie Moléculaire et Macroscopique, Combustion (EM2C) du CNRS et de l'ECP, Paris*, 2001. 101
- [85] M. El Morsli and P. Proulx. Two-temperature chemically non-equilibrium modelling of an air supersonic ICP. *J. Phys. D: Appl. Phys.*, 40, pp. 4810-4828, 2007. 111
- [86] M. El Morsli, P. Proulx and D. Gravelle. Chemical non-equilibrium modelling of an argon-oxygen supersonic ICP. *lasma Sources Sci. Technol.*, 20, 2011. 111
- [87] M. C. M. van de Sanden, R. J. Severens, W. M. M. Kessels, R. F. G. Meulenbroeks, and D. C. Schram. Plasma chemistry aspects of a -Si:H deposition using an expanding thermal plasma. *J. Appl. Phys.*, 84, 2426, 1998. 111
- [88] S. C. Hsu, E. C. Merritt, A. L. Moser, T. J. Awe, S. J. E. Brockington, J. S. Davis, C. S. Adams, A. Case, J. T. Cassibry, J. P. Dunn, M. A. Gilmore, A. G. Lynn, S. J. Messer, F. D. Witherspoon. Experimental characterization of railgun-driven supersonic plasma jets motivated by high energy density physics applications. *Physics of Plasmas*, 19, 2012. 111
- [89] P. M. Bellan, M. Livio, Y. Kato, S. V. Lebedev, T. P. Ray, A. Ferrari, P. Hartigan, A. Frank, J. M. Foster and P. Nicolai. Astrophysical jets: Observations, numerical simulations and laboratory experiments. *Phys. of Plasmas*, 16, 0410005, 2009. 111
- [90] R. P. Drake. Energy Balance and Structural Regimes of Radiative Shocks in Optically Thick Media. *IEEE Transactions on plasma science*, Vol. 35, No. 2., 2007. 111
- [91] S. Mazouffre and E. Pawelec. Metastable oxygen atom velocity and temperature in supersonic CO₂ plasma expansions. *J. Phys. D: Appl. Phys.*, 42, 015203 (8pp), 2009. 111, 112
- [92] K. Toki, S. Shinohara, T. Tanikawa, I. Funaki and K. P. Shamrai. Preliminary investigation of helicon plasma source for electric propulsion applications. *IEPC 03-0168, 28th Int. Electric Propul. Conf., Toulouse, France, 17-21 March, 2003*. 111
- [93] T. Hagiwara, A. Ando, Y. Kasashima, K. Hattori, and M. Inutake. Experiments of Ion Acceleration in a Magnetic Nozzle for an Advanced Plasma Thruster. *IEPC-2007-255 Presented at the 30th International Electric Propulsion Conference, Florence, Italy, 2007*. 111
- [94] B. W. Longmier, J. P. Squire, M. D. Carter, L. D. Cassady, T. W. Glover, W. J. Chancery, C. S. Olsen, A. V. Ilin, G. E. McCaskill, and F. R. Chang Díaz. Ambipolar Ion Acceleration in the Expanding Magnetic Nozzle of the VASIMR[®] VX-200i. *45th AIAA/ASME/SAE/ASEE Joint Propulsion Conference & Exhibit, Denver, Colorado, 2-5 August 2009*. 111

- [95] A. Ando, T. H. S. Jo, T. Taguchi, K. Hattori and M. Inutake. Experimental Study of Ion Heating and Acceleration in a Fast-flowing plasma for the Advanced Plasma Propulsion. *Plasma Fusion Res. SERIES*, Vol. 8, 2009. 111
- [96] M. Inutake, K. Yoshino, H. Tobar, H. Fukui, R. Sato, K. Hattori, A. Ando. Production of a Supersonic Plasma Flow through a Laval Magnetic Nozzle. *Proc. of 26th Int. Conf. on Phenomena in Ionized Gases, 1,*, pages pp.127–128, 2003. 111
- [97] K. Schoenberg, R. Gerwin, R. Moses, J. Scheuer, and H. Wagner. Magnetohydrodynamic flow physics of magnetically nozzled plasma accelerators with applications to advanced manufacturing. *Phys. Plasmas*, 5, 2090, 1998. 111
- [98] G. J. Meeusen, E. A. Ershov-Pavlov, R. F. G. Meulenbroeks, M. C. M. van de Sanden, and D. C. Schram . Emission spectroscopy on a supersonically expanding argon-silane plasma. *Journal of Applied Physics*, 71, 9, 1992. 111, 114
- [99] B. McAndrew, P. Barker, and R. Miles. Development of a supersonic plasma wind tunnel. *AIAA-2000-0533*, 2000. 111
- [100] J.B. Fenn, J.B. Anderson. Rarefied Gas Dynamics 2 . *J.H. de Leeuw Eds., New York: Academic*, 1966. 111
- [101] R. Campargue. *J. Chemical Phys.*, 52, pp. 1795-1802, 1970. 111
- [102] G. Abbate. Multi-Scale Modeling of Gas Flows with Continuum-Rarefied Transitions Application to Expanding Gas Jets in Thin Film Deposition Processes. *thesis*, 2009. 111
- [103] S. Mazouffre. Transport phenomena in plasma expansions containing hydrogen : a laser spectroscopic study. *Thesis, Eindhoven: Technische Universiteit Eindhoven*, 2001. 111, 115
- [104] P. Vankan, S. Mazouffre, D.C. Schram, R. Engeln. Inflow and shock formation in supersonic rarefied plasma expansions. *Phys. Plasma*, 12, 102303, 2005. 111
- [105] V. N. Snopko and L. I. Kiselevskii. Optical and spectroscopic studies of zones of retardation of supersonic plasma jets from a pulse discharge. *Zhurnal Prikladnoi Spektroskopii*, 5, No. 2 (pp. 148-152), 1966. 112
- [106] Z. Hubicka, M. Sícha, L. Pasajová, L. Soukup, L. Jastrabík, D. Cjvostoúa and T. Wagner. CN_x coatings deposited by pulsed RF supersonic plasma jet: hardness, nitrogenation and optical properties. *Surface and Coatings Technology*, 142-144, 681-687, 2001. 112
- [107] J. K. Ziemer, E. A. Cubbin and E. Y. Choueiri. V. Oraevsky and V. Dokukin. Pulsed plasma propulsion for a small satellite: Mission COMPASS P³OINT. *AIAA-96-3292*, 1996. 112
- [108] A. Abdelhafez, A. K. Gupta. Effect of Swirl on Shock Structure in Underexpanded Supersonic Airflow. *Journal of Propulsion and Power*, 26(2), pp. 215-229, 2010. 112
- [109] H. Askenas, F. S. Sherman. Rarefied Gas Dynamics Proceedings 4. *Academic Press, New York*, Vol. 2, pp 84, 1966. 112, 113, 114, 115
- [110] R. Ladenburg, C. C. Van Voorhis, J. Winkler. *Phys. Rev.*, 76, pp. 662-677, 1949. 112
- [111] J. Hartmann and F. Lazarus. *Phil. Mag.*, 31, pp. 35-50, 1941. 112
- [112] V. H. Reis. *Princeton Univ. Mech. Eng. Dept. Rept. FLD-7*, 1962. 112

- [113] E. P. Muntz, B. B. Hamel, B. L. Maguire. Some characteristics of exhaust plume rarefaction. *AIAA J.*, 8, 1651-1658, 1970. 112, 119
- [114] M. Gindrat, J-L Dorier, Ch. Hollenstein, A. Refke and G. Barbezat. Characterization of supersonic low pressure plasma jets with electrostatic probes. *Plasma Sources Sci. Technol.*, 13, 484, 2004. 112
- [115] K. Bier, B. Schmidt. Zur Form der Verdichtungstöße in frei expandierenden Gasstrahlen. *Z. Angew. Math. Phys.*, 13, 493-500, 1961. 112
- [116] W. N. Radicic, J. B. Olsen, R. V. Nielson, J. H. Macedone, P. B. Farnsworth. Characterization of the supersonic expansion in the vacuum interface of an inductively coupled plasma mass spectrometer by high-resolution diode laser spectroscopy. *Spectrochimica Acta Part B*, 61, (686 - 695), 2006. 112
- [117] B. Mate, I. A. Graur, T. Elizarova, I. Chirokov, G. Tejada, J. M. Fernandez and S. Montero. Experimental and numerical investigation of an axisymmetric supersonic jet. *J. Fluid Mech.*, vol. 426, pp. 177-197, 2001. 112, 113
- [118] P. Clancy, M. Saminy. Two-component planar Doppler velocimetry in high speed flows. *AIAA journal*, 35, 11, pp. 1729, 1997. 112
- [119] J. Panda, R. G. Seasholtz. Measurements of shock structure and shock-vortex interaction in underexpanded jets using Rayleigh scattering. *Physics of Fluid*, 11, 12, 1999. 112
- [120] D. J. Drake, S. Popović and L. Vusković. Characterization of a supersonic microwave discharge in Ar/ H₂ / Air mixtures. *Journal of applied physics*, 104, 2008. 113
- [121] D. J. Drake, S. Popović and L. Vusković. Characterization of a CO₂/N₂/Ar supersonic flowing discharge. *Journal of applied physics*, 106, 2009. 113
- [122] M Sabsabi, S Vacquie, D V Gravelle and M I Boulos. Emission spectroscopic study of a low pressure supersonic Ar-H₂ DC plasma je. *Journal of Physics D: Applied Physics*, Volume 25 Number 3, pp. 425, 1992. 113
- [123] M.C.M.van de Sanden. The expanding plasma jet: Experiments and model. *Thesis*, 1991. 113, 117
- [124] K. N. C. Bray. Electron-ion Recombination in Argon Flowing through a Supersonic Nozzle. *High Temperature Aspects of Hypersonic Flow*, W. Nelson ed., Pergamon Press, Ch. 4, 1964. 113
- [125] L. Talbot, Y. S. Chou, and F. Robben. Expansion of a Partially Ionized Gas through a Supersonic Nozzle. *Report No. AS-65-14*, 1965. 113
- [126] C. Park. Relaxation of Electronic State Populations in Expanding Flows of Ionized Nitrogen. *AIAA preprint No. 68-734*, 1968. 113
- [127] F. G. Meulenbroeks, R. A. H. Engeln, C. Box, I. de Bari, M. C. M. van de Sanden, J. A. M. van der Mullen, and D. C. Schram . Influence of molecular processes on the hydrogen atomic system in an expanding argon-hydrogen plasma. *Phys. Plasmas*, 2, 1995. 114
- [128] R.Yano, V.Contini, E.Plönjes, P.Palm, S.Merriman, S.Aithal, I.Adamovich, W.Lempert, V.Subramaniam, J.W.Rich. Supersonic nonequilibrium plasma wind-tunnel measurements of shock modification and flow vizualization. *AIAA Journal*, Vol.38:No.10, October 2000. 114

- [129] S.E.Selezneva, M.Rajabian, D.Gravelle, M.I.Boulos. Study of the structure and deviation from equilibrium in direct current supersonic plasma jets. *J. Phys. D: Appl. Phys.*, Vol.34: pp.2862–2874, 2001. 114
- [130] V.Sember, D.V.Gravelle, M.I.Boulos. Spectroscopic study of a supersonic plasma jet generated by an ICP torch with a convergent-divergent nozzle. *Journal of Physics D: Applied Physics*, Vol.35:pp.1350–1361, 2002. 114
- [131] R. Engeln, S. Mazouffre, P. Vankan, I. Bakker, D.C. Schram. Plasma expansion: fundamentals and applications. *Plasma Sources Sci. Technol.*, 11, A100, 2002. 114
- [132] I. R. Hurler, A. L. Russo, and J. Gordon Hall. Spectroscopic Studies of Vibrational Nonequilibrium in Supersonic Nozzle Flows. *J. Chem. Phys.*, 40, 2076, 1964. 114
- [133] D.C. Schram, S. Mazouffre, R. Engeln, M.C.M. van de Sanden. The Physics of Plasma Expansions, in Atomic and Molecular Beams. *R. Campargue, Springer, Berlin, pp 209*, 2001. 114
- [134] D. Bruno, M. Capitelli, F. Esposito, S. Longo, P. Minelli. Direct simulation of non-equilibrium kinetics under shock conditions in nitrogen. *Chemical Physics Letters*, 360, pp. 31-37, 2002. 115
- [135] M.C.M.van de Sanden, J.M.de Regt, D.C.Schram. Recombination of argon in an expanding plasma jet. *Physical review E*, Vol.47-Number 4, April 1993. 115
- [136] A. B. Witte. Part I. Experimental investigation of an arc-heated supersonic free jet. *Dissertation (Ph.D.)*, California Institute of Technology, 1967. 115
- [137] H. M. Mott Smith. *Phys. Rev.*, 82, 885, 1951. 116
- [138] W. M. Hilbun. Shock waves in non-equilibrium gases and plasmas. *Thesis, Air Force Institute of Technology*, 1997. 116
- [139] R. Saeks, S. Popovic, A. S. Chow. Shock Structure Analysis and Aerodynamics in a Weakly Ionized Gas Flow. *NASA/TP-2006-214602; M-1171*, 2006. 117
- [140] H. Ashkenas, F.S. Sherman. The structure and utilization of supersonic free jets in low density wind tunnels. *Proc. 4th Int. Symp. on Rarefied Gas Dynamics*, Vol.2:pp.84–105, 1996. 121

List of Tables

1.1.	Excitation/Reaction energies	2
1.2.	Radiative lifetime [s] of molecular ($\tau_{rad.}^{v'}$) [9] and atomic ($\tau_{rad.}$) [10] bound-bound transitions.	5
2.1.	Cutoff frequencies of the first modes in a WR-340 waveguide	14
2.2.	TE ₁₀ mode parameters	15
3.1.	Spectroscopic detection systems and associated experimental campaign.	46
3.2.	Synthetic profile used to test the Abel transform.	53
4.1.	Hydrogen Balmer lines spectroscopic data.	59
4.2.	Electron densities and temperatures selected from <i>CS</i> theoretical database for H _{β} line shape calculation.	63
4.3.	Thermal fitting parameters.	67
4.4.	Two-temperature fitting parameters.	72
4.5.	Vibrational non-equilibrium fitting parameters.	75
5.1.	Experimental operating conditions of subsonic air ICP plasma jet.	80
5.2.	Spectroscopic data of the considered O and N emission lines taken from [10] and [64] (indicated by a star).	91
5.3.	Experimental operating conditions of subsonic microwave nitrogen discharge.	100
7.1.	Characteristics of experimental ICP supersonic air plasma jet experiments.	120
7.2.	Nozzle exit computed parameters value.	125
7.3.	Flow properties calculated across the shock for adiabatic normal shock front and weakly ionized shock.	128
7.4.	Spectroscopic data of the considered O emission lines taken from [10].	129
7.5.	Electron configuration and level identification associated to oxygen transitions.	129
7.6.	Analytical profiles parameters.	133
7.7.	Characteristics of supersonic microwave nitrogen plasma jet experiment.	141

List of Figures

1.1. Prediction of non-equilibrium EAST experiment radiation: (courtesy of M. Panesi & al. [2]).	2
1.2. Schematic of the physico-chemical processes and flow field surrounding IXV vehicle during the re-entry phase (Schlieren visualization courtesy of S. Paris [7]). . .	3
1.3. Description and flow characterization of hypersonic facilities. Figure adapted from J.R. Maus & al. [36].	8
2.1. Representation of VKI microwave plasma source.	14
2.2. Electric field distribution for TE ₁₀ mode.	15
2.3. Schlieren pictures taken above the quartz tube during the ignition phase (left) and the established flow (right).	17
2.4. 0.8 kW air plasma flow at 0.1 g.s ⁻¹ (left) and 1.5 g.s ⁻¹ (right).	18
2.5. 0.8 kW N ₂ plasma flow at 0.1 g.s ⁻¹ (left) and 1.5 g.s ⁻¹ (right).	19
2.6. Argon streamer regime at 0.6 kW (left) and 1.0 kW (right) microwave power. . .	19
2.7. Intensity fluctuation for 0.8 kW air plasma jet.	20
2.8. Intensity fluctuation for 0.3 g.s ⁻¹ air plasma jet.	20
2.9. Component frequencies of the emission fluctuation for 0.8 kW (left) and 0.3 g.s ⁻¹ (right) air plasma jet (1 cm above the waveguide).	21
2.10. Component frequencies of the emission fluctuation (air, 0.3 g.s ⁻¹ , 0.8 kW). . . .	22
2.11. Instantaneous emission distribution - low mass flow rate case (0.9 g.s ⁻¹ , 0.8 kW). . .	22
2.12. Mean emission distribution - low mass flow rate case (0.9 g.s ⁻¹ , 0.8 kW).	23
2.13. Instantaneous emission distribution - high mass flow rate case (1.3 g.s ⁻¹ , 0.8 kW). . .	23
2.14. Mean emission distribution - high mass flow rate case (1.3 g.s ⁻¹ , 0.8 kW).	24
2.15. Forwarded (top) and reflected (bottom) RF microwave power at 0.1 g.s ⁻¹ with associated Fourier fluctuation analysis.	25
2.16. Forwarded (top) and reflected (bottom) RF microwave power at different mass flow rates with associated fourier fluctuation analysis.	26
2.17. Reflected power versus forwarded power for different configurations of the impedance matching screws.	27
2.18. Relative calibration curve using halogen/deuterium source.	27
2.19. Typical radiative signature of air discharge (top) operated at 0.6 (black), 0.8 (red) and 0.9 kW (blue) and associated scaled spectra (bottom).	28
2.20. Typical radiative signature of nitrogen discharge (top) operated at 0.6 (black), 0.8 (red) and 0.9 kW (blue) and associated scaled spectra (bottom).	29
2.21. Axial scaled intensity profiles (top) of nitrogen discharge operated at 0.6 (circles) and 0.9 kW (crosses) and associated temperature profiles (bottom).	31
2.22. Electrical scheme of VKI Plasmatron facility.	33
2.23. Component frequencies of the emission fluctuation for Plasmatron supersonic plasma flows.	33
2.24. Plasmatron converging throat (right) and MPT converging diverging nozzle (left) technical drawings.	35
2.25. Nozzle operating map ($\gamma = 1.3$) and hydrodynamic regimes associated to experimental configurations of Plasmatron and microwave plasma sources.	35
2.26. Geometry of contoured nozzle defined by Anderson [63].	36
2.27. Supersonic microwave discharge system (top) and plasma flow regimes (bottom). . .	37
2.28. Plasmatron subsonic (top) and supersonic (bottom) plasma jet.	38

3.1.	Top: N_2 internal partition function. Bottom: N_2^+ internal partition function. . .	44
3.2.	Top: Experimental arrangement for spatially resolved spectroscopic measurements. Bottom: Typical CCD frame.	47
3.3.	Top: Asymmetric intensity profiles: experimental (black) and filtered (red). Bottom: Corresponding Abel transform.	49
3.4.	Scheme of radiance I and the local emission ϵ assigned to axisymmetric geometry.	50
3.5.	Top: raw profile. Bottom: Abel inversion results	51
3.6.	Top: noisy profile and associated filtering. Bottom: Abel inversion results	52
3.7.	Abel transform of plasma flow emission around heat flux probe.	53
4.1.	Top: 273 mbar air plasma species concentration. Bottom: Scaled atomic emission.	56
4.2.	H_β line shape broadening contributions as a function of the electron number density and temperature in LTE air plasma at atmospheric pressure.	59
4.3.	Computations of H_β line shape with Stark and Doppler broadening at 10000 K and 10^{14} (top) and 10^{15} (bottom) cm^{-3} electron density. <i>VCS</i> (dotted), <i>MMM</i> (dashed) and <i>CS</i> (circle)	61
4.4.	Top: Computations of H_β Stark broadening line shape at 10000 K, 5.0×10^{14} cm^{-3} electron density for various relative reduced mass $\mu_r = 5.0$ (dashed), 1.0 (dotted), 0.5 (circle). Bottom: Stark broadening FWHM at $T_e = 5000$ K (dashed) and $T_e = 10\ 000$ K (circle) using <i>CS</i> simulation.	62
4.5.	Computed hydrogen H_α spectral line shape broadening at $N_e = 5.0 \times 10^{14}$ cm^{-3} , $T = 5000$ K (blue), 15000 K (red).	63
4.6.	Computed hydrogen H_β spectral line shape broadening at $N_e = 5.0 \times 10^{14}$ cm^{-3} , $T = 5000$ K (blue), 15000 K (red).	64
4.7.	Top: RMSE distribution. Bottom: Reference and computed H_β line at the first iteration	65
4.8.	Thermal equilibrium spectra fittings: first iteration [335-360] nm (top) and [335-430] nm (bottom)	68
4.9.	RMSE distribution for various spectral ranges.	69
4.10.	Synthetic spectrum - $T_{rot} = 7000$ K, $T_{vib} = 12000$ K - (top). Synthetic noisy spectrum and additional noisy background (bottom).	70
4.11.	Two-temperature spectra fitting first iteration: synthetic spectrum without background (top) and with noisy contribution (bottom).	71
4.12.	RMSE distribution (top) and RMSE isocontours (bottom).	73
4.13.	Noisy fitting RMSE distribution (top) and noisy fitting RMSE isocontours (bottom).	74
4.14.	Vibrational non-equilibrium synthetic spectrum and vibrational bands contribution (top) and first fitting iteration (bottom).	76
4.15.	Top: Spectra fitting final iteration. Bottom: Relative population of vibrational levels: 12000 K equilibrium distribution (dashed line), synthetic distribution (circle) and best fit (red cross).	77
5.1.	Centerline calibrated spectra.	80
5.2.	Best fits executed at 0.066 nm (first three figures) and 0.3 nm (last three figures) spectral resolution. Experimental (black) and computed equilibrium (red) spectra on the jet centerline.	82
5.3.	Top: Radial temperature profiles associated to 0.066 nm (triangle) and 0.3 nm (circle) spectral resolution fitting. Bottom: Squared correlation coefficient associated to 0.066 nm (triangle) and 0.3 nm (circle) spectral resolution fitting. . . .	83
5.4.	Top: Best fit accounting for N_2^+ , N_2 and CN molecular systems. Bottom: Synthetic representation of the relative contribution of each system.	84
5.5.	Top: Best fit accounting for N_2^+ , N_2 and CN molecular systems. Bottom: Synthetic representation of the relative contribution of each system.	85

5.6.	Top: Best fit accounting for N_2^+ , N_2 and CN molecular systems. Bottom: Synthetic representation of the relative contribution of each system.	86
5.7.	Top: Temperature (dashed line) and species concentration ratio N_2^+/N_2 (cross) radial profiles. Bottom: Radial LTE concentration computed using CEA equilibrium tool [66].	87
5.8.	Experimental spectra (top) and calculated LTE spectra (bottom).	88
5.9.	Radial evolution of the non-equilibrium scaling factor	89
5.10.	Top: Temperature profile used for radiative transfer calculation. Bottom: Experimental (black) and synthetic equilibrium (red) line of sight spectra (non-equilibrium factor at the centerline $\chi = 3.7$).	90
5.11.	Measured nitrogen atomic lines available from KURUCZ database [64]	91
5.12.	Top: Measured (black) and theoretical (red) emission for nitrogen line at 742 nm. Bottom: LTE temperature profile (solid line) and temperature profile corrected for self absorption (dashed line).	92
5.13.	Top: Measured (black) and theoretical (red) emission for oxygen triplet line at 777 nm. Bottom: LTE temperature profile (solid line) and temperature profile corrected for self absorption (dashed line).	93
5.14.	LTE temperature profiles (black) and mean LTE temperature profile (red) excluding the oxygen line at 777 nm.	94
5.15.	Line of sight reconstructed spectral radiance using optically thin (red line) or optically thick (dashed red line) LTE temperature profile and line of sight measurements of atomic lines (black circles).	95
5.16.	Boltzmann diagrams at various radial positions (black) and associated LTE distributions (red).	96
5.17.	Mean LTE (dashed line), electronic (solid line), molecular rotational and vibrational (dotted line) temperature profiles.	97
5.18.	H_β line measured at the center of the jet (black) and best fit (red).	98
5.19.	Measured electronic density profile (black) and density computed at equilibrium (red).	98
5.20.	Schematic of the setup.	100
5.21.	Experimental spectra (black) and associated best fits without CN contaminant (red) and with CN contaminant (blue circles).	101
5.22.	Top: Experimental spectra (black) and their associated best fits (red). Bottom: Best fits (red) and resolved contribution of N_2 2nd Positive (C-B) (blue) and N_2^+ First Negative (B-X) (green) systems.	102
5.23.	Top: Synthetic centerline spectra corresponding to <i>profile 1</i> - Line of sight (black), local (red). Bottom: Synthetic temperature profiles.	103
5.24.	Rotational and vibrational temperatures of $C^3\Pi_u$ and $B^3\Pi_g$ states of N_2 at 10 mbar (top) and 100 mbar (bottom) operating pressure.	104
5.25.	Top: Rotational and vibrational temperatures of $C^3\Pi_u$ and $B^3\Pi_g$ states of N_2 and vibrational temperature associated to $B^2\Sigma_u^+$ state of N_2^+ . Bottom: Corresponding geometric average temperatures.	106
5.26.	Top: Electronic population density ratio $N_{B^3\Pi_g}/N_{C^3\Pi_u}$. Bottom: Electronic population density ratio $N_{B^2\Sigma_u^+}/N_{C^3\Pi_u}$. Experiment (cross) and theoretical calculation (red).	107
6.1.	Wave structures that create the first expansion cell in under-expanded flow. . . .	110
6.2.	Oblique shocks that create the first compression cell in over-expanded flow. . . .	110
6.3.	Schematic of electronic double layer at a stationary shock front in weakly ionized gas.	117
7.1.	Locations of line of sight measurements in supersonic air plasma jets at 6 mbar (top) and 12 mbar (bottom) back pressure conditions.	120

7.2.	Raw and Abel inverted pictures of supersonic air plasma jets at 6 mbar (top) and 12 mbar (bottom) back pressure.	121
7.3.	Typical radiative signature of supersonic air plasma jet in the first expansion zone ($r = 0$ cm, $z = 2.5$ cm).	122
7.4.	Light intensity axial profiles for 6 mbar (top) and 12 mbar (bottom) back pressure conditions.	123
7.5.	<i>Case 1</i> ($p_b = 6$ mbar): Spectrally integrated radiance [$\text{W.m}^{-2}.\text{sr}^{-1}$] over [400-900] nm spectral range (left) and associated local emission [$\text{W.m}^{-3}.\text{sr}^{-1}$] (right).	124
7.6.	<i>Case 2</i> ($p_b = 12$ mbar): Spectrally integrated radiance [$\text{W.m}^{-2}.\text{sr}^{-1}$] over [400-900] nm spectral range (left) and associated local emission [$\text{W.m}^{-3}.\text{sr}^{-1}$] (right).	124
7.7.	Mach number axial profiles in the first expansion cell before the Mach disk.	125
7.8.	Computed axial expansion pressure (top) and temperature (bottom) profiles.	126
7.9.	LTE computation of species density profiles. <i>Case 1</i> (top), <i>case 2</i> (bottom).	127
7.10.	<i>Case 2</i> spectral emission at various axial locations on the symmetry axis [2.5 cm (orange), 6.5 cm (blue), 8.5 cm (pink) and 11.5 cm (green)].	130
7.11.	Best fit (red) and experimental spectra (black) at various axial locations on the symmetry axis. <i>case1</i> (top), <i>case 2</i> (bottom)	131
7.12.	Top: Calibrated spectra at 0.06 nm and 0.5 nm spectral resolution. Bottom: Typical best fit (red) and experimental H_β line	132
7.13.	Typical Boltzmann plot at $z = 2.5$, $r = 1.0$ cm (top) and $z = 12.5$, $r = 2.0$ cm (bottom).	133
7.14.	<i>Case 1</i> ($p_b = 6$ mbar): Interpolated temperatures and electron density iso-contours.	134
7.15.	<i>Case 2</i> ($p_b = 12$ mbar): Interpolated temperatures and electron density isocontours.	134
7.16.	Electron density interpolated profile on the symmetry axis (black). Analytical expansion and shock profiles (red). <i>Case 1</i> $p_b = 6$ mbar (top), <i>Case 2</i> $p_b = 12$ mbar (bottom).	135
7.17.	Top: Over-expanded jet. Bottom: N_2 First Positive spectra along the axis of the over-expanded jet.	138
7.18.	Vibrational equilibrium synthetic spectrum and corresponding vibrational bands contribution (top). Measured vibrational distribution (bottom).	139
7.19.	Top: Initial fitting condition at $T_{rot.} = T_{vib.} = 6000$ K (right). Bottom: Best fit obtained for $T_{rot.} = 5354$ K and $T_{vib.} = 5681$ K	140
7.20.	Equilibrium synthetic spectrum (black) and corresponding vibrational bands contribution at 2000 K (top) and 5000 K (bottom).	142
7.21.	Spectra fitting initial conditions. Top: Measured spectrum (black) and synthetic spectrum (red). Bottom: Synthetic vibrational population distribution.	143
7.22.	Spectra fitting iteration 101. Top: Measured spectrum (black) and synthetic spectrum (red). Bottom: Synthetic vibrational population distribution.	144
7.23.	Spectra fitting iteration 261. Top: Measured spectrum (black) and synthetic spectrum (red). Bottom: Synthetic vibrational population distribution.	145
7.24.	Spectra fitting converged solution. Top: Measured spectrum (black) and synthetic spectrum (red). Bottom: Synthetic vibrational population distribution.	146
7.25.	Sensitivity of the correlation coefficient R^2 relative to the fraction of the vibrational population at $T_{rot.} = 2708$ K.	147
7.26.	Meaningful synthetic vibrational population distribution (top) and corresponding vibrational band spectra contribution (bottom).	148
A.1.	Plasma cavity: overview.	153
A.2.	Plasma cavity: upper part.	154
A.3.	Plasma cavity: lower part.	155